Neutral Atom Ensemble Qubits and Rydberg Blockade

By

Matthew F Ebert

A dissertation submitted in partial fulfillment of

the requirements for the degree of

Doctor of Philosophy

(Physics)

at the

UNIVERSITY OF WISCONSIN – MADISON

2017

Date of final oral examination: 5/22/2017

The dissertation is approved by the following members of the Final Oral Committee:
Thad G. Walker, Professor, Physics
Mark Saffman, Professor, Physics
Deniz Yavuz, Professor, Physics
James E. Lawler, Professor, Physics
Randall Goldsmith, Professor, Chemistry

To my parents

Abstract

In this thesis, neutral atom ensemble qubits are discussed as a possible platform for future quantum information and quantum communication applications. Interactions between ensembles are mediated by the Rydberg interaction, which provides a switchable mechanisms for imposing large molecular interaction on length scales > 10 μm. Significant progress has been made towards a demonstration of an entangling gate operation between ensemble qubits. For example, clear demonstrations of the $\sqrt{N}$ collective Rabi frequency enhancement for mean ensemble populations of up to 16 atoms have been observed with no scaling factors. Also shown are very sub-Poissonian $\mathcal{N} = 1$ and 2 atomic Fock state generation fidelities of 62% and 48%, or Mandel parameters of -0.62 and -0.50. State tomography performed via two separate methods demonstrate that the intra-site $\mathcal{N} = 1$ Fock state that results has a postselected multi-partite entanglement threshold of $k/N = 0.82$ and 1.0. These indicated a high degree of $\mathcal{W}$-state entanglement in an ensemble qubit. The $\mathcal{W}$-state ensemble qubit coherence time has been measured to be 2.6 ms for $\bar{N} = 7.6$ atoms in the ensemble, and the coherence time appears to be limited by collisional dephasing, and not the fundamental operation. This coherence gives a coherence time to gate time ratio of 2600, and standard techniques exist in the field which should improve up this initial result. Finally, the first observation of Rydberg blockade between two ensemble qubits is also shown with a blockade fidelity of 0.89 and a result consistent with perfect ensemble-ensemble blockade if the data is postselected on an $\mathcal{N} = 1$ Fock state in the control ensemble. While a parity oscillation measurement was not performed,

the initial Bell state populations generated $(p_{01}, p_{10}) = (0.28, 0.26)$ would achieve a Fidelity of $F = 0.54$ assuming a maximal coherence measurement, which would exceed the $F = 0.5$ threshold for entanglement.

While we have observed the expected dynamics associated with perfect intra-ensemble and ensemble-ensemble blockade fidelities, evidence has also been accrued that suggest that an unanticipated fast Rydberg-Rydberg loss mechanism at long-range causes double Rydberg excitation events to appear as an $\mathcal{N} = 0$ Fock state event. An additional mechanism for short-range double excitations and molecular evolution is also discussed, which is posited to account for the discrepancy between the predicted $\sim 80\%$ $\mathcal{N} = 1$ Fock state fidelity and the observed $\sim 50 - 60\%$ fidelity.

A formalism is presented for efficiently modeling the evolution of Rydberg ensembles of up to about 30 atoms, given known sources of inhomogeneous broadening and decoherence. In-depth modeling of fluorescence signals under loss conditions, for different atom number ranges is discussed.

Finally, the development of a new experimental apparatus to replace the apparatus used in this thesis is presented.

Acknowledgments

The work presented in this thesis is not just the culmination of many years of effort by myself, but more so representation of the boundless teamwork, support, and faith that has been placed in me by more people in the department and my life, than I would have thought possible. Firstly, without my advisor, Thad Walker, his open door and enthusiasm for Physics, my graduate student career would be nowhere near as successful or enjoyable. I has been heartening to have such an exemplary role-model for success not just in Physics but in life as well. I have been lucky to also work closely with Mark Saffman, my Co-PI, over the years. I will always be grateful for the level of trust and autonomy afforded to me and my labmates. We had the space to make critical decisions, investigate interesting tangents, work on side-projects, and make the *occasional* mistake while simultaneously always having insights and advice from two incredibly experienced and complementary minds at our disposal.

My labmates, Alex Gill and Minho Kwon, were and are exceptional individuals to work with, both willing to put in late nights, and sometimes mornings, in the lab with and without me. None of the work in this thesis could have been acquired without the help of them. The "Rubidium" experiment has a long legacy of capable and hard-working people and while I haven't met all of them, I feel like I have gotten to know and appreciate the efforts of Erich Urban and Todd Johnson through their work. I did have the privilege of working with Larry Isenhower, while he was working on the AQuA project. I don't think I have ever had a conversation with Larry where his depth of knowledge on any

subject wasn't astounding. I am glad to have been a part of this tradition of students and I am glad to see it extending after. I am excited to see all that Minho and Chris Young, our newest addition, will accomplish in the coming years.

I have been fortunate to have been able to be a part of both the Walker and Saffman Labs, and the large number of people that I have worked with are too many to list here, but all are deserving of praise. Instead, I'd like to thank a few individuals who's mentoring was invaluable and those I have worked with closely. Larry, Jon Pritchard, Marty Lichtman, and Josh Issacs would without fail drop what they were doing to share their expertise when I was designing the new apparatus. In later years, I have had many similarly helpful conversations with Trent Graham, Donald Booth, and Mike Bulatowicz. Laura Fleming has been unequivocally irreplaceable in the lab. Every piece of custom electronics in the lab, including those in the appendices has either been designed, ordered, built, or at least maintained by her or under her supervision. I have also had the privilege of supervising many talented undergraduates over the years: Erik Meyers, Sydney Lybert, Josh Cherek, Andrew Micklich, Liev Birman, Alphonse Marra, Huaxia Zhou, Sebastian Malewicz, and our resident high school student who keeps everyone up on what is "cool" Ben Kufel. Erik and Sydney have been especially hard working and dedicated for multiple years, each taking on significant scale projects and always being willing to take on any task.

For a few years I also worked a couple hours a week as a space manager in Garage Physics the universities "maker space" lab, where I helped students design, build, and get funding for their personal projects. I attribute much of my technical knowledge to helping these kids develop their ideas into reality. I am grateful that Duncan Carlsmith and Brett Unks allowed me to participate for years at an early stage in this project.

The administrative ladies Aimee and Renee Lefkow, and Ann Austin (the classiest lady in Chamberlain) have done everything they could to make my time at Wisconsin enjoyable and bureaucratically stress-free. Each one of these ladies has bent over backwards to solve

any issue I had before I even could think to ask them about it. I am glad that I have been able to develop friendships with them over the course of my time here.

I don't think I could have made it through grad school without my partner in crime Ian Wisher, who could put a smile on any in the department's face without even trying. Ian helped me through my lowest points and was always there when I needed some encouragement or to complain about something. Nothing is better than working on a project on Saturday with Ian.

Finally, my family. Anne has been a more ideal partner in the last couple years than I could have imagined. She has somehow managed to help me figure out when it is important enough to stay at work and when I need to come home. She brings out the best in me and I can only aspire to the same. Amy, Will and Kala were always there when I needed family and I have loved watching Kala grow up so close by. My parents deserve the most credit for any success I have. I don't know how, but I think they knew I would be a physicist before I even knew what it meant. Without their constant love and support, I don't want to think about where I would be now. The only thing about my tenure at Wisconsin that I would have changed is that my grandparents could have seen me finally finish school. To them the only thing more important than my education, was making sure I knew I was loved.

Thank you all.

Contents

Chapter 1

Introduction

The development of useful quantum bits (qubits), quantum memories, and deterministic generation of remote entanglement promises significant advances in many areas of research and applications of the new technology. The search for an ideal physical platform to properly reproduce the idealized characteristics of a qubit spans two decades and has seen considerable progress. The technical challenges inherent in such an endeavor are considerable, but so is the promised return on investment in terms of new technology. Because of this promise, proposed physical platforms have abounded and demonstrations of excellent one- and two-qubit gates fidelities have been shown[1–4]. However, none of these same platforms have an engineering blueprint to achieve the level of scalability required to make a useful quantum computation device[5–7], which without new proposals will limit the number of logical qubits available for a computation. Scalability becomes even more of a limiting factor when recent theoretical results are considered[8, 9], which demonstrate the cost, in "overhead qubits", of limited qubit inter-connectivity and error-correcting schemes. In this work, we investigate the use of neutral atom ensemble qubits, with interactions mediated by the Rydberg blockade mechanism, to develop a scalable platform for qubits and quantum memories.

This thesis presents, in detail, the fundamental single-ensemble entangling operation,

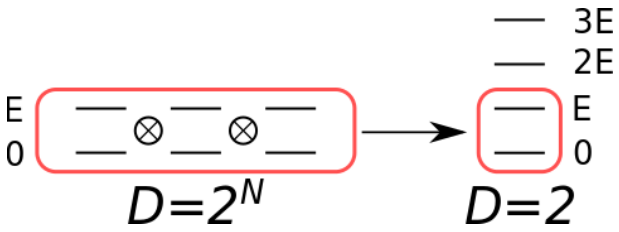

Figure 1.1: A diagram of an ensemble qubit composed of $N = 3$ constituent two-state systems. In the ensemble, the maximum energy of the system is restricted to a single excitation. Information is stored in the two lowest energy levels of the ensemble qubit.

proves a high degree of post-selected entanglement of the resulting excited state of the ensemble, and demonstrates strong interactions between two ensemble qubits in preparation for a demonstration of a two ensemble entangling gate. I also discuss the prospects for improvement of these metrics, propose a mechanism that is believed to be the leading contributor to limiting the fidelity of the operations, and propose a method for the mitigation of this mechanism.

Ensemble qubits are systems, composed of constituent sub-systems, where quantum information can be encoded in one or more effective two-state qubits[10, 11], see Figure 1.1. In the particular neutral atom implementation described in this work, an ensemble qubit is a collection of atoms that are manipulated in a way where the individual atoms are identical, not distinguishable, and addressed by external fields simultaneously. In atom qubit implementations, information is typically encoded in the hyperfine manifold of the ground state of the sub-systems, as these states are well isolated from environmental decoherence effects, which degrade the performance of the system.

While ensemble qubits complicate some aspects like collisional decoherence channels and inhomogeneous broadening, there are significant advantages that make ensembles a convenient qubit implementation. Deterministically preparing an array of single atoms quickly, simply, and efficiently is an outstanding problem in the field. Although much progress has been made in recent years[12–16], a solution which satisfies all three criteria is still wanting. In contrast, deterministically preparing an ensemble of atoms with $N > 1$ in every site in an array is a standard practice, requiring no additional complexity. With

information encoded in an ensemble, atom loss events are not a critical error, as with single atom qubits, and information can be recovered with an appropriate error correction scheme[11]. Finally, the ensemble experiences an increased coupling to a particular propagation mode of the light field enabling quantum repeater protocols with no external cavity enhancement[17].

There are many quantum information and communication schemes developed for ensemble systems. A few schemes that are relevant to our implementation will be discussed here. This work will focus on cataloging the progress made in developing a Rydberg interaction mediated ensemble qubit architecture for use in these applications.

1.1 Collective Enhancement

Before preceding, it is necessary to introduce the concept of a collective Rabi frequency enhancement. The excitation of a N-atom ground state to the entangled N-atom $\mathcal{W}$-state has an inherent $\sqrt{N}$ increase in the effective Rabi oscillation frequency over the single-atom Rabi frequency. In the case of strongly blockaded ensemble systems, the $\sqrt{N}$ collective Rabi frequency enhancement is apparent due to the suppression of higher excitation number states, and serves as an excellent observable for Rydberg blockade[18–21], as well as an indicator for the degree of $\mathcal{W}$-state entanglement[21].

For an ensemble qubit with stochastic atom number preparation, the $\sqrt{N}$ dependence of the collective Rabi frequency can cause pulse area timing errors if the atom number is not known. To mitigate this issue, the atom number could be measured before the pulse is applied. Alternatively, if the distribution of atoms in the trap is Poissonian, a larger mean number of atoms in the ensemble will decrease the sensitivity to the exact atom number. Otherwise, composite pulse schemes[22] or STIRAP/ARP pulses[23–25] can be introduced that minimize the effect of stochastic loading.

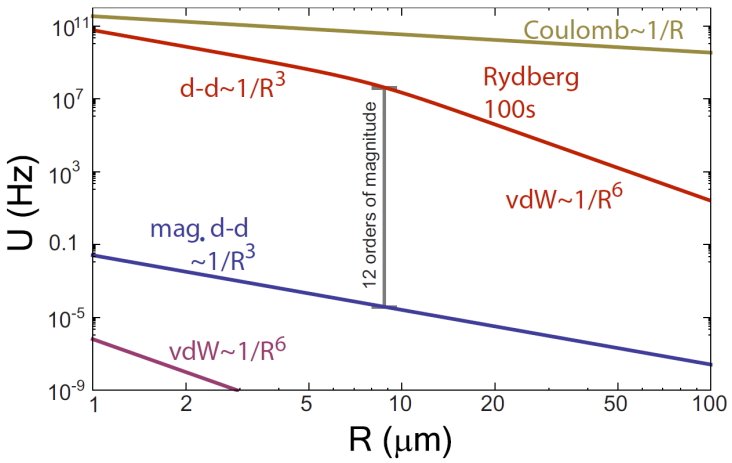

Figure 1.2: Figure is reprinted from reference [26], and shows the scale of the relative molecular interaction strengths at some inter-atomic distance (R) between ground state atom pairs (Van der Waals and magnetic dipole-dipole interactions), Rydberg atom pairs (electric dipole-dipole interactions), and ion pairs (Coulomb interactions). The Rydberg interaction goes as R^{-3} at short range in the Förster regime and R^{-6} in the Van der Waals regime at larger separation.

1.2 Ensemble Qubit Protocols

All qubit protocols discussed here utilize the "Rydberg blockade" phenomenon to provide a switchable interaction between qubits 12-orders of magnitude larger than interactions between ground state atoms[26], Figure 1.2. The Rydberg blockade is an effect of a strong interaction energy, $\Delta_{dd}(R)$, between atoms with inter-atomic separation R in Rydberg states which are highly excited principle quantum number states n. When the interaction energy is sufficiently large compared to the light single-atom coupling, Ω_1, excitations inside a volume surrounding the initial excitation are off-resonant and therefore suppressed, and we say that the atoms in this volume experience Rydberg blockade, Figure 1.3.

In the strong interaction limit, $\Delta_{dd} \gg \Omega$, the excitation of $|rr\rangle$ is negligible and effectively reduces the Hilbert space of the problem to a two-state system with a collective basis, denoted in this work by $\{|\bar{0}\rangle, |\bar{r}\rangle\}$, Figure 1.4. The $|\bar{0}\rangle \equiv |0^{(1)}...0^{(n)}\rangle$ state is the product state with all atoms in the ensemble in the initial non-interacting ground hyperfine state $|0\rangle$. The $|\bar{r}\rangle$ state is the entangled collective symmetric singly-excited state of the

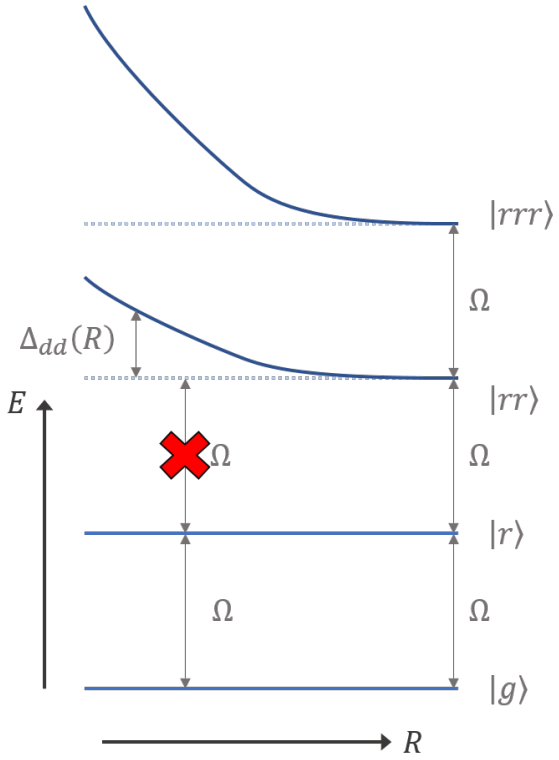

Figure 1.3: Energy level diagram of an ensemble of atoms with different number of Rydberg excitations separated by a distance R. At long range the interaction energy $\Delta_{dd}(R)$ is small and excitations of two or more Rydberg atoms is possible. At shorter ranges the interaction energy grows and prevents the excitation of the two atom state, which truncates the maximum excitation number to 1 within some volume.

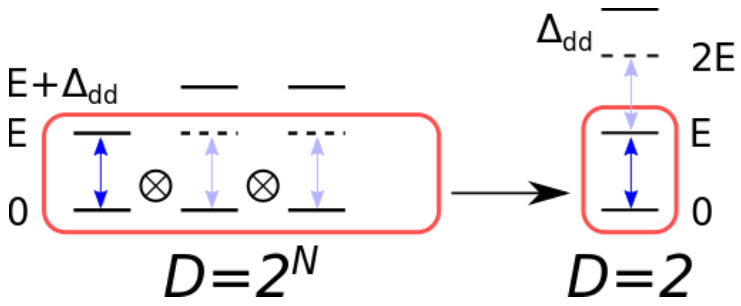

Figure 1.4: A diagram of an ensemble qubit composed of $N = 3$ constituent two-state systems with a single Rydberg interaction. The ensemble energy diagram (right) shows the effect of the Rydberg dipole-dipole interaction energy, which shifts the energy of the second excitation by Δ_{dd}. If the Rabi frequency driving state transitions is significantly larger than the interaction shift $\Omega \gg \Delta_{dd}$, the system will remain in the two-level Hilbert space defined by the ground and singly excited state.

ensemble and is defined as:

$$|\bar{r}\rangle \equiv \frac{1}{\sqrt{N}} \sum_{k=1}^{N} |0^{(1)}...r^{(k)}...0^{(N)}\rangle, \tag{1.1}$$

where $|r^{(k)}\rangle$ is the Rydberg state of the k^{th} atom in the ensemble. A symmetric singly-excited state of a system of spin 1/2 particles is known as the $\mathcal{W}$-state[27]. We therefore will refer to the state $|\bar{r}\rangle$ as the Rydberg $\mathcal{W}$-state.

If the Rydberg state was stable and well isolated, it would be reasonable to allow population to remain in $|\bar{r}\rangle$ for the duration of any computation. However, the Rydberg state has a short lifetime, $T_1 \sim 300$ μs for $n = 100$[26], relative to the lifetime of the ground hyperfine manifold, and is sensitive to external fields. It is therefore necessary to map the Rydberg population to a ground state, $|\bar{1}\rangle$, in another hyperfine manifold to achieve long coherence times. The state $|\bar{1}\rangle$ is also a $\mathcal{W}$-state of the ensemble. Since this is the state we detect directly, we will refer to this as the $\mathcal{W}$-state for most purposes, however in the text the specific $\mathcal{W}$-state should be able to be inferred from context. Since this third state is only ever used as a Rydberg population map for storage and is never simultaneously addressed with $|\bar{0}\rangle$, the system can still be considered a two-level system with an additional "overhead" state for most purposes.

Protocols using Rydberg interaction mediated ensemble qubits differ substantially from single atom qubit protocols in the implementation of local rotations. In typical single atom qubit local rotations, a Raman laser or microwave is used to drive transitions between qubit states[28]. However, for ensemble qubits, local rotations must be done through the Rydberg state to preserve control of excitation number, which encodes the state of the qubit. This means every ensemble qubit protocol will begin and end with a single-atom π rotation, $\hat{\pi}_1^1$, $|1\rangle \leftrightarrow |r\rangle$ so that the state of the qubit is stored in the "storage basis" $\{|\bar{0}\rangle, |\bar{1}\rangle\}$, but all gates occur in the "computational basis" $\{|\bar{0}\rangle, |\bar{r}\rangle\}$. A single qubit rotation with angle θ and phase ϕ between $|\bar{0}\rangle$ and $|\bar{1}\rangle$ is implemented by:

$$|\psi'\rangle = \hat{\pi}_1^1 \hat{\theta}(\phi)_{\bar{N}}^0 \hat{\pi}_1^1 |\psi\rangle,$$

Where the notation $\hat{\theta}_n^s$ indicates an n-atom collective rotation by pulse area θ between state s and the Rydberg state r. In this notation, two-qubit C_Z gate between two ensemble control and target qubits C, T is implemented by:

$$|\psi'\rangle = \hat{\pi}_1^{C1} \left(\hat{2\pi}\right)_1^{T1} \hat{\pi}_1^{C1} |\psi\rangle,$$

where the new superscript in $\hat{\theta}_n^{Ls}$, L, identifies the different ensembles.

Encoding multiple qubits into the different magnetic hyperfine sub-levels of an ensemble has been proposed as an extension of the basic protocol described previously[10, 11]. Here the storage basis is the excitation number in each of the hyperfine sub-levels, while the computational basis requires at least two separate Rydberg states to be used to prevent mixing since all qubits are spatially indistinguishable, and therefore must be spectrally multiplexed.

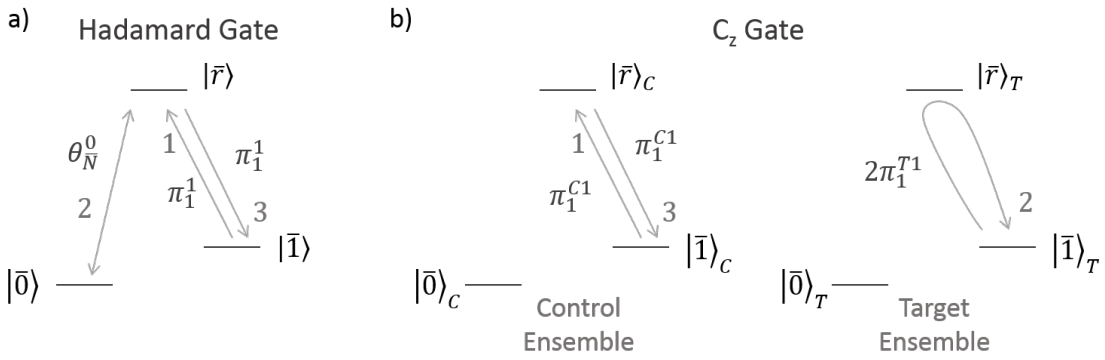

Figure 1.5: Gate protocols ensemble qubit schemes for (a) a Hadamard gate and (b) a C_Z two-qubit gate.

1.3 Quantum Communication with Ensembles

The distribution of quantum information between distant nodes has interesting applications, such as distributed quantum computing[29, 30], sensing, metrology[31, 32], and cryptography[33]. The Ekert protocol [33] can be implemented by direct transmission of an Entangled Pair Source (EPS) to generate remote entanglement between nodes, Figure 1.6(a). Since loss mechanisms in a distribution channel, such as an optical fiber, are exponential in the length of the fiber, there is a practical limit imposed on the distribution radius of the quantum information. For light in a telecom fiber the attenuation constant is 0.2 dB/km [34], which at a length scale of 300 km will reduce the effective data rate by 6 orders of magnitude. Quantum repeaters can be used to break up the length between nodes into smaller segments, reducing absorption losses and potentially extending the range of the network. However, without a quantum memory at the nodes all entanglement purification steps must simultaneously succeed, the probably of which also decreases exponentially with the number of nodes, Figure 1.6(b).

Quantum repeaters with quantum memories at EPS nodes, implemented using the DLCZ protocol[35], can extend the range of these quantum networks on lossy channels, using heralded entanglement and entanglement swapping to reduce the loss from expo-

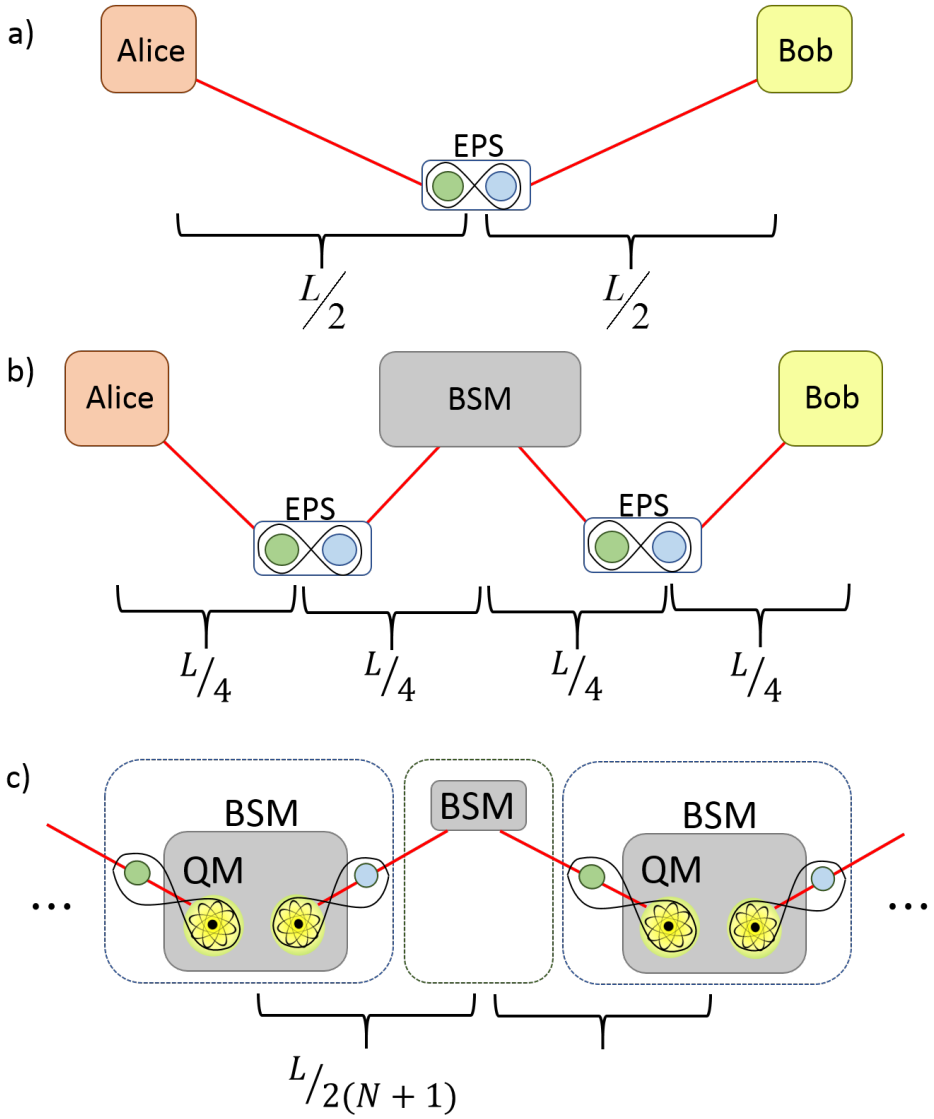

Figure 1.6: Variations of quantum communication channels between two end nodes Alice and Bob. (a) A single link network where an entangled pair source (EPS) is used. A single link is practically limited in distance by absorption or other losses in the channel. (b) A channel with a single repeater node implemented with entanglement purification implemented with a Bell state measurement device (BSM). Here the absorption losses are halved but both links must succeed simultaneously for the protocol to succeed. (c) Two nodes in a single channel with quantum memories (QM) implemented to store successful remote entanglement events. Entanglement swapping is performed on the QMs.

nential to polynomial. The DLCZ scheme is implemented by probabilistically generating entanglement, through a short collective excitation, between the internal state of both memory qubits at each node with a photonic qubit, Figure 1.7. The photons from each subsegment of the network, i.e. photon from nodes A and B or C and D, are directed to be incident on a 50/50 beamsplitter, such that detection of a photon on either detector does not determine the source of the photon. A measurement of a photon on either detector heralds the creation of an entangled state of the two remote node memory qubits with state: $|\psi\rangle = \frac{1}{\sqrt{2}}\left(|\bar{0}_L\rangle|\bar{1}_R\rangle + e^{i\phi}|\bar{1}_L\rangle|\bar{0}_R\rangle\right)$. If no photon is detected, the procedure is repeated until a photon is detected. Entanglement swapping between adjacent entangled segments can then be implemented to extend the distance spanned by an entangled pair. To do this the intermediate nodes, B and C, are addressed to produce a photon if they are in the singly-excited state. The generated photons are sent incident to another beamsplitter and pair of single-photon detectors, which if a single photon is detected implies that the remote nodes, A and D, share a single collective excitation and are entangled.

Since the DLCZ scheme relies on the production of the collective symmetric singly excited state ($|\bar{1}\rangle$) of the ensemble with negligible double excitation probability, incorporation of Rydberg blockade is a clear improvement over the original probabilistic scheme since it can produce collective single excitations in an ensemble with near deterministic fidelities. With some changes to the protocol, a two-photon coincidence event heralds the creation of remotely entangled nodes at significantly higher rates[36, 37]. The improved protocol is less susceptible to dark count induced errors since instead of measuring a photon Fock state, a two photon coincidence event is measured. Incorporation of quantum error correction protocols at the nodes further improves the rate of entanglement generation[38]. Since Rydberg blockade can be used to generate entanglement[3], create on-demand directionalized single photon emission[39, 40], and perform error correction routines it stands as a strong candidate for a quantum communication architecture at current entanglement generation fidelities. Recent demonstrations of photon-ensemble

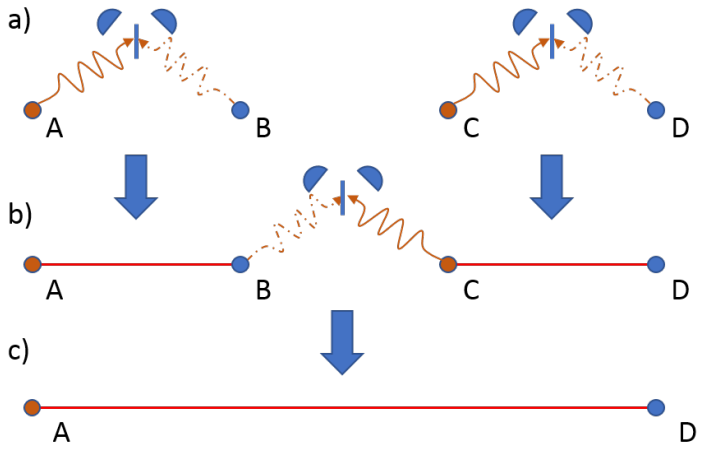

Figure 1.7: A schematic representation of a DLCZ protocol with 4 nodes A, B, C, and D. (a) Photons (curved lines) are entangled with the state of an atomic ensemble (circles) at each node and sent to a beamsplitter and pair of single-photon detectors for each pair of adjacent nodes. The solid and dashed photon lines represent that, in the original DLCZ protocol, at most a single photon will be emitted from the node pair. Entanglement (red line) is post-selected by the measurement of a single photon, which heralds the creation of a single collective excitation between the two nodes A(C) and B(D). If no photon is observed, then the photon generation step is repeated. (b) Once the nodes are determined to be entangled, then the entanglement distance is increased by entanglement swapping. Photon generation steps are implemented on ensembles B and C such that if the initial excitation Fock state was $|1\rangle$ then a photon is created and a similar post-selection measurement takes places between the two nodes. (c) If a photon is detected, then the entanglement is swapped between the segments and now A and D are in an entangled state which extends the entanglement distance.

entanglement by Li et al.[40], Rydberg blockade between ensemble qubits by Ebert et al.[41], and quantum memory lifetimes of a few ms by Ebert et al.[41] lay the groundwork for the demonstration of a simple Rydberg-mediated DLCZ based quantum repeater in the near future[42].

1.4 Apparatus

The apparatus used in the experimental work contained in this thesis was constructed and modified by the collective effort of many PhD students for about a decade before I joined the lab. Improvements have been made to the existing system to enhance performance, stability, and automation of the experimental process, however the basic underlying properties are the same. The intention of this section is to give a brief overview of the experiment and to provide an accurate snapshot of an ever-evolving apparatus, so that the reader can quickly proceed with the necessary knowledge to discussion of the experimental work in the following chapters. For a more in-depth discussion of parts of the apparatus the reader is referred to the following PhD theses: [25, 43–45]. A block diagram of the apparatus is shown in Figure 1.8. A functional diagram focusing on the individual FORT sites used in the experiments and an energy level diagram is shown in Figure 1.9.

It should also be noted that the experimental apparatus described in this section has been superseded by a new apparatus. The new apparatus is a complete overhaul of the system and is discussed in detail in Chapter 8.

1.4.1 Experiment Control and Data Acquisition

An experiment is preprogrammed into the data acquisition (DAQ) system via a LabView controller. The DAQ is able to generate digital timing sequences with 20 ns precision and analog waveforms with a 100 kHz update rate. A repurposed counter serves as an

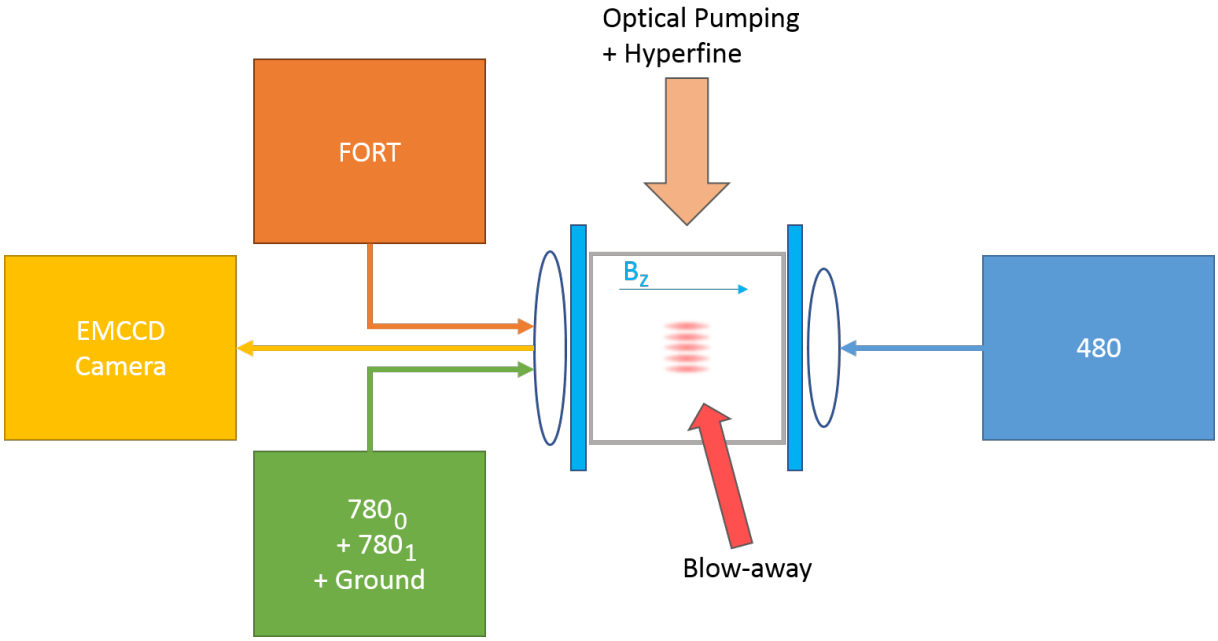

Figure 1.8: A simplified block diagram of the experimental apparatus. The 1064 nm FORT and is linearly polarized, while the $780_{0(1)}$ lasers, the ground state rotation laser, and the 480 nm laser are all σ_+ polarized, with respect to the quantization axis $\hat{z}$ defined by the magnetic field $\mathbf{B} = B_z\hat{z}$. All of these lasers are collinear and propagate along the z-axis which is horizontal. The 795 nm optical pumping laser propagates vertically along $\hat{y}$ and is linearly polarized along $\hat{z}$, such that it pumps into the $|F = 2, m_F = 0\rangle$ dark state. The 780 nm blow-away is circularly polarized and propagates along $\hat{x}$. The magnetic field is switched to point along $\hat{x}$ during the blow-away procedure to minimize Raman scattering events. The MOT beams are omitted for clarity.

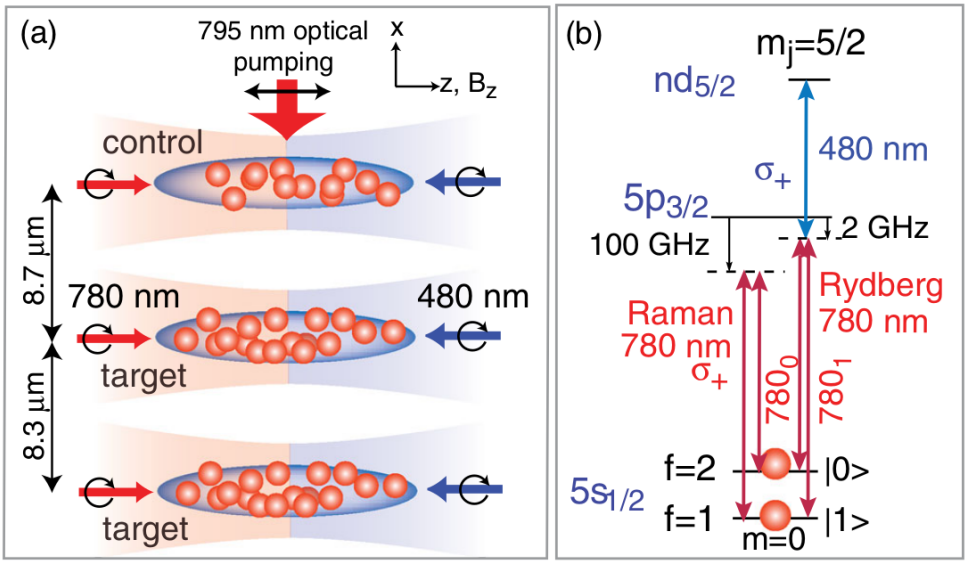

Figure 1.9: (a) A functional diagram of the experimental phase with multiple ensembles. The atoms are prepared in $|\bar{0}\rangle$ by the 795 nm optical pumping laser, and then ensemble sites are addressed via frequency shifts on 780 and 480 pointing AOMs, according to the specifics of the experimental control sequence. (b) The energy level diagram for single atoms. The Ground state rotation (Raman) laser is 100 GHz red-detuned from the D2 transition. The $780_{0(1)}$ lasers, along with the 480 nm laser is resonant with the $|0(1)\rangle$ ground state, but the lasers are red-detuned from the intermediate $5P_{3/2}$ state by 2 GHz.

automatic veto system, where data points can be excluded from the analysis if certain parameters are outside of predefined bounds, such as environmental magnetic fields, laser power, and laser servo state. The experiment repeats with a period of about 600 ms, which is set by the time to load the maximum number of atoms used in an experiment. The cycling time is kept constant for all data since the large quadrupole field coils are oriented parallel to the optical table, and will slowly magnetize the table over the course of a few hours based on the average magnetic field. This would cause drifts in the background magnetic field if the cycle time of the experiment was changed, so all experiments were performed with the same quadrupole duty cycle and the magnetic field was kept cycling overnight to minimize the drift.

The experiment can be broken into four distinct phases of operation: Atom preparation, State preparation, Experiment, and Detection. Relevant details about these phases are discussed below.

1.4.2 Atom Preparation

The vacuum chamber consists of a 4.5" spherical cube vacuum chamber, filled with $\sim 10^{-8}$ torr of background Rb^{87} . The atoms are cooled from the background and trapped in a Magneto-Optical Trap (MOT). The MOT is in a standard 3 orthogonal beam retro-reflection configuration, with a pair of 56 A water-cooled quadrupole field coils, see Figure 1.10. Five parallel Far Off Resonance Trap (FORT) locations are generated by a diffractive element from a single $\lambda = 1064$ input beam. The FORT axis is rotated about the vertical axis 45 degrees from the MOT quadrupole field. A variable number of atoms are loaded from the MOT into the FORT sites, by adjusting the MOT loading time and the time spent in the cooling phase, which induces light-assisted collisions. The MOT quadrupole field is turned off during the FORT loading phase and is negligible by the first camera exposure > 100 ms later.

Atoms in the FORT sites have an axial distribution of $\sigma_z = 7$ μm and σ_r=0.7 μm and

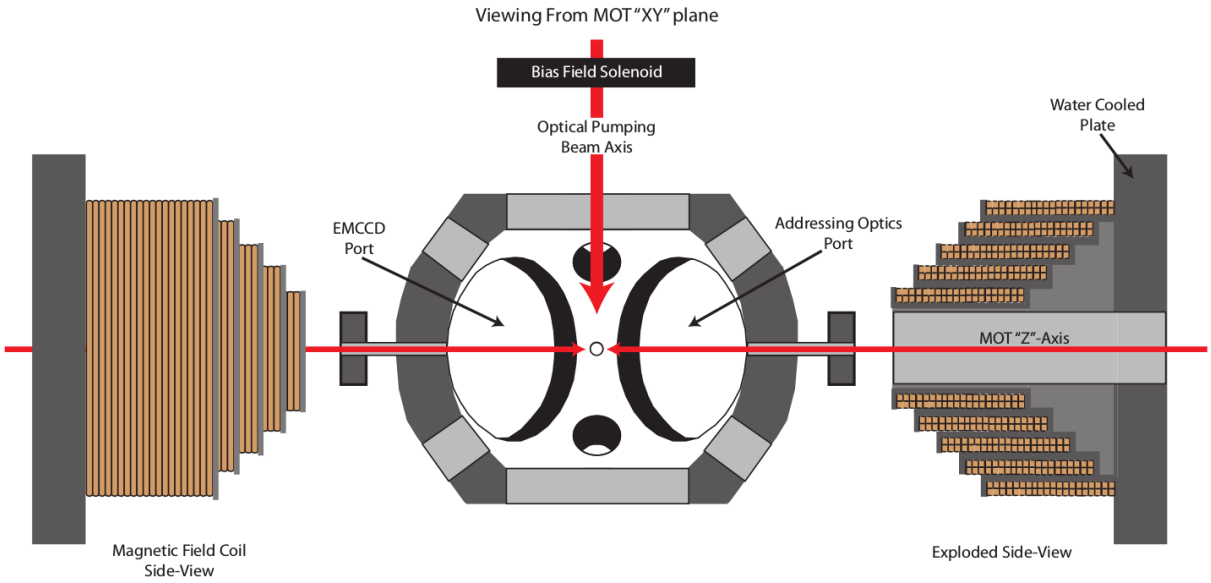

Figure 1.10: Diagram of the old MOT viewing along the XY-plane with water-cooled quadrupole coils, reused from reference [44]. Not to scale.

temperatures of 100-200 μK, measured by drop and recapture experiments. To a good approximation the atom clouds can be considered to be 1 dimensional.

1.4.3 Detection

Trapped atoms are detected via fluorescence collected on an Electron Multiplying CCD (EMCDD) camera from the MOT and Hyperfine (HF) repumping lasers, while the atoms are held in the FORT. The atom number is detected via threshold measurements of the background subtracted atom signal from an integrated 3x3 region of interest for each trap region. The FORT and MOT light are chopped out of phase at 1.25 MHz during this stage to prevent heating due to anti-trapping of the excited state. This reduces the time that the atoms are actually scattering photons by 50%. The fast chopping rate is significantly higher than the trap oscillation modes, so little energy is transferred to the atoms while chopping. Details on the fluorescence imaging are discussed in depth in Chapter 7. For single atom experiments an initial camera exposure is used to post-select events where an atom was present. Multi-atom experiments have only a single camera exposure at the

end, since it is assumed the loading rate is constant, since measuring the atom number in a multi-atom sample is a partially destructive process. After the first readout time slot (as is may not be performed), a cooling/light-assisted collision phase is implemented for 2-20 ms depending on the desired atom number for the experiment.

State-selective readouts are performed destructively via unbalanced radiation pressure near resonant with the $F = 2 \rightarrow F' = 3$ cycling transition, ideally heating and ejecting an atom in $F = 2$ before a Raman event changes the internal state to $F = 1$ and stops scattering photons. The "blow-away" light is circularly-polarized, and directed radially onto the FORT sites with a magnetic field in the same direction to maximize the number of scattering events before a Raman transition event.

1.4.4 State Preparation

The atoms must be prepared in a single initial state for the desired experiment. A 1.5 ms optical pumping phase where atoms are prepared in $|0\rangle = |5S_{1/2}, F = 2, m_F = 0\rangle$ is performed using a linearly polarized 795 nm laser resonant with the D1 $F = 2 \leftrightarrow F' = 2$ transition. Since the $\Delta m_F = 0$ transition is forbidden for electric dipole transitions if $\Delta F = 0$, the atomic population builds up in the $|0\rangle$ dark state. The transverse magnetic fields are shimmed to optimize the optical pumping fidelity for the state preparation phase and the experiment phase. Since the magnetic field is shimmed to the optical pumping polarization it is critical to align the polarization with the propagation vector of the FORT and addressing lasers. This ensures that the addressing laser polarization is well defined in the quantization direction defined by the magnetic field.

Local rotations to the atoms can be performed with a stimulated Raman laser which is fast and site-selective ($\Omega \sim 2\pi \times 600$ kHz), or a global microwave horn ($\Omega \sim 2\pi \times 5$ kHz) which can drive transitions between F hyperfine manifolds. Either system can be used to prepare the atoms in arbitrary mixtures of $|0\rangle$ and $|1\rangle$, but cannot be used for single atom rotations in ensembles.

1.4.5 Rydberg Excitation

The Raman laser, the 780_0, and the 780_1 lasers all enter the optical train through the same single mode PM optical fiber. The common path that all these lasers take through the system is known as the 780 addressing laser system, which consists of some optics to adjust the beam size and position, and also a pointing Acousto-Optic Modulator (AOM). The pointing AOM is in a Fourier plane from the trap sites so that changes in the deflection angle are mapped to the position of the light in the atom plane. Changing the pointing AOM frequency allows rapid sequential addressing of multiple trap sites during an experiment. The 780 addressing laser system has beam waists at the atom plane of $\omega_{(x,y)} = (9, 7)$ μm.

A similar pointing AOM scheme is implemented for the 480 addressing laser path, with the opposite diffraction order used to partially cancel the frequency shift from addressing different trap sites. The remaining frequency shift ($\sim$ 4 MHz/site) is then compensated upstream on the Rydberg $780_{0(1)}$ laser AOMs. The 480 addressing laser has beam waists of $\omega_{(x,y)} = (5.6, 4.7)$ μm at the atoms.

The single-photon Rabi frequencies for the Rydberg transition are typically $\Omega_{780} = 2\pi \times 160$ and $\Omega_{480} = 2\pi \times 17$ MHz with a -2 GHz detuning from the $D2$ transition, which gives a two-photon Rabi frequency of $\Omega_0 = 2\pi \times 750$ kHz. Rydberg excitation times are controlled by the timing of the 780 lasers, while the 480 laser remains on for the duration of the experiment phase.

1.5 Summary

This thesis discusses experiments and analysis performed in development of a Rydberg interaction mediated ensemble qubit architecture.

Single-site Rydberg blockade experiments are discussed in Chapter 2, where Fock states of the excitation number and trap population are produced for $\mathcal{N} = 1$ and 2[20].

The dynamics of the interaction are shown to conform to theoretical predictions. The observation of the excitation rate scaling as $\sqrt{\bar{N}}$ in a regime where inhomogeneous broadening allows for the observation to be done for up to $\bar{N} \sim 15$ atoms with no free parameters. Additionally no evidence was observed for two atoms in the $|1\rangle$ state that exceeded the measured background rate. However, the probability to produce a single $|1\rangle$ excitation is observed to be about 15% lower than the expected 80% success rate. Identification of a mechanism to explain the amplitude discrepancy motivated many of the subsequent experiments and analysis contained in this work. A full discussion of this observation will be reserved for Chapter 5, following discussion of the remaining experiments.

Chapter 3 presents evidence that the $\mathcal{N} = 1$ state generated is in fact the $\mathcal{W}$-state[41]. This is done by observation of a 2.6(3) coherence time in the storage basis via a Ramsey experiment and a $\mathcal{W}$-state tomography experiment. The state tomography is performed by measurement of the total internal angular momentum of the ensemble which is used as a witness observable for entanglement. The total angular momentum is measured both with a Z-rotation and an X-rotation. Thresholds for entanglement are exceeded without the assumption of no double excitations of $|1\rangle$. Using the fact that our system does not produce double excitations of $|1\rangle$ the threshold for entanglement exceeds the threshold for k-partite entanglement with 86% of the atoms in the ensemble.

Chapter 4 discusses the first demonstration of ensemble-ensemble Rydberg blockade[41]. We observe an 89% reduction of the target site amplitude, and a result consistent with perfect ensemble-ensemble blockade when post-selecting on a control ensemble excitation event. We also note an observed loss phenomenon of atoms in the Rydberg state by observing the success probability of an excitation as a function of a target site pulse. This is clear evidence of an unanticipated destructive Rydberg-Rydberg interaction between trap sites, especially when considering that the inter-site blockade appears to work better than expected.

Chapter 5 discusses possible sources of the amplitude discrepancy first noted in Chap-

ter 2, consolidating the observations of Chapters 2, 3, and 4 into a proposal for a hypothetical Rydberg-Rydberg loss mechanism and a potential experiment to test the hypothesis. In addition to the experiments already presented, a few supplementary experiments are discussed, which were less conclusive to solving the discrepancy, but carry weight in the discussion.

Chapter 6 lays out a formalism for modeling inhomogeneous broadening in Rydberg ensembles as well as single atom Rydberg systems. Additionally single site experiments are modeled for atom numbers up to $N = 30$ including the effect of imperfect Rydberg blockade shifts.

Chapter 7 presents various camera signal models employed in the experiment. Single-, multi-, and few-atom camera signal models are employed based on the atom number and collisional loss characteristics in the relevant experiment. This is how the ensemble atom number is measured for the rest of the experiment. Additionally the state selective readout method is described.

Finally, the new apparatus we have built to replace the apparatus used in this thesis is described in Chapter 8, and Chapter 9 discusses future directions for the experiment.

Chapter 2

Fock State Experiments

The deterministic preparation of a controlled, arbitrary number of neutral atoms, $\mathcal{N}$, occupying a trap site is an outstanding problem in the field. The special case of $\mathcal{N} = 1$, referred to as single-atom loading, is useful for deterministically producing a lattice of single atoms which is a starting point for many proposed protocols using neutral atoms in quantum computation [46], quantum key distribution[47], and simulation of condensed matter physics[48]. Techniques demonstrated in recent years have improved the state of the art beyond the 50% filling fraction limit obtained with two-body losses[49]. Single-atom preparation probabilities have reached 91% in 542 ms with blue detuned light assisted collisions [12] and 95% in $>$ 1 s by creating a Mott insulator [13]. Additionally moving tweezers methods have been demonstrated, where defect free arrays are created by compression from a low filling fraction array in 400 ms [14, 15]. In the case of fermions, generation of arbitrary atom number site preparation up to $\mathcal{N} = 10$ has been accomplished with fidelities of $\sim 90\%$, and 96% for $\mathcal{N} = 2$ [16]. In this chapter we discuss a procedure to prepare arbitrary numbers of atoms in a single site using Rydberg blockade. We will also demonstrate the site preparation procedure for $\mathcal{N} = 1$ and 2 atoms at rates of 63% and 48%, achieving sub-Poissonian loading with a Mendel factors of $Q = \sigma_N^2/\bar{N} = -0.62$ and -0.50 respectively[20].

A single atom can be selected from an ensemble of N atoms in a trap site by using Rydberg blockade to energetically limit the ensemble to a single collective excitation. A collective, coherent π_N-pulse, $t_{\pi_N} \equiv \pi/\sqrt{N}$ produces at most a single excitation. The single Rydberg excitation can then be mapped to the trap population by a state selective removal procedure. If the initial atom number cannot be accounted for in the π_N-pulse timing, then the N-dependence of the collective Rabi frequency, $\Omega_N = \sqrt{N}\Omega$, will contribute to shot-to-shot pulse area errors and limit the fidelity of the operation. The probability of a successful Rydberg excitation, P_r, for an instance of N atoms with a collective $\pi_{\bar{N}}$-pulse chosen for a Poisson distribution with mean $\bar{N}$ is given by:

$$\begin{aligned} P_r(t = \pi_{\bar{N}}) &= \sin^2\left(\sqrt{N}\Omega\pi_{\bar{N}}/2\right) \\ &= \sin^2\left(\frac{\pi}{2}\sqrt{\frac{N}{\bar{N}}}\right) \\ &= \sin^2\left(\frac{\pi}{2}\sqrt{1-\frac{\Delta N}{\bar{N}}}\right) \\ &\approx 1 - \left(\frac{\pi\Delta N}{4\bar{N}}\right)^2, \end{aligned} \tag{2.1}$$

where $\Delta N \equiv \bar{N} - N$. Averaging N over a Poisson distributed sample, the Rydberg excitation probability is given by:

$$\langle r \rangle \approx 1 - \frac{\pi^2}{16\bar{N}}. \tag{2.2}$$

With $\bar{N} = 10$ atoms the Rydberg excitation probability is $> 90\%$, and for fidelities of 99% $\bar{N} \sim 60$ is necessary. The atom number requirement can be lowered by using composite pulse sequences to minimize the pulse area errors for smaller mean atom numbers[26].

If the Rydberg excitation is then moved to a "storage" state, the Rydberg excitation and storage procedure can be repeated to transfer single atoms one at a time from the initial state to the storage state. This allows one to prepare, with high fidelity, an arbitrary

atom number state in the site. Since the transfer from Rydberg state to storage state is also energetically limited by the Rydberg blockade mechanism, atoms can be "pumped" discretely without worry of population leakage back into the initial state. When the desired number of atoms, $\mathcal{N}$ are occupying the storage state, the initial state can be selectively removed, leaving the discrete atoms number $\mathcal{N}$ remaining.

In this work, we refer to the number of atoms in the "storage" or excited state as the Fock state of the system. Fock states are typically discussed in the context of photon occupancy in an oscillator mode, however more generally Fock states are discrete eigenstates of a number operator, $\hat{\mathcal{N}}$, which for this work we will use the number of excited atoms in an ensemble defined as:

$$\hat{\mathcal{N}} \equiv \sum_{k=1}^{N} \hat{S}_z^{(k)} + N/2, \tag{2.3}$$

where $\hat{S}_z$ is the total spin projection of the ensemble along the quantization axis. In terms of the previous discussion $|-\rangle$ is the initial state and $|+\rangle$ is the storage state. The Fock state of the ensemble can be mapped to the trap site population by application of a state-selective blow-away procedure, which removes atoms in the $|-\rangle$ state from the trap, see Section 7.3. Therefore, the more general goal of Fock state preparation can be easily extended to the secondary goal of deterministic atom loading.

2.1 Procedure

Rydberg blockade is used to deterministically excite a single atom from an ensemble of atoms. Limiting the available Hilbert space to a single excitation in an ensemble enables deterministic population inversion with a collective π_N-pulse. Without a non-linear effect similar to Rydberg blockade, single excitations must be prepared stochastically and are governed by Poissonian statistics.

The procedure is to create a single excitation at a time from $|0\rangle \Rightarrow |r\rangle \Rightarrow |1\rangle$, and then

repeat $\mathcal{N}$ times, followed by a $|0\rangle$ state blow-away procedure, see Figure 2.1. Since the transitions are performed serially, as long as the ensemble is strongly blockaded ($\sqrt{\bar{N}}\Omega \gg \Delta_{dd}$), maximally one atom can transfer from $|0\rangle$ to $|1\rangle$ per pulse sequence. If the excitation probability from $|0\rangle$ to $|r\rangle$ is perfect then there can be no transfer of population from $|1\rangle$ to $|r\rangle$. The pulses are enumerated as pairs in a sequence, so the $780_{0(1)}$-pulse that couple k atoms (on average) to the Rydberg state with pulse area θ is denoted with the operator $\hat{\theta}_k^{0(1)}$. A collective π_k-pulse will be designated by $\hat{\pi}_k^{0(1)}$ for emphasis. The evolution operator $\hat{\mathcal{F}}_{\mathcal{N}}$ that describes the $\mathcal{N}$ Fock State procedure can be written generally as:

$$\hat{\mathcal{F}}_{\mathcal{N}} = \prod_{k=1}^{\mathcal{N}} \hat{\pi}_k^1 \hat{\pi}_{(\bar{N}-k+1)}^0. \tag{2.4}$$

The generic Fock State experiment can therefore be written as:

$$\hat{\mathcal{F}}_{\mathcal{N}}|\bar{0}\rangle = \prod_{k=1}^{\mathcal{N}} \hat{\pi}_k^1 \hat{\pi}_{(\bar{N}-k+1)}^0 |\bar{0}\rangle. \tag{2.5}$$

The resulting state, $\hat{\mathcal{F}}_{\mathcal{N}}|\bar{0}\rangle$, is measured by selectively removing the projection onto the $|0_i\rangle$ state for each atom with unbalanced radiation pressure, and counting the number of atoms that remain.

The $\sqrt{N}$ collective Rabi frequency enhancement, while being a signature of $\mathcal{W}$-state entanglement, introduces the consideration that, when dealing with statistical loading, there will be a range of Rabi frequencies dictated by the loading rate distribution. The pulse time could be corrected on a shot-by-shot basis if the atom number was able to be measured. We unfortunately cannot post-select on atom number due to light-assisted collisions which happen on a time-scale faster than our readout time. This may become a possible avenue in the future [50]. In this thesis, we show ensemble data that includes this unknown atom number parameter averaged into the data.

Since the $\hat{\pi}^0$-pulses couple the initial state $|0\rangle$ to the Rydberg state $|r\rangle$, these pulses will always deal with a near Poissonian atom number distribution. For these pulses, we need to

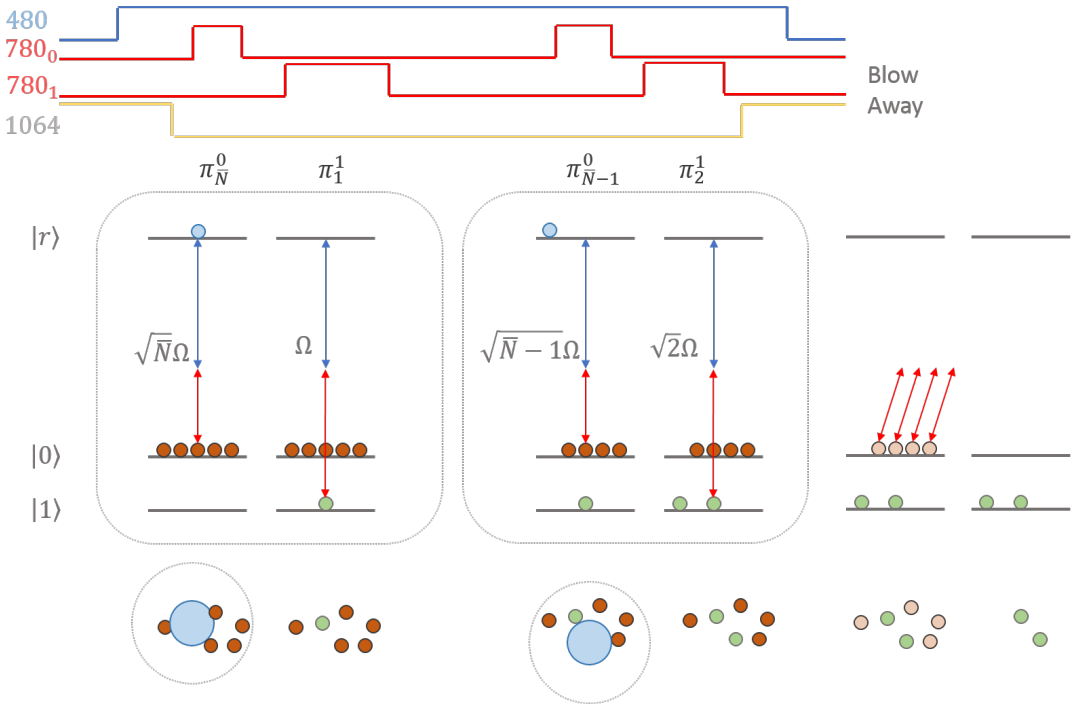

Figure 2.1: Fock state generation procedure shown for $\mathcal{N} = 2$. The 480 Rydberg laser is on for the duration of the experiment. The FORT is turned off while the 780 Rydberg lasers are pulsing so that excitations occur in free-space. The 780 Rydberg laser alternate such that collective π-pulses create a single Rydberg excitation or de-excite the Rydberg population to the $|1\rangle$ state. The collective π-pulses must be adjusted based on the current Fock state of the ensemble.

convolve the expected Rabi oscillations, $|\langle r|\psi(t)_N\rangle|^2 = \frac{1}{2}\left(1 - e^{-t/\tau}\cos\left(\sqrt{N}\Omega t\right)\right)$, with the atom number distribution. This results in the following simple model:

$$\begin{aligned} |\langle r|\psi(t)_{\bar{N}}\rangle|^2 &= \sum_{k=1}^{\infty} P_{\bar{N}}(k)|\langle 1|\psi(t)_k\rangle|^2 \\ &= \frac{1}{2} - \frac{e^{-t/\tau}}{2}\sum_{k=1}^{\infty} P_{\bar{N}}(k)\cos\left(\sqrt{k}\Omega t\right), \end{aligned} \tag{2.6}$$

where τ is an experimentally determined single atom Rydberg coherence time, $|\psi(\theta)_N\rangle$ is the wavefunction for the N-atom Fock state ensemble after a $\hat{\theta}^0_{\bar{N}}$ pulse, and $P_{\bar{N}}(N)$ is the probability distribution function (PDF) of the Poissonian loading function with mean $\bar{N}$ for atom number N. The Rabi frequency spread due to stochastic loading leads to a signal that appears to decay on a much faster time scale than the single atom coherence time. This is shown for $N = 1$ and $\bar{N} = \{6.4, 20\}$ in Figure 2.2 with single atom decay turned off. Note that for $\hat{\pi}^{(1)}$-pulses, we ideally only couple discrete Fock states, so no additional dephasing should be detected and the $\sqrt{\mathcal{N}}$ speedup should be apparent.

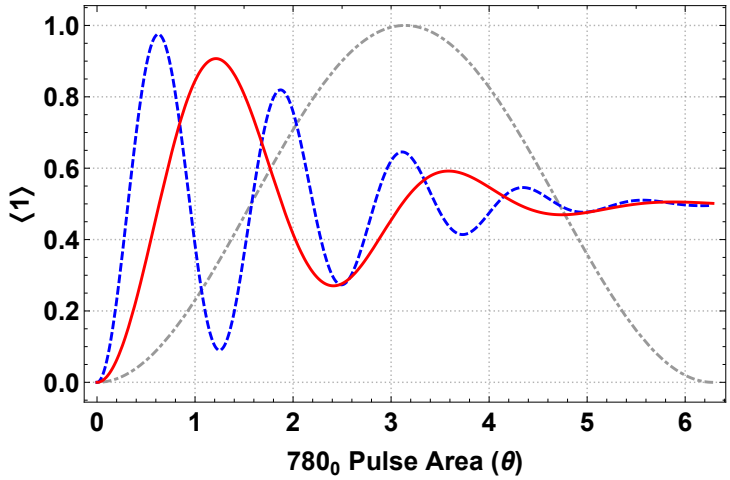

Figure 2.2: Example plots of the simple model from Equation 2.6 for various atom numbers. The solid red and dashed blue curves are for $\bar{N} = \{6.4, 20\}$ respectively. The dot-dashed grey curve is the exact $N = 1$ oscillation for comparison. No decay has been added ($\tau \to \infty$). The apparent decay comes exclusively from the averaging of the different Rabi frequencies for each ensemble atom number state.

2.2 $\mathcal{N} = 1$

We begin by demonstrating the $\sqrt{\bar{N}}$ collective enhancement for an ensemble with mean atom number loading $\bar{N}$. The atoms are prepared in the $|\bar{0}\rangle \equiv |2,0\rangle$ state after optical pumping as described in Section 1.4.4. The FORT is turned off for ~ 4 μs while the pulse area of the collective $\hat{\theta}^0_{\bar{N}}$-pulse is scanned to populate the Rydberg state. This pulse is followed by a single-atom $\hat{\pi}^1_1$-pulse to transfer the Rydberg population to the $|1\rangle \equiv |1,0\rangle$ state. The FORT is turned back on, anti-trapping any remaining $|r\rangle$ population. The atoms remaining in $|0\rangle$ are removed by the blow-away procedure, and the $|1\rangle$ population is then measured via fluorescence.

The results of scanning the $\hat{\theta}^0_{\bar{N}}$-pulse area during the $\mathcal{F}_1$ sequence is shown in Figure 2.3 for a range of mean atom numbers $\bar{N}$. The expected $\sqrt{\bar{N}}$ Rabi frequency enhancement can be easily seen in the difference between Figure 2.3(a,e) where for $\bar{N} \sim 16$ the peak is achieved at roughly $\theta^0_{16} = \pi^0_1/\sqrt{16}$.

The probability of producing a $\mathcal{F}_1$ Fock State is maximal when $\hat{\theta}^0_{\bar{N}} = \hat{\pi}^0_{\bar{N}} \equiv \hat{\pi}^0_1/\sqrt{N}$. The mean atom number $\bar{N}$ has been extracted from fits to Equation 2.6 where an overall scaling factor is used to match the amplitude. The $\bar{N}$ extracted from the collective enhancement of the Rydberg Rabi oscillation frequency is compared to the mean atom number measured via the fluorescence technique described in Section 7.2.3 in Figure 2.4. The excellent agreement of the two measurements supports the theoretical $1:1$ result shown as the black line. Allowing the slope to vary gives a best fit parameter of 0.96(4).

The probabilities of $\mathcal{N} = 1$ Fock state production are shown in Figure 2.5 as a function of $\bar{N}$ for many different trials of the experiment. We are consistently able to generate the $\mathcal{N} = 1$ Fock State with a fidelity of $60 - 65\%$ for initial ensemble means of $\bar{N} \approx 6$. The observation of $\mathcal{N} = 2$ events is consistent with the known blow-away infidelity. The resulting Fock state distribution is highly sub-Poissonian with a Mandel parameter of $Q = \sigma^2_{N_1}/\bar{N}_1 - 1 = -0.62(3)$. The results are shown along with the results of our model with infinite (dashed red line) and finite (blue solid line) blockade strengths, which are

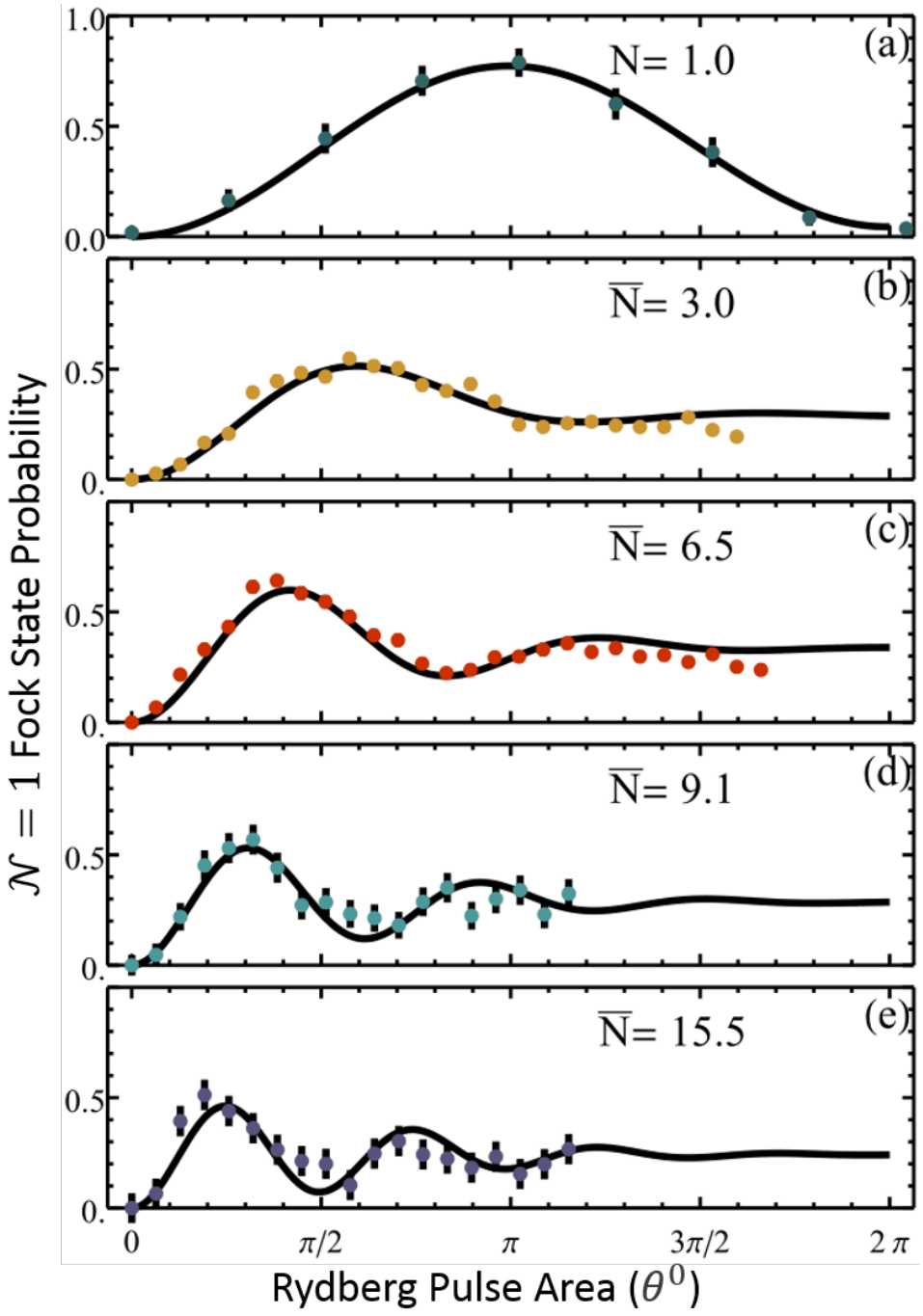

Figure 2.3: Rabi oscillations between $|0\rangle$ and $|r\rangle$ for various atom number distributions. A single-atom $\hat{\pi}_1^1$ pulse maps the Rydberg population down to the $|1\rangle$ state. The detection probability of $|\langle 1\rangle|^2$ is shown as a function of the single atom pulse area $\theta = \Omega_1 t$. (a) The first 2π rotation for exactly $N = 1$ atom, where single-atom loading events are post-selected from a stochastic loading procedure. The single-atom π_1^0-pulse takes 670 ns. (b)-(e) The $|1\rangle$ populations show an atom number dependent frequency for ensemble means of $\bar{N} = 3.0, 6.5, 9.1, 15.5$ respectively. The solid black lines are fits to Equation 2.6 with an overall scaling factor to match the oscillation amplitude. The data has been corrected for the measured $|0\rangle$ blow-away fidelity.

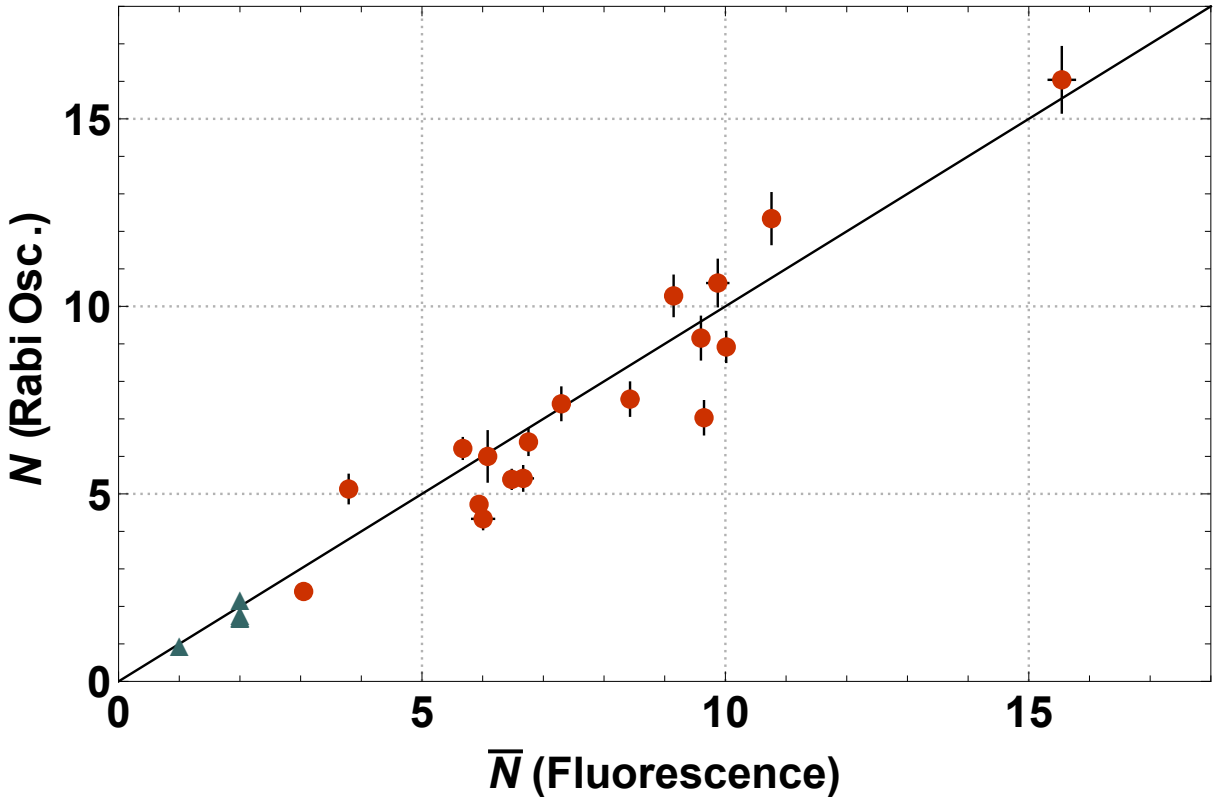

Figure 2.4: Mean number of atoms in the ensemble , as deduced from collective Rabi oscillations (ordinate) and by fluorescence (abscissa). The red circles are data from Poisson-distributed atom ensembles, the green triangles are for $\mathcal{F}_1$ and $\mathcal{F}_2$ Fock states. The solid black line, of slope 1, show that the collective oscillation frequency closely follows the predicted $\sqrt{N}$ dependence. The error bars are the uncertainty in the fit to the Ensemble mean for both cases, not the expected width of the ensemble population distribution.

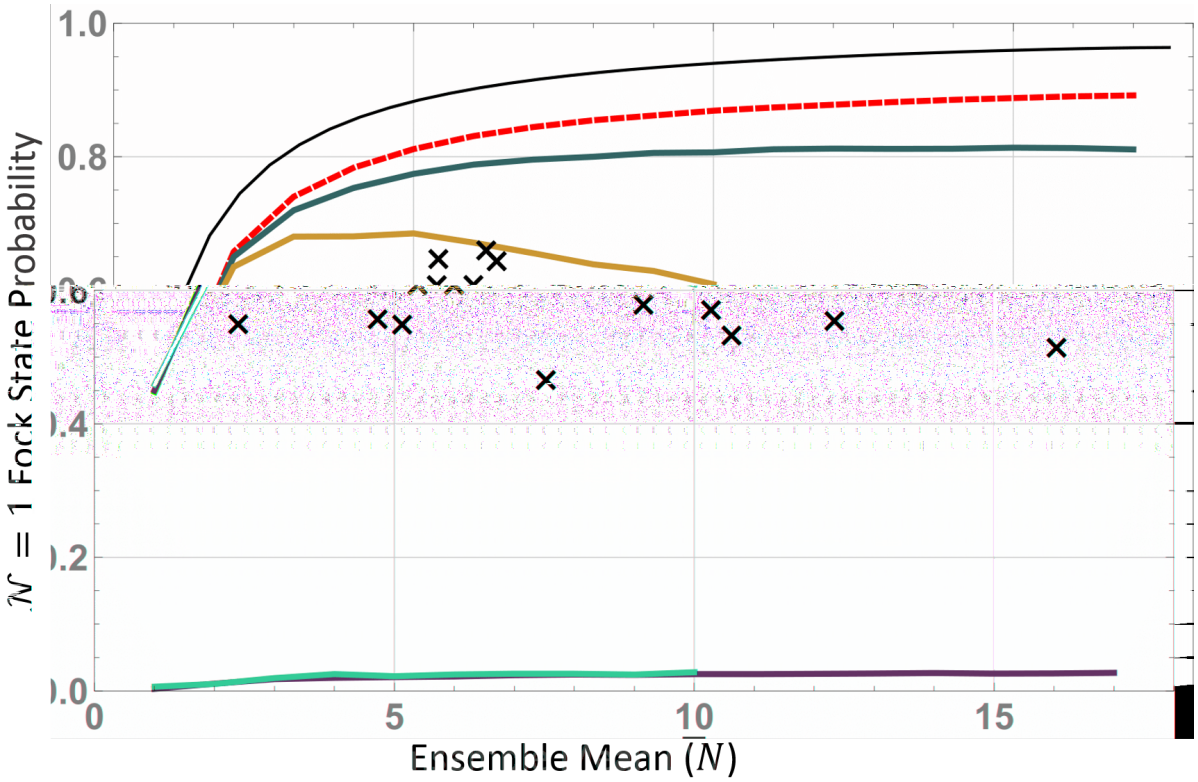

Figure 2.5: $\mathcal{N} = 1$ Fock state production fidelity as a function of mean ensemble number and quantum Monte Carlo simulations. The crosses denote measured peak values. The solid black line assumes ideal blockade and perfect excitation conditions. The red dashed line adds in realistic experimental imperfections but infinite blockade, and the blue line includes the predicted finite blockade strength. The blue line at the bottom shows the predicted two-atom production. The yellow line is the full model with finite blockade and an additional decay term $\Gamma_{gr} = 200kHz$ for each ground-Rydberg pair within a hard sphere of $R_c = 0.9$ μm. This decay is inspired by the observations of Niederprüm et al. [51], where an anomalously large Rb_2^+ cross section was observed. It should be noted that the parameters, Γ_{gr} and R_c, are chosen to emphasize a density dependent effect are not intended to be reasonable estimates and are significantly larger than expected.

described in detail in Chapter 6. The black line shows the result of the simple model described by Equation 2.6. The amplitudes of these trials are inconsistent with our models by about 15-20%, which suggest that the $\mathcal{F}_1$ amplitude should be $\sim 80\%$ for our system parameters.

The root cause of the amplitude discrepancy is unknown. However, the results of additional experiments have suggested possible mechanisms which may account for the discrepancy. The validity of the proposed mechanisms have been bolstered by observa-

tions and predictions reported by other groups. After completing the discussion of the experiment that will prove necessary for context we will return to the amplitude discrepancy in Chapter 5. For now, we note that this overall scaling factor will continue to show up in future experiments, so we focus instead on the accuracy of the dynamics until Chapter 5.

2.3 $\mathcal{N} = 2$

The preparation of the $\mathcal{F}_2$ Fock state is performed by following the $\mathcal{F}_1$ procedure immediately with a second pair of pulses, $\hat{\mathcal{F}}_2 = \hat{\pi}_2^1 \hat{\pi}_{(\bar{N}-1)}^0 \hat{\mathcal{F}}_1$. This time though, we instead vary the pulse time of the last 780_1 pulse to observe the $\sqrt{2}$ oscillation frequency for the created $\mathcal{F}_2$ state. This experiment is given explicitly by:

$$\hat{\mathcal{F}}_2 \left(\theta_2^1\right) |\bar{0}\rangle = \hat{\theta}_2^1 \hat{\pi}_{(\bar{N}-1)}^0 \hat{\pi}_1^1 \hat{\pi}_{\bar{N}}^0 |\bar{0}\rangle. \tag{2.7}$$

This experimental diagram is the example shown in Figure 2.1. The probabilities of producing 0, 1, or 2 atoms, denoted $\{p_0, p_1, p_2\}$, in the $|1\rangle$-state after this experiment are shown in Figure 2.6(a0-2).

Since the range of atom numbers for this case is $0 \leq n_1 \leq 2$ we use the fluorescence measurement procedure described in Section 7.2.4 to extract the probabilities $\{p_0, p_1, p_2\}$ from the camera signal histogram. An example camera histogram is shown in Figure 2.7 for clarity, note that the p_n probabilities are extracted from the amplitudes of the blue, yellow and red curve respectively. Since the camera signal probability distributions overlap non-negligibly, we cannot accurately apply a threshold measurement as we did for the $\mathcal{F}_1$ data sets. Instead we rely on extracting the data from the whole histogram.

To investigate the dynamics of this experiment it is necessary to understand the behavior of the system for each possible initial state, $|\psi(\theta = 0)\rangle$, leading into the $\hat{\theta}_2^1$-pulse. The possible states of this experiment are enumerated with the tuple (n_r, n_1), where the

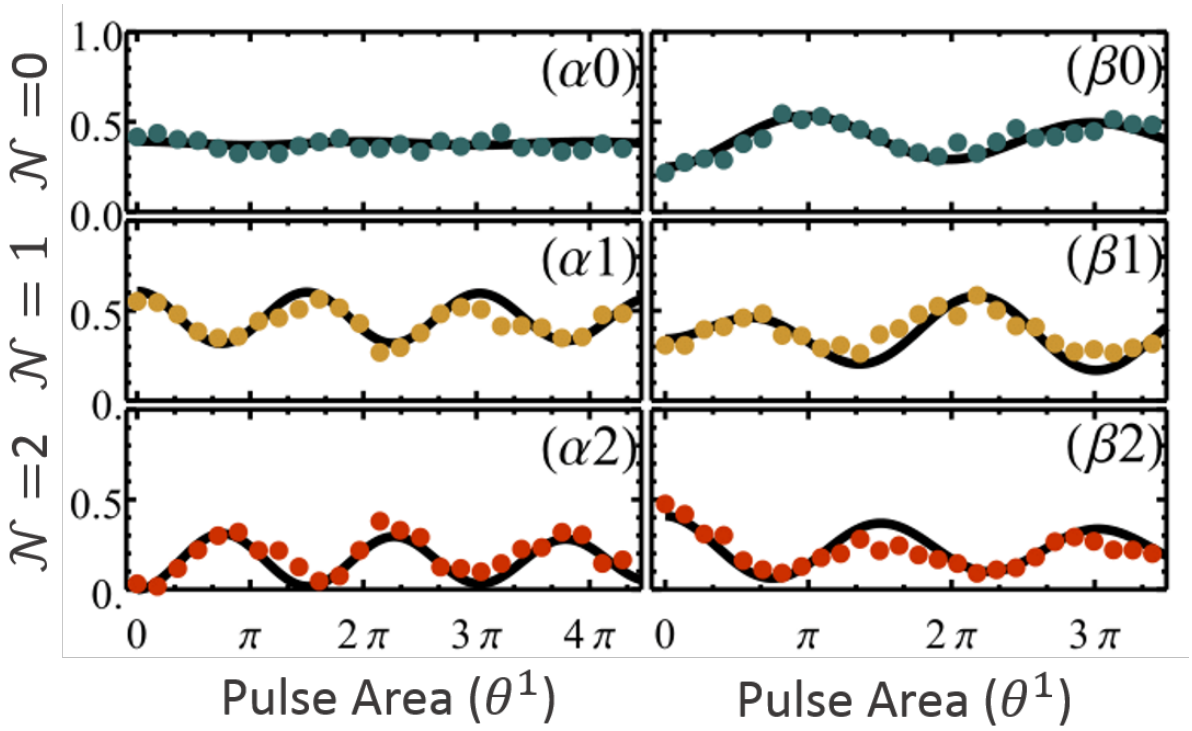

Figure 2.6: (α) The evolution of the $n_1 = 0, 1$, and 2 atom populations using the $\hat{\theta}_2^1 \hat{\pi}_{(\bar{N}-1)}^0 \hat{\mathcal{F}}_1$ protocol for $\mathcal{F}_{\mathcal{N}=2}$ fock state production. The black solid lines are simultaneous fits to Equation 2.8 with the free parameters being the initial $\theta = 0$ state populations, $\{P_{(0,0)}, P_{(0,1)}, P_{(1,0)}, P_{(1,1)}\} = \{0.099(5), 0.271(5), 0.291(5), 0.339(6)\}$. ($\beta$) The evolution for the pulse sequence defined by: $\hat{\theta}_2^1 U(t) \hat{\mathcal{F}}_2$, where $U(t)$ is the propagation matrix describing the state of the system when the FORT is turned back for a time t. The black lines represent a simultaneous fit to Equation 2.10 with the initial $\theta_1 = 0$ state populations, $\{P_{(0,0)}, P_{(0,1)}, P_{(0,2)}\} = \{0.247(3), 0.314(3), 0.438(5)\}$, as the only free parameters.

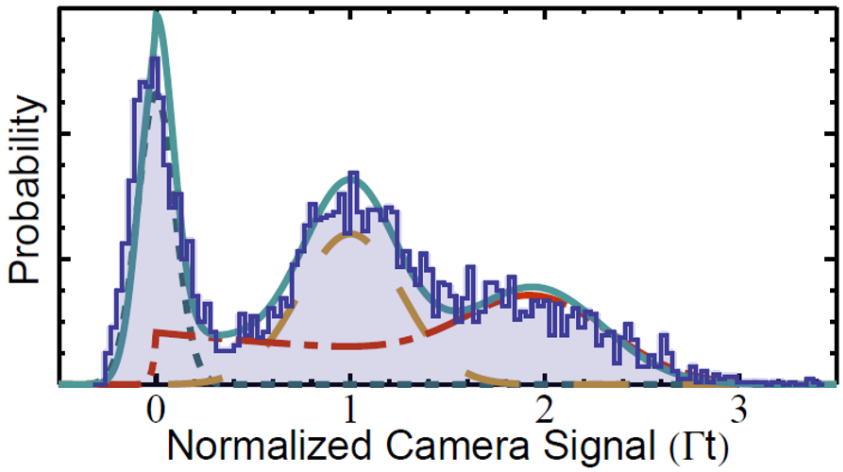

Figure 2.7: An example few atom readout histogram. Fock state probabilities, $\{p_0, p_1, p2\}$, are extracted from the amplitudes of the 0 (blue short dashed line), 1 (yellow long dashed line), and 2 atom (red dot-dashed line) fluorescence signal distributions. Details concerning these signal distributions are discussed in detail in Section 7.2.4.

number of atoms in $|r\rangle$ and $|1\rangle$ is given by n_r and n_1 respectively. Under ideal conditions, at $\hat{\theta}_2^1 = 0$ the state $\hat{\pi}^0_{(\bar{N}-1)}\hat{\pi}^1_1\hat{\pi}^0_{\bar{N}}|\bar{0}\rangle$ would be equivalent to $|(n_r = 1, n_1 = 1)\rangle$ with unity probability. Because the Rydberg blockade is still in effect, the state $|(2,0)\rangle$ is energetically forbidden and $\hat{\theta}_2^1|(1,1)\rangle$ will evolve as:

$$\hat{\theta}_2^1|(1,1)\rangle = \cos\left(\sqrt{2}\theta_1/2\right)|(1,1)\rangle + \sin\left(\sqrt{2}\theta_1/2\right)|(0,2)\rangle.$$

The result is that the observed n_1 expectation value will oscillate between 1 and 2, at the enhanced $\sqrt{2}$ Rabi frequency. If the first transfer succeeds, but the second Rydberg excitation does not the initial state is then $|(0,1)\rangle$, and the dynamics are described as

$$\hat{\theta}_2^1|(0,1)\rangle = \cos\left(\theta_1/2\right)|(0,1)\rangle + \sin\left(\theta_1/2\right)|(1,0)\rangle.$$

The n_1 expectation value will oscillate at the single atom Rabi frequency between 0 and 1 atom in $|1\rangle$. Likewise, if the first transfer does not succeed and the second Rydberg

excitation does the initial state is $|(1,0)\rangle$ and evolve as:

$$\hat{\theta}_2^1|(1,0)\rangle = \sin(\theta_1/2)\,|(0,1)\rangle + \cos(\theta_1/2)\,|(1,0)\rangle.$$

Note that this is exactly out of phase with the previous result. Finally, the state with no successes $|(0,0)\rangle$ does not evolve with $\hat{\theta}_2^1$. Therefore the probabilities for observing $n_1 = \{0,1,2\}$ atoms are given by:

$$\begin{aligned} p_0(\theta_1) &= P_{(0,0)} + P_{(1,0)}\cos^2(\theta_1/2) + P_{(0,1)}\sin^2(\theta_1/2), \\ p_1(\theta_1) &= P_{(1,0)}\sin^2(\theta_1/2) + P_{(0,1)}\cos^2(\theta_1/2) + P_{(1,1)}\cos^2\left(\sqrt{2}\theta_1/2\right), \\ p_2(\theta_1) &= P_{(1,1)}\sin^2\left(\sqrt{2}\theta_1/2\right), \end{aligned} \tag{2.8}$$

where $P_{(n_r,n_1)}$ is the probability for the system to have been in state $|(n_r,n_1)\rangle$ at $\theta_1 = 0$. Note that to the extent that $P_{(1,0)} = P_{(0,1)}$ the only θ dependence is the $|(1,1)\rangle$ state oscillating at the $\sqrt{2}$ enhanced Rabi frequency, due to the evolution of $|(0,1)\rangle$ and $|(1,0)\rangle$ being out of phase. This behavior is observed in the data shown in Figure 2.6(a0-2).

Of special significance is Figure 2.6(a2), where 3 full oscillations of the $\mathcal{N} = 2$ Fock state are observed with no atom number fluctuation induced decay. This is in contrast to the initial $\hat{\pi}_{\bar{N}}^0$-pulses from the previous section. To obtain three full oscillations, it was necessary to extend the FORT drop time to 6.34 μs incurring additional losses, which lowers the maximum $\mathcal{N} = 2$ preparation rate. An additional experiment, shown in Figure 2.8, is included where a shorter FORT drop time is used, which gives a more accurate measurement of the $\mathcal{N} = 2$ rate. For this data, we observe a maximal p_2 or 48% and a Mandel Q parameter of -0.50(5). The agreement of the data to the expected dynamics, shown in black, also serves to validate the camera signal fitting models used.

A second experiment was also performed where a normal $\hat{\mathcal{F}}_{\mathcal{N}=2}$ pulse sequence is applied to the ensemble, but after the sequence of 4 Rydberg π-pulses the FORT is turned back on for long enough to remove any $|r\rangle$ population remaining. Then the FORT

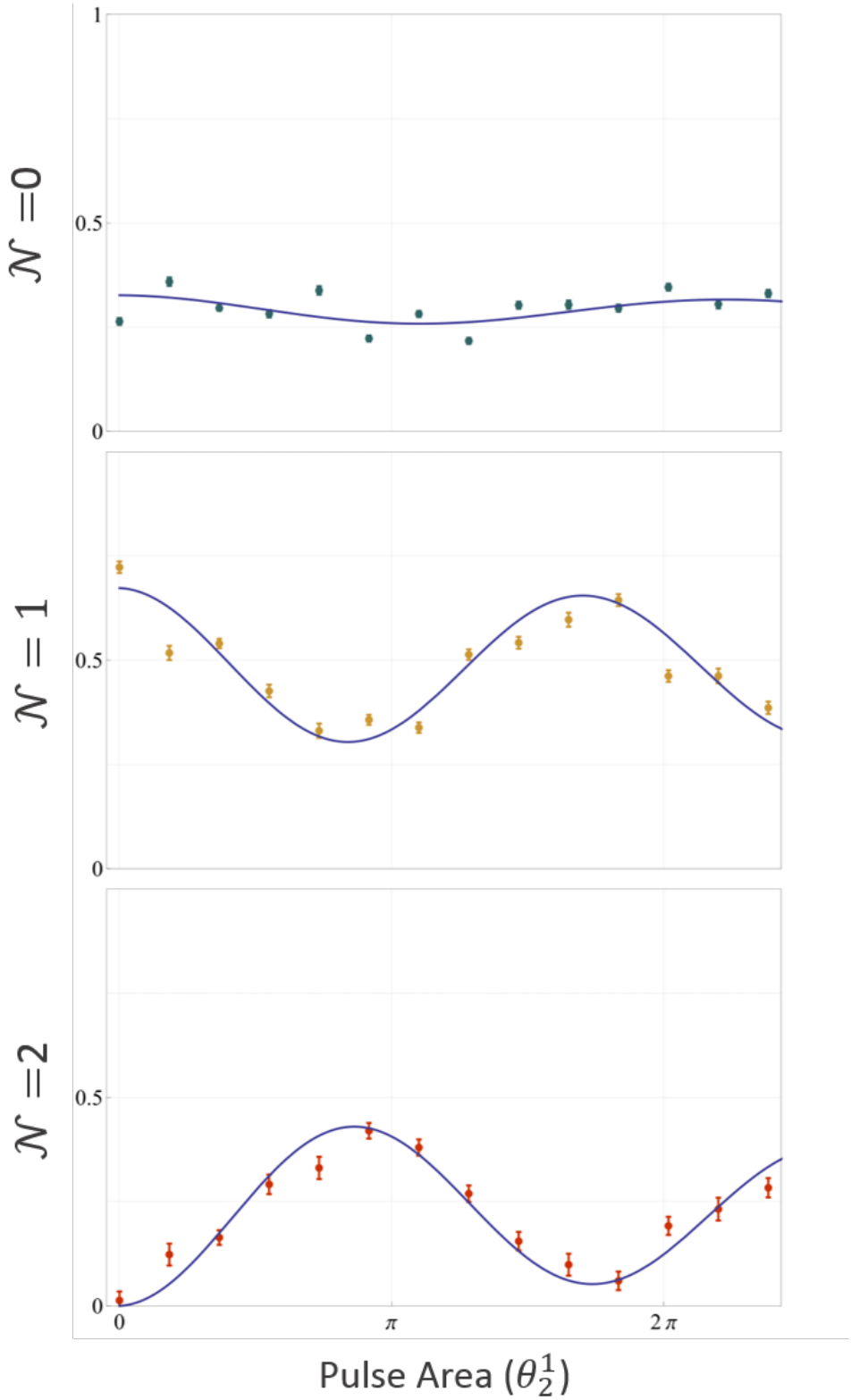

Figure 2.8: A similar data set to the on shown in Figure 2.6, but with a shorter FORT drop time to demonstrate the full amplitude of the $\mathcal{N} = 2$ Fock state oscillations.

is turned back off and a 5^{th} pulse $\hat{\theta}_2^1$ probes the populations in n_1. Turning the FORT on anti-traps the Rydberg state and acts as a partial measurement of the ground state, so we define the ground state partial measurement operator $\hat{g} \equiv \Pi_i \big(|0_i\rangle\langle 0_i| + |1_i\rangle\langle 1_i|\big) \otimes \mathbb{1}^{(N-1)}$. In the Fock state experiment notation, this experiment is defined as:

$$\hat{\mathcal{F}}_2' \left(\theta_2^1\right) |\bar{0}\rangle = \hat{\theta}_2^1 \hat{g} \hat{\mathcal{F}}_2 |\bar{0}\rangle. \tag{2.9}$$

This test, unlike the previous, depletes the Rydberg population and aligns the phases of oscillation at $\theta = 0$ so that no cancellations occur. The states evolve according to the their respective $\sqrt{\mathcal{N}}$ speed-up. The resulting behavior is shown in Figure 2.6(b0-2). Using the same state enumeration $|(n_r, n_1)\rangle$, the possible $\theta_1 = 0$ initial states here are: $\{|(0,0)\rangle, |(0,1)\rangle, |(0,2)\rangle\}$. These states will evolve as follows:

- $\hat{\theta}_2^1 |(0,0)\rangle = |(0,0)\rangle$,
- $\hat{\theta}_2^1 |(0,1)\rangle = \cos(\theta_1/2)|(0,1)\rangle + \sin(\theta_1/2)|(1,0)\rangle$,
- $\hat{\theta}_2^1 |(0,2)\rangle = \cos(\sqrt{2}\theta_1/2)|(0,2)\rangle + \sin(\sqrt{2}\theta_1/2)|(1,1)\rangle$,

This results in the final probability measurements of:

$$\begin{aligned} p_0 &= P_{(0,0)} + P_{(0,1)} \sin^2(\theta_1/2), \\ p_1 &= P_{(0,1)} \cos^2(\theta_1/2) + P_{(0,2)} \sin^2(\sqrt{2}\theta_1/2), \\ p_2 &= P_{(0,2)} \cos^2(\sqrt{2}\theta_1/2). \end{aligned} \tag{2.10}$$

The data in Figure 2.6(b0-2) is in good agreement with these dynamics, further supporting the models assumed.

Chapter 3

$\mathcal{W}$-State Tomography

In the previous chapter, we concerned ourselves primarily with the Fock state of the ensemble following an blockaded ensemble picture. A Fock state is, according to the definition presented in Equation 2.3, simply a measure of the atom number and does not specify any degree of coherence or entanglement in the state. In this chapter, we expand on the $\mathcal{F}_1$ methods explored in the previous chapter to include experiments that are sensitive to the degree of entanglement generated in the singly excited ensemble.

The output state following an ideal $\mathcal{F}_1$ Fock state experiment is given by:

$$\begin{aligned} \hat{\mathcal{F}}_1|0^{(1)}\dots 0^{(N)}\rangle &= \frac{1}{\sqrt{N}}\sum_{k=1}^{N}|0^{(1)}\dots 1^{(k)}\dots 0^{(N)}\rangle \\ &\equiv |\mathcal{W}\rangle, \end{aligned} \tag{3.1}$$

Note that the output state has well defined relative phase and is symmetric. This symmetric singly-excited state is commonly referred to as the $\mathcal{W}$-state[27]. It can be shown that the total angular momentum of this, or any other of the $N+1$ symmetric states, is $J = N/2$, and all other states have $J < N/2$, see Section 6.2.1. It can also be convenient to write the $\mathcal{W}$-state in the Dicke basis ($|J, M\rangle$) as $|\bar{1}\rangle = |\frac{N}{2}, \frac{N}{2} - 1\rangle$. A measurement of J enables a straightforward observable to test the $\mathcal{W}$-state character of the output from the

$\mathcal{F}_{\mathcal{N}=1}$ procedure, and will also serve as an entanglement witness. We will expand upon the formalism developed, and will now use a bar to denote a symmetric Fock state, for example $|\bar{0}\rangle \equiv |0^{(1)} \dots 0^{(N)}\rangle$, and $|\bar{1}\rangle \equiv \frac{1}{\sqrt{N}} \sum_{k=1}^{N} |0^{(1)} \dots 1^{(k)} \dots 0^{(N)}\rangle$. For convenience, we will also label the set of $N-1$ $\mathcal{F}_1$ states with $J < N/2$ as $|(\bar{1})_\perp\rangle$, following the example of [52].

The observation of the $\sqrt{N}$ Rabi frequency enhancement in Figure 2.3 is a clear signature that the transition being driven is, in fact, between $|\bar{0}\rangle$ and $|\bar{r}\rangle$. This has been exploited as a demonstration of k-partite entanglement with $k \sim 100$ in a sub-Poissonian ensemble of $\bar{N} \sim 130$ atoms[21]. This could be done in our system, however we choose to employ entanglement measurements that are distinct from the $\mathcal{F}_1$ experiment.

Besides the the observation of a $\sqrt{N}$ collective Rabi frequency enhancement discussed, two additional pieces of evidence are presented that demonstrate a significant degree of multi-partite entanglement. First, a Ramsey fringe-like oscillation experiment is presented in Section 3.1, from which a characteristic τ_2 coherence time of 2.6(3) ms[41], as well as a lower limit for the amplitude in $|\bar{1}\rangle$. Finally in Section 3.2, the output of the $\hat{\mathcal{F}}_1$ procedure is probed with a global microwave rotation, which is a more direct measurement of the amplitude in $|\bar{1}\rangle$.

3.1 Ramsey-Fringe Coherence Measurements

A typical Ramsey-fringe experiment can be expressed as a sequence of three rotations on the Bloch sphere, $R_x(\pi/2)R_z(\phi)R_x(\pi/2)$. Here ϕ is usually implemented by allowing the system to evolve for some time, t, where a phase, $\phi = \Delta t$, is accumulated at a rate equal to the energy difference, Δ, between the excitation energy and the energy during the phase evolution step. Since a multi-photon process is used, the primary source of phase accumulation is due to the AC Stark shift of the ground states arising from the mismatch in single photon Rabi frequencies of the $780_{0(1)}$ lasers and the 480 nm laser.

Because of the AC Stark shifts, the lasers must be detuned from the free space resonances. This detuning gives rise to a phase accumulation rate which is integrated over the full free evolution period. An additional source of phase accumulation is the differential AC Stark shift induced by the FORT laser.

As is the case with all Rydberg ensemble procedures in this work, the encoded state of the ensemble in the interaction basis $\{|\bar{0}\rangle, |\bar{r}\rangle\}$ must be mapped to the computational basis $\{|\bar{0}\rangle, |\bar{1}\rangle\}$. In the storage basis, coherence times of up to 7 seconds have been reported in the literature[53]. The procedure for measuring the τ_2 coherence is outlined in Figure 3.1, and is described as $\mathcal{R}$ below:

$$\hat{\mathcal{R}}(t_{gap}) = \hat{\pi}_1^1 \left(\hat{\pi/2}\right)_{\bar{N}}^0 \hat{\pi}_1^1 \hat{U}(t_{gap}) \hat{\pi}_1^1 \left(\hat{\pi/2}\right)_{\bar{N}}^0 . \tag{3.2}$$

Here $U(t_{gap})$ describes the evolution of the system during the gap time, and $\left(\hat{\pi/2}\right)_{\bar{N}}^0$ is a $\hat{\theta}_{\bar{N}}^0 = \pi_1/(2\sqrt{\bar{N}})$ pulse. The three $\hat{\pi}_1^1$ pulses are needed to map the Rydberg population to the storage basis state $|\bar{1}\rangle$. The first $\hat{\pi}_1^1$-pulse maps the $|\bar{r}\rangle$ state amplitude to $|\bar{1}\rangle$ to accumulate a phase, the second pulse returns the $|\bar{1}\rangle$ population to $|\bar{r}\rangle$ in preparation for the interference pulse, while the third is used for the final measurement after the interference pulse. The interference stage happens with the second $\left(\hat{\pi/2}\right)_{\bar{N}}^0$-pulse, as normal. Note that the FORT is turned off during the pulses to address the atoms, but during the gap time the FORT is turned back on to prevent atom loss.

In the limit of $\tau_2 \gg f_{\mathcal{R}}^{-1}$, where $f_{\mathcal{R}}$ is the Ramsey frequency, it is necessary to measure the visibility of the Ramsey oscillations for various gap times. The result of a few oscillation experiments with various t_{gap} values is shown in Figure 3.2(a), and (b) shows the visibility of the Ramsey oscillations at various gap times. We use a Gaussian visibility decay, $v(t)$, with functional form given by:

$$v_a(t_{gap}) = v_0 e^{-(t_{gap}/\tau_2)^2}. \tag{3.3}$$

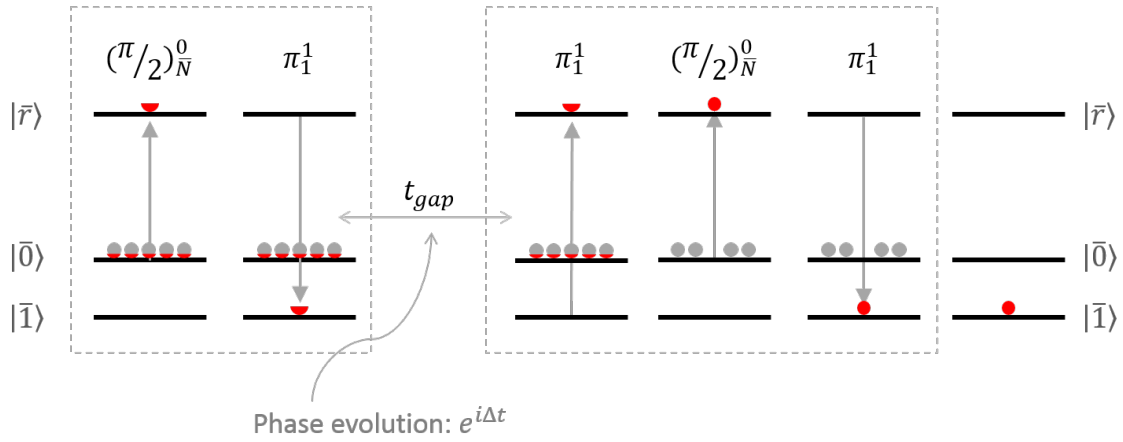

Figure 3.1: The Rydberg $780_{0(1)}$ addressing procedure for the Ramsey oscillation experiment. The 480 nm laser is turned on for duration of the Rydberg pulses, while the FORT is turned off to address $|\bar{r}\rangle$ but is turned back on during t_{gap} to prevent atom loss over long timescales.

We define visibility as the peak-to-peak amplitude of the oscillation. The statistics are not sufficient to distinguish between this form and the reversible decoherence form [54]:

$$v_b(t_{gap}) = \frac{v_0}{[1 + (e^{2/3} - 1)(t/\tau_2^\star)]^{3/2}}, \tag{3.4}$$

where $\tau_2^\star$ is the irreversible coherence time.

The result of multiple types of coherence experiments are shown in Figure 3.3. The result of product state coherence times, generated with the fast ground state rotation laser [55], are shown in blue with the coherence times from the $\mathcal{W}$-state coherence experiment described above in red. The unfilled markers denote post-selected single atom experiments with the ground or Rydberg lasers. The limiting decoherence processes for the $\mathcal{W}$-state are presumed to be the linewidth of the Rydberg lasers for $\bar{N} <\sim 4$ and collisional dephasing for $\bar{N} >\sim 4$. Both of these decoherence channels can be suppressed using established techniques, but with a coherence to gate time ratio of ~ 2600 we are not limited by these processes at the current level.

Because rotations on the Bloch sphere conserve total angular momentum J, the $R_z(\theta)$

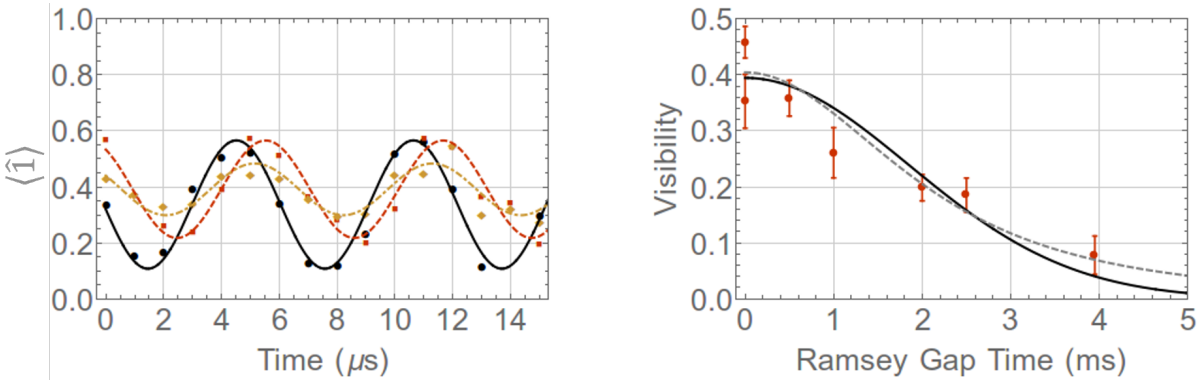

Figure 3.2: (a) Example Ramsey fringe-style oscillations for various gap times with $\bar{N} = 7.6$ atoms. The black, red, and yellow data point correspond to gap times: $t_{gap} = \{0, 0.5, 2.5\}$ ms. The lines show simple sinusoidal fits used to extract the visibility. (b) The visibility of the Ramsey oscillations is shown as a function of the gap time. The black solid line is a fit to Equation 3.3, where $\tau = 2.6(3)$. The grey dashed line is a fit to Equation 3.4, where $\tau^\star = 2.6(3)$ also. The data have been corrected for a $\sim 1.5\%$ per atom probability for an unintended $|0\rangle \rightarrow |1\rangle$ transition during the state selective measurement procedure. Data are from 5/30/2014.

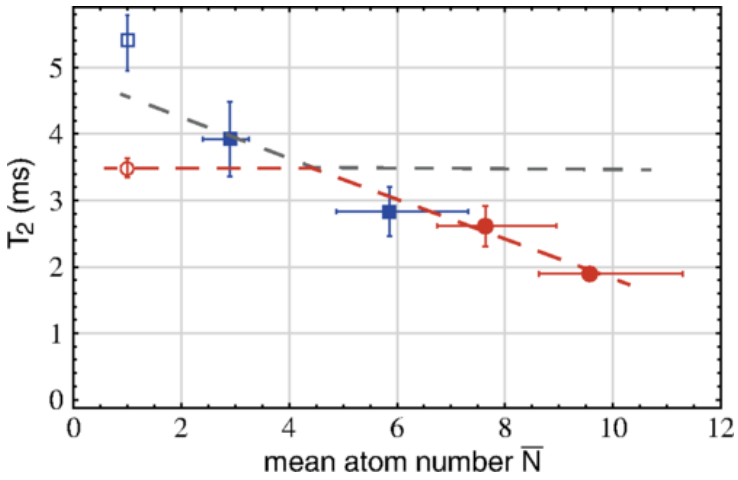

Figure 3.3: Dependence of ensemble coherence time on $\bar{N}$ for $\mathcal{W}$-states (red circles) and product states (blue squares). The horizontal error bars represent the bounds for atom number measurements interleaved between Ramsey measurements. The open symbols are for post-selected $\mathcal{N} = 1$ states. The dashed lines are a guide to the eye for the expected limiting decoherence processes.

rotation during the Ramsey oscillation probes the total angular momentum of the initial state. Since $|\bar{1}\rangle$ is the only state in the $|J, M = N/2 - 1\rangle$ manifold with total angular momentum $J = N/2$, it is the only singly excited state that can couple to the ground state $|\bar{0}\rangle = |N/2, N/2\rangle$. An $R_z(\theta)$ rotation will manifest as an oscillation between $|\bar{0}\rangle$ and $|\bar{1}\rangle$, where the amplitude is a measure of the coherent state population with total angular momentum $J = N/2$. For example, the singly excited state $|10...0\rangle$ would oscillate with amplitude of $|\langle\bar{1}|10...0\rangle|^2 = 1/N$.

From the $t_{gap} = 0$ Ramsey data shown again in Figure 3.4(a), the state probabilities for maximal $|\bar{1}\rangle$ production can be extracted, giving $\{p_{\bar{0}}, p_{\bar{1}}, p_{(\bar{1})_\perp}\} = \{0.44(2), 0.46(3), 0.10(4)\}$. The region defined by the visibility of the $\mathcal{N} = 1$ Ramsey oscillation (white) must have $J = N/2$ and defines the $\mathcal{W}$-state projection. The region of $\mathcal{N} = 1$ signal that does not oscillate (blue) has a single excitation but where $J = N/2 - 1$, preventing it from rotating into $|\bar{0}\rangle$. Finally the region of signal with no $\mathcal{N} = 1$ excitation (red) has $J = N/2$ since no excitations are present. As the state is allowed to evolve through an R_z rotation the states with $J = N/2$ will exchange population up to the limit of the $|\bar{1}\rangle$ population. The 46(3)% $\mathcal{W}$-state amplitude demonstrates a preparation rate that exceeds the incoherent single excitation limit $1/\bar{N} = 11.4\%$ for 8.8 atoms by a factor of 4. Additionally, it should be noted that a thermalized single excitation would not oscillate at all.

In Figure 3.4(b), the data from Figure 3.2(b) is replotted in the context of the $|\bar{1}\rangle$-state and the $|(\bar{1})_\perp\rangle$-states, where $|(\bar{1})_\perp\rangle$ is defined as the set of states with total angular momentum $J = N/2 - 1$.

3.2 Microwave Tomography

A second tomographic experiment based on the work in reference [56] has also been investigated. In reference [56], following a short unblockaded excitation with a low probability of generating $\mathcal{N} > 1$, a non-destructive Fock state measurement was performed to differen-

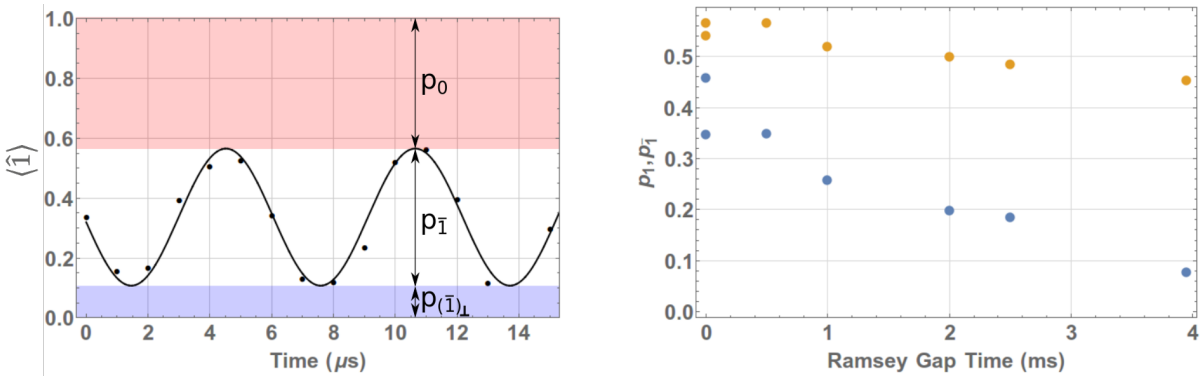

Figure 3.4: (a) The Ramsey oscillation data for $t_{gap} = 0$ is shown again from Figure 3.2(a) with visual aids to point out the source of the $\{p_{\bar{0}}, p_{\bar{1}}, p_{(\bar{1})_\perp}\} = \{0.44(2), 0.46(3), 0.10(4)\}$ measurements. The probability of creating the $\mathcal{N} = 1$ Fock state, p_1, is the maximum extent of the oscillations $p_1 = A + v_0/2$, where A is the mean of the Ramsey oscillation. The probability of creating the $\mathcal{W}$-state, $p_{\bar{1}}$, is the visibility of the oscillations $p_{\bar{1}} = v_0$. (b) The result of p_1 (yellow), and $p_{\bar{1}}$ (blue) are shown for the different Ramsey gap times in the experiment. Note how the probability of a $\mathcal{N} = 1$ Fock state remains nearly constant with the gap time, where the probability of the $\mathcal{W}$-state decreases by a factor of 6 due to decoherence, or 4.8 if normalized to p_1. The 20% drop in p_1 is attributed to systematic drifts in the apparatus over the course of the 12 hour experiment, for example $6.7 < \bar{N} < 9$ atoms.

tiate between $\mathcal{N} = 0$ and $\mathcal{N} \neq 0$. Since an excitation conserves total angular momentum as discussed before (ignoring non-ideal effects), the measurement of $\mathcal{N} \neq 0$ heralds the creation of the $\mathcal{W}$-state in the ideal limit, with only a partial measurement which preserves the entangled state. Following the detection of a $\mathcal{N} = 1$ event, a microwave pulse resonant with the $|0\rangle \leftrightarrow |1\rangle$ transition is used to perform a rotation $R_x(\theta)$ and the measurement sequence is repeated. By the same angular momentum conservation argument, only the population in $|\bar{1}\rangle$ can rotate back down to $|\bar{0}\rangle$. Based on this the authors are able to extract the state probabilities for $p_{\bar{0}}$, $p_{\bar{1}}$, and consequently $p_{(\bar{1})_\perp} = 1 - p_{\bar{0}} - p_{\bar{1}}$.

We can perform a similar microwave tomography measurement, even though we do not have the capability to non-destructively measure $|\bar{0}\rangle$. However, since we are able to prepare single excitations at a rate significantly higher than the stochastic method in reference [56] it is possible for us to extract the initial state probabilities from the statistical mixture of $|\bar{0}\rangle$, $|\bar{1}\rangle$, and $|(\bar{1})_\perp\rangle$. The measurement basis states $\{|\bar{0}\rangle, |\bar{1}\rangle, |(\bar{1})_\perp\rangle\}$

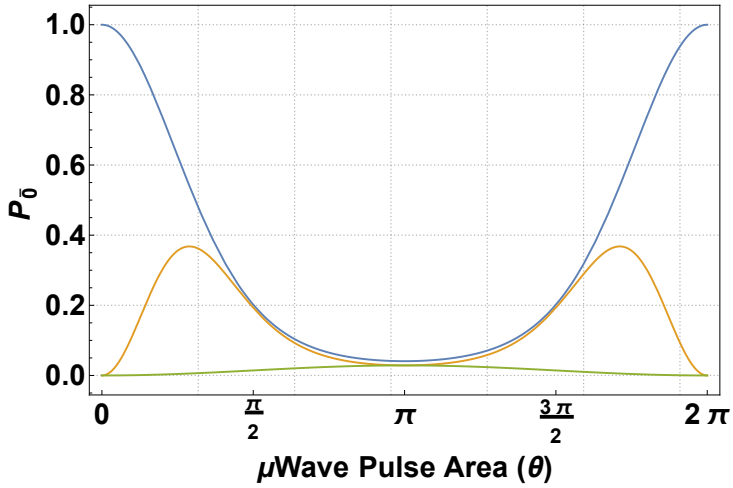

Figure 3.5: The projection onto $|\bar{0}\rangle$ during the evolution of the basis states for $\{|\bar{0}\rangle, |\bar{1}\rangle, |(\bar{1})_\perp\rangle\}$ are shown in blue, orange, and green respectively averaged over a Poisson distribution of $\bar{N} = 5.3$ atoms. There is a small amplitude for $|(\bar{1})_\perp\rangle$ since there is a non-zero probability to have a single atom in the ensemble, and for completeness we assign this state to $|(\bar{1})_\perp\rangle$.

evolve differently under a $R_x(\theta)$ rotation, as can be seen in Figure 3.5. Since the number of atoms in state $|1\rangle$ ranges from 0 to N and there are significant losses during the readout, the cleanest measurement is the population in $|0\rangle$, i.e. we perform a blow-away procedure then plot the probability of measuring no atoms. This is in contrast to a standard readout procedure where the probability of measuring the single atom remaining in $|1\rangle$ is shown. Here the $N-1$ dimensional subspace denoted by $|(\bar{1})_\perp\rangle$ is degenerate under the $\mathcal{N} = 0$ operator $\hat{0}$, $|\langle\psi(t)|\hat{0}|\psi(t)\rangle|^2 = 0$, where $|\psi(0)\rangle \subset |(\bar{1})_\perp\rangle$.

The resulting measurement can be seen in Figure 3.6 as the blue data points and the fit for the initial populations and microwave Rabi frequency is shown as the black line. The resulting initial state amplitudes are given by $\{p_{\bar{0}}, p_{\bar{1}}, p_{(\bar{1})_\perp}\} = \{0.47(2), 0.53(5), 0.00(5)\}$. The microwave Rabi frequency extracted from the fit in Figure 3.6 was within 5% of the last measured single atom microwave Rabi frequency. The clear plateau in the data around $\theta = 0$ and 2π is indicative of the $\mathcal{W}$-state as the $|(\bar{1})_\perp\rangle$ state would not evolve into $|\bar{0}\rangle$.

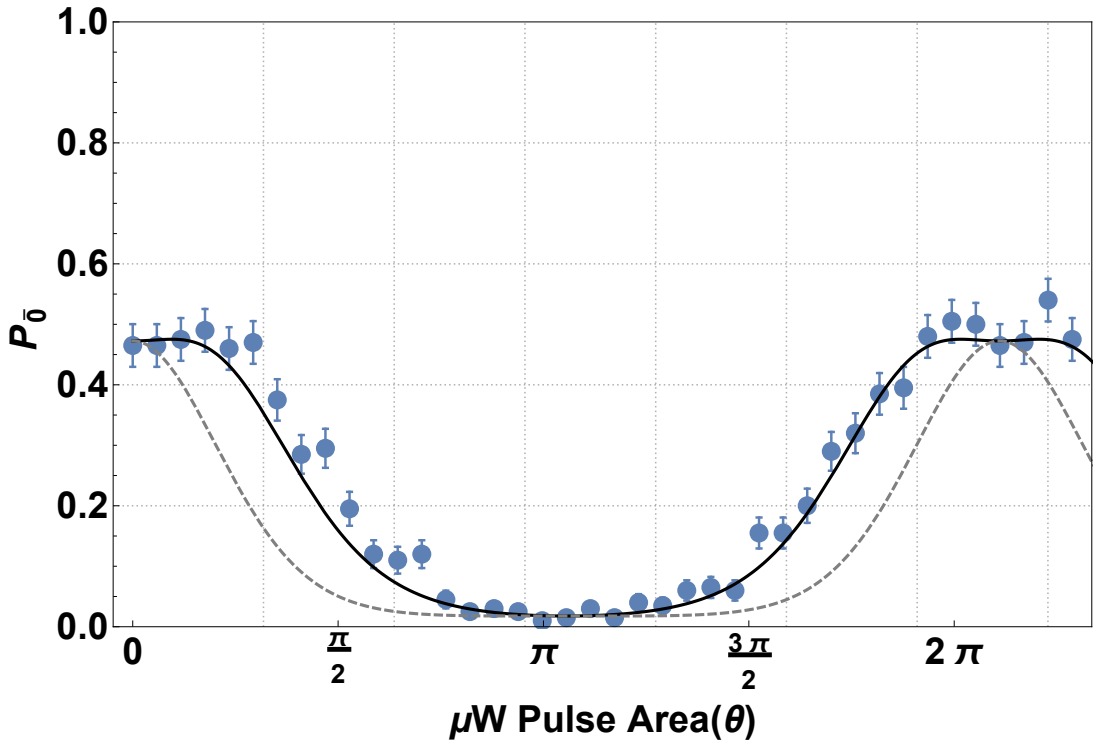

Figure 3.6: The probability to measure the ensemble in state $|\bar{0}\rangle$ after the microwave tomography experiment, data are shown in blue. A fit to the data for the initial populations and microwave Rabi frequency is shown as the black solid line. The grey dashed line shows the expected result if all the population in $|\bar{1}\rangle$ was instead in $|(\bar{1})_{\perp}\rangle$. Data was taken 5/30/2015.

3.3 Entanglement Thresholds for Partially Separable States

Following the lead of reference [56], thresholds for partially separable states can be imposed based on conservative assumptions. A state is said to be entangled if the state cannot be separated into two smaller product subspaces, thus we require the N-particle state in question $|\psi^{(N)}\rangle$ satisfy:

$$|\psi^{(N)}\rangle \neq |\psi_A^{(K)}\rangle \otimes |\psi_B^{(N-K)}\rangle,$$

for any $K < N$.

Therefore we continue with a proof by contradiction where a partially separable k-partite entangled state is assumed, and we can generate a threshold surface in the 2-dimensional space defined by the probability to generate $|\bar{0}\rangle$ and $|\bar{1}\rangle$, $\{p_{\bar{0}}, p_{\bar{1}}\}$. From the tomographic measurements we can extract the 2-dimensional coordinates $\{p_{\bar{0}}, p_{\bar{1}}\}$. If the coordinates exceed the threshold surface we can say that the generated state requires at least $k+1$-partite entanglement. A partially entangled state can be written as a product of m non-separable sub-spaces of dimension k_i, where i is the index of the subspace:

$$|\psi^{(N)}\rangle = |\psi_1^{(k_1)}\rangle \otimes |\psi_2^{(k_2)}\rangle \otimes ...|\psi_m^{(k_m)}\rangle$$

The partially separable state limit for $p_{\bar{1}}$ for a given $p_{\bar{0}}$ is maximal for $k_i = k$, where $0 < i < m$, and $k_m = N - k(m-1)$ and $|\psi^{(k_i)}\rangle = \cos(\theta_i)|\bar{0}^{(k_i)}\rangle + \sin(\theta_i)e^{i\phi_i}|\bar{1}^{(k_i)}\rangle$ [56]. This allows the substitution:

$$|\psi^{(N)}\rangle = \prod_{i=1}^{m} \left[\cos(\theta_i)|\bar{0}^{(k_i)}\rangle + e^{i\phi_i}\sin(\theta_i)|\bar{1}^{(k_i)}\rangle\right], \tag{3.5}$$

and therefore the points in the 2 dimensional k-partite separable space, $\{p_{\bar{0}}, p_{\bar{1}}\}$, are given

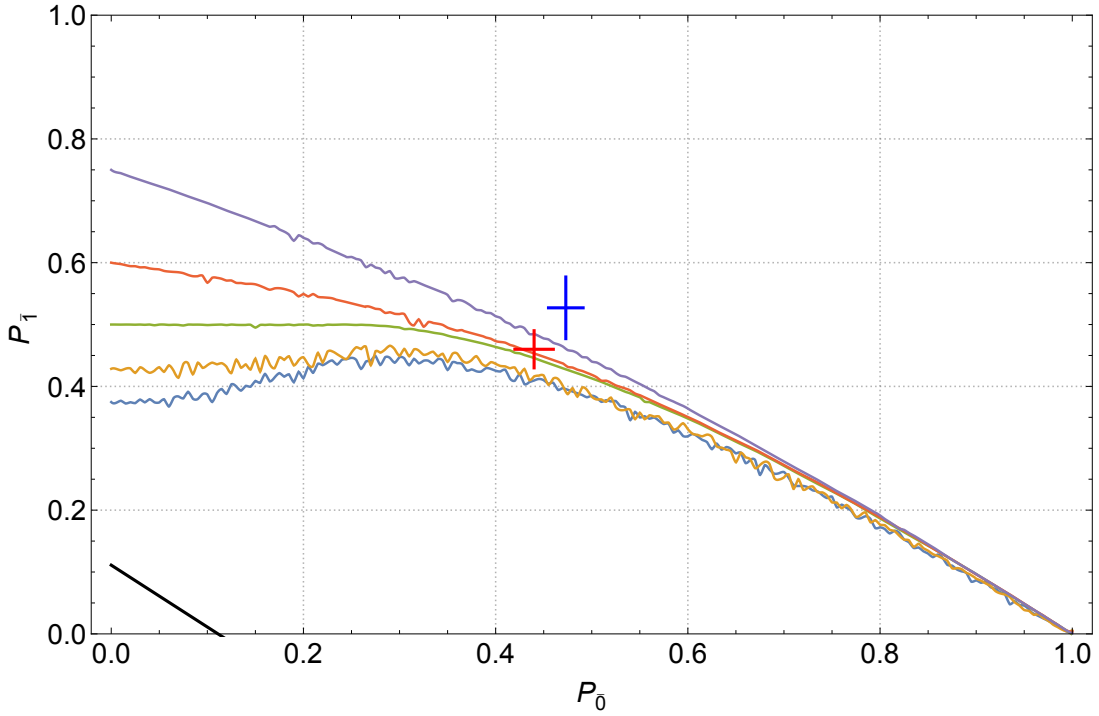

Figure 3.7: Numerically approximated thresholds for 3-partite entanglement with $N = \{4, 5, 6, 7, 8\}$ top to bottom. The maximal value for $\{p_{\bar{0}}, p_{\bar{1}}\}$ is shown from the fits to the Ramsey oscillation (red) and the microwave tomography data (blue). A higher threshold the more difficult it is to demonstrate k-partite entanglement.

by:

$$
\begin{aligned}
p_{\bar{0}} &= |\langle \bar{1}^{(N)} | \psi^{(N)} \rangle|^2 = \prod_{i=1}^{m} \cos^2(\theta_i) \\
p_{\bar{1}} &= |\langle \bar{1}^{(N)} | \psi^{(N)} \rangle|^2 = \frac{1}{N} \left| \sum_{i=1}^{m} \left[\sqrt{k_i} e^{i\phi_i} \sin(\theta_i) \prod_{j=1, j\neq i}^{m} \cos(\theta_j) \right] \right|^2
\end{aligned}
\tag{3.6}
$$

for all $0 \leq \theta_i < 2\pi$ and $0 \leq \phi_i < 2\pi$. To generate an approximation of the threshold surface we can perform a Monte Carlo where all θ_i and ϕ_i values are chosen randomly, then the maximal $p_{\bar{1}}$ results binned for $p_{\bar{0}}$ are shown in Figure 3.7.

This analysis of the entanglement witness described above ignores additional information we have constraining our system. For instance, the resulting output state from a $\mathcal{F}_{\mathcal{N}=1}$ experiment is observed to be consistent with perfect blockade. However, the state

described by Equation 3.5 can have significant doubly excited population. Therefore under the assumption of perfect blockade, $p_{(>1)} = 0$, we can modify Equation 3.5 to:

$$|\psi^{(N)}\rangle = \cos(\theta)|\bar{0}^{(N-k)}\rangle + e^{i\phi}\sin(\theta)|\bar{1}^{(k)}\rangle \tag{3.7}$$

The 2D threshold surface then simplifies to the analytical result:

$$p_{\bar{1}} = \frac{k}{N}(1 - p_{\bar{0}}), \tag{3.8}$$

the result of which is shown in Figure 3.8. Using Equation 3.8, we can take the result of the Ramsey and microwave tomographic data and extract a postselected k-partite entanglement threshold. We obtain entanglement fractions of $k/N = 0.82(6)$ for the Ramsey tomography and $k/N = 1.0(1)$ for the microwave tomography. This implies that when the ensemble is in the $\mathcal{F}_1$ Fock state, 82(6)% and 100(10)% of the atoms are participating in the entanglement on average.

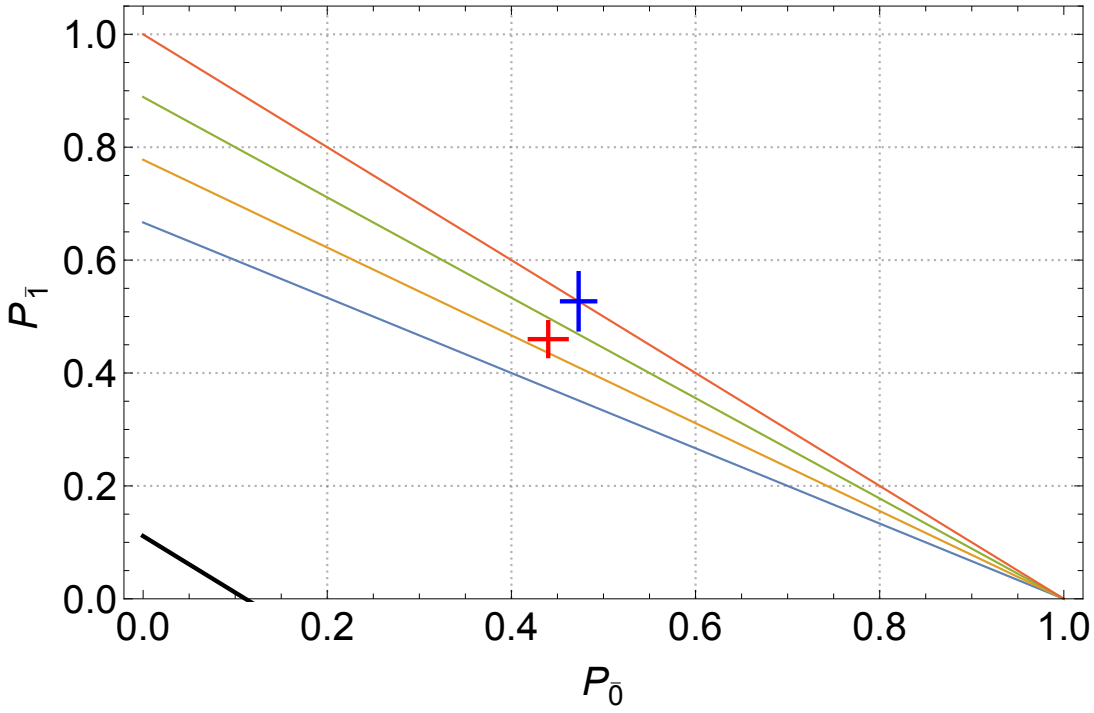

Figure 3.8: Thresholds for an $N = 9$ ensemble with $\{9, 8, 7, 6\}$-partite entanglement from top to bottom. The maximal value for $\{p_{\bar{0}}, p_{\bar{1}}\}$ is shown from the fits to the Ramsey oscillation (red) and the microwave tomography data (blue).

Chapter 4

Ensemble-Ensemble Blockade

The previous chapters have presented experiments that probe the behavior of single ensemble qubits, and Rydberg blockade interactions between atoms in the same trap site, or intra-site blockade. In this chapter, multi-site experiments are presented, where both intra- and ensemble-ensemble Rydberg blockade occurs. The first observation of Rydberg blockade between ensemble qubits is presented with a fidelity of 0.89(1) and a fidelity of ~ 1.0 when post-selected on the successful creation of the $\mathcal{F} = 1$ Fock state in the control ensemble[41]. The demonstration of Rydberg blockade between two optically resolvable ensemble qubits represents significant progress towards the goal of ensemble-ensemble entanglement via the Rydberg blockade mechanism. The progress toward generating entanglement between ensemble qubits is discussed at the end of this chapter in Section 4.4.

4.1 Procedure

The procedure for suppressing the excitation of a nearby ensemble via Rydberg blockade is a straight-forward interleaving of the procedure for creating a W-state in a single ensemble. The site that is addressed first is called the control ensemble, while the later ensemble is the target, in reference to the control and target qubits in a CNOT gate. In the notation

of Section 2.1, the experimental sequence, $\hat{\mathcal{B}}$, is written as:

$$\hat{\mathcal{B}}(\theta) \equiv \hat{\pi}_1^{C1}\hat{\pi}_1^{T1}\hat{\theta}_{\bar{N}_T}^{T0}\hat{\pi}_{\bar{N}_C}^{C0},$$

where $\hat{\pi}_n^{C(T)0(1)}$ represents an n-atom collective π-rotation between $|\bar{0}(\bar{1})\rangle$ and $|r\rangle$ for the control (C) or target (T) ensemble. The populations in the four possible output states $|CT\rangle = \{|\bar{0}\bar{0}\rangle, |\bar{0}\bar{1}\rangle, |\bar{1}\bar{0}\rangle, |\bar{1}\bar{1}\rangle\}$ are then measured with a state-selective blow-away. This experimental sequence is shown schematically in Figure 4.1.

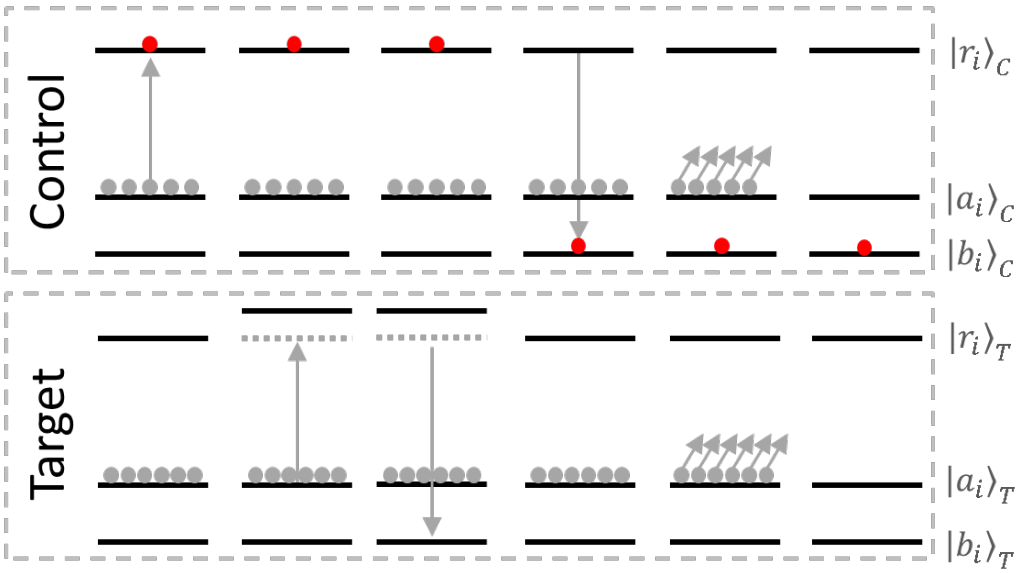

Figure 4.1: Pulse sequence for inter-ensemble blockade experiment $\hat{\mathcal{B}}$.

To provide a background measurement, an identical experiment is also performed except with the control site pulse, $\hat{\pi}_{\bar{N}_C}^{C0}$, omitted. This experiment is denoted as:

$$\hat{\mathcal{B}}_{off}(\theta) \equiv \hat{\pi}_1^{C1}\hat{\pi}_1^{T1}\hat{\theta}_{\bar{N}_T}^{T0}.$$

Under ideal conditions where the Rydberg blockade and the ensemble Rydberg excitation are both perfect, the expected result for $\hat{\mathcal{B}}_{off}$ is $|\psi_f\rangle = |\bar{1}\bar{0}\rangle$ since the target rotation

should be completely suppressed. If blockade is perfect, but the excitation rate is not unity, denoted p_{ex}, then the expectation would be to observe $|\bar{1}\bar{0}\rangle$ at a rate of p_{ex}, $|\bar{1}\bar{0}\rangle$ at a rate of $(1-p_{ex})p_{ex}$, and $|\bar{0}\bar{0}\rangle$ at a rate $(1-p_{ex})^2$, but never $|\bar{1}\bar{1}\rangle$. If blockade is imperfect, then we would observe $|\bar{1}\bar{1}\rangle$ at some rate, ignoring molecular loss channels.

4.2 Experiment

4.2.1 Main Results

Example target $\mathcal{W}$-state production $p_T = |\,|1\rangle_C \otimes \langle 1|_T]\,\hat{\mathcal{B}}(\hat{\mathcal{B}}_{off})|\bar{0}\bar{0}\rangle|^2$ data with the lowest blow-away leakage rate, 0.002/atom, is shown as the black (red) data points in Figure 4.2(a). To extract an ensemble-ensemble blockade fidelity, the simple $\mathcal{N} = 1$ model from Equation 2.6 is fit to the red points acquired with no blockading interaction (experimental sequence $\hat{\mathcal{B}}_{off}$) for an overall amplitude ϵ and mean target site atom number $\bar{N}_T$. The fit is then rescaled, with $\bar{N}_T$ fixed, to the nominally blockaded (black) data points, from experimental sequence $\hat{\mathcal{B}}$. The amplitude ratio of the two excitation curves reveals the ensemble-ensemble blockade fidelity. For this data set, the blockaded Rabi oscillation curve is 11% of the $\hat{\mathcal{B}}$ amplitude, implying that at least one atom is excited to the Rydberg state, $|r0\rangle$, from the control site during a multi-atom $\hat{\pi}^{C0}_{\bar{N}_C}$ pulse at a rate of $p_{ex} \geq 0.89(1)$. The observed p_{ex} is actually comparable to the p_{ex} expected in the ideal case, shown in Figure 2.5. This clearly rules out the situation where the $\mathcal{W}$-state production rate is low due to a decreased Rydberg excitation rate.

To investigate the ensemble-ensemble blockade fidelity the data are post-selected on a control transfer event, i.e. only final states measured as $|1\rangle_C$ are admitted into the data set. The resulting target $F = 1$ probability is shown as the green data set in Figure 4.2(b). The dashed green line represents the expected rate of background $|11\rangle$ events based on the calibrated blowaway background rate; for the details of this calculation see Appendix B. There is good agreement between the expected $|11\rangle$ background and the observed rate,

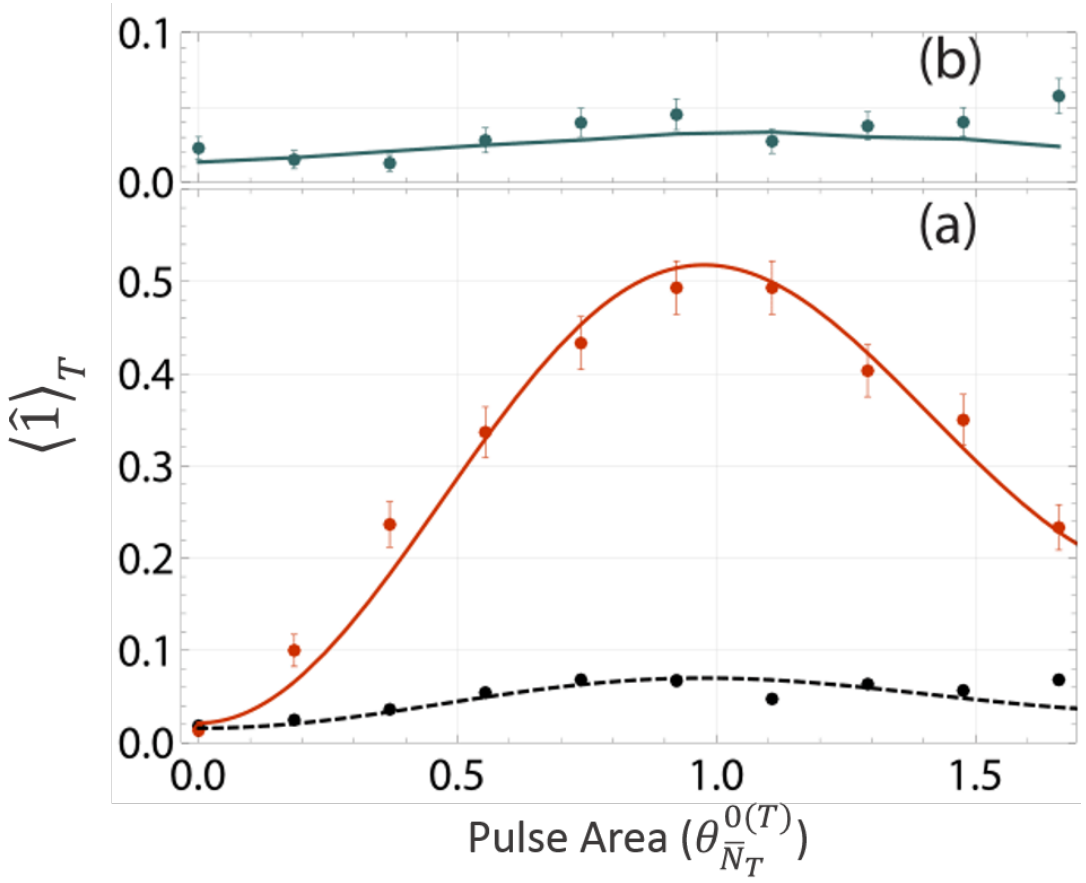

Figure 4.2: (a) The results of the ensemble-ensemble Rydberg blockade pulse sequence $\hat{\mathcal{B}}$ is shown in black shown in comparison with the non-blockaded rabi oscillation shown in red. The solid red line is a fit to the non-blockaded data set with $N_T = 6.2$ and an overall scaling factor as free parameters. The dashed black line is the same function with N_T set to 6.2 and the scaling factor as the only free parameter, resulting in a reduced amplitude of 0.11 of the non-blockaded oscillation. (b) The results of the same experiment after post-selecting on a successful transfer in the control site. Ideally this should be zero for all target pulse areas, but imperfect state selective readout creates some background signal estimated by the green line shown. Clearly no evidence of the $|\bar{1}\bar{1}\rangle$ state beyond the background rate is present.

therefore we can say that this subset of data are consistent with perfect blockade within the sensitivity of the experiment. The experiment is most sensitive to blockade leakage when the blowaway leakage is small since those are the only two channels where $|11\rangle$ population can be accumulated. Note that this result is unexpected as the trap geometry should allow for double excitations, as described in Section 6.2.

4.2.2 Control Ensemble Transfer Reduction

By post-selecting on $|1\rangle_C$ events, it becomes apparent that the number of successful control transfer events decreases as a function of the increasing target pulse area. This behavior is shown in Figure 4.3(a) for various atom numbers, site separations, and single-atom Rydberg Rabi frequencies. To study the results in a quantitative manner, the results are parameterized based on a figure of merit F, that should scale with the doubly excited Rydberg probability, p_{rr} , given by[52]:

$$F = \Omega_{\bar{N}_T}^2 \left[\frac{(n/n_0)^{12}}{(R/R_0)^6}\right]^{-2} \propto p_{rr},$$

where n is the principle quantum number, R is the ensemble-ensemble separation, $n_0 = 97$, and $R_0 = 8.7\mu$m. In Figure 4.3(b), the figure of merit F is plotted against the initial linear slope, $dp_C/d\theta_T$, of the normalized control transfer probability, $p_C = |\,[\langle 1|_C \otimes \mathbb{1}_T]\,\hat{\mathcal{B}}|00\rangle|^2$. Limits on the points considered as "initial linear slope" were selected manually. A larger slope implies that the blockade leakage occurs on a faster time scale and therefore the sample is less well blockaded. The monotonic increase in the initial slope with F is evidence for long-range Rydberg blockade leakage, which quickly evolves into a molecular state dark to the excitation lasers. The addition of an appropriate fast molecular evolution to the ensemble formalism developed in Chapter 6 could be done, but would require significant modifications to the formalism to correctly account for the possible states resulting from such a decay. A simple model of the expected ensemble-ensemble blockade

leakage is discussed in Section 4.3 in lieu of a full predictive calculation.

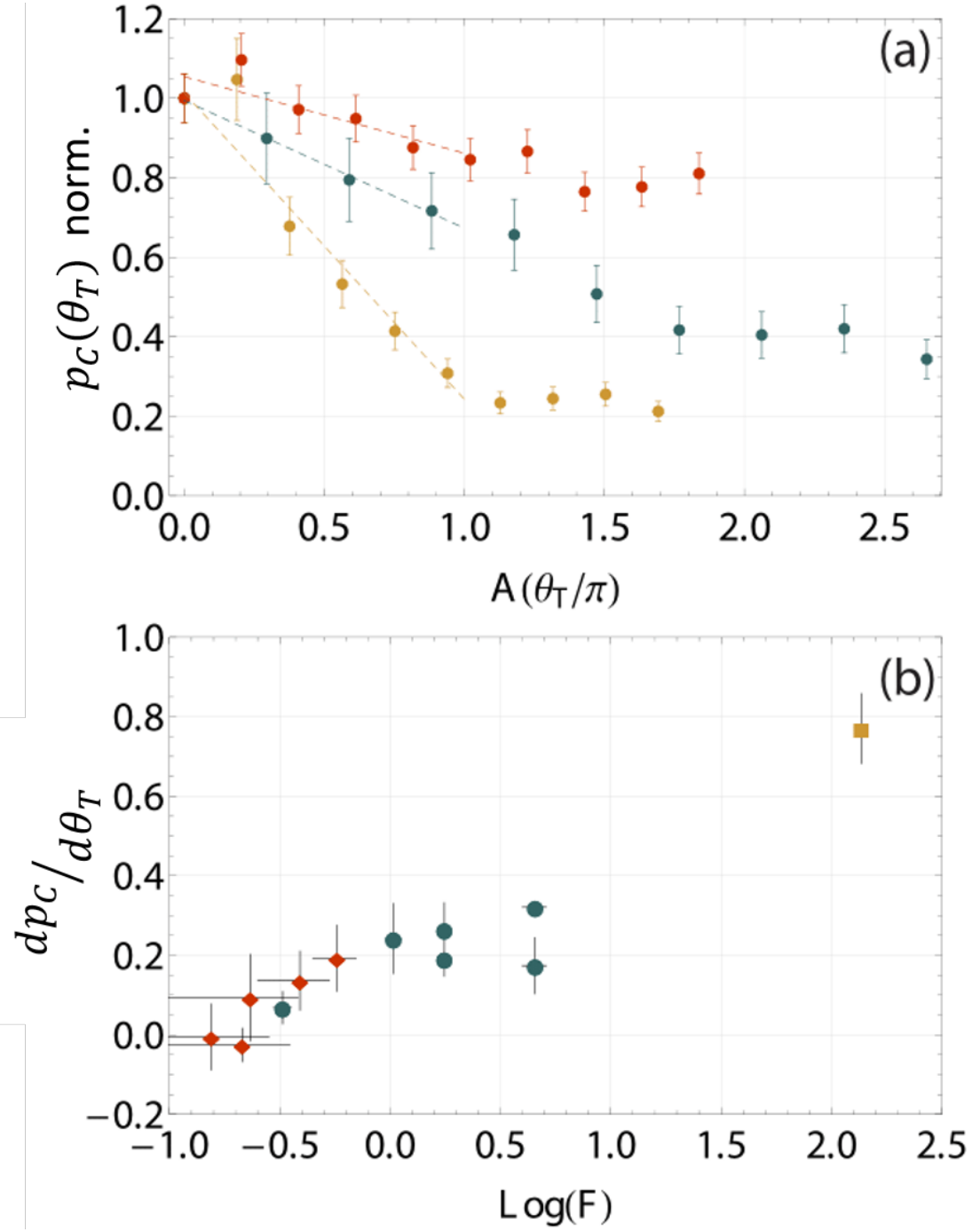

Figure 4.3: (a) Probability of preparing state $|1_C\rangle$ as function of the target ensemble pulse area θ_T. (a) Probability for several parameter sets: (111d5=2, $R = 8.3$ and 8.7 μm) (red diamonds), (97d5=2, $R = 8.3$ and 8.7 μm) (green circles), (97d5=2, $R = 17$ μm) (yellow squares). The data have been normalized to 1 at $\theta = 0$ for clarity, with typical success probability 40%-60%. (b) Comparison of the slope of the data in panel (a) with the scaling parameter F from Eq. (3). The color markers are the same as in panel (a).

This implies that there is, in fact, blockade leakage in the ensemble-ensemble blockade, which is expected since the second site is not completely blockaded (Section 6.2). However, what is unexpected is that no measurable amplitude of the ensemble-ensemble double excitations is returned to $|1\rangle$, and are instead lost, creating an unanticipated trap loss channel $|rr\rangle \rightarrow |0_{(\bar{N}_C-1)}0_{(\bar{N}_T-1)}\rangle$.

4.2.3 Discussion of Results

The results of the ensemble-ensemble blockade experiment suggest a possible, non-intuitive, cause for the lower than expected $\mathcal{W}$-state production rate, namely that there is a breakdown of blockade at short inter-atomic distances. If it can be assumed that when the blockade breaks down, the resulting molecular state undergoes some evolution to another state not addressable by the laser system, but remains in the area for the remainder of the Rydberg pulses continuing suppress excitation in the nearby ensembles. This would likely manifest as a better long-range blockade for the remaining atoms, but would result in an excess of observed $|0\rangle$ states. This is well in-line with our experimental observations. The short range intra-site blockade leakage loss channel may have been observed in an earlier experiment (Section 5.2) but the repeatability of the result was not sufficient to be convincing, and may be worth revisiting.

Predicting the molecular structure of the Rydberg states at close range is a formidable task due to the high density of states that must be considered even in a small energy band, and it is therefore difficult to predict behavior [57–60], see Section 6.2.4.

4.3 Simulations

A first approximation of the expected signal can be made by assuming perfect excitation of a control atom. The position of the atom in the control site is made to be proportional to the atomic density along z. and performing the same Monte Carlo analysis as described

in Section 6.2 with the addition of an additional interaction term for the singly excited target Rydberg state $U_{ctrl}(|z_C - z_T|)$. The result of this analysis for the $97D_{5/2}, m_J = 5/2$, $97S_{1/2}, m_J = 1/2$, and $113D_{5/2}, m_J = 5/2$ states is shown in Figure 4.5. Due to the stronger interaction long range doubly excited states have been ignored in the simulation. As can be seen there is an expectation that when the control atom is excited that there will be 6-8% excitation in the target. Since these are long range excitations, the attractive force on the atoms is small ($F \propto R^{-5}$) and the expected change in atomic position is small during the ~ 1 μs Rydberg pulse, leading to negligible detuning shifts during the de-excitation pulse, $R_1^T(\pi)$. Therefore according to the theory, with a single excitation in the control we should see 6-8% excitations in the target when a control atom is excited, which from Figure 4.2(b) is clearly not the case.

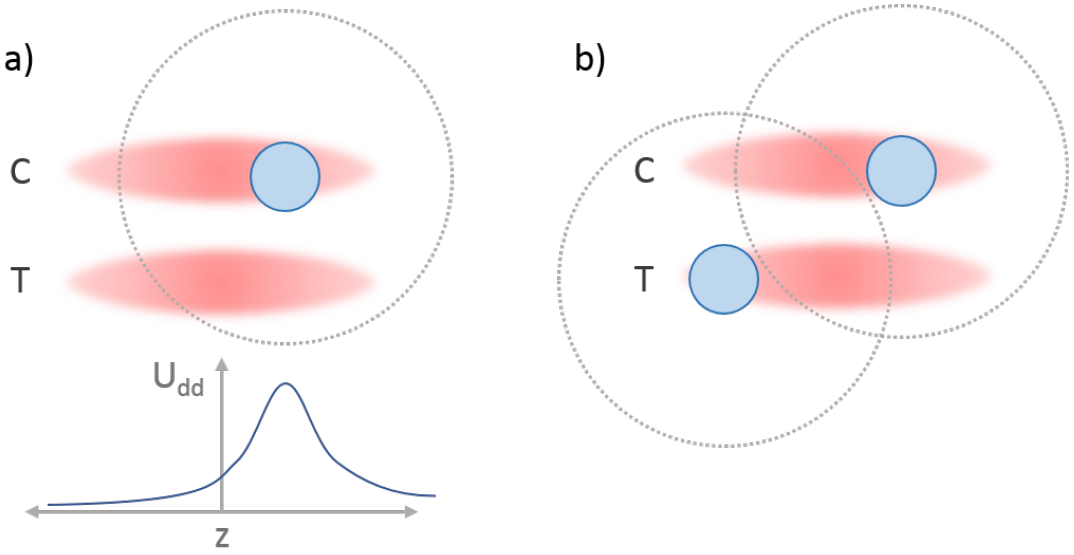

Figure 4.4: A cartoon model that the ensemble-ensemble blockade leakage simulation is based on. (a) An atom in the control site (C) is assumed excited to the Rydberg state, and based on the position of the atom an interaction term $U_{dd}(z)$ is added to each atom in the target site (T) based on its randomly generated z position. (b) Then the atoms in the target site undergo a collective Rydberg excitation pulse, and the Rydberg population is measured. In this example an excitation occurs in the control site to one side of the atom cloud. This allows a Rydberg excitation at the far end of the target site atom cloud to be excited to the Rydberg state since the interaction energy is small.

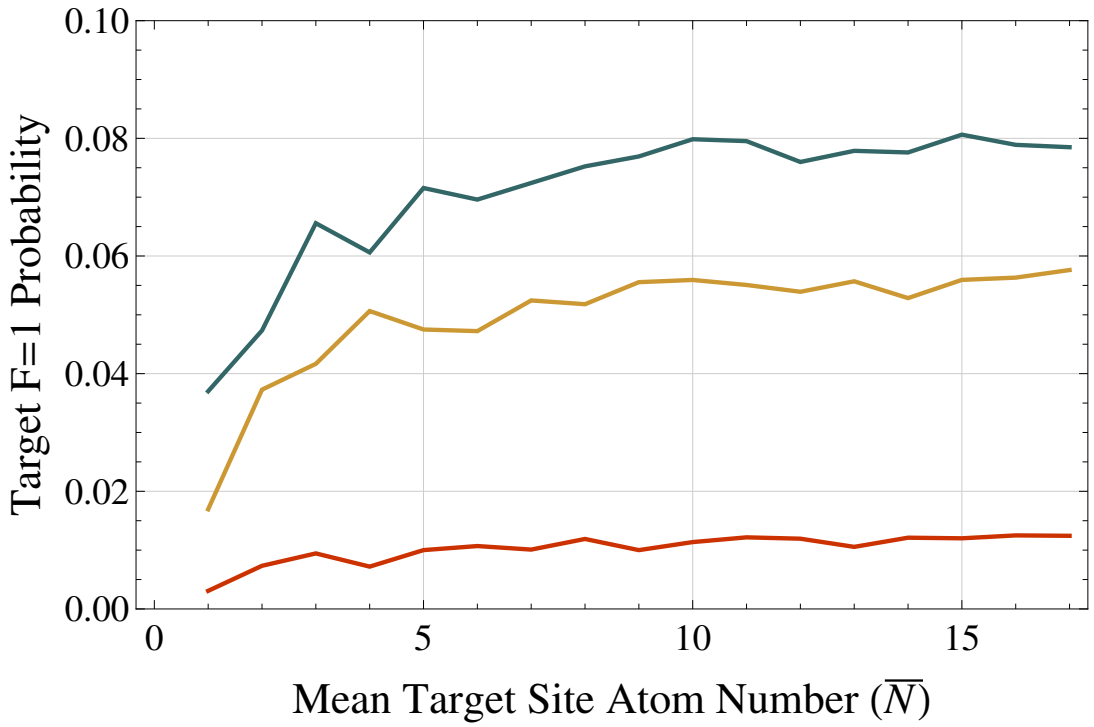

Figure 4.5: Example ensemble-ensemble blockade leakage calculations for various Rydberg states, assuming a Rydberg excitation in the control ensemble where the excitation probability density is proportional to the atom cloud distribution. The curves shown are for $97D_{5/2}, m_j = 5/2$ (blue), $97S_{1/2}, m_j = 1/2$ (yellow), $113D_{5/2}, m_j = 5/2$ (red). Note that measurable numbers of atoms in $|11\rangle$ are expected for the blue and yellow curves.

4.4 Entangling Gates

For Rydberg blockade-mediated ensemble qubits to be useful as a quantum computational architecture, it is necessary to demonstrate deterministic entanglement between distinct ensemble qubits. This would typically be done by measuring observables that serve as entanglement witnesses, similar to Chapter 3. In this case we would try to create the Bell state $|01\rangle + |10\rangle$, so the observables are the parity operator $\hat{P} \equiv \hat{p}_{00} + \hat{p}_{11} - \hat{p}_{01} - \hat{p}_{10}$ and the coherence C[1]. The relevant witness is given by the "Fidelity", $F = \frac{1}{2}(p_{01} + p_{10}) + C$. It can be shown that separable states are bound by $F \leq \frac{1}{2}$, so measuring an $F > \frac{1}{2}$ implies that some degree of entanglement exists between the qubits[61].

[1]The coherence C is the coherence of the Bell State produced. For example the Bell state $|01\rangle + |10\rangle$, C would be the coherence term between p_{01} and p_{10}.

With the amplitude of $\mathcal{W}$-state production in a single ensemble limited at present to 50-65%, a Bell's inequality violation to prove entanglement is not feasible. Figure 4.6 shows typical initial Bell state populations, with excess $|\bar{0}\bar{0}\rangle$ population, but notably low $|\bar{1}\bar{1}\rangle$ population.

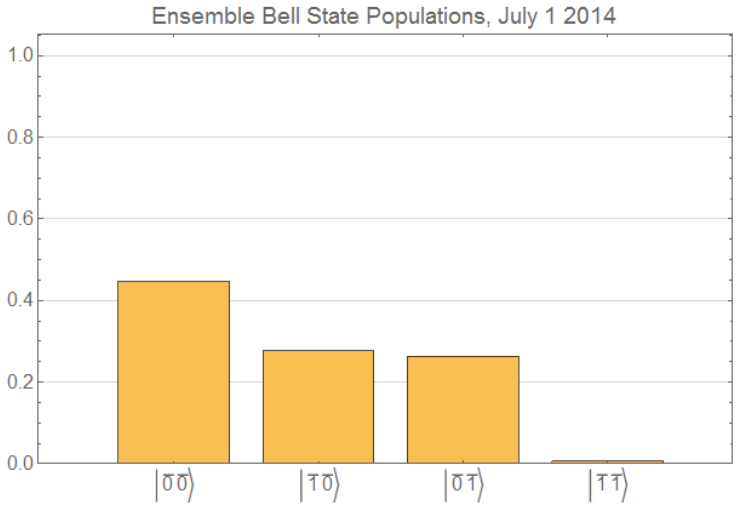

Figure 4.6: Initial bell state populations for a $\hat{\pi}_1^{C1}\hat{\pi}_1^{T1}\hat{\pi}_{\bar{N}_T}^{T0}\left(\hat{\pi/2}\right)_{\bar{N}_C}^{C0}$ experiment showing an excess of $|\bar{0}\bar{0}\rangle$ but notably low $|\bar{1}\bar{1}\rangle$ population. The ideal case would be $(|\bar{0}\bar{0}\rangle, |\bar{0}\bar{1}\rangle, |\bar{1}\bar{0}\rangle, |\bar{1}\bar{1}\rangle) = (0, 0.5, 0.5, 0)$. The actual output is $(|\bar{0}\bar{0}\rangle, |\bar{0}\bar{1}\rangle, |\bar{1}\bar{0}\rangle, |\bar{1}\bar{1}\rangle) = (0.45, 0.28, 0.26, 0.007)$.

If we were to perform the parity measurement with this initial state, assuming full coherence amplitude $C = \sqrt{p_{01}p_{10}} = 0.27$, we would obtain a Fidelity of $F = 0.54$, which would imply some degree of ensemble-ensemble entanglement.

Chapter 5

Double Rydberg States

The previous chapters have demonstrated that, apart from the $\mathcal{W}$-state amplitude, the dynamics of the Rydberg ensemble qubits agree well with simple theoretical predictions. Discussion of the $\mathcal{W}$-state preparation amplitude discrepancy between the best observed $\sim 65\%$ and the predicted $\sim 80\%$, had been withheld until all experiments had been presented. It is extremely likely that when the mechanism causing the amplitude discrepancy is identified and mitigated, that significant advances in the current state of the art for Rydberg ensemble qubits will be demonstrated shortly thereafter, as a demonstration of ensemble qubit entangling gates and Fock state production for $\mathcal{N} > 2$ are extensions of the basic framework demonstrated in this thesis.

Now that the majority of the relevant experiments have been discussed, we can take a step back and discuss the observation with all of the context. This chapter will discuss two mechanisms, a long- and a short-range Rydberg blockade leakage that leads to loss of both Rydberg atoms. A case for these Rydberg-Rydberg loss mechanisms to explain the discrepancy in $\mathcal{W}$-state amplitude and the ensemble-ensemble Rydberg interactions will be made. For reference, we will be discussing the proposed hypothesis' conformance to the results of the following experiments:

1. $\mathcal{N} = 2$ Fock state preparation tests (Section 2),

2. $\mathcal{W}$-state tomography and coherence (Chapter 3),

3. Ensemble-Ensemble Blockade tests (Chapter 4),

4. Differential atom number tests (Section 5.2), and

5. Sequential site single-atom loading tests (Section 5.3).

The last two experiments in this list are included at the end of this chapter, and are not as conclusive or straightforward as the experiments occupying their own chapters.

5.1 Discussion

All of the experiments listed above demonstrate that, while the amplitude of $|0\rangle \rightarrow |r\rangle \rightarrow |1\rangle$ transfer is lower than expected, the dynamics of this system are consistent with the expected Rydberg physics. The results of the ensemble-ensemble blockade experiment (Section 4.2.1) clearly demonstrate that the single-atom $|0\rangle \rightarrow |1\rangle$ transfer probability discrepancy is due to a sub-optimal de-excitation, and not from a suppression of the excitation to the Rydberg state. If the converse were true, there would be no way to explain the reduction of the target site Rabi oscillation amplitude by a factor of 9, without invoking a unsubstantiated correlation between the control and target sites. This observation is also consistent with the initial populations measured in the $\mathcal{F}_2$ Fock state experiments. What remains unknown is a sufficient explanation for this unanticipated de-excitation rate reduction. In this section, two loss channels for doubly excited Rydberg states are posited, one at long-range ($R > R_B$) and another at short-range ($R < R_s$), that both contribute to the observed loss. Here the inter-atomic separation designations refer to the blockade radius where $\Delta_{dd}(R_B) = \Omega$, $R_B \sim 15$ μm, and the so-called "spaghetti-regime" $R_s < 4$ μm for $n \sim 100$.

5.1.1 Long-Range Double Excitations

Interactions between Rydberg atoms on length scales around the blockade radius, R_B and further are weak enough that doubly-excited Rydberg states can be excited with non-negligible amplitude, see Section 6.2.4 for an in-depth discussion. If the interaction between atoms is small enough to allow double excitations on a timescale on the order of $\pi/(\sqrt{\bar{N}}\Omega)$, then the $\hat{\pi}_1^1$ Rydberg de-excitation should be sufficient to produce measurable population in the ground $\mathcal{N} = 2$ Fock state. Note also that, even though the D-state interaction potential curves are attractive, the acceleration experienced by a Rydberg-Rydberg molecule goes as R^{-5} at long-range. The small acceleration experienced over the course of the excitation pulse implies that a frozen gas model is valid.

We do not see any evidence for $\mathcal{N} = 2$ population above the background rate from imperfect blow-away in the single-ensemble $\mathcal{F}_1$ Fock state procedure. However, it is expected that some $\mathcal{N} = 2$ population should exist for our parameters. See the bottom blue line in Figure 2.5. To explain the "missing" doubly excited population, we introduce a fast molecular evolution mechanism for long-range Rydberg atom pairs, where atoms are far enough away to be excited, but close enough to interact on short timescales and evolve into a molecular state that is not optically addressable, either due to angular momentum selection rules or ionization.

We can see evidence for long-range blockade leakage and then subsequent molecular evolution in a two ensemble experiment by examining the control ensemble transfer reduction observation (Figure 4.3). Here the success of a Rydberg excitation and subsequent de-excitation in a control ensemble was dependent on the Rydberg excitation pulse area on a target ensemble. The larger the pulse area on the target ensemble, the less likely the control ensemble would be to successfully de-excite its Rydberg population. Since the control ensemble Rydberg population immediately following the control excitation pulse cannot depend on the pulse area of the later target ensemble pulse area, the control ensemble Rydberg excitation must interact at long-range ($R > 9$ μm) with the target

ensemble. The only way to have a long-range interaction at this scale would be to also have Rydberg population in the target site. In order to explain the observation that no double excitations be observed in the ground state, the long-range Rydberg pair would then need to be lost from the system.

The molecular evolution mechanism has also been suggested in references [62] and [63] where both groups report that the Electromagnetically Induced Transmission (EIT) of Rydberg D-states is observed to decrease on μs timescales. Both groups report the rate of transmission decay increases with increasing probe photon flux, which increases the density of Rydberg excitations in the sample. To explain this phenomenon, the authors invoke a fast evolution mechanism from Rydberg excitations pairs to other nearby long-lived Rydberg state pairs uncoupled by the control field. These dark Rydberg states continue to blockade subsequent excitations leading to a reduction in transmission. We note that these observations are consistent with our residual blockade observations (Figure 4.2(b)) and the control ensemble transfer reduction observation (Figure 4.3).

Molecular evolution explains our ensemble-ensemble dynamics extremely well and with the additional confirmation provided by the referenced papers, we are confident in the long-range molecular decay interaction. This behavior has not been observed to be an issue in Rydberg S-states for EIT, which may be a path forward if this was the dominant problem. Another tactic for avoidance is to increase the blockade figure of merit, R_B/σ_z, either by increasing the density by cooling or increasing the blockade radius. To test whether this is the issue for the intra-site $\mathcal{F}_1$ case, we increased the Rydberg n-level from 97 to 111, which should have improved the figure of merit by $(111/97)^{11} = 4$. No improvement in $\mathcal{F}_1$ intra-site production was observed at $n = 111$. Similarly, we have also not observed any improvement switching to the $97S$ Rydberg state, although R_B also decreases when switching to S.

As further evidence that long-range molecular evolution is not responsible for the $\mathcal{F}_1$ discrepancy alone, the long-range blockade interaction is well understood [64], but the

intra-site long-range double excitation rate predicted by the model is significantly below the double-excitation rate necessary to explain our intra-site data (Figure 2.5). Note also that in the intra-site blockade case the geometry for long-range interactions is effectively 1 dimensional and the angular dependence to the interaction is negligible. Therefore it is unlikely, that the long-range molecular decay is the the cause of the $\mathcal{W}$-state amplitude discrepancy, even though it explains the ensemble-ensemble interactions well. This has led us to propose an additional unexpected mechanism at short-range, elaborated on in the next section.

5.1.2 Short-Range Double Excitations

While the long-range interaction offers a satisfactory explanation for the ensemble-ensemble Rydberg-Rydberg loss, it does not explain the magnitude of the intra-site blockade leakage necessary to explain our observations. Instead we investigate the possibility of a short-range double Rydberg excitation mechanism. Note that calculating the interaction potential in the spaghetti-regime ($R < 4$ μm for $n \sim 100$) is notoriously difficult. In this regime the number of nearby levels and higher-order interactions required to accurately calculate the interaction energy increases substantially as the inter-atomic distance decreases, $R \to 0$. The solutions also become highly sensitive to external fields, adding additional technical complexity to the calculation. The density of weakly-coupled molecular resonances may be enough to overcome the low coupling strengths and narrow resonances to provide a mechanism for non-negligible coupling to molecular Rydberg states.

It has been shown that for Rydberg S-states molecular resonances begin occurring at medium range $R < 6$ μm for $n = 100$[57], Figure 5.1. These resonances also have steeper potential curves than long-range Van der Waals potentials, and can lead to significant acceleration away from the resonant inter-atomic separation condition. In reference [57], the authors calculate molecular loss rates for a homogeneous atom density, and derive an effective dephasing term. We have verified the continuation of these molecular resonance

patterns in Rydberg D-states, see Section 6.2.4 and Figure 6.11, but if a 1D geometry is considered instead of the 3D geometry presented in the paper, little dephasing is expected. This is because in a 3D sample the number of atoms in a spherical shell of radius R will scale as the volume of the shell, but for a 1D sample the number of atoms in the shell has no dependence on R. We do note, however, that the calculation for $R < R_s$ is inaccurate and the 1D geometry assumption becomes invalid at short range. Further, for our trap parameters a 6 atom sample, on average, will have 7 out its 15 atom pairs with $R < 5$ μm. Therefore, we suggest the mechanism from reference [57] as the most probable mechanism for short-range blockade leakage.

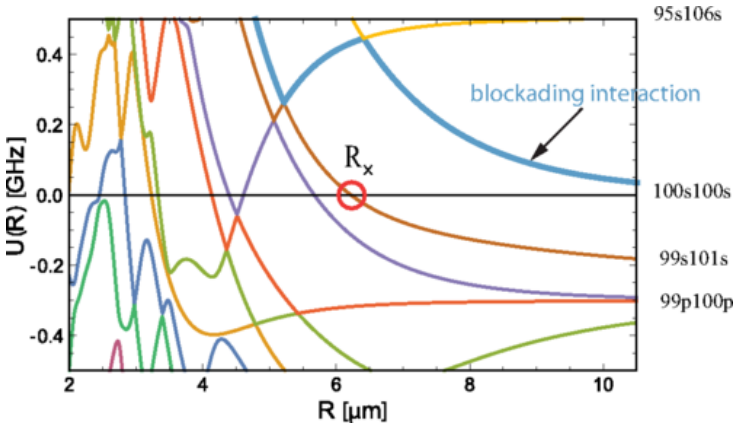

Figure 5.1: Reprinted from reference [57]. Molecular interaction potentials centered around the $100S + 100S$ Rydberg molecular state in the disassociation limit. The eigenstate with dominant $100S+100S$ character is shown in blue and bolded. Blockade leakage is possible at internuclear separations when the molecular potential is near the resonance condition (0 on the graph). The resonances begin around $R \sim 6$ μm and closer.

Besides short-range Rydberg blockade leakage, ground-Rydberg interactions are another avenue to explain the apparent loss of Rydberg atoms in the data. For Rydberg atoms with $n \sim 100$ the electron cloud is extremely large and extends to a radius on the order of 1 μm. There is a reasonable probability to have a ground state atom overlapping the Rydberg electron wavefunction, which can cause potential shifts, due to the electron scattering on the ground state atom, and even bound ground-Rydberg states[65, 66]. A notably old result from Fermi shows the energy shift decreases with n but the effective

number of atoms enclosed by the electron cloud increases, and the two effects cancel the n dependence on average[67]. However, this is only the case for an isotropic density distribution, and our 1D case changes the result in favor of energy shifts smaller than the Rabi frequency. At our densities, the number of atom pairs that are close enough to experience ground-Rydberg interactions are small. Additionally, this mechanism offers no explanation for the increased ensemble-ensemble blockade effectiveness, which has been observed.

Also of interest is the unusual observation, by Niederprüm et al. [51], of an anomalously large Rb_2^+ molecular ion formation cross section between a Rydberg atom and a ground state atom. The cross section was observed to scale as the size of the Rydberg atom and not the expected molecular ion internuclear separation which is three orders of magnitude smaller. To explain this an "efficient directed mass transport" mechanism was posited, which serves to catalyze the associative ionization. This mechanism also suffers from the low $R < 1$ μm event rate, however production of a molecular ion would massively increase the ability to suppress subsequent excitations in neighboring sites.

We plan to test for short-range molecular resonance channels by overlapping a blue-detuned 770 nm crossed dipole lattice in the axial dimension of the FORT sites, Figure 5.2. The lattice spacing will be 1.5 μm. The lattice will serve to impose a minimum spacing between atoms, so if an improvement in $\mathcal{N} = 1$ is observed with the extra lattice we will be able to assume that the short-range molecular resonance hypothesis is correct.

5.2 Differential atom number test

Since the Rydberg state is anti-trapped in the FORT and possibly photoionized, the ensemble population left in the Rydberg state will exhibit trap loss with high-fidelity. Therefore instead of measuring the population that was successfully transferred from $|0\rangle$ to $|1\rangle$, the trap population can be used to measure Rydberg population in an ensemble.

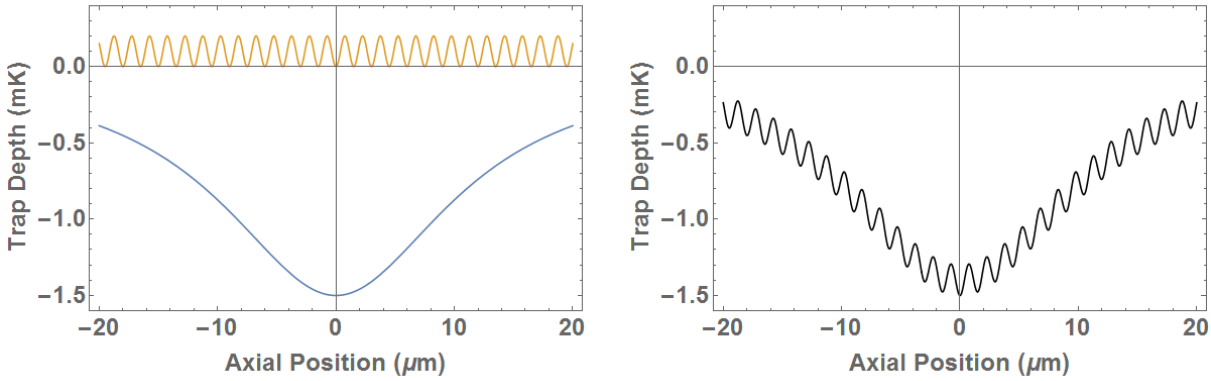

Figure 5.2: Cartoon of the superimposed 770 blue-detuned lattice and the 1064 FORT, with approximate trap depths. (a) The potentials on axis ($r = 0$) are shown separately. (b) The potentials are combined. Single atoms will sit in the lattice potential wells separated by some minimum distance.

The only issue is that, due to the readout loss mechanisms discussed in the Section 7.1, the measurement fidelity between 0 and 1 atom is significantly higher than the measurement fidelity between n and $n-1$ atoms. Therefore, with our apparatus it is not currently possible to perform this measurement on a shot-by-shot basis and instead we must rely on measurements of the atom distribution. This makes the experiment sensitive to changes in the trap loading rate over the time scale of the measurement. To minimize the sensitivity to loading rate drifts, the collective Rydberg $\pi_{\bar{N}}$-pulse data sets are interleaved every 50 data points with background data sets where no excitation occurs. The combined data sets are shown in Figure 5.3.

Under ideal conditions, the expected trap loss on average should be dependent on the ensemble mean atom number as shown in Figure 5.3. If the reduced $|0\rangle \rightarrow |r\rangle \rightarrow |1\rangle$ transfer probability is due to a low collective excitation probability and not the stimulated emission pulse, then we would expect to see a smaller difference in atom number than Figure 5.3 suggests. If the reduction is due to the stimulated emission step, then we should expect to see an atom number difference nearly equivalent to the simulated result. A reduction above the result from Equation 2.6, shown as the black line suggests double excitations and breakdown of blockade. Since we do not observe $\mathcal{N} = 2$ Fock states, any

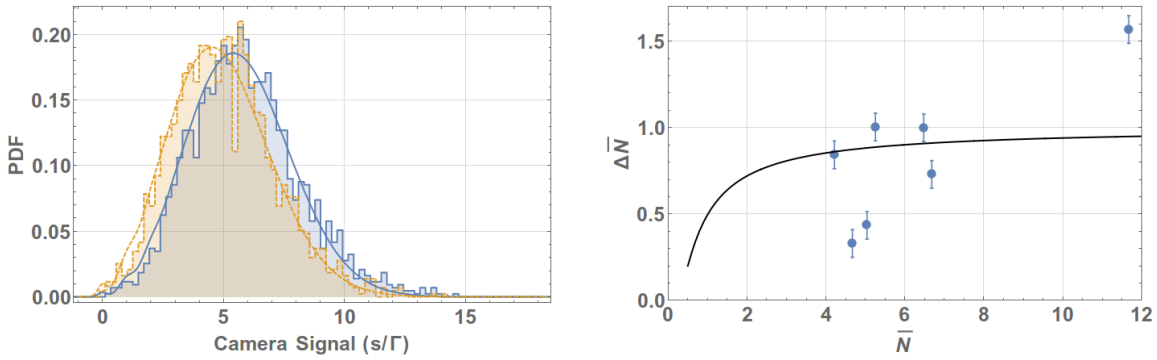

Figure 5.3: (a) Example camera signal histograms for an ensemble of atoms after no collective Rydberg pulse (solid blue) and a collective Rydberg $\pi_{\bar{N}}$-pulse (dashed yellow). The decrease in trap population is measured to be $\Delta\bar{N} = 0.99$ atoms, with $\bar{N} = 6.48(5)$ using the techniques defined in Section 7.2.3. Using the discrete models instead of the continuous changes the loss at the 0.01 atom level and the mean atom number by less than 1%. Data are from 4/26/2013. (b) A compilation of differential atom number data derived from camera signal histogram data. The black line is the ideal collective excitation limit for a Poissonian ensemble due to the atom Equation 2.6, with $\tau \to \infty$. Data above the black line suggest the existence of double excitations to the Rydberg state. Data below the black line suggest a lower collective excitation probability. Error bars are estimated error due to typical daily scattering rate fluctuations, $\sigma_\Gamma = \epsilon\Gamma = 0.045\Gamma$, and the sensitivity to the single atom scattering rate $d(\Delta\bar{N})/d\epsilon = -1.37$.

double Rydberg excitations must not be addressable by the stimulated emission laser. The results shown are not consistent, this is most likely due to atom number or single atom scattering drifts during the experiment. The total MOT and repumper laser power are stabilized before the switchyard where the X, Y, Z, and blow-away paths are siphoned from the main beam. The servo improves the stability of the laser powers and consequently the loading rate in the trap is more stable as well. However, the light coupled through the fibers to the experiment are outside the servo loop and can drift unknown amounts during an experiment since the powers are not monitored. In the next iteration of the hardware discussed in Section 8.0.2, the 6 individual MOT beam powers can be monitored and corrected during operation, which should serve to mitigate some of the technical issues affecting this measurement.

The existence of loss data $\Delta\bar{N}$ near or above the theoretical limit and the measured transfer rate to $|1\rangle$ is worth further investigation. A sequential loading test is discussed below which uses the neighboring sites to test for residual Rydberg excitation is discussed in Section 5.3.

5.3 Sequential Loading test

The results of Section 5.2 and Chapter 4 imply the existence of residual Rydberg excitation not coupled down to the $|1\rangle$ state. In order to further test this, we sequentially excite three FORT sites in a line axially separated by 9 μm and look for residual blockade in the second and third site addressed, from the site addressed before it, see Figure 5.4. The experiment in terms of operators is given by:

$$p_1^{(k)} = |(\langle 1^{(k)}| \otimes \mathbb{1}^2)\hat{\pi}_1^{(1)1}\hat{\theta}_{\bar{N}_1}^{(1)0}\hat{\pi}_1^{(3)1}\hat{\theta}_{\bar{N}_3}^{(3)0}\hat{\pi}_1^{(2)1}\hat{\theta}_{\bar{N}_2}^{(2)0}|0,0,0\rangle|^2,$$

where the single atom populations in sites $k = 1, 2, 3$, $p_1^{(k)}$, are measured simultaneously, and the superscript in the parentheses denotes the ensemble number addressed. The

background procedure is similar but with the FORT turned back on before addressing the next site. Turning the FORT on after an $\mathcal{N} = 1$ procedure removes any residual Rydberg population from the trap and so each site should not be coupled to the other sites. This is shown as the blue data in Figure 5.5, the yellow data shows the result of simultaneously increasing the collective pulse area for the collective excitation pulse proportionally so that each site reaches it's collective $\pi_{\bar{N}}$-pulse area in the same iteration. The data show a few features of interest. First for short excitation times, $\theta_{\bar{N}} < 3\pi/4$, there is little ensemble-ensemble interaction and the $\mathcal{F}_1$ probabilities follow the same evolution as in blue the uncorrelated case. Second, $p_1^{(3)}$ is decreased from 0.54(3) in the uncoupled case to 0.39(3) when a collective $\pi_{\bar{N}}$ is performed on region 2 immediately before. This implies that at least one atom is left in the Rydberg state from the region 2 excitation in at least 27% of the data sets. Likewise $p_1^{(1)}$ is decreased from 0.54(3) to 0.30(3), but the analysis here is not as straightforward since excitations could be blockaded by residual Rydberg population in either site 2 or 3. The correlations between the sequentially addressed sites are strong evidence for high efficiency collective Rydberg excitation of at least one atom, that is, however, not returned to the ground state via the $\hat{\pi}_1^{(i)1}$-pulse.

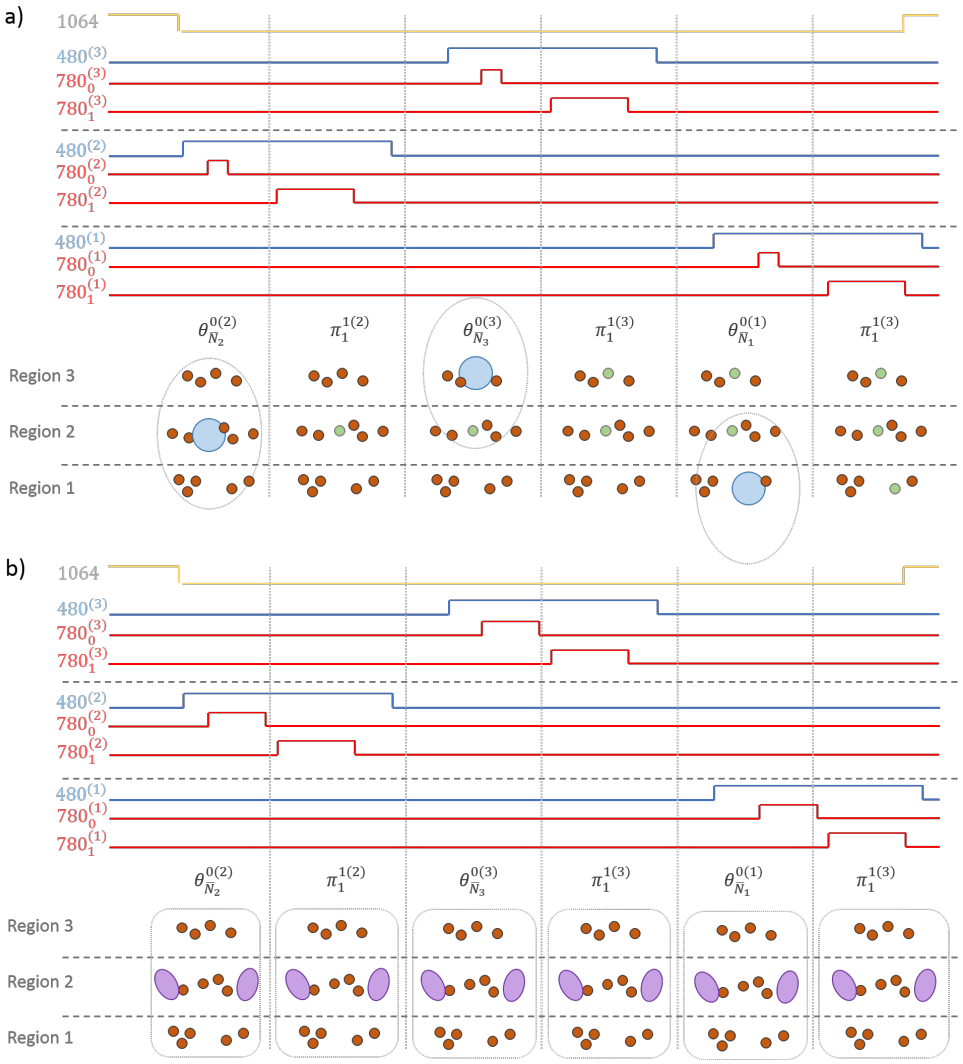

Figure 5.4: Pulse sequence diagram for the sequential loading test, the same collective pulse area $\hat{\theta}_{N_i}^{(i)0}$ is used for each ensemble for a given iteration, normalized for atom number $\bar{N}_i$ and single atom Rabi frequency Ω_0. The FORT is turned off while all 3 ensembles are addressed in order to maintain any correlations due to population remaining in the Rydberg state. Ensembles are addressed in the order: $2 \Rightarrow 3 \Rightarrow 1$. (a) The ideal case where no population (blue circles) is left in the Rydberg state between $\mathcal{W}$-state preparation operation. The blockade radius for the Rydberg excitation is shown as a gray oval around the Rydberg excitation. A single atom in each ensemble is successfully prepared in the $|1\rangle$ state. (b) An example of a long-range double excitation in the the first ensemble address (region 2). The double excitation is shown as a pair of purple circles to indicate that the Rydberg pair has evolved into a molecular state that is dark to the Rydberg lasers. The atoms remain in this excited state until the FORT is turned back on when they are ejected. The blockade radius here is shown to take up a larger area, implying a strong blockade across the ensembles in regions 1 and 3, therefore no $|1\rangle$ population will be measured in any region. A double excitation in region 3 (the second ensemble to be addressed) would similarly cause Rydberg excitation suppression in region 1, but would not effect region 2.

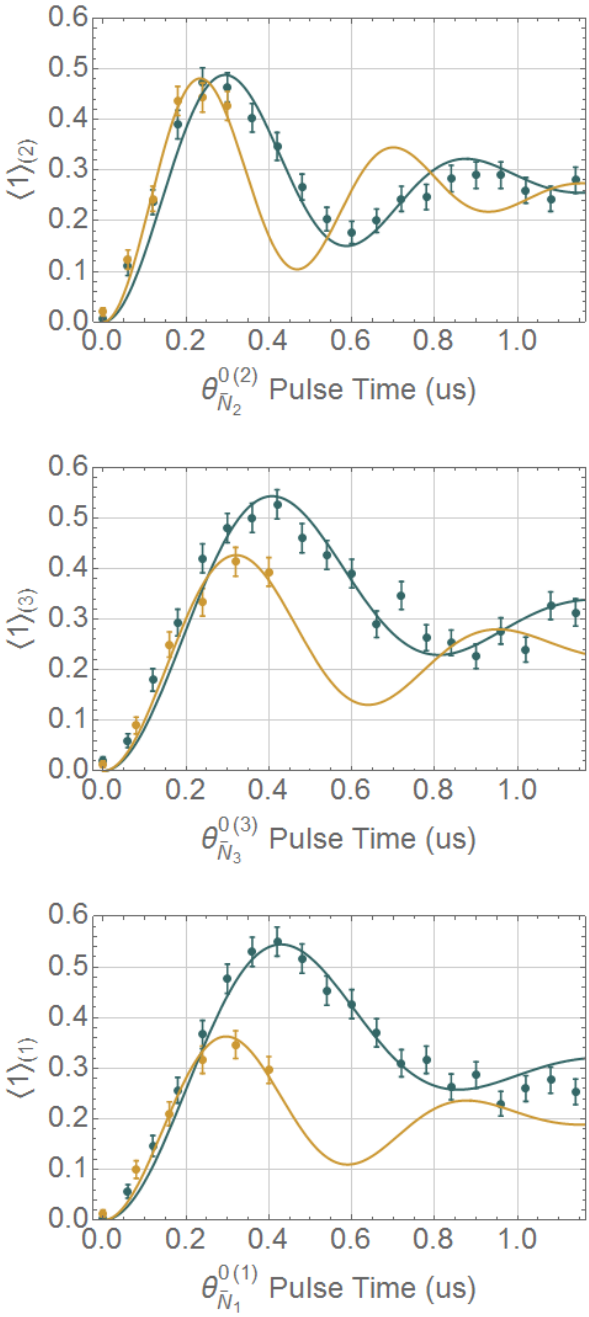

Figure 5.5: The data shown are $\mathcal{N} = 1$ Fock state preparation procedures in 3 sites (regions 1(c), 2(a), and 3(b)) when performed in separate FORT drops where remaining Rydberg population is lost (blue) and when performed back-to-back in the same FORT drop (yellow). The three sites are addressed in the order: $2 \rightarrow 3 \rightarrow 1$ and an approximate 20% reduction in $|0\rangle \rightarrow |r\rangle \rightarrow |1\rangle$ transfer probability is observed in each subsequent site that is addressed in the back-to-back procedure compared to the separate addressing procedure. The discrepancy implies that there is residual Rydberg population left after the stimulated emission $R_1(\pi)$ pulse. Error bars are statistical. The data has not been corrected for the imperfect state-selective readout. Data are from 7/01/2014.

Chapter 6

Single Atom and Ensemble Dynamics

In this chapter modeling realistic single-atom and ensemble Rydberg excitation dynamics is discussed. We begin by discussing the sources of inhomogeneous broadening such as Doppler shifts (Section 6.1.1), AC Stark shift gradients (Section 6.1.1), and intermediate state scattering (Section 6.1.2). In Section 6.2, the formalism for ensemble excitation is presented in two state bases, the internal state basis (Section 6.2.1) and the Dicke basis (Section 6.2.1). Homogeneous ensemble excitations with and without perfect Rydberg blockade are presented. Sources of amplitude degradation and decoherence are introduced, including the sources of inhomogeneous broadening discussed earlier, but now in the context of collective ensemble excitations and $\mathcal{W}$-state fidelity (Section 6.2.3). We also introduce a simple imperfect Rydberg blockade potential into the formalism (Section 6.2.4).

6.1 Single Atom Excitation

The non-ideal effects present in ensembles of interacting atoms are mostly present in single atom excitations as well, so we begin by discussing these effects in this comparatively

easier non-interacting regime. The effects of a single atom in a near-resonant light field can be broken down into spatially-dependent, velocity-dependent, and internal effects. Spatially, we are concerned with the atom sampling the spatial inhomogeneity of the excitation beams as well as the position dependent AC Stark shifts. The thermal velocity of the atoms in the beams leads to a velocity dependent detuning from the differential Doppler shifts. Additionally, there are deleterious effects from having a finite intermediate state detuning during the two-photon transition. If we were instead to use a single photon transition, then the AC Stark shifts and finite intermediate state detunings would no longer contribute, but the Doppler shift wouldn't partially cancel and the temperature would become more critical. In this analysis we ignore the effect of shot-to-shot power fluctuations since the laser powers are servoed and monitored to remove data where power fluctuations exceed a given range around nominal. We also assume Rydberg laser linewidths significantly narrower than any relevant spectral features, which is also valid for our experiment.

6.1.1 Inhomogeneous Broadening

Inhomogeneous broadening is a class of broadening mechanisms that effect each atom in a sample differently based on its location, velocity, and interactions with other atoms. The atoms will evolve coherently, but with different rates due to atom specific differences in coupling and detuning. However, when the atoms are not resolvable inhomogeneous broadening appears to dephase the evolution. This is different than, for example, scattering which does in fact dephase evolution even if the atoms are resolvable.

Doppler Shifts

The Doppler shift is a special relativistic frequency shift due to the velocity of the atom along the propagation axis of the laser beam relative to the lab frame. The frequency shift is given by $\delta = -\bar{k} \cdot \bar{v}$, where $\bar{k}$ is the wavevector of the laser and $\bar{v}$ is the atomic

velocity in the relevant reference frame. In this experiment, the Rydberg excitation lasers are counter-propagating so the differential Doppler shift is given by: $\Delta_D = -k' v_z$, where $k' = k_1 - k_2$ and k_i is the wavenumber of the i^{th} beam. The closer the excitation laser wavelengths are, the smaller the differential light shift and the broader the addressable velocity class. In this experiment $\lambda_{1(2)} = 780(480)$ nm, and $k'/2\pi = 0.8$ MHz/(m/s). The Doppler shift does not depend on the laser power so increasing the intensity of the excitation laser decreases the sensitivity to thermal velocities.

The effect of Doppler broadening in a non-interacting ensemble can be estimated analytically. The velocity distribution in z is given by:

$$\sigma_{v_z} = \sqrt{\frac{k_B T}{m}}, \tag{6.1}$$

where m is the atomic mass. The detuning distribution is then:

$$\sigma_{\Delta_D} = k' \sigma_{v_z}. \tag{6.2}$$

The expression for the excitation probability of a coherently driven near resonant two-level system with Rabi frequency Ω and detuning Δ is given by the familiar expression:

$$P_e(t) = \left(\frac{\Omega}{\Omega'}\right)^2 \sin^2\left(\Omega' t/2\right), \tag{6.3}$$

where $\Omega' \equiv \sqrt{\Omega^2 + \Delta^2}$. After a time $t = \pi/\Omega'$ the system is maximally inverted with amplitude $A(\delta) = (1+\delta^2)^{-1}$, where $\delta \equiv \Delta/\Omega$ is the normalized detuning. In the regime of small δ the frequency error effect on the amplitude is approximated as:

$$\sin^2\left[\sqrt{(1+\delta^2)}\pi/2\right] \approx 1 - \frac{\pi^2 \delta^4}{16} + \mathcal{O}(\delta^6),$$

for an ideal π-pulse ($t_\pi = \pi/\Omega$). The amplitude term, $A(\delta) = (1+\delta^2)^{-1} \approx 1 - \delta^2 + \mathcal{O}(\delta^4)$,

dominates the deviation from unity inversion. In the remainder of this section, we expand on this basic result to develop an analytic expression for the average amplitude for some Gaussian detuning distribution σ_δ.

The amplitude probability density function (PDF) at $t = t_\pi$, due to a distribution of Doppler shifts with normalized width $\sigma_\delta \equiv \sigma_{\Delta_D}/\Omega$, is given by:

$$\begin{aligned} P(A') &= \lim_{\epsilon \to 0} \left[\frac{2}{\epsilon} \int_{A^{-1}(A'-\epsilon/2)}^{A^{-1}(A'+\epsilon/2)} \frac{1}{\sigma\sqrt{2\pi}} e^{-\left(\delta/\sqrt{2}\sigma_\delta\right)^2} d\delta \right] \\ &= \frac{1}{\sigma_\delta A'^{3/2}\sqrt{2\pi\,(1-A')}} \exp\left[(A'-1)/(2A'^2\sigma_\delta^2)\right]. \end{aligned} \tag{6.4}$$

Note that $P(A')$ is singular at $A' = 1$, but since the physically relevant parameter $P(A_1 < A' < A_2) = \int_{A_1}^{A_2} P(A')dA'$ is finite for $A_2 = 1$, this is not a concern. The cumulative distribution function (CDF) $P(0 < A' < A_2)$ is shown in Figure 6.1(a) for $\sigma_\delta = \{0.01, 0.05, 0.1, 0.3\}$, which for Rb^{87} corresponds to $T = \{1.6, 41, 160, 1500\}$ μK at $\Omega = 1$ MHz. The CDF is useful for comparing probability distributions of greatly different widths without a log scale, since the magnitude is constrained. For example, having a CDF that spikes quickly is indicative of a repeatable amplitude, while a CDF that rises slowly will have a larger amplitude distribution.

The expectation value for A is given by:

$$\langle A(\sigma_\delta)\rangle = \sqrt{\frac{\pi}{2\sigma_\delta^2}} \left(1 - \mathrm{erf}\left[1/(\sqrt{2}\sigma_\delta)\right]\right) e^{1/(2\sigma_\delta^2)}.$$

The result of $\langle A(\sigma_\delta)\rangle$ is shown in Figure 6.1(b) along with a numerical evaluation of $(1+\delta)^{-1}\sin\left[\sqrt{(1+\delta^2)}\pi/2\right]$, with the same σ_δ, for comparison.

Expected parameters for our single atom excitation are: $\Omega = 0.7$ MHz, $k' = 0.8$ MHz/(m/s), $T = 100$ μK. The width of the Doppler detuning is $\sigma_D = 78$ kHz and $\sigma_\delta = 0.11$. Therefore the projected amplitude is $\langle A(0.11)\rangle = 0.988$, a 1.2% deviation from the ideal excitation rate due to Doppler broadening.

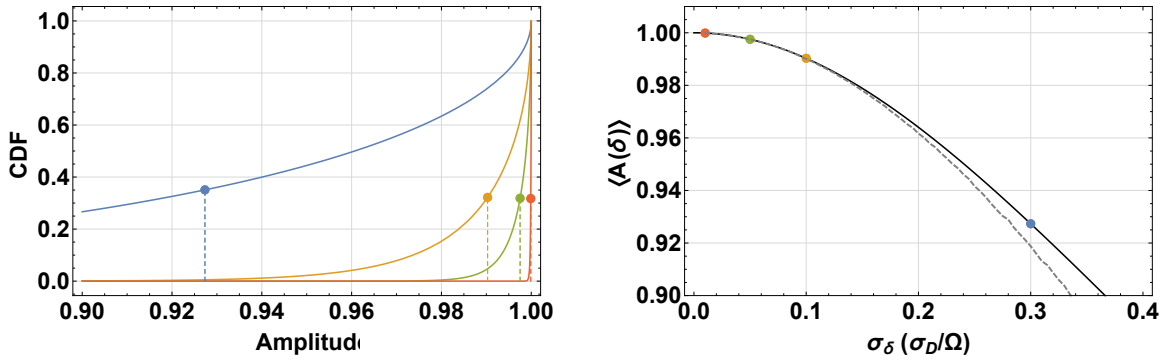

Figure 6.1: (a) Cumulative distribution function for the excitation amplitude A of a near resonant two-level system with on resonance Rabi frequency Ω and a normal detuning distribution of width $\sigma_\delta = \sigma_D/\Omega = \{0.01, 0.05, 0.1, 0.3\}$ shown in red, green, yellow, and blue respectively. The points on the graph denote the mean amplitude for the corresponding value of σ_δ. For Rb^{87} atoms with $\Omega = 1$ MHz and $k' = 0.8$ MHz/(m/s) the σ_δ's represent Doppler broadening due to temperatures of $T = \{1.6, 41, 160, 1500\}$ μK. (b) The mean excitation amplitude $\langle A \rangle$ as a function of σ_δ is shown in black, plotted along a numerical calculation of the full expression (Equation 6.3) shown as a dashed gray line. The points represent where the CDF lines in (a) are located.

Differential AC-Stark Shifts

Spatially dependent AC Stark shifts during excitation pulses are a consequence of the 2-photon transition used to couple the atom to the Rydberg state. The Hamiltonian for the 3-level system $\{|1\rangle, |e\rangle, |r\rangle\}$, with no spontaneous emission, is given by:

$$H = \begin{pmatrix} 0 & \Omega_1/2 & 0 \\ \Omega_1/2 & \Delta & \Omega_2/2 \\ 0 & \Omega_2/2 & \delta_{2\gamma} \end{pmatrix},$$

where $\Omega_{1(2)}$ is the Rabi frequency of the 780(480) nm photon, Δ is the intermediate state detuning, and $\delta_{2\gamma}$ is the 2-photon detuning, as depicted in Figure 1.9. For $\Delta \gg \{\delta_{2\gamma}, \Omega_1, \Omega_2\}$, the population in state $|e\rangle$ is small and oscillates rapidly allowing us to perform an adiabatic elimination, $c_e'(t) = 0 = -\frac{i}{2}\left(\Omega_1 c_1(t) + \Omega_2 c_2(t) + 2\Delta(t) c_e(t)\right)$. Making

the replacement $c_e(t) = -\frac{1}{2\Delta}\left(\Omega_1 c_1(t) + \Omega_2 c_2(t)\right)$, results in the effective Hamiltonian:

$$H_{eff} = \begin{pmatrix} 0 & \frac{\Omega_{2\gamma}}{2} \\ \frac{\Omega_{2\gamma}}{2} & \delta_{2\gamma} - \delta_{AC} \end{pmatrix}, \tag{6.5}$$

where $\Omega_{2\gamma} \equiv \Omega_1\Omega_2/(2\Delta)$ is the 2-photon Rabi frequency and $\delta_{AC} \equiv \left(\Omega_1^2 - \Omega_2^2\right)/(4\Delta)$ is the differential AC Stark shift. The differential AC Stark shift is minimized when the single photon Rabi frequencies are equal $\Omega_1 = \Omega_2$. In our case $\Omega_1 \sim 10\Omega_2$ so we are dominated by the spatial inhomogeneity of the 780 nm laser.

Since the atomic cloud has some finite extent and the addressing lasers have a narrow waist to achieve low-crosstalk site-selective addressing, the atom will sample different laser intensities each iteration. This causes differences in the excitation parameters shot-to-shot due to spatially dependent $\Omega_{2\gamma}(\bar{\mathbf{x}})$ and $\delta_{AC}(\bar{\mathbf{x}})$. Most of the effect of differential AC Stark shifts in our system can be obtained by considering only the 780 shift due to the variation of the radial coordinate r in the beam since the extent of the atomic cloud is substantially shorter than the Rayleigh length, $\sigma_z \ll z_R$.

To do this we will employ a method similar to the previous section. There is an additional complication though since the AC Stark shift is not symmetric about $\delta = 0$ like the Doppler shift. Mitigating this will require that the 2-photon detuning is set to the mean shift to minimize detuning errors, $\delta_{2\gamma} = \langle\delta_{AC}\rangle$. The PDF for the atomic position in cylindrical coordinates is:

$$P(\rho) = \frac{2\rho}{\sigma_\rho^2} e^{-(\rho/\sigma_\rho)^2}, \tag{6.6}$$

and therefore the PDF for the AC Stark shifts, assuming the 780 and 480 nm laser waists are equal $\omega = \omega_{1(2)}$, is related to the PDF for $\Omega^2 = \Omega_1^2 - \Omega_2^2$ via a change of variable

transformation:

$$\begin{aligned} P(\Omega^2) &= \lim_{\epsilon \to 0} \left[\frac{2}{\sigma_\rho^2 \epsilon} \int_{(\Omega^2)^{-1}(\Omega^2+\epsilon/2)}^{(\Omega^2)^{-1}\left(\Omega^2-\epsilon/2\right)} \rho e^{-(\rho/\sigma_\rho)^2} d\rho \right] \\ &= \frac{\omega^2}{2\sigma_\rho^2 \Omega^2} \left(\frac{\Omega^2}{\Omega_0^2} \right)^{\omega^2/(2\sigma_\rho^2)} \\ &= \frac{\chi^2}{2\Omega^2} \left(\frac{\Omega^2}{\Omega_0^2} \right)^{\chi^2/2}, \end{aligned} \tag{6.7}$$

where $\chi \equiv \omega/\sigma_\rho$ and the domain of $P(\Omega^2)$ is $\Omega^2 \leq \Omega_0^2$. If matched beam waists are assumed ($\omega_1 = \omega_2$), the detuning distribution is:

$$P(\delta_{AC}) = \frac{\chi^2}{2\delta_{AC}} \left(\frac{\delta_{AC}}{\delta_{AC}^0} \right)^{\chi^2/2}, \tag{6.8}$$

where the domain of $P(\delta_{AC})$ is $0 \leq \delta_{AC} \leq \delta_{AC}^0 \equiv \Omega_0^2/(4\Delta)$. The mean shift $\langle \delta_{AC} \rangle$ under these conditions is given by:

$$\langle \delta_{AC} \rangle = \frac{\delta_{AC}^0}{1 + 2\chi^{-2}} \tag{6.9}$$

To minimize the differential AC Stark shift the laser waists must be significantly larger than the atom cloud ($\chi \gg 1$). Note that since $\omega_1 = \omega_2$ is assumed, the analysis can be extended to derive an expression for the mean two-photon Rabi frequency:

$$\langle \Omega_{2\gamma} \rangle = \frac{\langle \Omega_1 \Omega_2 \rangle}{2\Delta} = \frac{1}{1 + 2\chi^{-2}} \left(\frac{\Omega_1^{(0)} \Omega_2^{(0)}}{2\Delta} \right) \tag{6.10}$$

Generating an analytic result for the amplitude PDF can be done, however since the detuning is asymmetric with respect to the mean shift the calculation becomes difficult and not particularly enlightening. Monte-Carlo simulations of the amplitude PDF and time series models at different temperatures are shown in Figure 6.2.

Expected parameters for our single atom excitation are: $\Omega = 0.7$ MHz, $T = 100$ μK, $\chi = 15.1$, and $\delta_{AC}^0 = 3.47$ MHz. Therefore the projected amplitude is $\langle A \rangle = 0.998$, a 0.2% deviation from the ideal excitation rate due to AC Stark shift broadening.

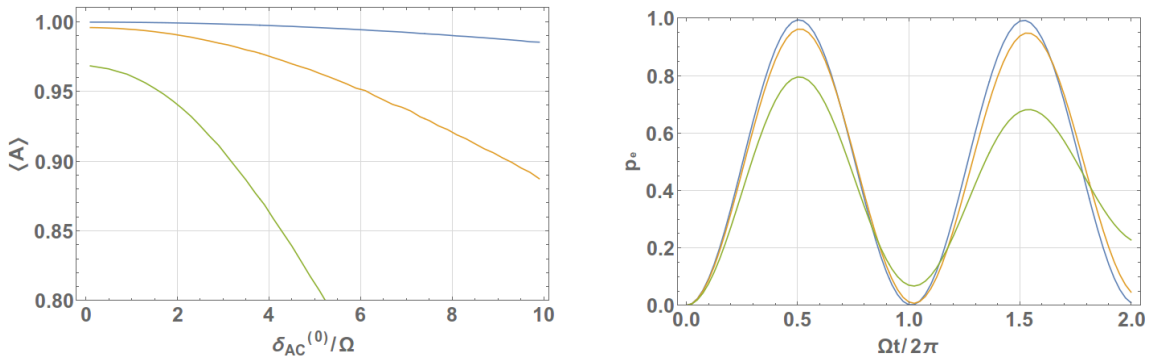

Figure 6.2: (a) Monte-Carlo simulations of the mean excitation amplitude A of a two-level atom vs peak AC Stark shift, $\delta^0_{AC}/\Omega^0_{2\gamma}$, for different values of $\chi \equiv \omega/\sigma_\rho = 12.34$ (blue), 6.76 (orange), and 3.90 (yellow). These values of χ correspond to Rb^{87} temperatures of 150, 500, and 1500 μK respectively with a $\omega = 8$ μm excitation beam waist. (b) The excitation probability is shown as a function of time for the same χ values and with $\delta^0_{AC} = 4.95\Omega^0_{2\gamma}$. Only AC Stark shifts are included in the model.

6.1.2 Intermediate State Scattering

Coherent two-photon excitation processes are typically performed with the constituent laser frequencies near an intermediate state transition in order to increase the Rabi frequency. For a two-photon process, the Rabi frequency, $\Omega_{2\gamma}$, is given by:

$$\Omega_{2\gamma} = \frac{\Omega_1 \Omega_2}{2\Delta},$$

where Δ denotes the detuning from the intermediate state. Decreasing Δ increases the Rabi frequency allowing excitation pulses to occur in less time, but this comes at the cost of increasing the intermediate state population. Since the intermediate state has a finite scattering rate that is significantly faster than the two-photon Rabi frequency, any population build up in the intermediate state will be redistributed in the ground state magnetic sub-levels, most of which are not addressable by the Rydberg lasers, due to the large magnetic field present during an excitation, and therefore cease participating in the computation. However the atoms continue to be trapped and the magnetic sub-levels are not distinguishable by the state-selective readout procedure that we implement, and can

show up in potentially erroneous F-states during the readout.

The probability of an intermediate state scattering event occurring during a π-pulse is given by [26]:

$$P_{se} = \left(\frac{\pi\Gamma}{4\Delta}\right)(q + q^{-1}),$$

where $q \equiv |\Omega_2/\Omega_1|$ and Γ is the intermediate state scattering rate. As with the AC Stark shift errors, the system is optimal when $q = 1$. For us typically $q = 0.1$, since the transition matrix element for $5P_{3/2} \rightarrow nD_{5/2}$ is so much much smaller than the $5S_{1/2} \rightarrow 5P_{3/2}$ transition. This limits the achievable single-photon Rabi frequency for the blue laser. With our parameters we expect a spontaneous emission event probability of $P_{se} = 2.3\%$ for a π-pulse.

6.2 Ensemble Excitation

The single atom modeling technique discussed is sufficient for non-interacting atom samples, but is not capable of describing ensembles with large interactions accurately. In order to model systems with large interactions, the system cannot be treated as independent components with independent energy levels. Instead we must write down the Hamiltonian in a basis that is convenient, then if necessary transform to a basis that is convenient to model the evolution. The bases that are well suited for these tasks are discussed in Sections 6.2.1 and 6.2.1.

In this section, the $\mathcal{W}$-state is discussed in depth and the ensemble excitation formalism is presented. Then the effects of inhomogeneous broadening and intermediate state scattering will be discussed in the context of Rydberg ensembles. The effects of finite Rydberg blockade interactions will also be addressed.

6.2.1 The $\mathcal{W}$-state

The $\mathcal{W}$-state, or $|\bar{1}\rangle$, is an entangled state of N two-state systems defined by Equation 1.1. Creation of the $|\bar{1}\rangle$ state can be accomplished stochastically, via a short excitation pulse[56], or deterministically, using a process that limits the Hilbert space of the ensemble. By performing an excitation to the Rydberg state under strong blockade conditions, the effective Hilbert space is limited to $|\bar{0}\rangle \equiv |0^{(1)}...0^{(N)}\rangle$ and $|\bar{1}\rangle$ (ignoring effects of inhomogeneous broadening), which allows for deterministic preparation of $|\bar{1}\rangle$.

Some of the properties of the $|\bar{1}\rangle$ state are non-intuitive to those familiar with a typical non-interacting ensemble, and it is helpful to demonstrate some fundamental properties. We will consider the system to consist of N spin 1/2 particles, $|0(1)\rangle \rightarrow |-(+)\rangle$, and will investigate the problem in two bases: the internal state basis ($|\pm^{(1)}\rangle \otimes |\pm^{(2)}\rangle \otimes ...|\pm^{(N)}\rangle$) and the Dicke basis ($|JM\rangle$). For more information, the interested reader should refer to [68].

Internal State Basis

The interaction of a generic ensemble excitation with a light field can be written in the basis of individual atom excitations ($|\pm^{(1)}\rangle \otimes |\pm^{(2)}\rangle \otimes ...|\pm^{(N)}\rangle$). The interaction Hamiltonian, $\mathbf{H}_{int}$, describing the evolution of the system is a block tridiagonal matrix where the basis states associated with main block diagonals, $\mathbf{\Delta}_n$, are degenerate under the excitation Fock state operator, $\hat{\mathcal{N}} \equiv \sum_{k=1}^{N} \hat{S}_z^{(k)} + N/2$, where $\hat{S}_\mu^{(k)} = \frac{1}{2}\hat{\sigma}_\mu^{(k)}$ is the spin projection operator along the axis defined by μ. The basis states of the system are denoted as $|n_k\rangle$, where n denotes the eigenvalue of $\hat{\mathcal{N}}$ and the index k breaks the degeneracy of the operator, e.g. $|1_1\rangle = |+-\cdots-\rangle$, $|1_2\rangle = |-+-\cdots-\rangle$, and $|2_1\rangle = |++-\cdots-\rangle$. The matrices on the other diagonals couple the system between excitation number (Fock) states, i.e. a double excitation occurs by coupling a singly excited state, $|1_k\rangle$ to a doubly excited state $|2_j\rangle$, instead of second order process directly from the ground state. In this

basis $\mathbf{H}_{int}$ is given by:

$$\mathbf{H}_{int} = \mathbf{A} + \mathbf{\Delta} = \begin{bmatrix} \mathbf{\Delta}_0 & \mathbf{A}_{(0,1)} & 0 & & \cdots & & 0 \\ \mathbf{A}^T_{(0,1)} & \mathbf{\Delta}_1 & \mathbf{A}_{(1,2)} & & & & \\ 0 & \ddots & \ddots & \ddots & & & \vdots \\ & & \mathbf{A}^T_{(n-1,n)} & \mathbf{\Delta}_n & \mathbf{A}_{(n,n+1)} & & \\ \vdots & & & \ddots & \ddots & \ddots & 0 \\ & & & & \mathbf{A}^T_{(N-2,N-1)} & \mathbf{\Delta}_{N-1} & \mathbf{A}_{(N-1,N)} \\ 0 & & \cdots & & 0 & \mathbf{A}^T_{(N-1,N)} & \mathbf{\Delta}_N \end{bmatrix} \tag{6.11}$$

The matrix $\mathbf{H}_{int}$ dimension is 2^N, the dimension of N 2-level systems. The dimension of the block diagonal sub-matrices is given by the binomial coefficient, $\dim(\mathbf{\Delta}_n) = \binom{N}{n} \equiv N_n$. The block diagonal sub-matrices, $\mathbf{\Delta}_n$, contain information concerning the sub-system's specific energy levels.

$$\mathbf{\Delta}_n = \sum_{k=1}^{N_n} \delta_k^{(n)} |n_k\rangle\langle n_k| \tag{6.12}$$

$$\mathbf{\Delta}_n = \begin{bmatrix} \delta_1^{(n)} & 0 & \cdots & 0 \\ 0 & \delta_2^{(n)} & \cdots & 0 \\ \vdots & \vdots & \ddots & \vdots \\ 0 & 0 & \cdots & \delta_{N_n}^{(n)} \end{bmatrix}, \tag{6.13}$$

where $\delta_k^{(n)}$ refers to the energy of the k^{th} basis state in the subspace with eigenvalue n.

The coupling sub-matrices, $\mathbf{A}_{(n,n+1)}$, contain the specific coupling strength between each subsystem's spin up and down states, $|-^{(k)}\rangle \leftrightarrow^{\alpha_k} |+^{(k)}\rangle$. The matrix elements are given by:

$$\left[\mathbf{A}_{(n,n+1)}\right]_{(i,j)} = |(n+1)_i\rangle\langle(n+1)_i|\hat{A}|n_j\rangle\langle n_j|, \tag{6.14}$$

where the operator $\hat{A}$ is given by:

$$\hat{A} = \sum_{k=1}^{N} \alpha_k \left(\mathbb{1}^{\otimes(N-1)} \otimes \hat{S}_x^{(k)} \right). \tag{6.15}$$

In other words, two states only have non-zero coupling matrix elements if they differ only in the excitation state of a single sub-system.

It is convenient to investigate inhomogeneous effects and system-specific couplings using this formalism. For example, perfect Rydberg blockade can be implemented by removing all states with $n > 1$, dramatically reducing the size of the dimension of the problem from 2^n to $n + 1$. Near perfect blockade can also be implemented by removing $n > 2$ and adding in the interaction energies to $\mathbf{\Delta}_2$. Inhomogeneous broadening can be added by inserting appropriate values for $\delta_k^{(n)}$ and α_k.

For a first attempt at modeling the system, consider the homogeneous case where $[\mathbf{\Delta}_n]_{(i,j)} = 0$ and $\alpha = \alpha_i$. This is a typical model for a non-interacting ensemble, so we should intuitively expect to observe full inversion of the atomic population from the ground to the excited state for all N atoms. The time evolution of this system is plotted in Figure 6.3 for different observables $|\langle n|\psi(t)\rangle|^2$(a), $\langle \hat{N}(t)\rangle$(b).

By including a blockade shift, $\delta_k^{(n>1)} = \delta_{dd} >> \alpha$, the Hilbert space of the problem is reduced to $n = \{0, 1\}$, and $\mathbf{H}_{int}$ becomes:

$$\mathbf{H}_{int} = \begin{bmatrix} 0 & \alpha_1 & \alpha_2 & \cdots & \alpha_N \\ \alpha_1 & \delta_1^{(1)} & 0 & \cdots & 0 \\ \alpha_2 & 0 & \delta_2^{(1)} & & 0 \\ \vdots & \vdots & & \ddots & \vdots \\ \alpha_N & 0 & 0 & \cdots & \delta_N^{(1)} \end{bmatrix} \tag{6.16}$$

The detunings $\delta_k^{(1)}$ are nominally 0, so it makes sense to treat the $\delta^{(1)}$ entries as a perturbation. Under the condition of perfect blockade, the energy eigenstates of $\mathbf{A}$ are the 2

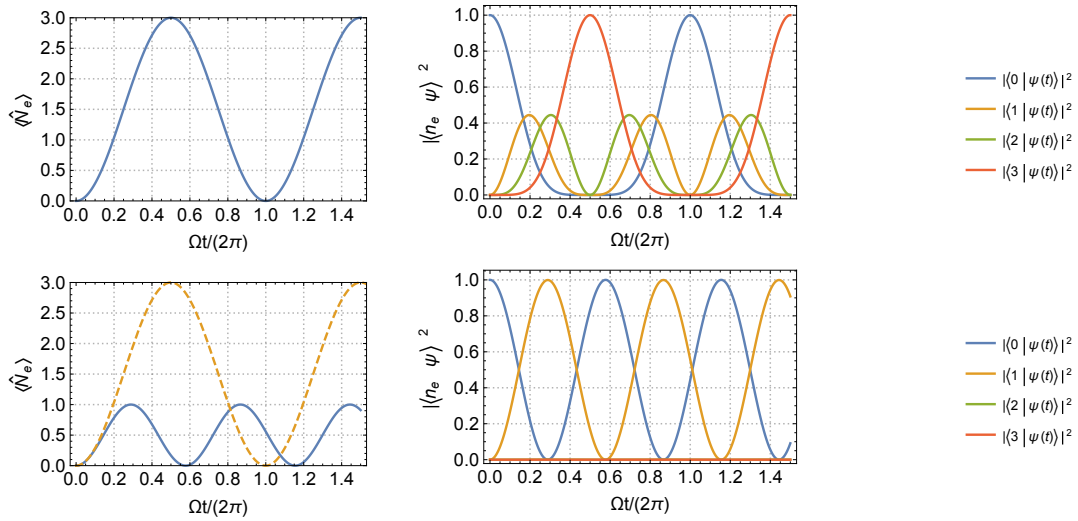

Figure 6.3: Example homogeneous (a,b) and blockaded (c,d) Rabi oscillations with $N = 3$ atoms with initial state $|\bar{0}\rangle$. (a) The average excitation number and (b) the excitation Fock state probabilities as a function of coupling time for an uncoupled sample. (c) The average excitation number and (d) the excitation Fock state probabilities as a function of coupling time for a blockaded sample.

dressed states with total angular momentum $J = N/2$, $\frac{1}{\sqrt{2}}(|\bar{0}\rangle \pm |\bar{1}\rangle)$, and the $N-1$ orthogonal states with $J = (N/2-1)$: $|(\bar{1})_\perp\rangle$, where $|\bar{1}\rangle \equiv \sum_{k=1}^{N} \frac{\alpha_k}{\alpha_N}|1^{(k)}\rangle$ and $\alpha_N^2 \equiv \sum_{k=1}^{N} \alpha_k^2$. If the initial state is $|\bar{0}\rangle$, then the system will remain in the symmetric subspace defined by $\{|\bar{0}\rangle, |\bar{1}\rangle\}$. The eigenvalues determine the rate that population amplitudes will oscillate, for $\frac{1}{\sqrt{2}}(|\bar{0}\rangle \pm |\bar{1}\rangle)$ this speed is $\pm\alpha_N$ implying a collective enhancement of $\sqrt{N}\alpha$ with homogeneous coupling strengths, see Figure 6.3(c,d). The collective enhancement of the Rabi frequency is the hallmark of a strongly blockaded ensemble[18–21].

Dicke Basis

If the homogeneous problem is reformulated in the total angular momentum basis $|J, M\rangle$, it is compartively easier to see the collective Rabi frequency enhancement. In this basis the quantum numbers that describe the system are the total angular momentum J, with associated operator $\hat{J}^2 = \hat{J}_x^2 + \hat{J}_y^2 + \hat{J}_z^2$, where $\hat{J}_\mu = \sum_{k=1}^{N} \hat{S}_\mu^{(k)}$, and M is the eigenvalue of the $\hat{J}_z$ operator. The interaction Hamiltonian is still given by $\mathbf{H}_{int} = \mathbf{A} + \mathbf{\Delta}$, and since $\mathbf{A}$ cannot couple states of unequal angular momentum, the evolution of the system is

constrained to $J = J(t = 0)$, to the extent that $\mathbf{\Delta}$ is negligible. The typical initialization condition is $|\psi(t = 0)\rangle = |\bar{0}\rangle \equiv |N/2, -N/2\rangle$ which can only evolve into state with the maximum total angular momentum. The Dicke states $|J = N/2, M\rangle = |M\rangle$ are equivalent to the set of $N + 1$ symmetric states $\{|\bar{0}\rangle, |\bar{1}\rangle, |\bar{2}\rangle, \cdots, |\bar{N}\rangle\}$. When a binary interaction energy sufficient to neglect double excitations is included as before, we are left only with the $| - N/2\rangle = |\bar{0}\rangle$ and $| - N/2 + 1\rangle = |\bar{1}\rangle$ states which form an effective 2-state system for the ensemble.

Explicitly, the Hamiltonian in the Dicke basis is given by:

$$H = \sum_{k=-J}^{J} \delta_k |k\rangle\langle k| + \frac{\alpha}{2} \sum_{m=-J}^{J} \sqrt{(J - m + 1)\,(m + J)} \Big(|m - 1\rangle\langle m| + |m\rangle\langle m - 1| \Big). \quad (6.17)$$

This exactly reproduces the results of the substantially larger dimensional system, for the homogeneous case with initial condition $J = N/2$, since the dark states with $J < N/2$ are ignored. The generic collective enhancement factor is contained in the term $\epsilon \equiv \sqrt{(J - M + 1)(J + M)}$, where M is the quantum number for the higher state in the excitation ladder. This reduces to the familiar $\epsilon = \sqrt{N}$ expression when $M = -J + 1$.

In this formalism, it is clear that the excitation enhancement factor is inherent in any ensemble excitation, a blockade interaction simply limits the Hilbert space making the increased oscillation frequency clearly observable.

6.2.2 Rydberg Ensemble Formalism

For this system we will consider the "good quantum number" to be the number of excited atoms within the ensemble, because the Blockade shift will limit the number of energetically allowed excited states in the system. In the case of perfect blockade the system is limited to a single excitation. For our system the blockade is not perfect, but a triple excitation state can be ignored so we will allow for at most a double excitation. Therefore

the generalized case of Equation 6.11 becomes:

$$\mathbf{H}_{int} = \mathbf{A} + \mathbf{\Delta} = \begin{bmatrix} \mathbf{\Delta}_0 & \mathbf{A}_{(0,1)} & 0 \\ \mathbf{A}_{(0,1)}^T & \mathbf{\Delta}_1 & \mathbf{A}_{(1,2)} \\ 0 & \mathbf{A}_{(1,2)}^T & \mathbf{\Delta}_2 \end{bmatrix}, \tag{6.18}$$

where the atom-specific energy levels are encoded as:

$$\begin{aligned} \mathbf{\Delta}_0 &= 0 \\ \mathbf{\Delta}_1 &= \sum_{k=1}^{N} (\delta + \delta_D(\mathbf{v}_k) + \delta_{AC}(\mathbf{x}_k)) |r^{(k)}\rangle\langle r^{(k)}| \equiv \sum_{k=1}^{N} \delta^{(k)}(\mathbf{x}_k, \mathbf{v}_k) |r^{(k)}\rangle\langle r^{(k)}| \\ \mathbf{\Delta}_2 &= \sum_{j=1}^{N} \sum_{k=1}^{k<j} \left(\delta^{(j)}(\mathbf{x}_j, \mathbf{v}_j) + \delta^{(k)}(\mathbf{x}_k, \mathbf{v}_k) + \Delta_{dd}^{(j,k)}(|\mathbf{x}_j - \mathbf{x}_k|) \right) \left(|r^{(j,k)}\rangle\langle r^{(j,k)}| + \text{c.c.} \right), \end{aligned} \tag{6.19}$$

where δ is the laser detuning from the free-space resonance, $\delta_D(\mathbf{v}) = -\mathbf{k} \cdot \mathbf{v}$ is the differential Doppler shift from the motion of the atom in the two-color light field, $\delta_{AC}(\mathbf{x})$ is the position dependent AC-Stark shift of the atom in the light fields, and $\Delta_{dd}^{(j,k)}(|\mathbf{x}_1 - \mathbf{x}_2|)$ is the dipole-dipole interaction of the doubly excited state. The single and double Rydberg excited states are denoted as $|r^{(j)}\rangle$ and $|r^{(j,k)}\rangle$, where j and k are the excited atom indices.

To coupling sub-matrices for $n \leq 2$ are explicitly:

$$\begin{aligned} \mathbf{A}_{(0,1)} &= \frac{1}{2} \sum_{k=1}^{N} \alpha_k |r^{(k)}\rangle\langle \bar{0}| \\ \mathbf{A}_{(1,2)} &= \frac{1}{2} \sum_{k=1}^{N} \sum_{j=1, j\neq k}^{N} \alpha_k |r^{(j,k)}\rangle\langle r^{(j)}|. \end{aligned} \tag{6.20}$$

For $N = 3$ atoms the Hamiltonian can be written as:

$$H = \frac{1}{2}\begin{pmatrix} 0 & \alpha_1 & \alpha_2 & \alpha_3 & 0 & 0 & 0 \\ \alpha_1 & \delta^{(1)} & 0 & 0 & \alpha_2 & \alpha_3 & 0 \\ \alpha_2 & 0 & \delta^{(2)} & 0 & \alpha_1 & 0 & \alpha_3 \\ \alpha_3 & 0 & 0 & \delta^{(3)} & 0 & \alpha_1 & \alpha_2 \\ 0 & \alpha_2 & \alpha_1 & 0 & \Delta_2^{(1,2)} & 0 & 0 \\ 0 & \alpha_3 & 0 & \alpha_1 & 0 & \Delta_2^{(1,3)} & 0 \\ 0 & 0 & \alpha_3 & \alpha_2 & 0 & 0 & \Delta_2^{(2,3)} \end{pmatrix}. \tag{6.21}$$

Here $\delta^{(k)} = \delta + \delta_D + \delta_{AC}$ is used for clarity to represent the sum of all single atom detuning contributions. Likewise, $\Delta_2^{(j,k)} = \delta_1 + \delta_2 + \Delta_{dd}^{(j,k)}$ represents the single atom detunings and the Rydberg interaction of atoms j and k.

The effect of inhomogeneous broadening can be modeled in a Monte Carlo simulation using the Hamiltonian above. Since the scattering off the intermediate state is small ($\sim 0.02/\sqrt{n}$ per atom) we do not account for re-population of the ground state as it would require either a density matrix approach or a Monte Carlo Wavefunction solution [69], both of which would add significant computational overhead especially for large numbers of atoms. Instead we implement the intermediate state scattering as a non-Hermitian modification to the Hamiltonian, by replacing the intermediate state detuning Δ with $\Delta + i\Gamma/2$ in the AC Stark Shift term δ_{AC}. The effect of this is that there is population leakage out of the system at the rate of intermediate state scattering events, so the system amplitude will drop from 1 over time and re-population of $|0\rangle$ is ignored.

Additionally, since we are not interested in small blockade leakage effects at this juncture we can reduce the dimension of the problem further by removing all well-blockaded doubly excited states. This is done by defining a cutoff blockade shift (typically $\Delta_{dd} > 10\alpha$) and removing doubly excited states matching the criteria from the problem space. This leaves intact the dynamics from unblockaded long range atom pairs, but

disregards the doubly excited fraction estimated in [26]. Using a standard propagator method and the dimension reduction technique described we can model the dynamics with ensembles of up to $N = 40$ atoms regularly on a standard laptop computer.

6.2.3 Inhomogeneous Broadening

The ideal blockaded ensemble solution was discussed in Section 6.2.1. In this section, we build on the previous results adding in the effects of inhomogeneous broadening. The sources of inhomogeneous broadening for infinite blockade are the single-atom effects introduced in Section 6.1. Because inhomogeneous broadening is a source of coupling into singly-excited states with no $\mathcal{W}$-state amplitude, denoted $|(\bar{1})_\perp\rangle$, the implications will be discussed here.

For the case of a two-level system the excited state amplitude is given by:

$$c_e = -i\frac{\Omega}{\Omega'}\sin(\Omega' t/2)e^{-i\delta t/2}, \tag{6.22}$$

where the probability of being detected in the excited state is $p_e = |c_e|^2$, and $\Omega'^2 \equiv \Omega^2 + \delta^2$. At small times t, atoms in a blockaded ensemble evolve similarly to independent two-level systems, since the probability of a double excitation is low. In an ensemble, the term, $e^{-i\delta^{(j)}t/2}$, enables the coupling to $|(\bar{1})_\perp\rangle$, due to inhomogeneous phase discrepancies $\phi_j = \delta^{(j)}t/2$. Therefore, we write the resulting state after a near-ideal π-pulse, $t_\pi = \pi/\Omega_n$, in terms of each atom's specific phase ϕ_j:

$$|\psi(t_\pi)\rangle = \frac{1}{N}\sum_{j=1}^{N} e^{-i\phi_j}|1_j\rangle.$$

Note that $|\psi(t_\pi)\rangle$ is constructed so that $p_1 \equiv 1$. Now, the projection onto the $\mathcal{W}$-state is

given by:

$$\begin{aligned} p_{\mathcal{W}} &= |\langle \bar{1}|\psi(t_\pi)\rangle|^2 \\ &= \frac{1}{N^2}\left|\sum_{j=1}^{N}\cos(\phi_j) - i\sin(\phi_j)\right|^2 \\ &= \frac{1}{N^2}\left(\sum_{j=1}^{N}\cos(\phi_j)\right)^2 + \frac{1}{N^2}\left(\sum_{j=1}^{N}\sin(\phi_j)\right)^2 \\ &\approx \frac{1}{N^2}\left[N^2 - N\sum_{j=1}^{N}\phi_j^2 + \left(\sum_{j=1}^{N}\phi_j\right)^2\right] \end{aligned} \tag{6.23}$$

Since the probability to not have amplitude in the $\mathcal{W}$-state is given by $p_\perp = p_1 - p_{\bar{1}}$, where for the assumed $|\psi(t_\pi)\rangle$, $p_1 \equiv 1$, the projection onto the $|(\bar{1})_\perp\rangle$ basis is then:

$$p_\perp \approx \frac{1}{N^2}\left[N\sum_{j=1}^{N}\phi_j^2 - \left(\sum_{j=1}^{N}\phi_j\right)^2\right] \tag{6.24}$$

Notice that for large N the first term dominates. Therefore let us assume that the distribution is dominated by the first term and we will apply a corrective coordinate shift equal in magnitude to the mean of the second term later.

$$p_\perp \approx \frac{1}{N}\sum_{j=1}^{N}\phi_j^2 \tag{6.25}$$

We can continue the analysis if we assume a specific shape for the detuning distribution. For a Gaussian distribution of phase errors, $\sigma \equiv \sigma_\phi/\Omega = 2\sigma_\delta/\sqrt{N}$, the PDF for the first term is given by:

$$P(p_\perp) \cong \frac{N(Np_\perp)^{(N-2)/2}}{(\sigma\sqrt{2})^N\left[\Gamma(\frac{N}{2}) - \Gamma(\frac{N}{2}, \frac{N}{2\sigma^2})\right]}e^{-Np_\perp/2\sigma^2}. \tag{6.26}$$

For our atom numbers ($N \sim 10$), the corrective coordinate transform, $p_\perp \to p_\perp + \langle\left(\sum_j \phi_j\right)^2\rangle = p_\perp + \sigma^2/N$, for the second term in Equation 6.24 is non-negligible. With

the coordinate transform added in Equation 6.26 becomes:

$$P(p_\perp) = \frac{N(Np_\perp + \sigma^2)^{(N-2)/2}}{(\sigma\sqrt{2})^N \left[\Gamma(\frac{N}{2}) - \Gamma(\frac{N}{2}, \frac{N}{2\sigma^2})\right]} e^{-(Np_\perp/\sigma^2+1)/2}. \tag{6.27}$$

The mean of Equation 6.27 can be calculated analytically and is given by:

$$\langle p_\perp \rangle = \sigma^2 \left[\frac{\Gamma(\frac{N}{2})}{\Gamma(\frac{N}{2}) - \Gamma(\frac{N}{2}, \frac{N}{2\sigma^2})} - \frac{1}{N} \right]. \tag{6.28}$$

The results of Equations 6.27 and 6.28 are shown in Figure 6.4 for $N = 6$ and 10.

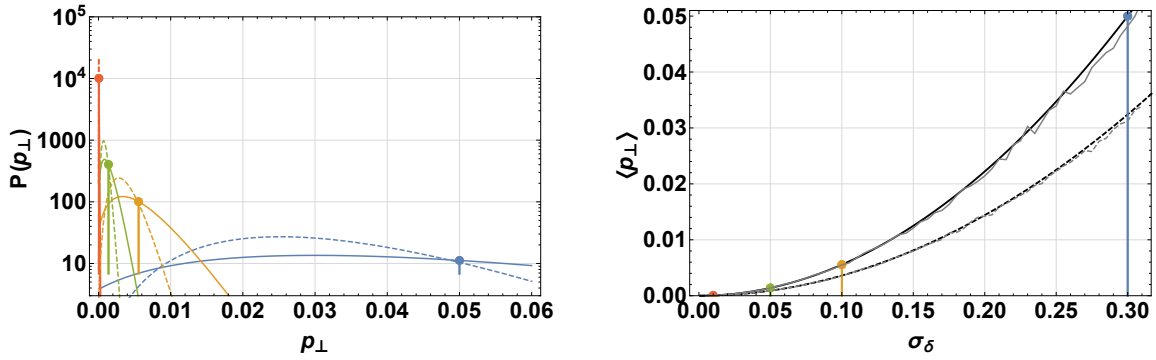

Figure 6.4: (a) Probability density functions for the projection into the non-$\mathcal{W}$-state basis $|(\bar{1}_\perp\rangle$ with Gaussian detuning distributions, where $\sigma_\delta = \{0.01, 0.05, 0.1, 0.3\} = \sigma_\Delta/\Omega$ is denoted by red, green, yellow and blue curves respectively. For our system the σ_δ values correspond to Doppler shifts of temperature $T = \{1.6, 41, 160, 1500\}$ μK. The solid lines are for $N = 6$ and dashed denotes $N = 10$. (b) The mean projection into $|(\bar{1})_\perp\rangle$ as a function of σ_δ. Black curves are Equation 6.28 and gray are from a Monte Carlo simulation. The solid lines are calculated for $N = 6$ and the dashed lines are with $N = 10$.

It is an intrinsic feature of the $\mathcal{W}$-state that the sensitivity to detuning errors decreases with increasing atom number. This is due entirely to the $\sqrt{N}$ Rabi frequency enhancement which lowers the significance of the detuning errors by the same factor. Therefore:

$$P(p_\perp) \propto \sigma^2 \propto 1/N, \tag{6.29}$$

and to the degree that detuning errors are the dominant contribution to the infidelity the fidelity can be improved by increasing the atom number. Increasing the atom number

too much, however, can jeopardize the blockade figure of merit: $\Delta_{dd}/\sqrt{N}\Omega$, so a balance must be reached. Additionally increasing the atom number will exacerbate any density dependent effects, which are hypothesized to contribute to the amplitude discrepancy observed in the $\mathcal{W}$-state production probability.

Additionally a time series Monte Carlo with $N = 6$ atom is shown in Figure 6.5 to demonstrate the relative contributions of differential AC Stark shifts and Doppler shifts. For our experimental parameters, the contribution to $|(\bar{1})_\perp\rangle$ is dominated by Doppler shifts, and $P(p_\perp) \sim 3\%$. At temperatures of just 50 μK the AC Stark shift contribution is less than 0.2%, with $P(p_\perp) \sim 0.8\%$.

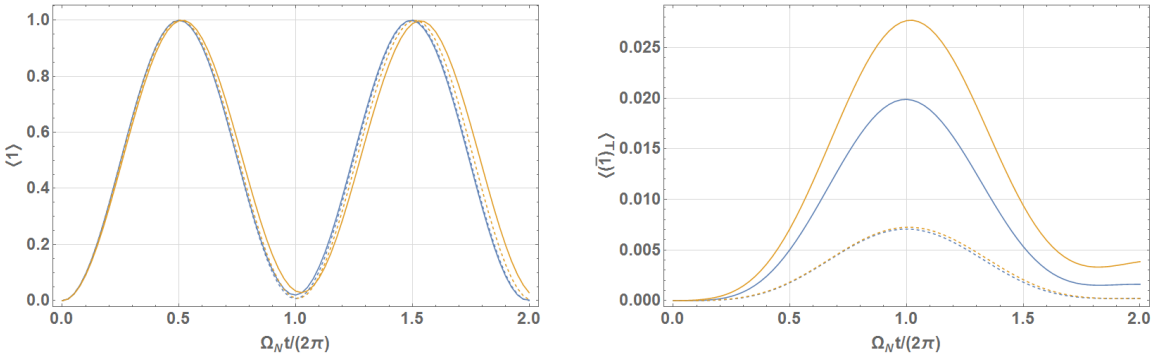

Figure 6.5: (a) Monte Carlo model of the $\mathcal{N} = 1$ Fock state during a collective Rabi oscillation with $N = 6$ atoms and inhomogeneous broadening from Doppler broadening (blue), and both Doppler Broadening and AC Stark shifts (yellow). The results are shown for temperatures of 150 (solid) and 50 (dashed) μK. (b) The leakage into $|(\bar{1})_\perp\rangle$ due to the same inhomogeneous broadening effects. Intermediate state scattering is not included in the model. The detuning is adjusted to cancel the mean AC Stark Shift. Note that the peak $|(\bar{1})_\perp\rangle$ population occurs at the 2π-pulse time not at the π-pulse time.

While high fidelity intra-site $\mathcal{W}$-state entanglement due to inhomogeneous broadening is not necessary to explain the Rydberg Rabi oscillation dynamics from Chapter 2, or the ensemble-ensemble blockade dynamics in Chapter 4 it becomes important when considering the coherence time for a quantum memory. This can be demonstrated by considering an ensemble with the general form for the singly excited state given by $\sum_k \frac{\Omega^{(k)}}{\Omega'_N}|k\rangle$, where $\Omega'^2_N \equiv \sum_k (\Omega^{(k)})^2$. The individual atom Rabi frequencies, $\Omega^{(k)}$, will change as the atom changes velocity and position during a long evolution time and after a certain amount of

time will no longer map the initial single excited state back to $|\bar{0}\rangle$ after a π_N-pulse.

6.2.4 Imperfect Rydberg Blockade

Sources of inhomogeneous broadening are well understood in the context of non-interacting atoms as demonstrated in the previous section However, imperfect Rydberg blockade can add significant non-intuitive behavior to the problem. Imperfect blockade in this context means that the ensemble is almost fully blockaded, $\Delta_{dd} \gg \Omega_N$, but there are atom pairs such that the blockade shift, Δ_{dd}, is on the order of or less than the enhanced Rabi frequency, Ω_N. This breakdown of strong blockade can be due to either long range atom pairs or short range molecular crossings [57]. Long-range atom pairs are straight forward to add into the model system described by Equation 6.18 once a simple interaction energy, $U_{dd}(R)$, is known. Alternatively, short-range interactions are difficult to calculate due to the sheer number of states that can be mixed due to the scale of the Rydberg-Rydberg interaction at small R[59]. Both regimes will be discussed here.

Long-Range Atom-Pairs

The effective 1-dimensional geometry of our traps allow us to formulate the problem in terms of the interatomic separation parameter, R, only, with no angular terms. At long range the dipole-dipole interaction scales as R^{-6}, so the force between the two atoms scales as R^{-5} resulting in little change in velocity for a long-range Rydberg pair over a few μs. For the $97D_{5/2}, m_j = 5/2$ Rydberg state typically used, $R = 16$ μm when $\Omega_{\bar{1}\bar{0}}(R) = \Delta_{dd}$, and $a = -\frac{h}{m}\nabla\Delta_{dd} = 0.008$ $\mu\text{m}/\mu\text{s}^2$. Therefore, a frozen gas model is sufficient on the 5 μs timescale of the experimental sequence. The Monte-Carlo simulation shown in Figure 6.6 shows the result of long-range atom pair for different temperature atom clouds with $N = 6$ atoms. All analysis done in this section is with $|r\rangle = 97D_{5/2}, m_j = 5/2$ and $\Omega_1 = 1$ MHz.

The atom cloud size grows as $\sqrt{T}$, so the higher the temperature, the more likely

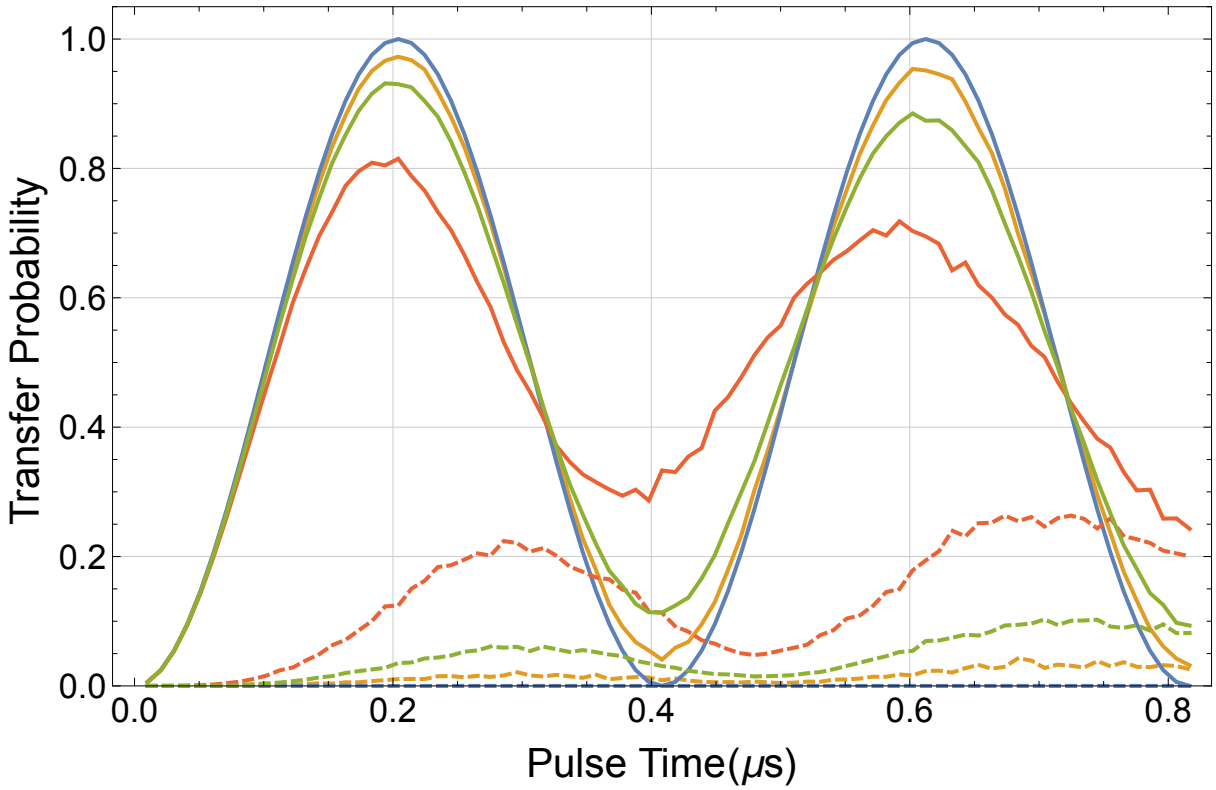

Figure 6.6: Collective Rabi oscillations for $N = 6$ for our typical experimental parameters with temperatures $T = \{10, 100, 150, 300\}$ μK corresponding to blue, yellow, green, and red traces respectively. Solid and dashed lines represent $\mathcal{N} = 1$ and 2 atom Fock states in $F = 1$.

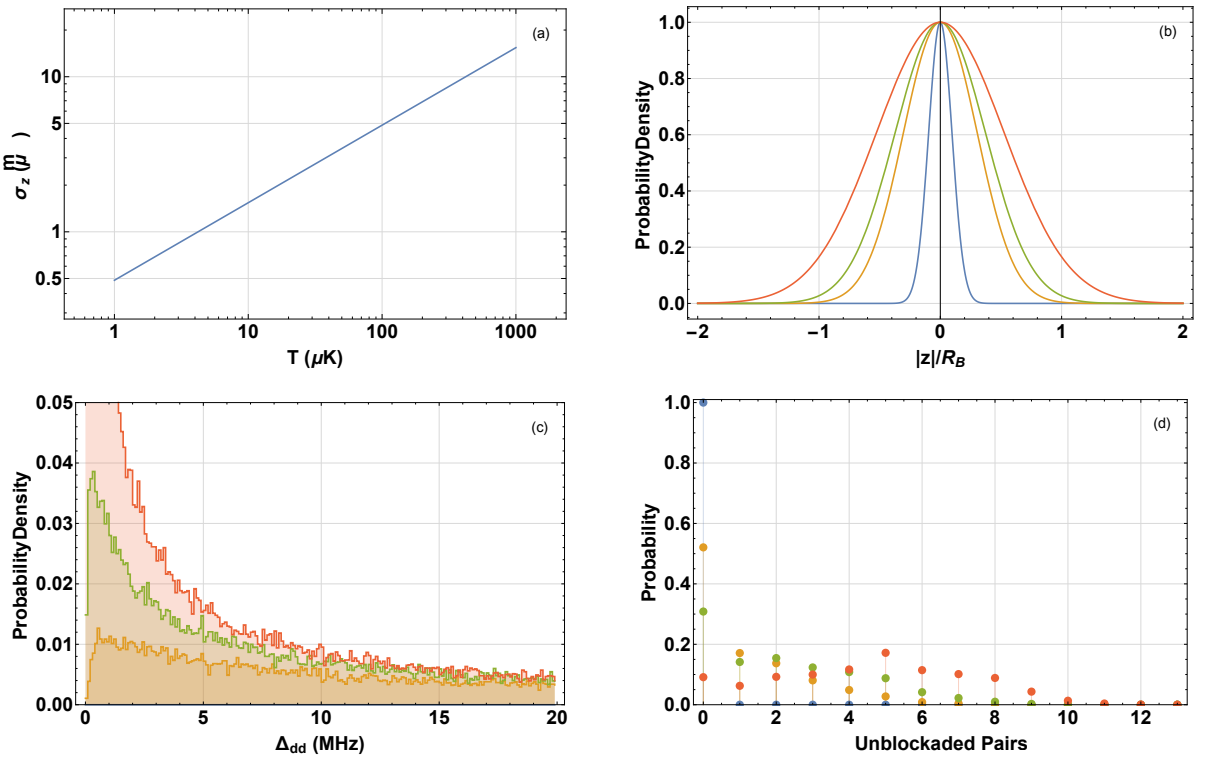

Figure 6.7: Example plots with $N = 6$ of (a) atom cloud length σ_z, (b) thermal atom cloud PDF scaled to the nominal blockade length $R_B = 16$ μm (normalized at $z = 0$), (c) dipole-dipole energy shift probability distributions, and (d) the probability of having a certain number of "weakly blockaded" atom pairs ($\Delta_{dd} < 10\Omega_1 = 10$ MHz) in a sample for temperatures $T = \{10, 100, 150, 300\}$ μK, corresponding to blue, yellow, green, and red traces respectively.

there is to be long-range weakly blockaded atom pairs. Figure 6.7 is intended to give some intuition about the effect of temperature on long-range atom pairs. For $T = 10$ μK, the atomic distribution is completely contained within a blockade radius ($\Delta_{dd}(R_B) = \Omega_1$) and there are no weakly blockaded atom pairs with $\Delta_{dd}(z) < 10\Omega_1 = 10$ MHz. As the temperature is increased to our typical multi-atom temperatures (~ 150 μK) the number of weakly blockaded pairs increases, and the fidelity of a π pulse decreases, while the probability to observe double excitations is increased.

Figures 6.8, 6.9, and 6.10 are pedagogical single instances of a Monte Carlo showing the different dynamics of various types of blockade breakdown based on different atom configurations. In the case of moderate blockade, Figure 6.8, where there is a single pair

that could be excited ($10\Omega_1 > \Delta_{dd} >\sim 5\Omega_1$) there is a tiny amount of leakage into the doubly excited state. In the case of weak blockade, Figure 6.9, a single pair is near enough to resonance that could be excited ($5\Omega_1 > \Delta_{dd} \gtrapprox \Omega_1$) there is a non-negligible amount of doubly excited state amplitude, but the characteristic enhanced Rabi oscillations are still clearly observable. Finally, in the case of blockade breakdown ($\Omega_1 > \Delta_{dd}$) Figure 6.10, the atoms are far enough apart that more than a single pair is non-blockaded and the behavior devolves into something that no longer resembles the collective behavior expected. The code to generate these images can be found at the URL in reference [70].

Short-Range Atom-Pairs

At certain interatomic distances the full molecular structure of the Rydberg-Rydberg interaction reveals resonant molecular states [57, 59]. Most of these molecular crossings have little to no coupling from the single excited state and are only accessible via higher order photon interactions. These resonances can be ignored. However, there can be a significant amount of state mixing due to the Rydberg-Rydberg interaction. Mixing enables molecular Rabi frequencies that are comparable to the single-atom Rabi frequency for the singly excited state.

In reference [57], the outermost crossing for $100S + 100S$ occurs at 6.22 μm and the molecular Rabi frequency is $\Omega_m = 0.55\Omega$. It is reasonable to assume that there is a detrimental effect of having a relatively weakly coupled molecular state excitation occurring at this range. Derevianko et al. [57] found that double excitations that are quickly removed from the cloud can be modeled as an effective decay parameter. The net decay is a sum of the decay due to each molecular resonance. Their analysis was done for an isotropic cloud of Rb atoms, but for our 1D geometry, mid-range interactions ($R_s < R < R_B$) do not have the same scaling as in the isotropic case. So while molecular resonances are not predicted to be an issue at moderate length scales, the result is a reminder that, at short interatomic distances, the large number of densely packed molecular resonances with weak

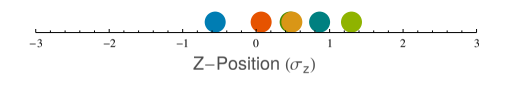

Mean Blockade Shift B: | 27. MHz
Mean Double Ex. Detuning D: | -73. MHz

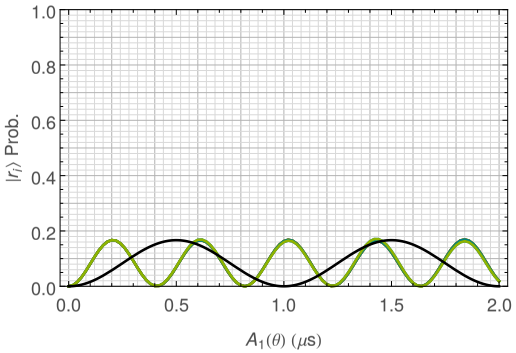

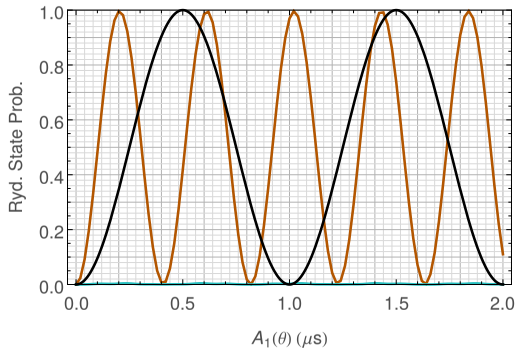

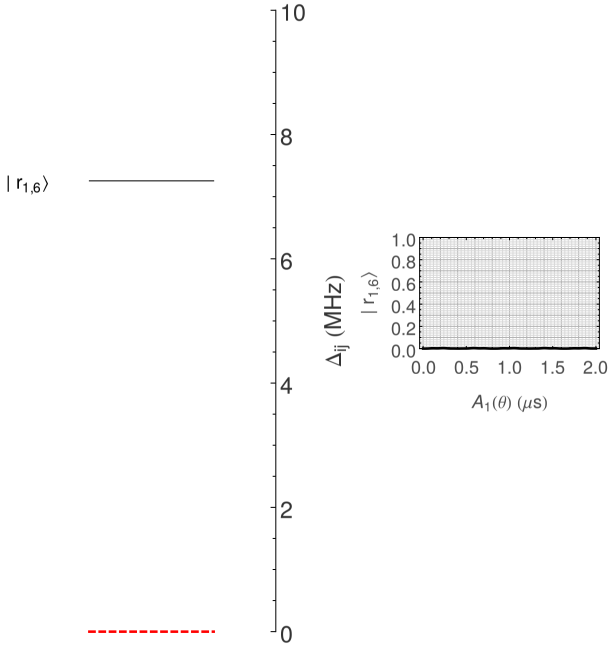

Inter-Atomic Distances (μm)

	1	2	3	4	5	6
1	0.	4.4	7.1	7.3	9.9	13.
2	4.4	0.	2.8	2.9	5.6	8.6
3	7.1	2.8	0.	0.16	2.8	5.8
4	7.3	2.9	0.16	0.	2.6	5.7
5	9.9	5.6	2.8	2.6	0.	3.
6	13.	8.6	5.8	5.7	3.	0.

Rydberg Pair Blockade Shift (MHz)

	1	2	3	4	5	6
1	0	-970.	-160.	-140.	-32.	-7.3
2	-970.	0	-4200.	-3500.	-420.	-68.
3	-160.	-4200.	0	-2.2×10^7	-4000.	-350.
4	-140.	-3500.	-2.2×10^7	0	-4800.	-390.
5	-32.	-420.	-4000.	-4800.	0	-3100.
6	-7.3	-68.	-350.	-390.	-3100.	0

Figure 6.8: Example Rabi oscillation for $N = 6$ from atom distribution instance, with moderate blockade, $\sigma_z = 7$ μm. The atom positions, individual atom oscillations $|r_i\rangle$, $\mathcal{N} = 1$ and 2 oscillations, double excitation energy level diagram, and imperfectly blockaded double atom state oscillations are shown in the figure. Additionally the mean blockade shift B and the mean double excitation detuning Δ are calculated according to [52]. The code for generating these figures can be found at the URL in ref [70].

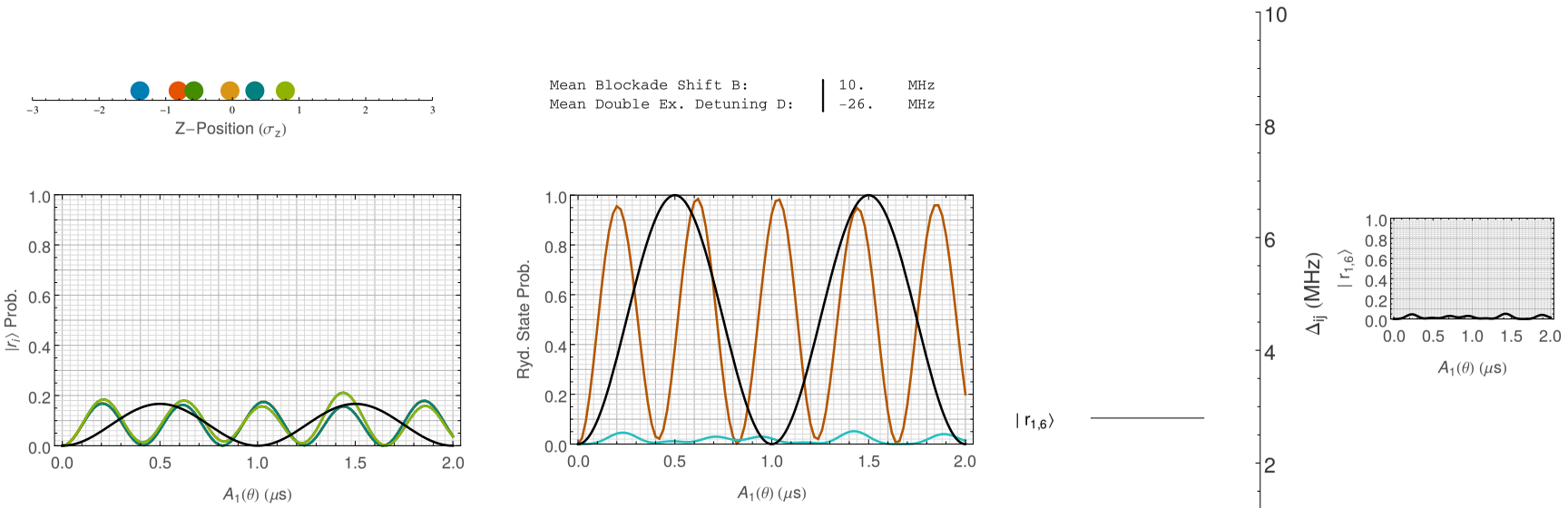

Inter-Atomic Distances (μm)

	1	2	3	4	5	6
1	0.	4.	5.7	9.5	12.	15.
2	4.	0.	1.7	5.4	8.1	11.
3	5.7	1.7	0.	3.8	6.4	9.6
4	9.5	5.4	3.8	0.	2.6	5.8
5	12.	8.1	6.4	2.6	0.	3.2
6	15.	11.	9.6	5.8	3.2	0.

Rydberg Pair Blockade Shift (MHz)

	1	2	3	4	5	6
1	0	-1300.	-390.	-42.	-11.	-2.8
2	-1300.	0	-20000.	-460.	-93.	-16.
3	-390.	-20000.	0	-1600.	-250.	-39.
4	-42.	-460.	-1600.	0	-4900.	-360.
5	-11.	-93.	-250.	-4900.	0	-2600.
6	-2.8	-16.	-39.	-360.	-2600.	0

Figure 6.9: Example Rabi oscillation for $N = 6$ from atom distribution instance, with weak blockade, $\sigma_z = 7$. The atom positions, individual atom oscillations $|r_i\rangle$, $\mathcal{N} = 1$ and 2 oscillations, double excitation energy level diagram, and imperfectly blockaded double atom state oscillations are shown in the figure. Additionally the mean blockade shift B and the mean double excitation detuning Δ are calculated according to [52]. The code for generating these figures can be found at the url in ref [70].

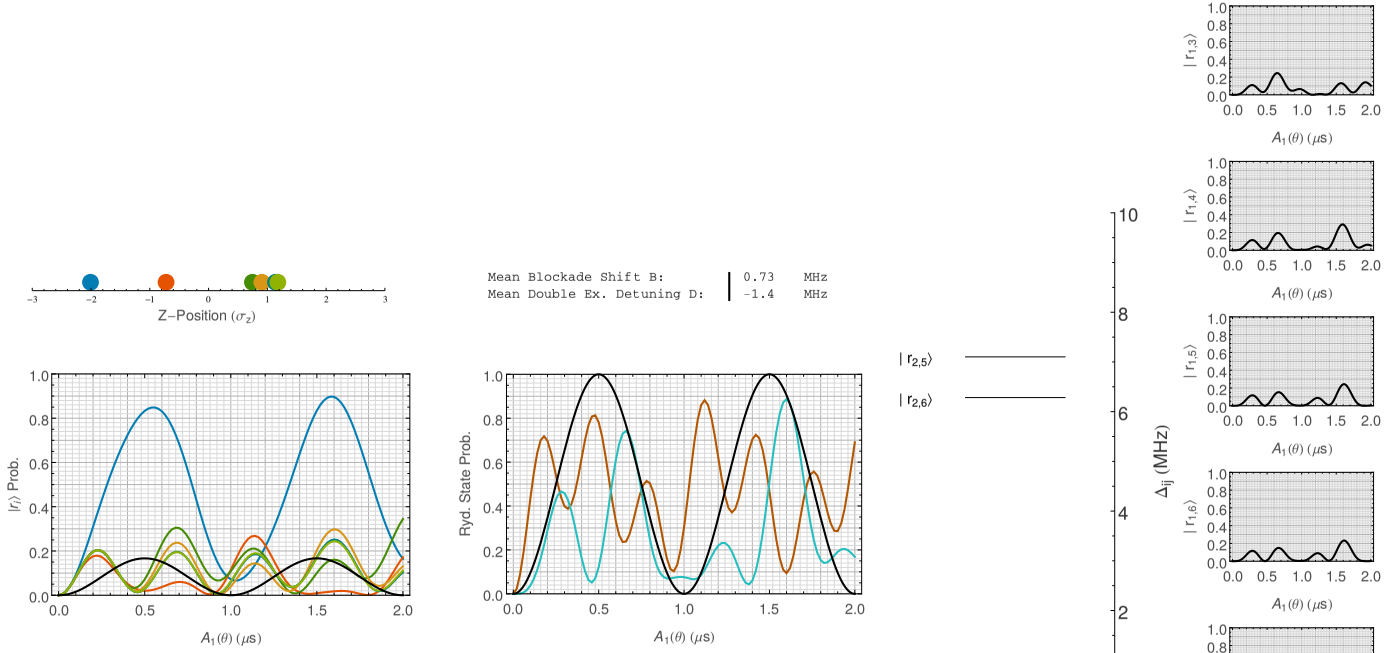

Inter-Atomic Distances (μm)

	1	2	3	4	5	6
1	0.	9.	19.	20.	22.	22.
2	9.	0.	10.	11.	13.	13.
3	19.	10.	0.	1.1	2.7	3.
4	20.	11.	1.1	0.	1.6	1.9
5	22.	13.	2.7	1.6	0.	0.28
6	22.	13.	3.	1.9	0.28	0.

Rydberg Pair Blockade Shift (MHz)

	1	2	3	4	5	6
1	0	-54.	-0.7	-0.5	-0.31	-0.29
2	-54.	0	-27.	-15.	-7.1	-6.3
3	-0.7	-27.	0	-63000.	-4200.	-3200.
4	-0.5	-15.	-63000.	0	-21000.	-13000.
5	-0.31	-7.1	-4200.	-21000.	0	-4.3×10^6
6	-0.29	-6.3	-3200.	-13000.	-4.3×10^6	0

Figure 6.10: Example Rabi oscillation for $N = 6$ from atom distribution instance, with complete blockade breakdown, $\sigma_z = 7$. The atom positions, individual atom oscillations $|r_i\rangle$, $\mathcal{N} = 1$ (brown) and 2 (blue) oscillations, double excitation energy level diagram, and imperfectly blockaded double atom state oscillations are shown in the figure. Additionally the mean blockade shift B and the mean double excitation detuning Δ are calculated according to [52]. The code for generating these figures can be found at the url in ref [70].

coupling might add up to a significant decoherence rate. This so-called "spaghetti"-region is notorious for difficult calculations and results that are extremely sensitive to external fields [59].

In the remainder of this section, our method for calculating molecular potential curves for Rydberg D-states is presented. The states used in this thesis are $|r\rangle = 97D_{5/2}, m_j = 5/2$ and $111D_{5/2}, m_j = 5/2$, but this calculation gives qualitatively similar results, so only the $97D$ state will be shown.

Calculating molecular resonance curves involves including nearby molecular states in a larger range of angular momentum states, but the 1D geometry of our experiment limits the angular complexity since to a good approximation the atoms are separated along the z-axis. The Hamiltonian for the applied magnetic field $\mathbf{B} = B\hat{z}$ is diagonal in the z basis and since the total projection of angular momentum is conserved by the dipole-dipole interaction to first order $\mathbf{B}$ is a near constant energy offset which has little effect on the dynamics.

The accuracy of the result will depend on the number of relevant molecular states included in the basis. However, the blind inclusion of any molecular state within a certain energy range can quickly saturate the computational power of a desktop computer, and most states will not effect the calculation. To alleviate this, a simple iterative algorithm for inclusion of a particular molecular state in the computation has been developed. For an initial energy cut, E_{cut}, and figure of merit, $F_{cut} = C_3/(\Delta R_0^3)$, at some distance R_0 of interest. The parameter R_0 should be chosen as the closest interatomic distance of interest. The algorithm to build up the basis state list is as follows:

1. Begin with the molecular state of interest denoted $|\psi_a\rangle + |\psi_b\rangle = |n_a L_a J_a m_{j_a}\rangle + |n_b L_b J_b m_{b_2}\rangle$. For us $|\psi_a\rangle = |\psi_b\rangle$.

2. Next produce a list of all $|n_\alpha L_a J_a m_{j_a}\rangle + |n_\beta L_b J_b m_{j_b}\rangle$ molecular states within the energy range defined by E_{cut} and the dissociation energy for $|\psi_a\rangle + |\psi_b\rangle$. Reasonable bounds should be chosen for $n_i \in [n_{min}, n_{max}]$. For example $n_1^0 = n_2^0 \sim 100 \rightarrow n_i \in$

$[n^0 - 10, n^0 + 10]$. These are the 0^{th} order basis states.

3. Calculate a list of all molecular states that are accessible by an ED transition from the previous order of basis states that are also within E_{cut} and the bounds on n_i.

4. Calculate the C_3 coupling coefficient and molecular detuning Δ between each potential molecular state from the new list and each molecular state from the previous order's basis states. If the figure of merit $C_3/(\Delta R_0^3)$ exceeds the F_{cut} threshold then the new state should be appended to this order's basis state list.

5. Repeat step 2 and 3 for each order of ED (or other interaction) transitions desired.

6. Delete any duplicate states.

Once the basis states have been compiled the Hamiltonian can be constructed and diagonalized for a given interatomic separation R.

The results of applying this algorithm for the 97D molecular state results in Figure 6.11. In this image the molecular Rabi frequency is denoted in grey scale, so many resonances that don't couple are hidden. Molecular resonances can be seen around $R = 3.5$ and 6 μm. Even though the calculations are inaccurate, at short range many steep weakly coupled resonances can be seen by the seemingly unconnected dots for $R < 4$ μm. Since the total effective decay induced by molecular resonances is the sum of the decay of individual resonances, a sufficient density of decay channels at close range could add to a non-negligible decay rate even for 1D.

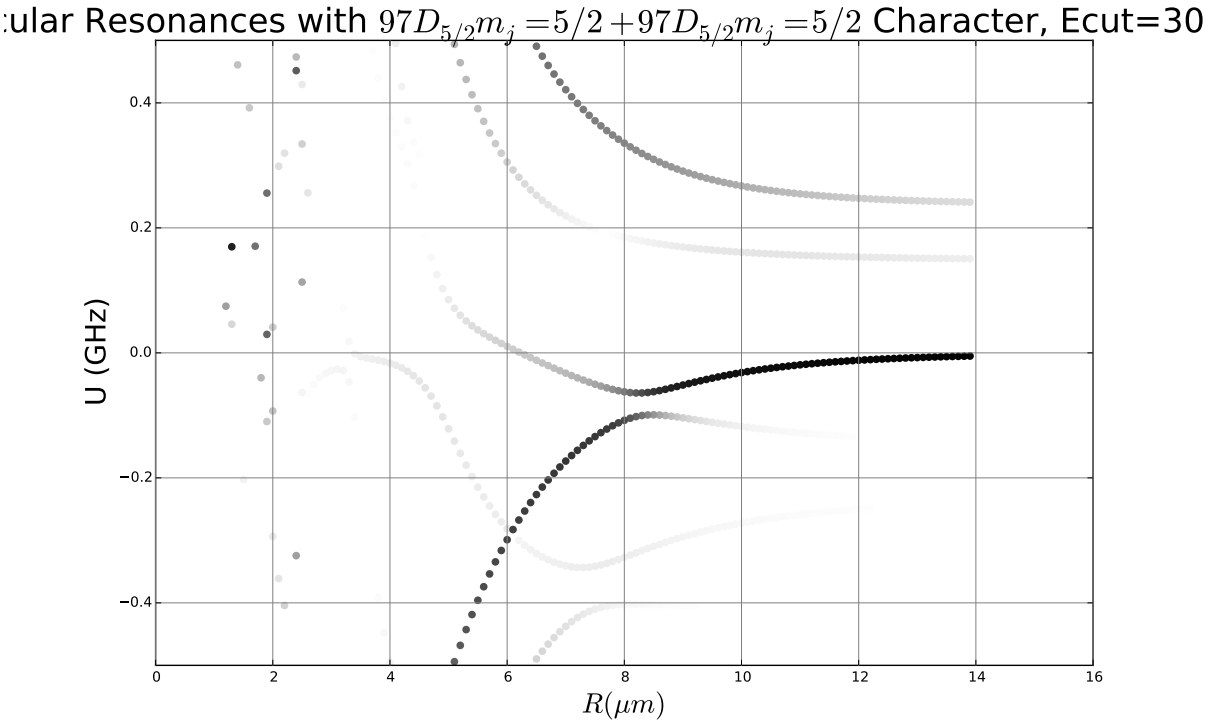

Figure 6.11: Molecular Rydberg energy curves due to the dipole-dipole interaction. The data points are scaled by the amount of $97D_{5/2}, m_j = 5/2 + 97D_{5/2}, m_j = 5/2$ character they contain, which is denotes the coupling from the single excited state. For this dataset $E_{cut} = 30$ GHz and $F_{cut} = 3$. Note the high sensitivity to position for $R < 4$ μm, this is known as the "spaghetti" regime.

Chapter 7

Atom Number Measurements

This chapter details the different atom detection schemes employed in this thesis and some relevant technical details. Atom loss mechanisms related to the readout are discussed in Section 7.1.

In this work, all atom detection is based on atom fluorescence, where photons scattered from probe lasers are collected by a high numerical aperture (NA=0.35) lens and imaged onto an Electron-Multiplying Charge Coupled Device (EMCCD) camera. The total signal reported by the camera is proportional to the number of integrated photo-electrons generated during the exposure time. Both the total number of photo-electrons generated, and the signal after the camera readout are governed by stochastic processes, and therefore have some associated intrinsic noise. Camera noise models are discussed in Section 7.2.

The detection schemes utilized can be categorized into the following regimes based on the resolvability of the discrete atom number signal histograms: single-atom detection (Section 7.2.1), few-atom detection (Section 7.2.4), and multi-atom detection (Section 7.2.3). In case of single-atom detection, the loading rate is lowered to nominally 0.3 atoms per measurement such that the rate of having more than 1 atom in a trap site, $P(n > 1) = 1 - P(n = 0) - P(n = 1) \sim 4\%$, is small. The MOT lasers are used to probe

the atom while the camera collects photons for a time long enough to resolve the difference between the single-atom photon scattering rate and the background count rate, but not too long to cause significant heating or one-body loss. Since the trap sites are separated by $> 10\lambda$ the sites are optically resolvable and pixels can be attributed with high fidelity to a specific trap site. For all data taken, a 3×3 pixel region of interest (ROI) is integrated with equal spatial weighting to generate a single number for the camera signal for each site. Two camera shots are employed to post-select on measurements containing one-atom during the initial camera shot. Measurements that contain an atom can be post-selected with high-fidelity using a threshold measurement on the first camera shot.

For ensemble measurements the loading rate is increased, usually in the regime where the probability of loading zero atoms is negligible, $P(n = 0) = e^{-\lambda}$. With no losses we would be able to perform high fidelity atom number measurements every camera shot. However, due to the relatively high peak densities in the FORT, $\rho_0 = N \prod_i \left(\sqrt{2\pi}\sigma_{x_i}\right)^{-1} = 5N \times 10^{10}$ atoms/cm^3, and our FORT depth of 1.5 mK, inelastic collisions can cause significant atom losses. Loss processes during the readout cause the scattering rate to decrease over the integration time, which in turn smears out what would be resolvable peaks in the camera histograms. This broadening forces us in most situations to revert to a probabilistic approach to measuring the atom number. What's more, if the losses are not accounted for the atom number can be severely underestimated. However, a good understanding of the readout process and available experimental parameters can help mitigate some of this sub-optimal behavior.

Finally, a discussion of the state-selective readout method used to determine the ground hyperfine-manifold of the atoms can be found in Section 7.3.

7.1 Loss Mechanisms

The population in the conservative potential created by the FORT laser will decrease over time from its initial value of n_0 according to the general rate equation:

$$\frac{dn}{dt} = -\alpha n - n(n-1)\beta, \tag{7.1}$$

where α and β are the single- and two-body loss rates. Both α and β will be time-dependent during the experiment due to changes in how the atoms are addressed during the protocol. The generic solution to Equation 7.1 is given by:

$$n(t) = n_0 \frac{(\alpha - \beta)}{(\alpha + (n_0 - 1)\beta)\, e^{(\alpha-\beta)t} - n_0\beta}. \tag{7.2}$$

For $\beta = 0$ this simplifies to normal exponential decay. For $\alpha = 0$ the result is:

$$n(t) = n_0 \frac{e^{\beta t}}{1 + n_0(e^{\beta t} - 1)}. \tag{7.3}$$

In this chapter, we are concerned with undesirable losses that occur during or between the readouts, so that is where attention will be focused. Specific loss mechanisms are discussed below.

7.1.1 Single-Body Losses

The single-atom trap lifetime, τ, is on the order of seconds, while the time between successive measurements is $\Delta t = 115$ ms. The lifetime is limited by collisions with room temperature background atoms.[1] The trap loss thus limits the retention to $\exp(-0.115s/\tau)$. In the case of multiple atoms, since only one readout is performed, the effective $\Delta t = 15$ ms is the time difference between the experiment and the readout.

[1] Even though this is a collisional two-body loss, it is between an atom in the ensemble and an atom external to the ensemble, so it occurs at a rate proportional to $N \times P$, where N is the number of atoms in the ensemble and P is the pressure of the vacuum chamber, and not N^2.

Atoms can also be ejected due to heating during interrogation. The readout procedure has a smaller probe detuning ($\Delta_{readout} \sim 2.5 - 3\Gamma$) than the cooling procedure ($\Delta_{cooling} \sim 15\Gamma$), which introduces enough heating to eject atoms. If the loss due to heating is small, then the loss is most likely to occur at the end of the readout procedure, thus there should be enough scattered photons to pass the single-atom cuts, but no atom will be detected during the second readout. The retention due to this effect can be optimized by balancing the probe beam powers and magnetic fields. When the heating is well optimized the total retention can be as high as 95%, most likely limited by background collisions, which imply a background limited lifetime of $\tau = 2.2$ s. Previous measurements of the trap lifetime put τ at 3.5 s[45]. A lifetime of $\tau = 2.2 - 3.5$ implies a background pressure of $< 10^{-8}$ torr[71]. Reducing the time between exposures would increase the maximum retention linearly. Based on some preliminary testing a reduction by at least a factor of 5 is possible. However, a technical issue in the current implementation of the experiment controller prevents us from doing this, which we hope to resolve when upgrading the controller software soon.

7.1.2 Two-Body Losses

The rate of collisions between atom pairs is proportional to the number of possible atom pairs in the sample, which is given by: $n(n-1)/2$. If the energy released during an inelastic collision is much greater than twice the trap depth, then both atoms will be ejected. There are a few processes for such binary inelastic collisions:

1. ground-ground hyperfine changing collisions (HCC),
2. excited-ground light-assisted collisions.
3. and excited-excited collisions.

The HCC and light-assisted collisional processes are discussed in detail in the subsequent sections. The effect of any doubly excited collisions should be small since during a normal

cooling or readout procedure the excited state probability is small, $c_e \sim 0.1$, and this loss channel shouldn't be detectable in our apparatus.

Two body trap loss during a readout is typically measured to be $\beta \sim 0.02$ atoms^{-1}·ms^{-1}. For our peak trap densities this translates to loss rate in terms of density of $\sim 4 \times 10^{-10}$ cm^3/s.

Ground-Ground Collisions

A ground state hyperfine-changing collision (HCC) is represented in our qubit notation as:

$$|0\rangle + |x\rangle \rightarrow |1\rangle + |x\rangle + h\nu_{HF},$$

or:

$$|0\rangle + |0\rangle \rightarrow |1\rangle + |1\rangle + 2h\nu_{HF},$$

where one or both of the atoms changes from the upper ($F = 2$) to the lower ($F = 1$) hyperfine manifold during the collision and $h\nu_{HF} = 330$ mK of internal energy is released as kinetic energy per nuclear spin flip, more than enough energy to eject both atoms from the 1.5 mK FORT. At peak densities of $10^{11} - 10^{12}$ atoms/cm^3 these collisions occur at a negligible rate on the order of 1 s^{-1}[72, 73]. A more precise study of the HCC rate in our FORT and the state dependence is warranted to estimate the effect on the $\mathcal{W}$-state fidelity.

Light-Assisted Collisions

Light-assisted collisions are caused by excitation to the attractive molecular potential of the $S_{1/2}$ and $P_{3/2}$ states and the finite lifetime of the excited state. If the light addressing the atoms is red-detuned, then the molecular excitation from $S + S \rightarrow S + P$ is resonant at some inter-atomic distance R, see Figure 7.1. The potential is attractive and therefore R will decrease over time, assuming 0 atom temperature The excited atom will eventually

decay back to the ground state by scattering a photon, but from a lower point on the molecular energy curve. The energy gained during this process is then equal to $h\Delta\nu$, and is manifested in the kinetic energy of the atom pair. This extra kinetic energy is usually enough to easily eject both atoms. Since any light assisted collision can cause loss, the further red detuned from the free-space resonance the addressing light is, the smaller the effective collisional volume will be. Alternatively, blue detuning the light could also be effective. This is less interesting for cooling procedures, but has been shown to be effective for single-atom loading[12].

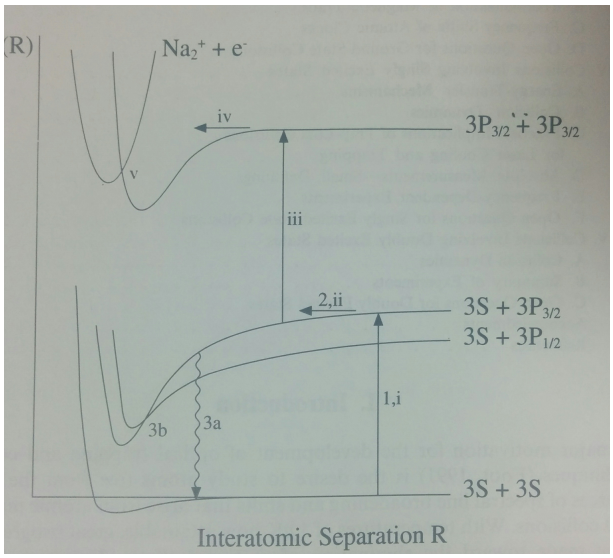

Figure 7.1: Collisional trap loss channels for Na atoms in a MOT. The light-assisted collisional path is $1 \rightarrow 2 \rightarrow$ 3a. The path through 3b is a fine-structure changing light-assisted collision and would manifest in a similar manner. Reprinted from reference [74].

7.2 Camera Signal Models

The signal observed during a camera exposure is proportional to the number of photons incident on the photo-detector. The atom cloud is a Gaussian distribution with width $\sigma_r \sim 0.7\mu m$ and length $\sigma_z \sim 7\mu m$. The fluorescence from the atom clouds is collected by the $NA = 0.35$ custom triplet, passes through a polarizing beamsplitter, capturing 50% of the light, and travels through spatial and spectral filtering to be imaged on the plane

of an EMCCD camera. Due to the geometry of the apparatus, the camera integrates the fluorescence along the axial dimension of the trap ($\hat{z}$), and the trap sites appear as a row of circular spots on the camera.

A ROI is defined for each site by a 3x3 pixel square around the fluorescence image of each trap site. The camera signal for a site is defined as the sum of the pixel values in the ROI minus the background per pixel from two groups of camera pixels outside the ROI. This procedure is designed to return a near zero signal when no atom is present in the trap.

The readout procedure toggles the FORT and MOT lasers via AOMs out of phase at 1.25 MHz with a 50% duty cycle. Chopping is necessary because of the large AC Stark shift gradient imposed by the FORT, and the heating due to the population in the anti-trapped $5P_{3/2}$ state. The chopping is at a much higher frequency than the trap radial and axial oscillation frequencies, which has been measured by parametric heating to be $\omega_{r(z)} = 40(3.2)$ kHz. Therefore, the energy transfer to the atoms due to the chopping should be inefficient, so minimal heating will occur during the readout due to parametric heating.[75] Loss during the readout is due to slightly unbalanced light pressures and magnetic fields. Typically the losses during readout can be minimized by appropriately shimming the power balance and magnetic fields during the readout phase. To increase sensitivity to the parameters, the readout phase can be temporarily extended beyond the end of the actual first camera exposure.

The camera signal is fundamentally Poissonian in nature, since there is some effective scattering rate from the background of the 9 pixels in the ROI $\Gamma_0 \sim 8kHz$, combined with the rate of collected fluorescence from the atom cloud $\Gamma_{sig} = n\Gamma_1$, where $\Gamma_1 \sim 10kHz$ is the time-averaged single-atom photon collection rate. The camera signal probability density, $S(s)$, in the ideal case is then given by:

$$S(s) = \sum_{n=0}^{\infty} P_{\bar{N}}(n) P_{(\Gamma_0 + n\Gamma_1)t}(s), \tag{7.4}$$

where $\bar{N}$ is the mean atom number, t is the camera exposure time, and $P_\mu(k)$ is the Poisson distribution for mean μ with discrete variable k. An example probability density is shown in Figure 7.2, where $P_{(\Gamma_0+n\Gamma_1)t}(s)$ has been replaced by the continuous approximation $(\Gamma_n t)^s \exp[-\Gamma_n t]/\Gamma(s+1)$, where $\Gamma_n \equiv \Gamma_0 + n\Gamma_1$ and Γ is the gamma function.

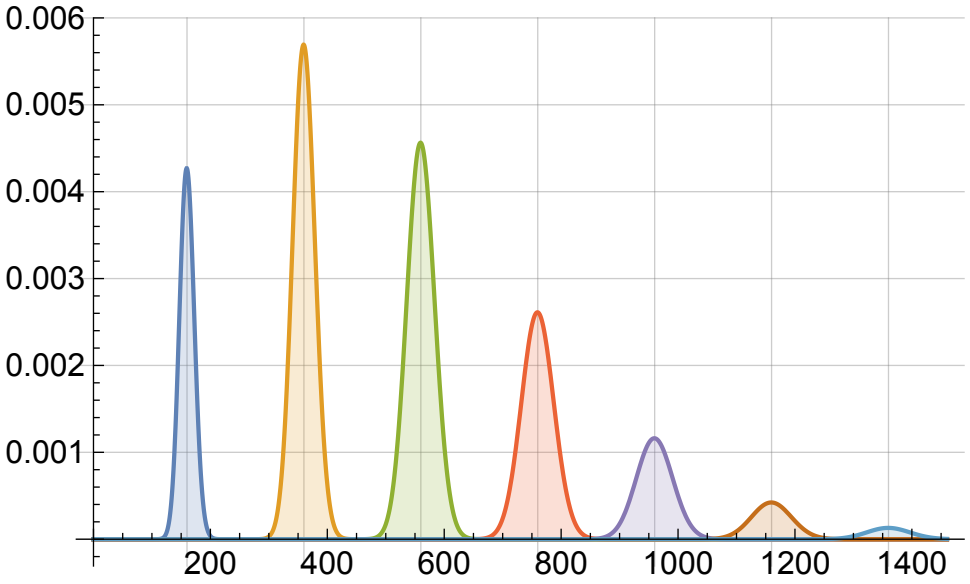

Figure 7.2: The ideal camera signal distribution for $\bar{N} = 2$ atoms with $\Gamma_0 = 8$ kHz, $\Gamma_1 = 10$ kHz, and $t = 20$ ms, with no loss. The peaks correspond to incrementally larger numbers of atoms, and are color-coded for clarity. Because the peaks are well separated, the distribution of atom numbers could be extracted with high fidelity.

7.2.1 Single Atom Camera Signal Model

Due to the high loss rates for $n \geq 2$, the single-atom camera signal model is only applicable for site loading rates where the probability of getting two atoms is negligible. For additional discussion of the single-atom readout, the interested reader should refer to previous group theses [25, 44, 45].

A typical single-atom readout camera signal histogram is shown in Figure 7.3(a) along with a fit to the single-atom readout model:

$$S(s) = \sum_{n=0}^{2} P_{\bar{N}}(n) G_{n\Gamma_1 t}(s), \tag{7.5}$$

shown in red. Here $G_{s_0}(s)$ is a normalized Gaussian distribution, centered at s_0. For reference, the result of a purely Possionian version of Equation 7.5 with the same parameters $\bar{N}$ from the Gaussian fit function is also shown. The super-Possionian behavior in the single-atom peak is most likely due to shot to shot fluctuations in the probe light's interference pattern on the atom cloud. The shot-to-shot fluctuations due to the interference patterns can be mitigated by modulating the retro-reflecting mirror position with a piezo element at a few kHz, or alternatively using independent counter-propagating probe beams with a differential frequency shift of a few kHz. Using independent beams adds complexity and doubles the power requirement but adds the ability to fully balance the light pressures. The 2-atom peak for the data set shown lacks significant statistics to determine the distribution, which is typical.

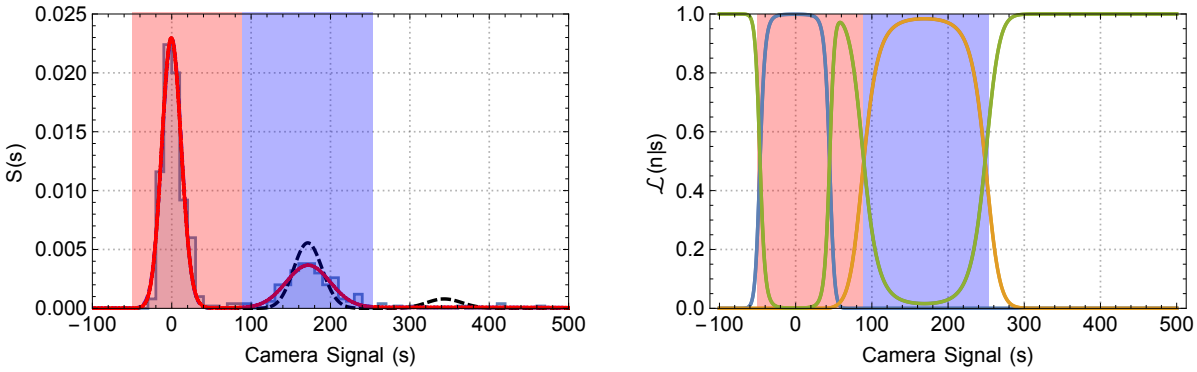

Figure 7.3: (a) An example daily 500 shot single-atom readout from 06/13/2013, with a t=20 ms camera exposure time. A fit based on Equation 7.5 is shown in red with best fit parameters: $\bar{N} = 0.36 \pm 0.01$ atoms, $\Gamma_1 = 8.6 \pm 0.1$ kHz, $\sigma_0 = 12.3 \pm 0.2$, $\sigma_1 = 27 \pm 2$, and $\sigma_2 = 200 \pm 200$. $P_{\bar{N}}(2) = 4.4 \pm 0.2\%$ The Possionian model from Equation 7.4 is shown as the black dashed line using the same parameters, demonstrating the super-Possionian nature for $n > 0$ photon count distributions. The typical $\pm 3\sigma_1$ cut thresholds are overlaid in red and blue for the zero- and one-atom cuts respectively. (b) The atom number likelihoods Equation 7.6 are shown from the fit parameters in (a). The 0-, 1-, and 2-atom curves are shown in blue, orange, and green respectively. For reference the thresholds are also shown. Note that the large σ_2 causes the 2-atom likelihood to dominate for regions where the PDF is small.

The most probable atom number given a camera shot signal magnitude, s, can be determined based on the prior knowledge from the measurement of the camera signal

model parameters. This is done by comparing the ratios of the various atom number camera signal distributions to the probability density reported by the model at s. For Equation 7.5 the likelihood of having interrogated n atoms when s photons are received by the camera is stated as:

$$\mathcal{L}(n|s) \equiv P(n)S_n(s)/S(s) = P_{\bar{N}}(n)G_{n\Gamma_1 t}(s)/S(s), \tag{7.6}$$

here $S(s)$ is the single-atom camera signal model determined from the daily readout test. The likelihood plots are shown in Figure 7.3(b).

For single-atom experiments the likelihood analysis is unnecessary and it is preferable, for the sake of sanity, to employ a threshold cut procedure. The typical threshold cuts used in single-atom experiments are "$3\sigma_1$" cuts, where a "one-atom" event is defined as a camera signal in the range: $[\Gamma_1 t - 3\sigma_1, \Gamma_1 t + 3\sigma_1]$, and a "zero-atom" event is defined as the camera signal range $[-50, \Gamma_1 t - 3\sigma_1 - 1]$. Everything outside of these two ranges is considered to be an anomaly and is dropped for shot 0 and counted as a zero-atom signal for shot 1. The $3\sigma_1$ threshold cut fidelities for the data set shown in Figure 7.3 are $\zeta(0, T_0) = 99.4\%$ and $\zeta(1, T_1) = 96.2\%$ for the zero- and one-atom cuts respectively. In other words, 96.2% of the one-atom cut events are valid and $\zeta(2, T_1) = 3.7\%$ of the events are actually mislabeled 2-atoms events. Of course, a valid 2-atom distribution is required for an accurate error representation and fidelities can only be calculated a posteriori from a known distribution. These fidelities ζ are calculated via the following relation:

$$\zeta(n, T_{n'}) \equiv \int_{T_{n'}} P_{\bar{N}}(n)G_{n\Gamma_1 t}(s)\mathrm{d}s \Big/ \int_{T_{n'}} S(s)\mathrm{d}s, \tag{7.7}$$

where n is the atom number and $T_{n'}$ is the threshold domain for atom number n'.

7.2.2 Two-Body Loss Rate Calibration

In order to calibrate the two-body loss rate, we measure the fluorescence of the sample as a function of the camera exposure time. For short times, t we expect the number of photons collected to be equal to be $n\Gamma_1 t$, where n is the number of atoms and Γ_1 is the single-atom photon collection rate. As the camera exposure time is increased the rate of collected photons will decrease as the number of atoms in the sample decreases due to losses. The probability p_n of finding atom number n is given by the set of simultaneous differential equations:

$$\frac{dp_n(t)}{dt} = -\frac{\beta}{2}\left[(n+2)(n+1)p_{n+2} - n(n-1)p_n\right], \tag{7.8}$$

where β is the two-body loss rate.

Discrete Model

If a finite maximum $n = n_f$ is imposed, the system of equations given by Equation 7.8 can be solved analytically for an arbitrary initial atom distribution. A Mathematica package that contains the solution with $n_f = 50$ atoms along with definitions for the equations corresponding to this discrete model can be found at this URL: [76]. While this solution is complex, it is most useful in situations that require long exposure times where there is a distinct possibility of reducing the atom distribution to only 0 and 1 atoms.

Using the analytical solution we can develop a model for the camera signal as a function of integration time. The rate of collected photons is equal to $R(t) = \bar{N}(t)\Gamma$ where $\bar{N}(t) = \sum_{n=1}^{n_f} p_n(t)n$ is the mean atom number at time t. Therefore the mean integrated camera signal is:

$$\bar{s}_{\bar{N}}(t) = \int_0^t dt' R(t) = \Gamma \sum_{n=1}^{n_f} \left[n \int_0^t dt' p_n(t) \right], \tag{7.9}$$

which can also be solved analytically. An example simulation data set is shown along with the solution to Eq. 7.9.

An interesting aside that can be easily modeled with Eq. 7.8 is the time evolution, due to pure two-body loss, of the Q-parameter defined by:

$$Q = \frac{\Delta N}{\bar{N}} - 1, \tag{7.10}$$

where ΔN is the distribution variance. A $Q < 0$ indicates sub-Poissonian behavior, and $Q = -1$ is deterministic preparation in a Fock State, i.e. the variance is zero. The result is shown in Figure 7.4.

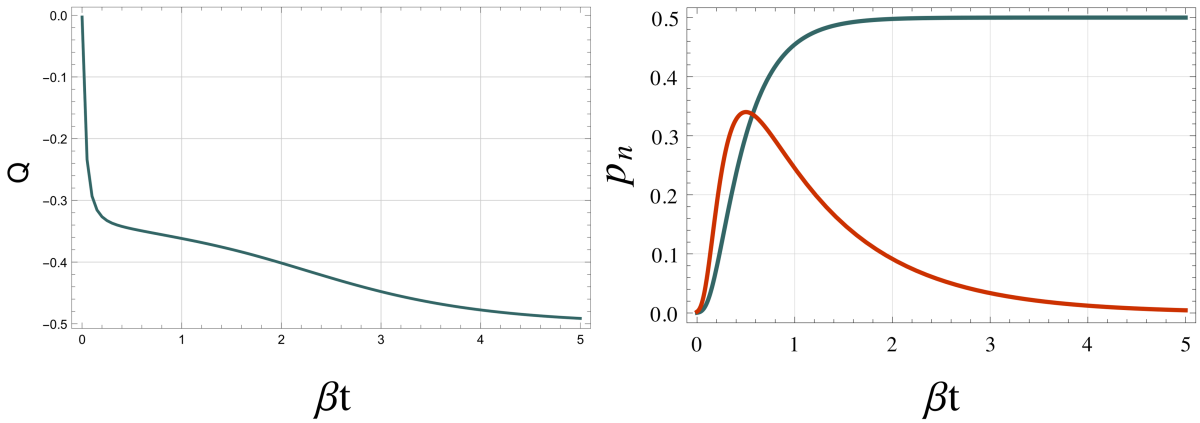

Figure 7.4: (a) The Mandel Q-parameter evolving during a simulated two-body loss experiment. The Q-parameter is limited to Q=-0.5 from two-body loss mechanisms. (b) $\mathcal{F} = 1$ (green) and $\mathcal{F} = 2$ (red) Fock State creation probabilities as a function of time undergoing two-body loss for $\bar{N}(0) \gg 1$.

Continuous Model

If the accumulation in states p_0 and p_1 during the readout is small then we can use the more familiar simplified continuous model:

$$\frac{d\bar{N}}{dt} = -\beta \bar{N}(\bar{N} - 1). \tag{7.11}$$

Notice that for $\bar{N}(0) > 1$, $\bar{N}$ will approach a mean of 1. This is not the correct behavior as it should approach 50%, and why it is not accurate if p_0 and p_1 are not negligible.

Integration of Equation 7.11 results in the continuous version of Equation 7.9, given by:

$$\bar{s}(\bar{N}, t) = \frac{\Gamma}{\beta} \ln\left[1 + \left(e^{\beta t} - 1\right) \bar{N}\right]. \tag{7.12}$$

Figure 7.5 shows a comparison of the continuous and discrete models. Note that for longer exposures the camera signal is overestimated in the continuous model as expected due to the asymptotic behavior of the continuous model. As can be seen for the short time scales used in the multi-atom number measurements ($t_{ex} = 3$ ms), the camera signal is approximately linearly sensitive to the atom number, and is sensitive at a higher order to the two-body-loss rate. Therefore, as will be shown in the multi-atom number measurement section, Section 7.2.3, the atom number measurement is insensitive to the small errors from using the continuous model, and we use the continuous model to determine the two-body loss rate because it is vastly simpler to implement.

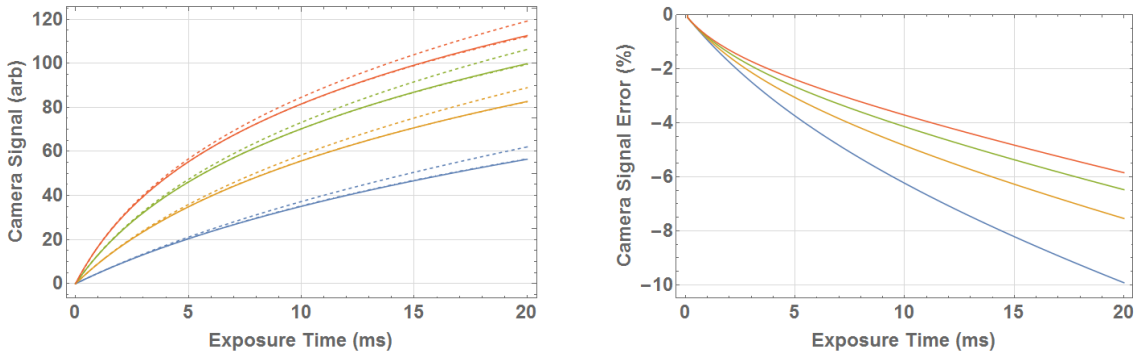

Figure 7.5: (a) A comparison of the simulated integrated camera signals resulting from the discrete (solid) and continuous (dashed) atom population models for a typical two-body loss rate $\beta = 0.02$ atom^{-1} ms $^{-1}$. (b) The systematic error due to the use of the continuous model $\bar{s}_{discrete}(t_{ex}) - \bar{s}_{cont}(t_{ex})$, note that the error is linear after sometime. This is due to the build up of population in p_0 and p_1 that is incorrectly counted in the continuous model.

For a simple improvement to the continuous model the rate equation can be modified by adjusting the parameter n_{asy} to make the discrete and continuous curves agree well

with little additional complication.

$$\frac{dn}{dt} = -n(n - n_{asy})\beta. \tag{7.13}$$

A value of $n_{asy} = 0.25$ reproduces the discrete result well for this parameter range.

7.2.3 Many-Atom Number Measurements

Once β is known we can use it to calibrate the camera signal observed during a static integration time. In the limit of $\beta \to 0$, the number of photons collected during an integration time t is fundamentally Poissonian with a mean of $\bar{s} = n\Gamma t$. Our atom detection scheme works best when $\bar{N}\Gamma t \sim 100 - 200$ photons, which allows us to approximate the photon counts, s, as Gaussian:

$$G_n(s, \bar{s}, \sigma) = \frac{1}{\sqrt{2\pi}\sigma_n} \exp\left[-\frac{1}{2}\left(\frac{s - \bar{s}}{\sigma}\right)^2\right], \tag{7.14}$$

with standard deviation σ. If no σ is specified, it is assumed that $\sigma = \sqrt{\bar{s}}$. Typically Γ_1 is between 8-10 photons/ms, with a background rate of $\Gamma_0 = 8$ photons/ms, derived from the width of the background camera signal distribution assuming Poissonian statistics. Since we automatically subtract the background from the signal, we measure the value of σ_1 during our readout procedure and use $\sigma_n \equiv \sqrt{n}\sigma_1$. We approximate the background (0 atom) peak as a Gaussian distribution with measured width σ_0.

For finite β, as the readout progresses pair-loss events occur which will create a "tail" on the unperturbed Gaussian distribution. If the exposure time is short then the Gaussian distribution with a tail can be approximated as a Gaussian centered at the expected mean $\bar{s} = \bar{s}(n, t)$, and the camera signal distribution is then given by:

$$\bar{S}(s) = \sum_{n=0}^{n_f} P_{\bar{N}}(n) G_n\left[s, \bar{s}(n, t)\right], \tag{7.15}$$

where σ_0 is the background standard deviation. Note that the mean atom number $\bar{N}$ is the only free parameter in $\bar{S}(s)$. We typically use an exposure time $t = 3$ ms, and the analysis is performed with experimentally measured parameters $\sigma_0 = 0.188$ and $\sigma_1 = 0.448$ atoms. An example data set and fit are shown in Figure 7.6.

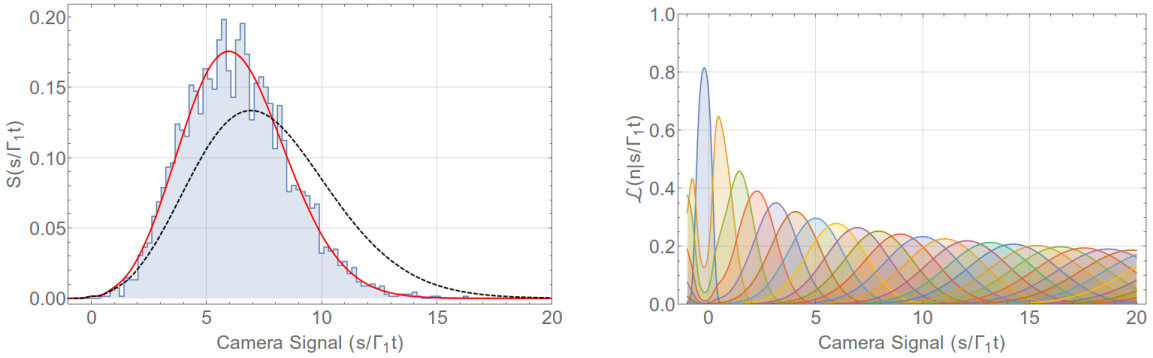

Figure 7.6: (a) The camera signal histogram for $\bar{N} = 7.6$ atoms, normalized to the single atom signal $\Gamma_1 t$. The fit to Equation 7.15 where $\bar{N}$ is the only free parameter, is the solid red line. The expected camera signal assuming no losses, $\beta = 0$ is the dashed black line, for the same $\bar{N}$. (b) The likelihood plots for the many atom measurement from Equation 7.6 using the same parameters. The indistinguishably of the individual histograms causes low maximum likelihoods. The distortion at $s < 0$ is due to the simplification of Gaussian instead of Possionian distributions. However, note that $s < 0$ and $s > 15\Gamma_1 t$ are low probability events.

Since the procedure only integrates the camera signal for a short time, we are not very sensitive to the two-body loss rate by design. For the data set shown in Figure 7.6, a 50% change in β only changes the atom number result by 8.5%.

7.2.4 Few-Atom Distribution Measurement

Due to the short exposure time required to stay in the near linear signal regime, the individual atom peaks are not well resolved and therefore are not reliable for measuring the atom probability distribution. For small $\bar{N}$ the actual atom probabilities can be measured by using a longer integration time than described in Section 7.2.3, allowing the peaks to separate enough for a reasonable fidelity measurement even with two-body losses.

For $n < 2$, no collisions occur and therefore the signal distribution is simply Gaussian: $S_n(s,t) = G_n(s, n\Gamma t)$. For $n = 2$ or 3 a maximum of one mutually destructive collision event can occur, and therefore the signal distributions can be split into 2 cases:

1. $S_n^{(0)}(s,t)$, no loss event occurs during the integration time: $p(t_{loss} > t) = e^{-n(n-1)\beta t}$,
2. $S_n^{(1)}(s,t)$, a loss event occurs at time t_{loss} with probability: $p(t_{loss})dt' = n(n-1)\beta e^{-n(n-1)\beta t'}dt'$.

For case 1. the signal is, once again, $S_n^{(0)} = G_n(s, n\Gamma t)$. For case 2. the atoms will scatter photons until the loss event at t_{loss}, at which point photon collection from atoms will cease ($n = 2$), or continue at the single-atom rate ($n = 3$). This creates a tail for the Gaussian distribution, discussed in Section 7.2.3, with formula:

$$\begin{aligned} S_n^{(1)} &= G_n^{\star}(s,t) \\ &= \left(\frac{n(n-1)\beta}{1-e^{-n(n-1)\beta t}}\right)\int_0^t dt' e^{-n(n-1)\beta t'} G_n\left[s, \big((n-2)t+2t'\big)\Gamma, \sqrt{\sigma_2^2 t'/t + \sigma_{(n-2)}^2}\right]. \end{aligned} \tag{7.16}$$

To the best of my knowledge, this integral can not be calculated analytically. However, for the case of $\sigma_{(n-2)} = 0$ the integral can be calculated analytically. The result for $n = 2$ is shown below:

$$S_2^{(1)} \sim \mathcal{G}_2^{\star} \equiv \frac{2\beta}{4(1-e^{-2\beta t})}\sqrt{\frac{t}{\Gamma^2 t + \beta\sigma_2^2}}\exp\left[2s\Gamma t/\sigma_2^2\right](A_+ + A_-), \tag{7.17}$$

where the terms $A_\pm$ are defined as:

$$A_\pm \equiv \exp\left[\pm 2|s|\sqrt{t(\Gamma^2 t + \beta\sigma_2^2)}/\sigma_2^2\right]\left(\mathrm{erf}\left[\frac{2\sqrt{t(\Gamma^2 t + \beta\sigma_2^2)} \pm |s|}{\sqrt{2}\sigma_2}\right] \mp 1\right). \tag{7.18}$$

The analytic result above can be convolved to produce the loss event signal from a two or three atom sample, $S_n^{(1)}(s,t) = \int_{-\infty}^{\infty} ds' \mathcal{G}_2^{\star}(s',t) G_{(n-2)}(s-s',t)$, but this too cannot be

calculated analytically. Since the effect of the finite σ_0 width is only applicable for a small number of events where $s \sim 0$, it is ignored to reduce the complexity of the analysis. A Monte-Carlo simulation of an exactly two-atom signal with $\beta = 0.02$ atoms$^{-1}\cdot$ ms^{-1} is shown in Figure 7.7 along with $S_2(s,t)$ using $G_2^\star(s,t)$ (solid black) and the approximation $\mathcal{G}_2^\star(s,t)$ (dashed red) using the same parameters (not a fit).

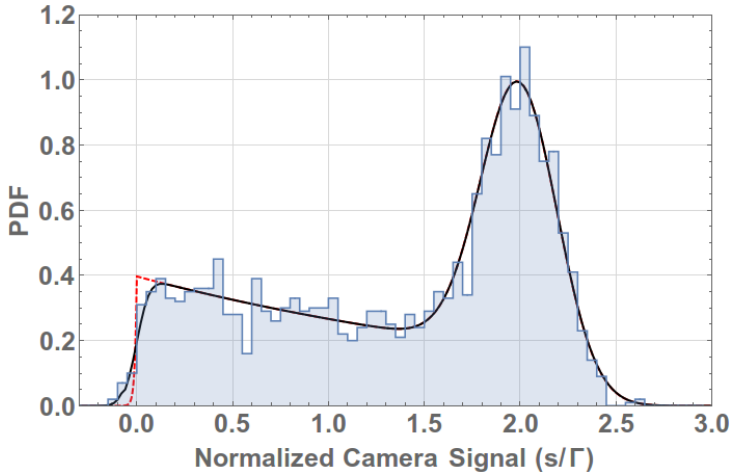

Figure 7.7: A Monte Carlo simulation of a two-atom signal is shown in blue along with the two-atom camera signal model $S_2(s,t)$ in solid black for the same parameters (not a fit). The camera signal model approximation $S_2(s,t) \sim e^{-2\beta t}S_2^{(0)}(s,t) + (1-e^{-2\beta t})\mathcal{G}_2^\star(s,t)$ used in the analysis is shown as a dashed red line. Note that convolution with the background signal is only significant around $s/\Gamma \sim 0$. The parameters for the simulation are: $\{\beta, \Gamma, t, \sigma_0, \sigma_2\} = \{0.02\,\text{atoms}^{-1}\cdot\text{ms}^{-1}, 1\,\text{ms}^{-1}, 20\,\text{ms}, 0.075\,\text{ms}^{-1/2}, 0.2\,\text{ms}^{-1/2}\}$.

The signal distribution for $n \leq 3$ is then given by:

$$\begin{aligned} S(s,t) =& p_0 G_0(s,0) + p_1 G_1(s,\Gamma t) + \\ & p_2\left[e^{-2\beta t}G_2(s,2\Gamma t) + (1-e^{-2\beta t})G_2^\star(s,t)\right] + \\ & p_3\left[e^{-6\beta t}G_3(s,3\Gamma t) + (1-e^{-6\beta t})G_3^\star(s,t)\right]. \end{aligned} \tag{7.19}$$

For $n > 3$ one would have to include $n/2$ loss events, and one might be able to do this efficiently in a recursive manner, but for our experimental parameters $n = 2$ is our maximum detectable atom number.

We have decided to use an exposure time of $t = 10$ ms to minimize the overlap integral

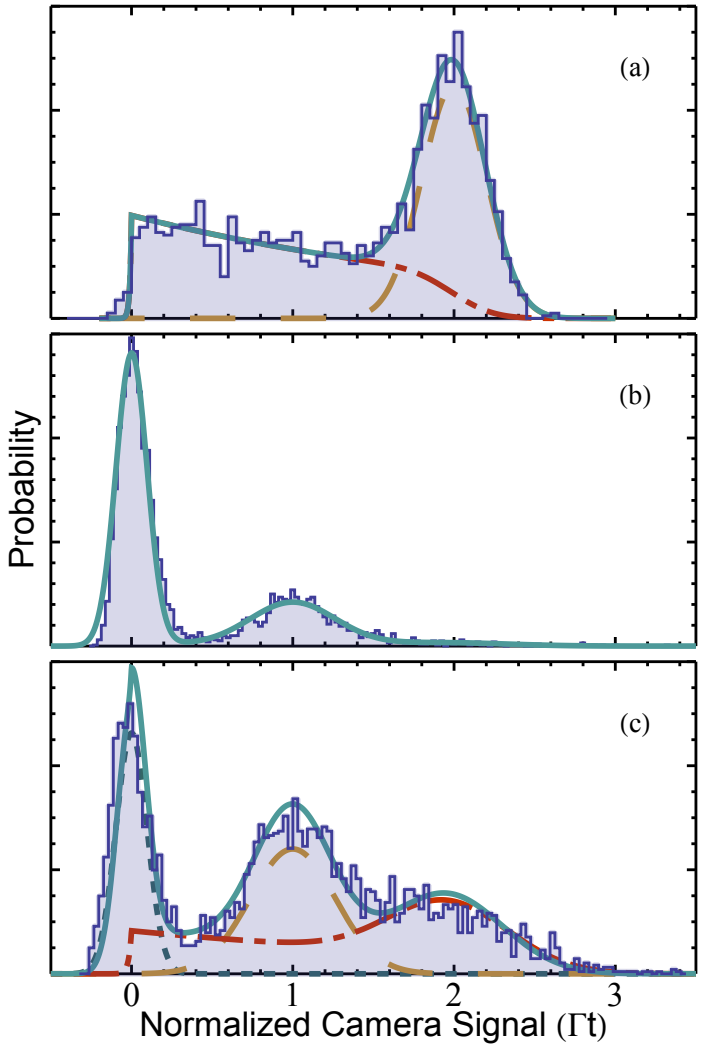

Figure 7.8: (a) A Monte Carlo simulation (same as Figure 7.7) of a two-atom signal is shown in blue along with the two-atom camera signal model $S_2(s)$ in red for the same parameters (not a fit). The solid blue line is $S_2^{(1)}(s)$, the component where no loss event has occurred. The solid yellow line is $S_2^{(2)}(s)$ the component where a loss event has happened during the camera exposure. (b) A single-atom readout camera signal data set with minimal two-atom preparation. (c) A high statistics data set with significant two-atom preparation shown with a fit to Equation 7.19 ($n < 3$). The individual atom signal components are shown for comparison. Note that the gap between the background and 1 atom peaks is not preserved due to the "tail" of the 2 atom distribution from the two body loss.

between the 1 and 2 atom distributions. Typical experimentally measured (normalized to the single atom scattering rate) parameters used for $n = 2$ measurements are $\sigma_0 = 0.236$ and $\sigma_1 = 0.883$ counts/$\sqrt{\text{ms}}$ for $\Gamma = 1$ count/ms.

This improved model for two-atom camera signal distribution also enables improvements to the accuracy of the single atom readout fidelity where two-atom loading events occur at a small non-negligible percentage. A Poissonian loading rate of $\mu = 0.3$ atoms ($P_{0.3}(2) = 0.033$) is shown in Figure 7.9 for similar parameters. With these assumptions the threshold measurement fidelities are $\zeta(0, T_0) = 99.3\%$ and $\zeta(1, T_1) = 95\%$, where now $\zeta(2, T_1) = 5\%$.

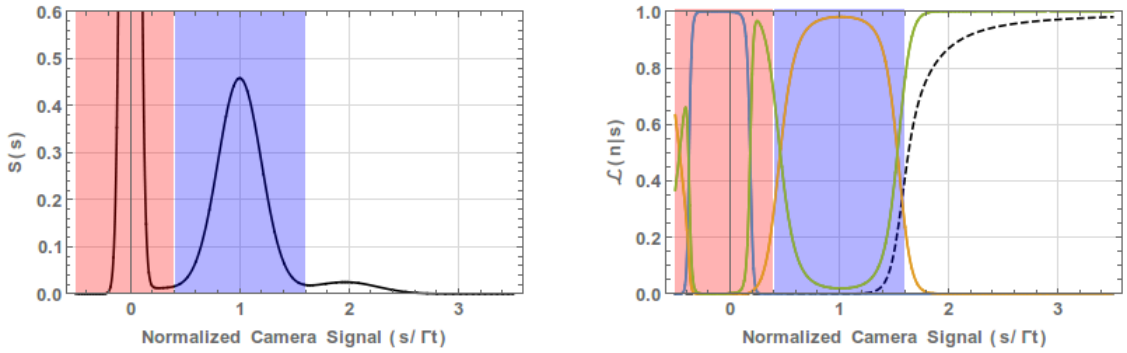

Figure 7.9: (a) The improved camera signal histogram model, Equation 7.19, in the context of a single atom readout. The initial atom distribution is Poissonian with mean $\mu = 0.3$ atoms, $P_\mu(n > 2)$ forced to 0 and all probabilities are re-normalized. The y-axis is expanded to show the two-atom peak at the expense of the 0-atom peak visibility. Threshold regions are shown in red (0-atom) and blue (1-atom). (b) The likelihood functions for 0- (blue), 1- (orange), and 2-atoms (green) for the same distribution. The two-atom fidelity with two-atoms remaining after the readout is shown as the black dashed line.

7.3 State-Selective Measurements

Measurement of the atomic population in a state is an essential component of any atom-based quantum computation system. State-selective measurements are implemented in this experiment by removing atoms in the $|0\rangle$ state, with an unbalanced laser nearly

resonant with the D2 $5S_{1/2}, F = 2 \leftrightarrow 5P_{3/2}, F' = 3$ transition. The hyperfine splitting between $F = 1$ and $F = 2$ is sufficient to negate any off-resonant excitation from $F = 1$. Therefore, we ideally perform an operation that maps the $|1\rangle$ population to the trap population, which can be measured with any of the procedures outlined earlier in this chapter.

To the extent that the transition is closed an atom will continue to cycle between $F = 2 \leftrightarrow F' = 3$ absorbing momentum from photons propagating in a single direction, until it has gained too much energy to be contained in the trap. However, it is possible to excite the $F' = 2$ or $F' = 1$ and subsequently decay to the $F = 1$ state, at which point heating will cease and an erroneous $|1\rangle$ signal will be recorded. To mitigate this decay channel we implement a few modifications to the fundamental procedure.

1. chopping the FORT and blow-away light out of phase,

2. circularly polarized blow-away light collinear with a magnetic field,

3. instantaneously lower the trap depth to $\sim 10\%$ during blow-away

Chopping the FORT and blow-away light out of phase allows the atoms to only be addressed in free space. This allows for the atoms to always be addressed on resonance minimizing coupling to $F' \neq 3$. Using circularly polarized light adds an additional polarization selection rule to the excitation once the ensemble is optically pumped into $F = 2$, $m_F = 2$, the magnetic field is necessary to define the quantization axis. Under conditions of perfect σ_+ polarized light, the only available excitation channel is $F' = 3$, $m_F = 3$. Finally, lowering the trap depth instantaneously for 2 ms has little effect on non-addressed atoms since they stay cold enough to be retained when the FORT is increased to full power. However, atoms that are affected by the blow-away light see a shallower and wider potential allowing the spatial extent of the atoms in $|0\rangle$ to expand more than in a deeper potential as they are heated. Then when the trap is turned back on $|0\rangle$ atoms not fully removed from the low-power FORT will gain additional kinetic energy due to

being located on a steeper slope of the potential energy curve. With these modifications, blow-away infidelities, defined as the probability to miscategorize atoms in $|0\rangle$ as $|1\rangle$, as low as 0.2 %/atom have been observed, see Figure 7.10.

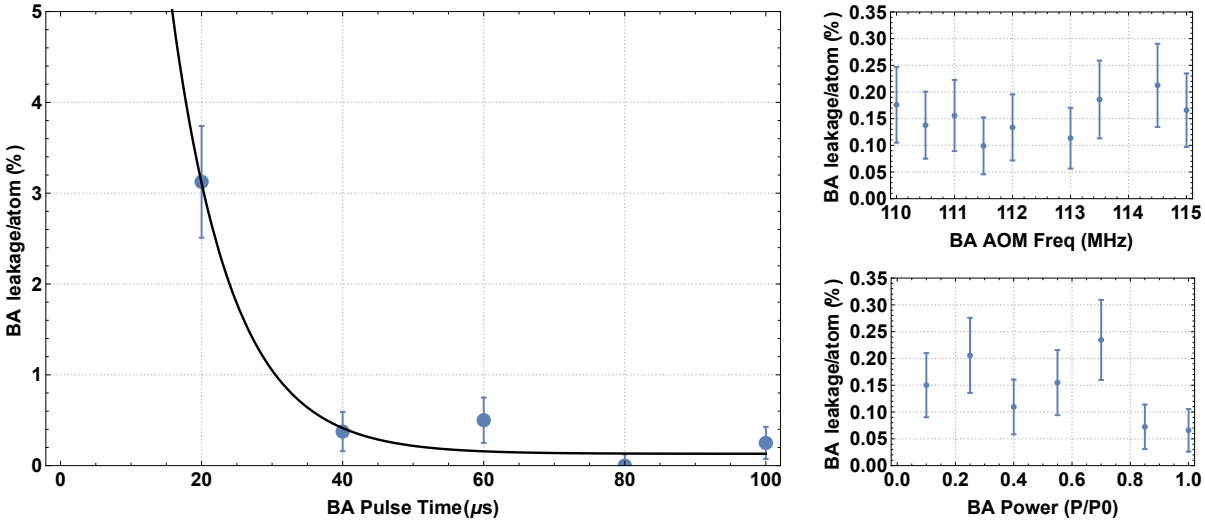

Figure 7.10: (a) The data points (blue dots) are collected for different blow-away pulse time scan starting with $\bar{N} \sim 4$ atoms in site 2. A single-atom readout sequence is used since the expected two-event leakage signal ρ_2 will occur at a negligible rate. Rates are extracted from the number single-atom counts, n_1, and the expected number of atoms loaded during the test, $\rho_1 = n_1/(\bar{N} * m)$, where the Poisson mean, $\bar{N}$ has been measure in a separate experiment and m is the number of data runs taken. The exponential fit, shown as the black line, gives a time constant $\tau = 8(4)$ μs and an asymptote of 0.1(1)%/atom leakage. Data taken 06/13/2014. The blow-away leakage sensitivity to the (b) double pass AOM frequency and (c) relative BA power. Data is averaged over sites 1,2 and 3 with 3-6 atoms per site. Data taken 06/15/2014.

These rates are low enough that the signal to noise ratio is 1:1 for a sample of 1000 atoms, opening the possibility for observation of single photon absorption with significant atom-photon cross sections[77]. For the data shown in Figure 7.10, the $|1\rangle$ state retention during the blow-away pulse was measured to be 99(3)% (corrected for the normal daily retention). Of considerable interest is the implementation of a non-destructive state-selective readout (ND-SSRO) procedure. This has been achieved recently using an EMCCD camera and a single probe beam[78, 79], and two counter-propagating beams to minimize heating[79]. ND-SSRO in neutral atoms has been previously demonstrated using a well polarized beam and a single photon avalanche photodiode (SPAD).[80].

Chapter 8

Apparatus

This chapter is devoted to documenting a large overhaul of the experimental system, however no data will be shown from the apparatus outside of the section itself unless explicitly noted. The combination of the long-term stability of the original apparatus and the maximum achievable repetition rate of the experiment was becoming a limiting factor in the complexity of experiments that could be performed. The goals of the rebuild were to compactify the entire system to lessen the impact of any temperature gradients over the extent of the system, increase the loading rate while also increasing the background limited lifetime, decrease the experimental cycle time, automate significant portions of the daily optimization experiments, and improve the photon collection optics to lessen the effects of two-body loss in our multi-atom readout procedure. The changes documented in this chapter were made with these goals in mind, but a summary of these points are presented in the table below:

Parameter	old	new
Approximate bounding vol.	0.95 m^3	0.4 m^3
Cycle time	600 ms	125 ms
Exposure time	20 ms	2 ms
Retention	0.93	0.98

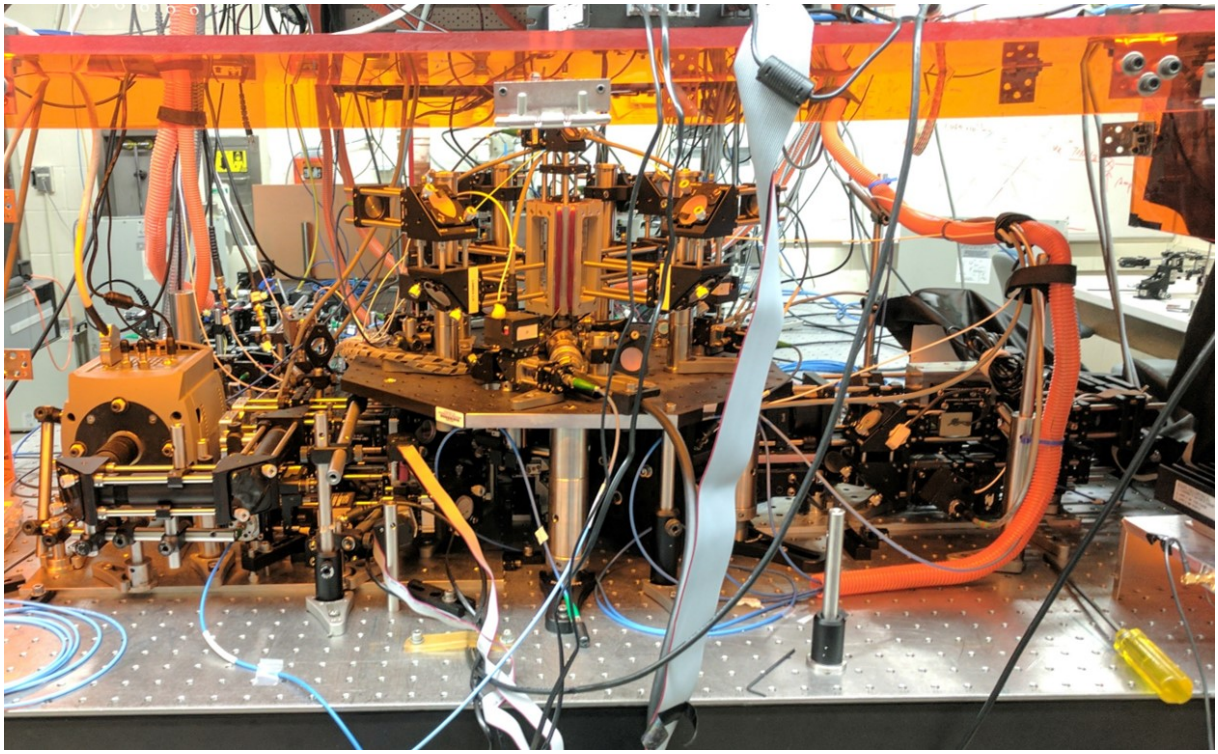

Figure 8.1: Image of the new apparatus in the orange acrylic enclosure for the old apparatus FORT, camera, and 780 addressing optics. On the left is the new FORT, camera, and 780 addressing optics on a 303 stainless steel breadboard, and on the right is the 480 addressing optics and the alignment camera, on a cast Al breadboard. A slight bend was noticed in the stainless steel breadboard, so we went with aluminum for the second one. The 2D- and 3D-MOT optics are all referenced to the black "lofted-breadboard" black in the center, while all of the FORT and addressing optics are directly on the optical table. Each piece is modular and can be moved relative to the other two (including the MOT) while maintaining subsystem alignment.

An image of the new apparatus is shown in Figure 8.1.

8.0.1 Vacuum System

The vacuum system has been changed to a two-stage vacuum chamber separated by a differential pumping tube that imposes a pressure difference, creating high pressure and low pressure regions. Since any atom in a 10 mK trap subjected to a elastic collision with a 300 K atom or molecule will be ejected from the trap, the limiting factor for atom retention is typically collisions with the background gas. Therefore a lower pressure is

required for extended trapping lifetimes to achieve high fidelity operations. However, the MOT loading rate is proportional to the density of cold atoms ($v \lessapprox 30$ m/s [81]) that pass through the capture volume. For Rb^{87} at 300 K, the fraction of atoms with $v < 30$ m/s is $< 0.2\%$, therefore trapping from the background is inefficient, and increasing the loading rate comes at a cost of decreasing the lifetime in the traps, increasing retention errors. However, an increased loading rate shortens the atom collection phase of the experiment, which is the dominant phase in the past accounting for about 70% of the cycle time. Shortening the loading phase can dramatically increase the data rate, allowing better statistics and more complicated experiments. With the single chamber system it was necessary to find an appropriate balance between data rate and retention losses.

With a two-stage vacuum system, the loading rate and background gas collision rates are no longer strongly coupled and the two parameters can be independently optimized. The 2D-MOT cools atoms in 2 dimensions from a relatively high pressure background region ($\sim 10^{-7}$ torr) with large cooling beams ($\omega = 5$ mm), the atoms still have a thermal velocity in the transverse direction, and travel approximately along a line perpendicular to the plane of the cooling beams. This atomic beam is positioned inline with the 3D-MOT and a differential pumping tube (DPT) allowing the atom beam to pass between vacuum chambers. An image of the assembled vacuum system is show in Figure 8.2.

Differential Pumping Tube

The DPT is a 2.3 mm diameter hole drilled along the axis of a #8-32x1/4" 316 Stainless Steel socket cap screw. For a ballistic gas in the molecular flow regime the conductance of a tube is given by[82]:

$$C = \left(\frac{\bar{v}\pi}{12}\right)\frac{d_t^3}{l_t}, \tag{8.1}$$

Figure 8.2: Image of the double vacuum system. The 2D-MOT chamber with dispenser is on top. The 3D-MOT science region is below in a ColdQuanta hexagonal vacuum cell. The dispenser electrical connection can be seen on the right and the ion pump is in the back left.

where $\bar{v}$ is the mean velocity, d_t is the diameter of the tube, and l_t is the length. For a circular orifice of diameter d_o instead, the conductance is given by:

$$C = \left(\frac{\bar{v}\pi}{16}\right) d_o^2. \tag{8.2}$$

For a constant conductance $l_t = 4d_t^3/3d_o^2$, meaning that an orifice can be traded for a tube of some length to gain an increased cross section without increasing the thermal atom flux. However, for a directional (non-thermal) atom beam, an increased diameter means an easier target to hit, while additional length is of no consequence. Therefore, the optimal choice is a long differential pumping tube with a diameter selected to provide the desired conductance, maximizing the conductance contrast for the thermal and non-thermal samples, see Figure 8.3. Since alkali atoms do not behave ballistically, there is a further improvement of the contrast by the fact that atoms striking a vacuum wall will adhere to the surface, reducing the conductance for thermal Rb atoms. For room temper-

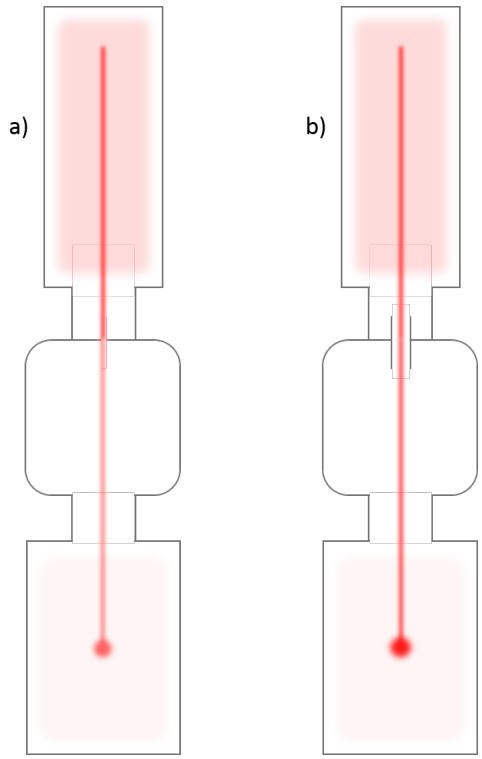

Figure 8.3: Cartoon showing the conductance contrast of thermal atoms and the 2D-MOT cold atom source, (a) with a pinhole and (b) with a differential pumping tube. A larger diameter tube can be made with the same thermal atom conductance, than a similar conductance pinhole. This leads to an easier to align system due to the larger target for the 2D-MOT and most likely higher cold atom flux into the science region.

ature air at $T = 20$ C, the conductance of the differential pumping screw is estimated to be 0.15 L/s, which includes the socket cap of the screw in the calculation. The ion pump is specified at 3 L/s so the pressure differential is approximately a factor of 20, for N_2, and likely more for Rb.

Dispensers

The background vapor is created in a Triad Technologies Pyrex cell by heating a stainless steel 25 mg Rb^{87} dispenser with a custom bend configuration (Alvatec product number AS-2-Rb87(98%)-25-X purchased through Trace Sciences).[1] Two dispensers are installed

[1] As of 2017, Alvatec has gone out of business and another source for isotopically enriched dispensers has not been found. However we note that a two-chamber vacuum system with a 2DMOT acts as an isotope selector element, and we would not need to worry about additional Rb^{85} background pressure in the 2DMOT region.

for redundancy as 25 mg ($\sim 10^{23}$ atoms) of Rb should last the lifetime of the experiment. Heating is accomplished by running 1.5-3 A through the dispenser, which causes the Bi_2Rb_3 alloy to sublimate Rb, leaving the Bi behind. The alloy raises the sublimation point to conditions that exceed a typical UHV bake-out procedure, meaning that the Rb will stay in a solid phase until it is released via the resistive heating procedure. After the initial testing, we rarely need to heat the dispensers to load enough atoms.

The dispensers need to be heated resistively and therefore electrical vacuum feedthroughs are required. In order to keep the size of the system as small as possible only a single 1.33" CF spherical cube element is used. The ion pump (Gamma Vacuum 3S-CV-1D-5K-N-N 3 L/s) must be attached to the lower pressure chamber. Because of this and the fact that the DPT is built into the gasket connecting the 2DMOT cell to the spherical cube, the electrical connections must enter from the lower pressure side and pass through an intra-vacuum feedthrough (IVFT) to the higher pressure atom source chamber. The feedthrough wires are then electrically and mechanically mated to the dispenser leads with custom barrel connectors. The electrical connections cannot short to the vacuum chamber and must not block the atom beam axis. This required the construction of custom BeCu barrel to dispenser lead connectors, shown in Figure 8.5. The feedthroughs and DPT pass through a custom machined blank OFHC 1.33" copper gasket to separate the chambers. Finally, the uninsulated wires are held away from the copper gasket using a custom ceramic spacer and ceramic beads, and the assembly is secured by the DPT screw. The gasket is held in place by the CF flange, and no adhesive is used in the assembly. The ceramic spacer turned pink during a high-temperature pre-bake. The color changing process is not known, but besides a cheerier color palette there does not appear to be any vacuum pressure consequences.

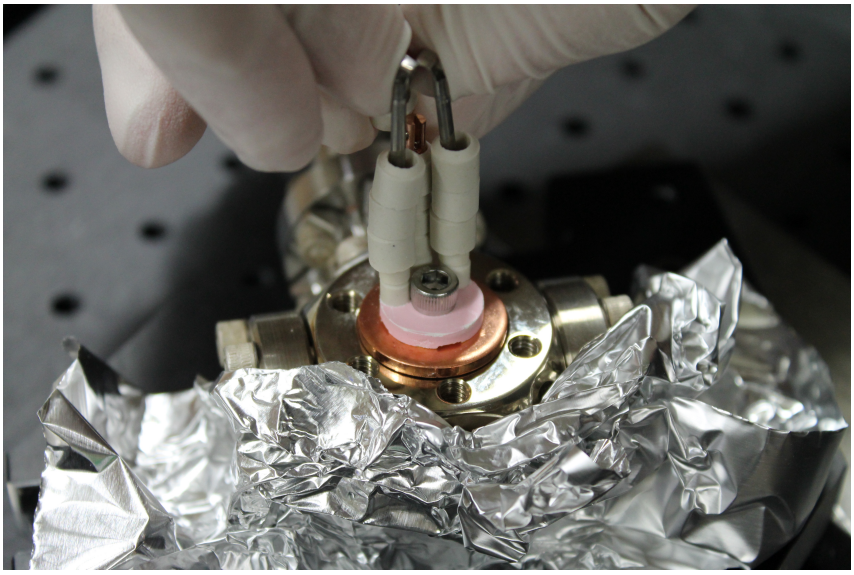

Figure 8.4: Image of the Intra-Vacuum Feedthrough (IVFT) being assembled with the dispensers.

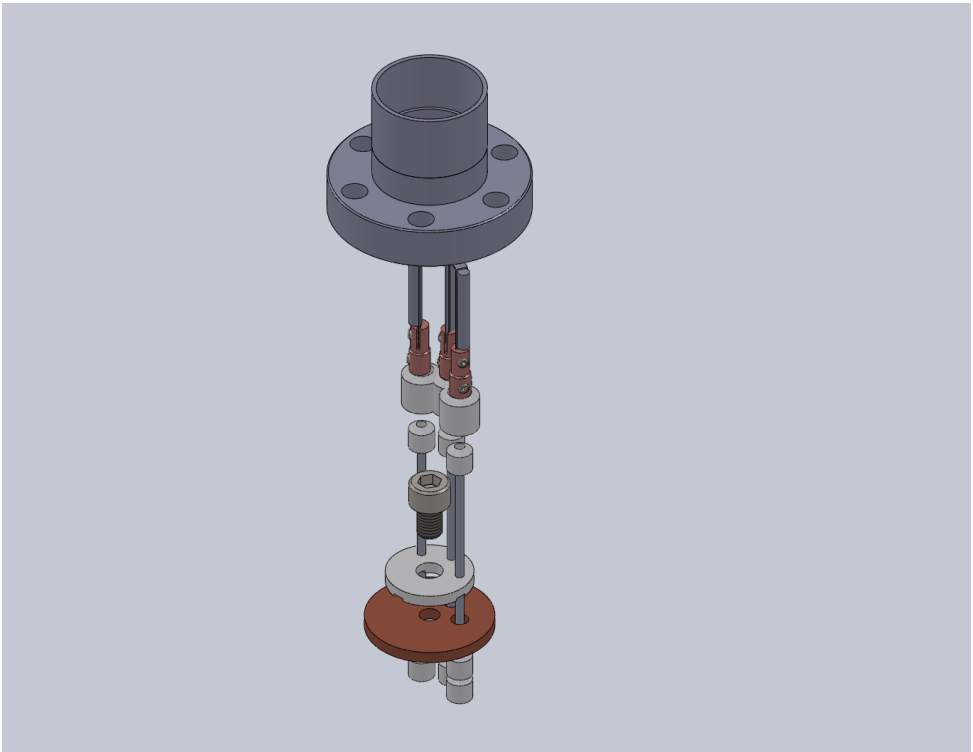

Figure 8.5: Exploded view of the IVFT assembly. A screw with a differential pumping tube holds an insulating ceramic wire spacer, where the wires to the Rb dispensers pass through. A custom BeCu wire-to-dispenser barrel-connector mates the electrical wires to the dispensers. Ceramic beads along the wire act as insulators on the bare wire.

Hexagonal Vacuum Cell

The science (low pressure) region is a hexagonal cell made from optically contacted 7.3 mm Pyrex windows AR coated on both sides from ColdQuanta. The birefringence of the top 7.3 mm window was not detectable with two Glan-Taylor polarizers.

An initial high temperature baking procedure was performed on the non-glass vacuum components then the vacuum chamber was assembled and baked for a month connected to a turbo pump. The long bake time is due to the low conductance to the atom source region. After the baking procedure the was completed the chamber was cooled and the copper tube connecting the chamber to the turbo pump was pinched off using a hydraulic press forming a cold-welded UHV compatible permanent seal.

Initial pressure readings from the ion pump controller suggested pressures around 10^{-11} torr in the science region, however during a fluorescence check in the atom source region an internal arcing event, in the power supply heating the dispensers, caused an excess of 6 A through the dispensers causing a significant increase in the vapor pressure. The vapor pressure on the ion pump controller reads around 10^{-8} torr. MOT lifetimes, extrapolated to 0 density to account for the effect of two-body losses, and single atom FORT lifetimes are measured around 5 s implying a background pressure in the science region of $\sim 4 \times 10^{-9}$ torr [71].

8.0.2 MOTs

The 2D-MOT is formed by 2 sets of counter-propagating beams from 4 independent fiber launchers and 4 independent gradient field coils. The gradient coil currents and power balances are set to balance the light forces the atoms experience. Independent, as opposed to retro-reflected, beams mean that the intensity can be fully balanced despite the fact that the cell is not AR coated. The transverse velocity distribution is cooled by the 4 beams, while the longitudinal velocity is still the room-temperature velocity. The trappable atom flux are atoms with $0 < v_z <\sim 30m/s$, this flux can be significantly increased with an

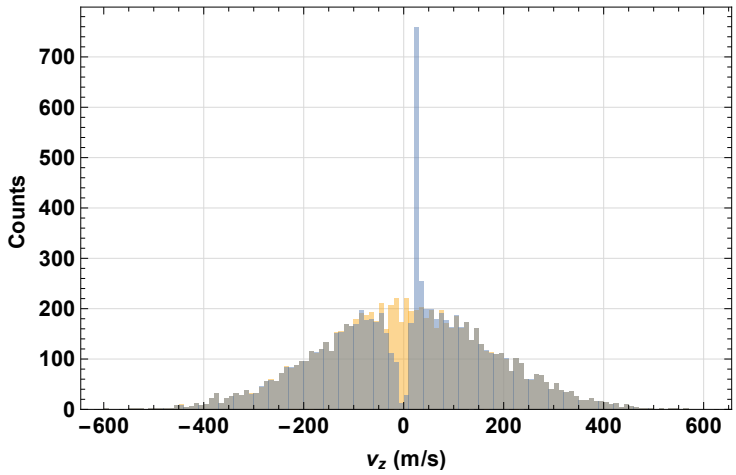

Figure 8.6: A simulation of the z-velocity distribution of Rb^{87} atoms (yellow) at 300 K and (blue) after a 1 ms push beam laser pulse with $s_0 = 1$, demonstrating the depletion of atoms in the velocity class inside the Doppler profile of the laser. There is build-up of atoms just outside the Doppler profile which can be adjusted by changing the push-beam detuning.

additional push beam in the $+\hat{z}$ direction, near resonant with the cycling transition. The push beam increases the z velocity of atoms within the Doppler profile of the laser and increases the probability to find an atom in the trappable velocity range[83]. A simple 1D toy simulation demonstrating this is shown in Figure 8.6.

The 3D-MOT is formed by 3 sets of counter-propagating beams from 6 independent fiber launchers and a quadrupole field coil. There are 3 sets of magnetic field bias shim coils that are oriented with the FORT, and are therefore rotated 60 degrees relative to the MOT quadrupole axis. The MOT z beams are aligned along the quadrupole field axis, normal to a pair of the hexagonal faces. The MOT X and Y beams form an "X" in the plane 75 degrees from the z-axis and the X and Y beam cross at an angle of 80 degrees.

The 2D- and 3D-MOT beams derive from the same master oscillator as shown in Figure 8.7. The master oscillator is pre-shifted red before the Modulation Transfer Spectroscopy (MTS) Lock so that the Master oscillator is $\sim$ 225 MHz blue of the $F = 2 \rightarrow F' = 3$ hyperfine manifold. This makes sure that any leakage, when the laser light is heavily attenuated, is off resonant with the trapped atoms. Additionally, shutters based on DC

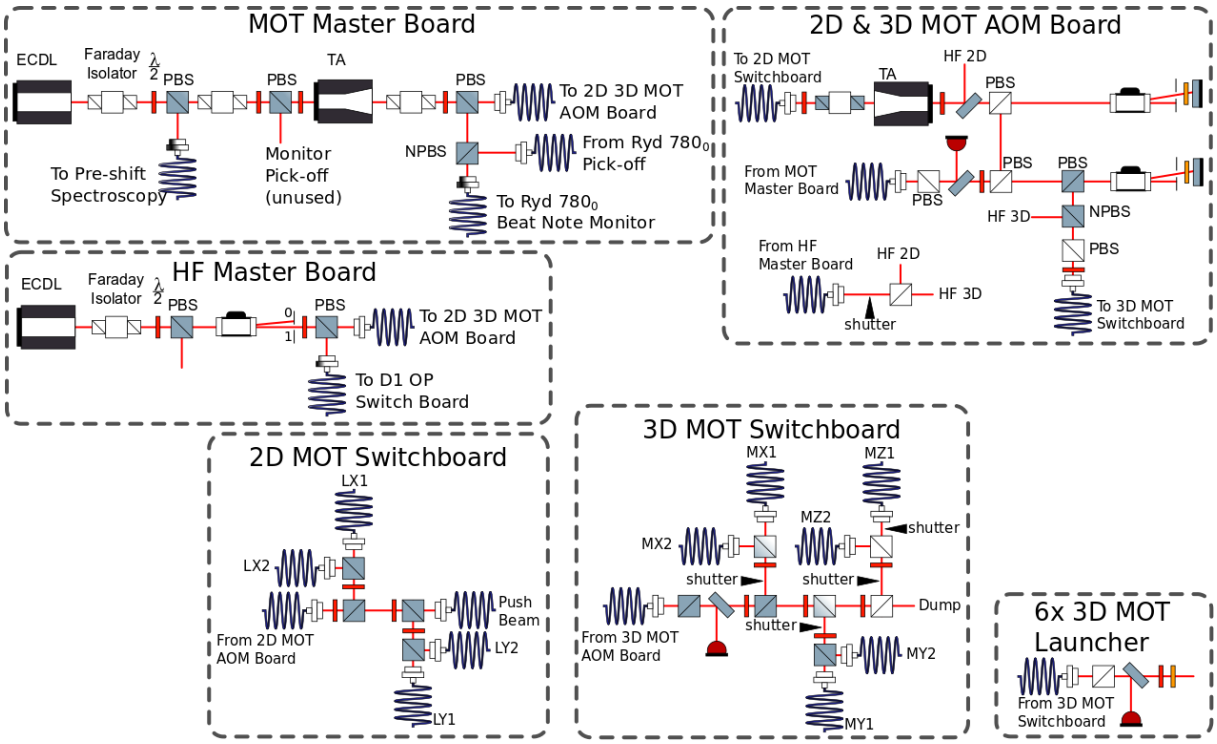

Figure 8.7: A functional diagram of the lasers required to generate the 2D- and 3D-MOTs. All lenses and beam steering have been omitted for clarity. Optical element symbols are from the ComponentLibrary package[85].

motors described in reference [84] are used to completely block the 3D-MOT beams from the optical pumping stage to the readout stage. The blow-away procedure is accomplished by having one of the MOT Z shutters open before the rest and turning on the MOT light with the AOM near resonant with the cycling transition. This provides a state selective unbalanced radiation pressure, and eject the $|0\rangle$ population from the trap.

8.0.3 Ground Raman Laser

The fast ground Raman laser [55] has not changed functionally during the upgrade, however it was condensed to take up less table space. A functional diagram is shown in Figure 8.8. The Raman laser is combined with the Rydberg $780_{0(1)}$ lasers on a switchboard. The Raman laser has a DC motor shutter to prevent leakage from affecting the qubit state.

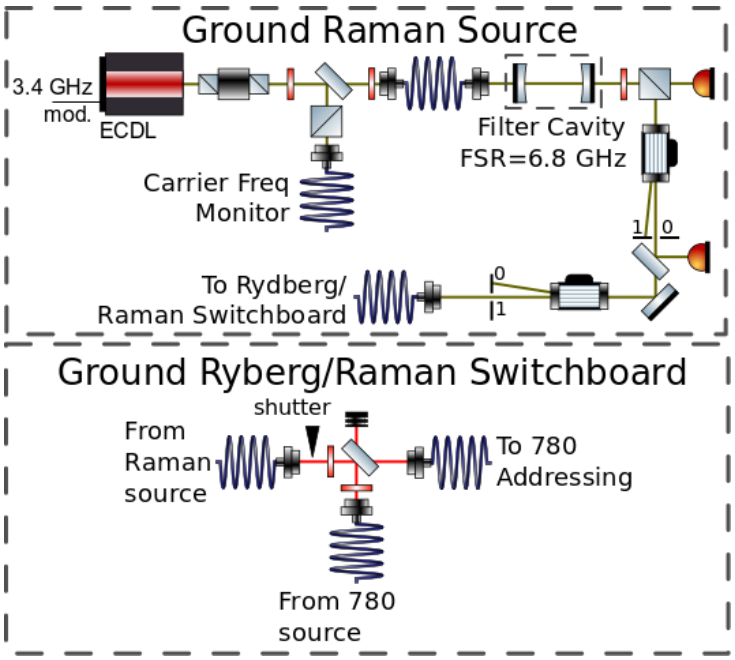

Figure 8.8: A functional diagram of the fast ground Raman laser used to rotate individual site qubit states. This laser is used for diagnostic experiments, since all ensemble protocols require state rotations to be through the Rydberg state to correctly limit the Hilbert space. All lenses and beam steering have been omitted for clarity. Optical element symbols are from the ComponentLibrary package[85].

8.0.4 Rydberg Lasers

A functional diagram of the Rydberg laser sources are shown in Figure 8.9.

The Rydberg lasers are all simultaneously locked to the same ULE cavity. This was actually the case for the "main apparatus", as the 780_1 was changed from a phase-lock due to performance issues in reference [25]. The 780 lasers are modulated at different frequencies and have orthogonal polarizations to decouple the PDH error signal generation from each other. The old homemade 780_0 grating based ECDL laser was replaced with a commercial Moglabs Interference Filter ECDL (IF-ECDL). The servo-loop is for this laser has been replaced with the Moglabs laser driver with some homemade modifications.

All Rydberg lasers servos have been modified so that the medium loop now includes a "PDH boost" circuit after the demodulation and low-pass filter, see Figure 8.10. The boost circuit includes a zero in the transfer function to counter the pole in the error signal at half the ULE cavity linewidth, $\nu \sim 5$ kHz $f_{zero} = \nu/2$. This addition has made the cavity locks significantly more robust, see Figure 8.12 which shows the cavity transmission.

8.0.5 Addressing Laser Systems

The 780 addressing laser system optics are combined with the co-propagating 1064(1038) nm FORT laser optics and the counter-propagating 780 atom fluorescence signal optics on a single 1/4" Stainless Steel breadboard. The optical train is shown in Figure 8.13. The optical train is functionally similar to the original design but the optical path length of the FORT train has been decreased from ~ 1.7 to ~ 0.57 m and the 780 Addressing train from ~ 2.4 to ~ 0.52 m. Due to the change to a small all-glass vacuum chamber, the NA of the collection optics have been increased from 0.35 to 0.4 while simultaneously decreasing the diameter of the optics from 120 mm to 25.4 mm. The PBS used in the old design to deflect the fluorescence from the addressing laser path to the EMCCD camera has been replaced with a custom beamsplitter with 70% s-polarized and $> 95\%$ p-polarized transmission coefficients, see Figure 8.14. Therefore the transmission for unpolarized light

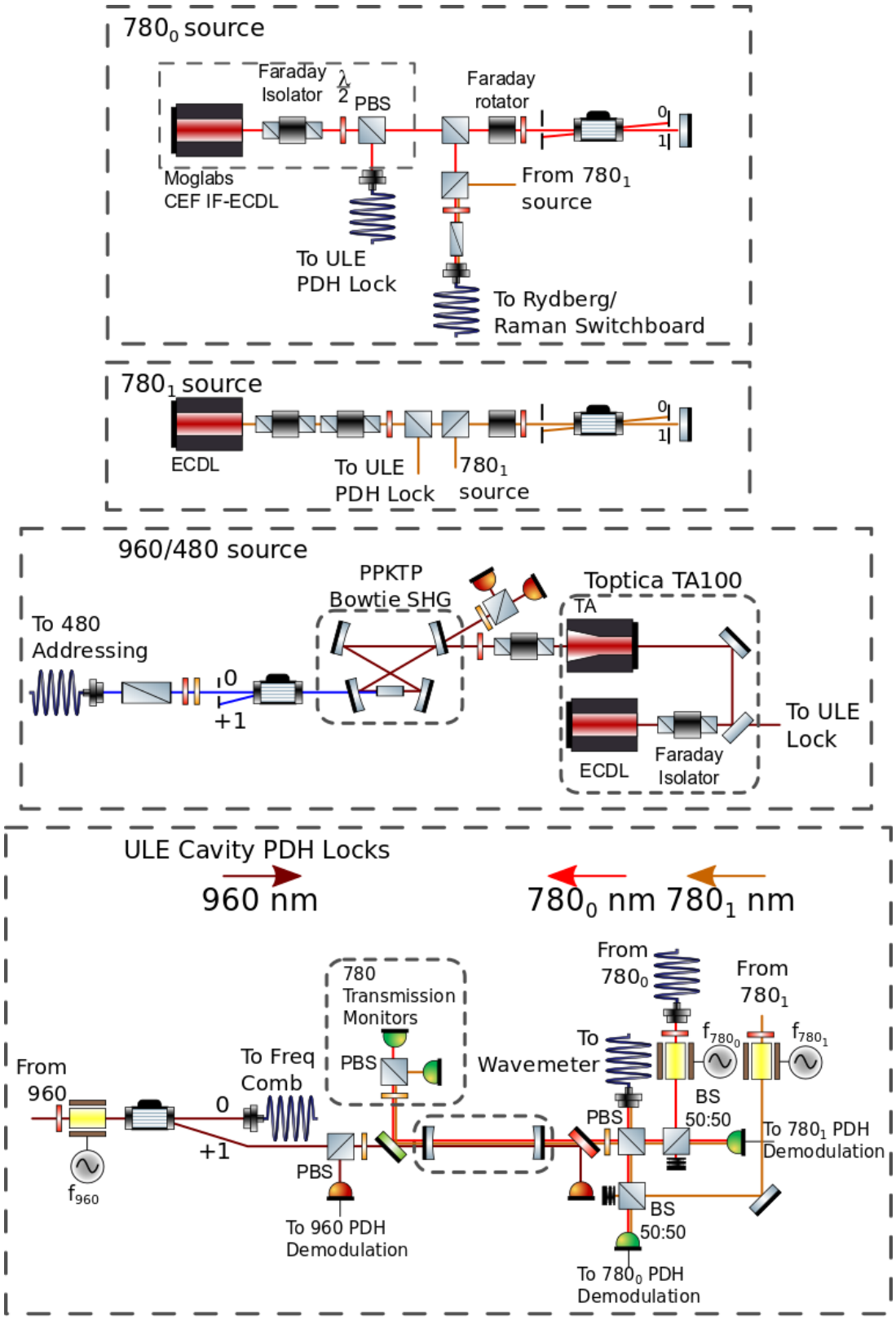

Figure 8.9: A functional diagram of the Rydberg laser sources. Note that all Rydberg lasers are now locked simultaneously to the ULE reference cavity. All lenses and beam steering have been omitted for clarity. Optical element symbols are from the ComponentLibrary package[85].

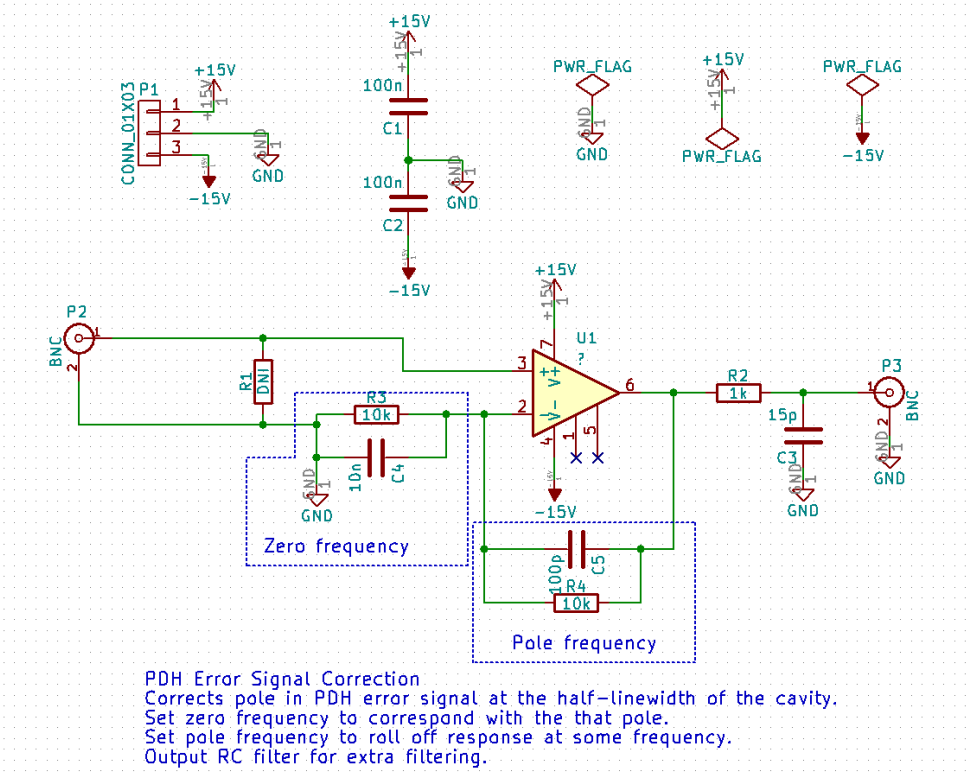

Figure 8.10: PDH boost circuit.

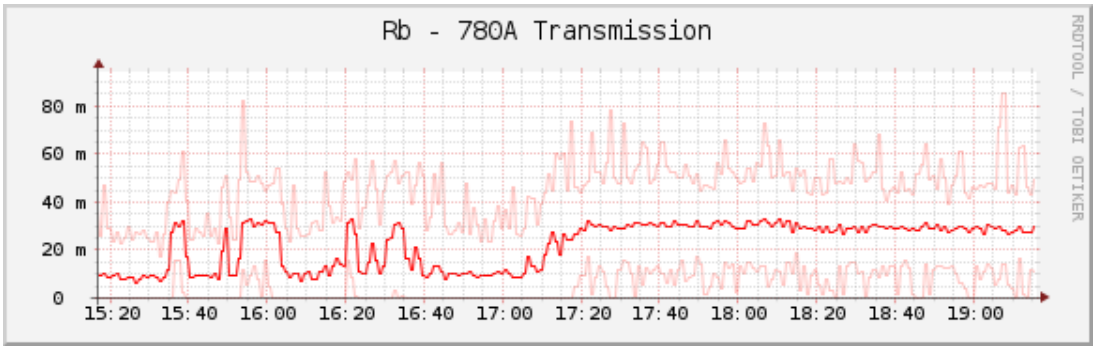

Figure 8.11: ULE cavity transmission for 780_0 laser. The laser is locked when the transmission is high and unlocked when it is low. The PDH boost circuit was added around 17:00, compare to the cavity lock stability before. The laser will stay locked for $>$ 24 hours regularly under typical lab conditions.

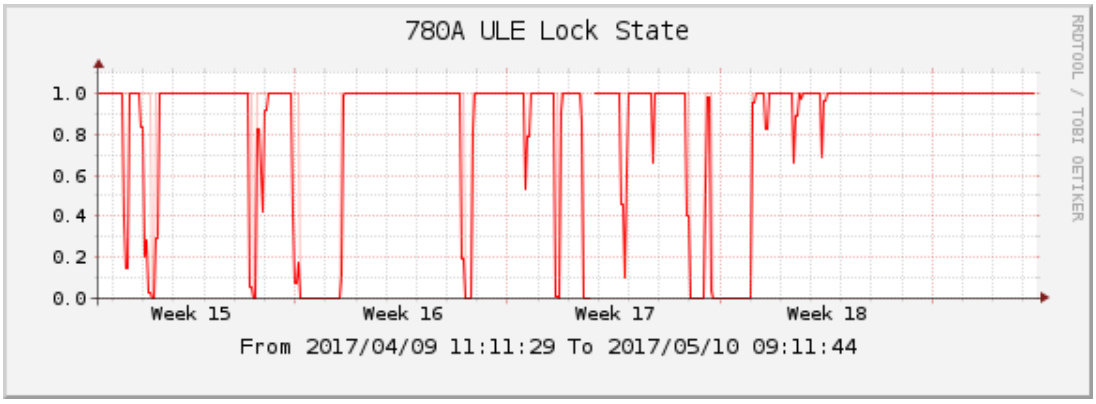

Figure 8.12: The binary lock state of the 780_0 laser to the ULE cavity, measured by comparison of the 780_0 cavity transmission to a threshold. The laser is locked when the lock state is high and unlocked when it is low. During the month time period shown, the laser was mostly left alone and no special precautions were taken to either maintain or relock the laser. The most likely cause for the laser unlocking is the piezo voltage drifting out of range of the servo.

is 82% increasing the collection efficiency by 164%.

Closed-Loop Picomotor Alignment

In order to maintain high-fidelity operation, the relative alignment of the 780 and 480 nm addressing lasers with respect to the atoms must be maintained. The 2-photon Rabi frequency and the AC stark shift spatial gradients are minimized when the addressing lasers are centered on the atoms. The alignment is most sensitive to micron scale drifts of addressing laser systems in the plane transverse to the optical axis, since the Rayleigh length of the lasers is much longer than the beam waist at the focal plane. On long timescales the addressing laser systems drift from the aligned condition due to thermal cycling and mechanical drifts, and must be re-aligned in the transverse plane on a regular basis.

To control the transverse position of the 780 and 480 lasers in the plane of the atoms, we have implemented an automated closed-loop actuator system that translates a lens in the XY plane. The actuators are linear piezo inertial actuators where a screw is driven by piezo actuators attached to opposite sides of a split nut that the screw passes through.

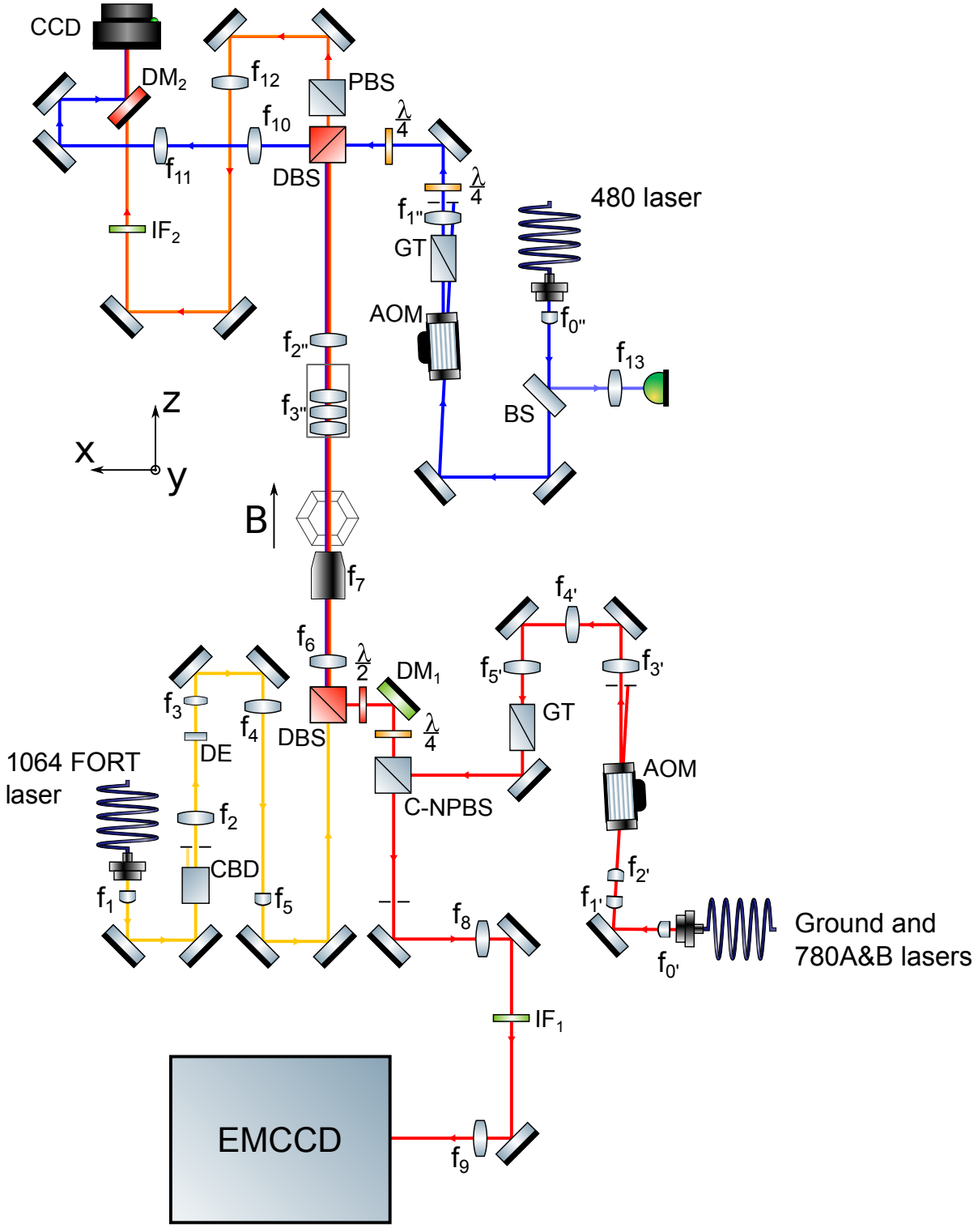

Figure 8.13: The optical train for the new Addressing, FORT, and camera optical trains. Optical element symbols are from the ComponentLibrary package[85].

Name	Parameters	Part No.
f1	f=6.24 mm	C110TME-1064
CBD	Calcite Beam Displacer	
f2	f=60 mm	AC254-060-C
DE	5 Spot Diffraction Element	
f3	f=19 mm	AC127-019-C
f4	f=80 mm	AC254-080-B
f5	f=8 mm	C240TME-B
DBS	Dichroic Beamsplitter	
f6	f=200 mm	AC254-200-B
f7	f=23.125 mm	JenOptik Custom 0.4 NA

Table 8.1: Major optical element from the FORT optical train. Names are referenced to the names given in Figure 8.13.

Name	Parameters	Part No.
f0'	f=4.0 mm	PAFA-X-B
f1'	f= mm	
f2'	f= mm	
AOM	Acusto-Optical Modulator (+160MHz)	
f3'	f=60 mm	LA1134-B
f4'	f=35 mm	LA1027-B
f5'	f=50 mm	AC254-050-B
GT	Glan-Taylor Polarizer	
$\lambda/4$	quarter wave retarder @ 780 nm	
DM1	Dichroic Mirror	
$\lambda/2$	half wave retarder @ 780 nm	
DBS	Dichroic Beamsplitter	
C-NPBS	Custom Non-Polarizing Beamsplitter	
DBS	Dichroic Beamsplitter	
f6	f=200 mm	AC254-200-B
f7	f=23.125 mm	JenOptik Custom 0.4 NA

Table 8.2: Major optical element from the 780 Addressing optical train. Names are referenced to the names given in Figure 8.13.

Name	Parameters	Part No.
f0”	f=8 mm	C240TME-A
BS	Beam Sampler	
AOM	Acusto-Optical Modulator (-160MHz)	
GT	Glan-Taylor Polarizer	
f1”	f=50 mm	PAC15AR.15
$\lambda/4$	quarter wave retarder @ 488 nm	
$\lambda/4$	quarter wave retarder @ 488 nm	
DBS	Dichroic Beamsplitter	
f2”	f=400 mm	JML DB14215
f3”	f=110 mm	Custom Triplet

Table 8.3: Major optical element from the 480 Addressing optical train. Names are referenced to the names given in Figure 8.13.

Name	Parameters	Part No.
f7	f=23.125 mm	JenOptik Custom 0.4 NA
f6	f=200 mm	AC254-200-B
DBS	Dichroic Beamsplitter	
$\lambda/2$	half wave retarder @ 780 nm	
DM1	Dichroic Mirror	
$\lambda/4$	quarter wave retarder @ 780 nm	
C-NPBS	Custom Non-Polarizing Beamsplitter	
f8	f=150 mm	47-380
IF	Interference Filter (780 nm Bandpass)	
f9	f=100 mm	45-806
EMCCD	Electron Multiplying CCD Camera	Andor

Table 8.4: Major optical element from the EMCCD camera optical train. Names are referenced to the names given in Figure 8.13.

Name	Parameters	Part No.
f10	f=TDB mm	TBD
f11	f=TBD mm	TBD
DM2	Dichroic Mirror	
PBS	Polarizing Beamsplitter	
f12	f=100 mm	45-806
IF	Interference Filter (780 nm Bandpass)	
CCD	CCD Camera	Point Grey

Table 8.5: Major optical element from the Automatic Alignment System optical train. Names are referenced to the names given in Figure 8.13.

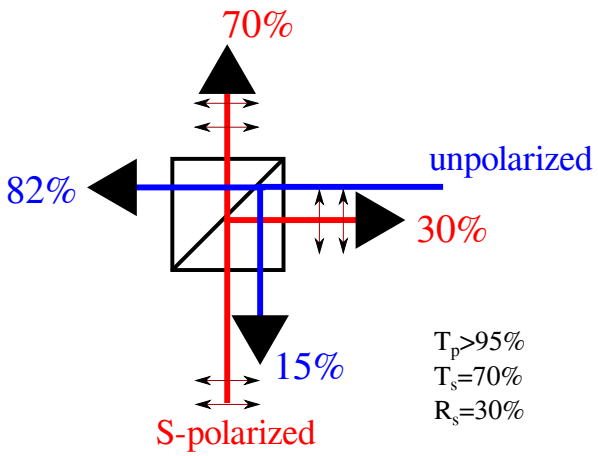

Figure 8.14: Diagram of the custom beamsplitter that picks off the back-propagating fluorescence signal to the EMCCD camera. The blue path represents the atomic fluorescence signal back propagating, while the red path shows the 780 addressing laser where the refelcted light is going towards the atoms and the transmitted is blocked.

This means that the piezo is only on when moving the actuator. When the unit is not moving it has a similar level of stability to a typical screw actuator system. This removes any issue of high frequency oscillations from improperly compensated traditional piezo motion stages. The closed-loop Picomotor system is described in detail in Appendix C.

Automated alternatives to Picomotors include piezo actuators and stepper motors. Piezo actuators have a limited range of motion which is insufficient for the application, while stepper motors vibrate in the holding position enough to disturb our measurements. Picomotors also have the convenient characteristic that they only require power when under motion.

Automatic Alignment System

The Automatic Alignment System (AAS) uses an off-the-shelf CCD camera to provide long-term relative stabilization of the FORT, 780, and 480 addressing systems, as shown in Figure 8.13, to maximize the time between scans based on an atomic signal. Alignment scans for the 780 addressing laser are performed on single atoms by performing a ground state rotation laser pulse at some position $\hat{R}(\theta, x, y)$, where $\theta < \pi$ and $|\langle 1|\hat{R}(\theta, 0, 0)|0\rangle|^2 \sim$

0.7, to partially rotate the internal state of the atom. As the laser is moved across the atoms during the scan the Rabi frequency and detuning (due to AC Stark shits) degrade the state transfer probability. The 480 addressing laser alignment is performed by a similar procedure using Rydberg excitation and therefore depends on the correct alignment of the 780 addressing laser. From the resulting data, the position of the atom cloud is assumed from the center of a Gaussian fit to the data, an example data set is shown in Figure 8.15. The alignment scan in Figure 8.15 has 12 data points, 70 measurements per position, a cycle time of 400 ms, and an assumed loading rate of 25%. Therefore without overhead it should take 23 minutes to complete (the scan actually took 30 minutes). In the older apparatus, a 780 addressing alignment was required once a week with a 480 addressing alignment required daily, assuming no environmental temperature swings. In the old apparatus the cycle time was > 600 ms, so the alignment maintenance could add over 9 hours a week of alignment maintenance or 22% of a 40 hour work week.[2] Decreasing the maintenance overhead by performing measurements with a camera instead could increase the effective uptime of the experiment significantly.

The FORT and 780 Addressing lasers are re-imaged onto a Point Grey BFLY-PGE-12A2M-CS CCD camera after passing through the vacuum chamber. The magnification for the 780 and 1064 imaging is determined by measuring the separation between trap sites, which is a known quantity and is not affected by a reduction in image quality. The relative positions of the FORT and 780 Addressing laser are found on the camera by taking the average position from 2D fits to many images. The FORT and 780 Addressing lasers are toggled out of phase with each other at approximately 50 Hz so that the camera images are interleaved between the two lasers at high speed. This reduces the susceptibility of the measurement to common mode vibrations. The 480 Addressing laser is imaged onto the camera by taking the leakage through the dichroic beamsplitter and combining it with the FORT and 780 path via a dichroic mirror reflective at 480 nm. The EMCCD camera

[2] Or equivalently 7.1% of a work week assuming an ideal graduate student

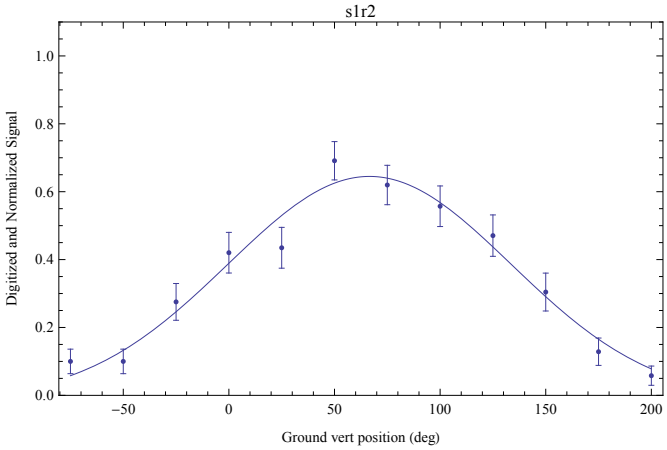

	Estimate	Standard Error	t-Statistic	P-Value
Private`bg	−0.0130992	0.0854715	−0.153258	0.88199
Private`amp	0.658101	0.0779916	8.43811	0.0000296913
Private`center	66.5709	3.46951	19.1874	5.64254×10^{-8}
Private`FWHM	157.984	23.939	6.59945	0.000169483

Figure 8.15: An example 780 addressing laser alignment along the vertical axis. The ground state rotation laser pulse is set to be approximately 70% state rotation when aligned. The state transfer probability degrades as the addressing laser moves away from the center of the atom cloud. The horizontal axis is in degrees of the Picomotor actuator screw, the calibration from degrees to position in the plane of the atoms is approximately 0.113 μm/deg. The vertical beam waist of the 780 Addressing laser is 10.2 μm.

is also capable of imaging the 480 nm laser, from leakage through the 780 nm notch filter, and could be used as a second camera to remove common mode fluctuations. Finally if necessary, there is also an additional dichroic mirror built into the 780 Addressing path that transmits 480 nm light which could be imaged onto a third camera if necessary.

Chapter 9

Outlook

In this thesis critical initial demonstrations of neutral atom ensemble qubits with interactions mediated by Rydberg blockade were presented. We presented observations of the $\sqrt{N}$ collective Rabi frequency enhancement (Section 2.2), generation of $\mathcal{N} = 1$ and 2 Fock states with very sub-Poissonian Mandel parameters of $Q = -0.62(3)$ and $-0.50(5)$ respectively (Section 2.3) We also characterized the output $\mathcal{N} = 1$ Fock state and the $\mathcal{W}$-state character of the resulting ensemble state using two separate measurements of total angular momentum as an entanglement witness (Sections 3.1 and 3.2). These two method give k-partite entanglement limits of $k/N = 0.82(6)$ and $k/N = 1.0(1)$. Ensemble $\mathcal{W}$-state excitation coherence times of 2.6(3) ms were presented, which give a coherence to gate time ratio of ~ 2600. The limiting factor in the ensemble coherence time appears to be collisional dephasing (Section 3.1). We then moved on to the first demonstration of Rydberg blockade between two ensemble qubits (Section 4.2.1. An ensemble-ensemble blockade fidelity of 0.89(1) is shown and a fidelity consistent with 1.0 when postselected on a control ensemble excitation.

Based on the observed $\mathcal{N} = 1$ amplitude discrepancy between the experiment and the current theory, we also propose two mechanisms, one at long-range ($R > R_B$) and one at short-range ($R < R_s$), for the creation of doubly excited Rydberg states (Chapter 5).

The doubly excited state undergoes a fast molecular evolution to states that are dark to the Rydberg excitation lasers. These molecules remain in the area of the ensemble and continue to suppress subsequent excitations, but are not de-excited and as such are not detectable by our experiment. This results in an unanticipated postselection that aids us in observing "clean" ensemble Rydberg dynamics at a lower amplitude than expected, since any Rydberg blockade leakage destroys itself and results in the apparent observation of the $|\bar{0}\rangle$ state.

We then discussed the theoretical models used in these experiments (Chapter 6), as well as camera signals models for interpreting various atom number measurement experiments (Chapter 7).

Finally, we discussed the improved experimental apparatus that has been built to replace the apparatus that took the data in this thesis (Chapter 8). The apparatus is physically smaller, has a shorter duty cycle, a shorter single-atom camera exposure time, and higher retention. All of which should combine to reduce downtime, improve stability, and reduce the amount of data that is necessary to achieve the same statistical uncertainty.

The major experimental thrust of the new apparatus will be to reduce the short-range blockade leakage proposed in Chapter 5. To do this a 1D 770 nm crossed dipole blue-detuned lattice is planned, which will impose a minimum spacing along the axial dimension of the existing pencil shaped red-detuned FORT sites. The planned opening angle for the crossed dipole will impose a minimum spacing of 1.5 μm. If an improvement in the ensemble $\mathcal{F}_1$ procedure amplitude is observed with this minimum spacing, we will have confirmed the existence of the short-range molecular excitation channels. We could then implement additional plans to mitigate the effect of the interaction. If the source of the amplitude discrepancy can be minimized such that even the predicted 80% $\mathcal{F}_1$ amplitude is achieved, the first demonstration of ensemble-ensemble entanglement via Rydberg blockade can be performed with a straightforward parity oscillation measurement. A demonstration of an entangling gate for ensemble qubits would fulfill the last

of the requirements to realize Rydberg mediated ensemble qubits as a viable quantum information platform.

In the new apparatus, our ability to detect single excitations has improved drastically due to the increased NA of the imaging lens ($0.3 \rightarrow 0.45$), the installation of a custom beamsplitter cube designed to transmit 82% of the scattered photons during the imaging stage, and the reduction of the EMCCD camera magnification from a 3x3 to a 2x2 ROI which cuts down the background while maintaining an equivalent photon signal. The improved signal to noise has allowed us to reduce the total number of scattering events necessary to achieve the same fidelity of readout. This has put us in range of being able to implement a non-destructive state-selective readout procedure (ND-SSRO), see Section 7.3. A reliable ND-SSRO has the promise to greatly improve the data collection rate, since multiple experiments can be performed following the FORT loading phase which accounts for about half of the total duty cycle. Additionally with the current blow-away infidelity of 0.2%/atom, $\mathcal{N} = 1$ Fock states in ensemble of up to about 500 atoms can now be detected with unity SNR. This should allow us to test single photon emitters and receivers with no cavity enhancement in the near future[77]. The ND-SSRO procedure has not yet been tested in an ensemble, but it may be able to detect $\mathcal{N} = 1$ states at a similar or better level as well.

Appendix A

Blockade Shift Calculations

The Rydberg Blockade shift arises from the large dipole-dipole interactions between Rydberg-Rydberg molecular states. In general the magnitude of the van der Waals effect will scale as R^{-6}, where R is the interatomic distance. However, in the case of a second (or more) nearly-degenerate, dipole-allowed Rydberg-Rydberg molecular state(s), $2E(|nj\rangle) \sim E(|n_1 j_1\rangle) + E(|n_2 j_2\rangle)$, Förster coupling between the molecular states results in an enhanced energy shift in the doubly excited $|nj\rangle + |nj\rangle$ state that scales as R^{-3} at close distances.

The dipole-dipole operator V_{dd}, where the internuclear separation axis is along z, is:

$$V_{dd}(R) = -\frac{\sqrt{6}e^2}{R^3} \sum_p C^{20}_{1p1\bar{p}} a_p b_{\bar{p}}, \tag{A.1}$$

where $a_p(b_p)$ is the position of atom $a(b)$'s electron [52].

If we assume $j - j_1 = 1$, then the dipole-dipole molecular coupling matrix element is:

$$\begin{aligned}
\langle \psi' | V_{dd} | \psi \rangle &= {}_a\langle n_1 l_1 j_1 m_{j1} |_b \langle n_2 l_2 j_2 m_{j2} | V_{dd} | nljm \rangle \\
&= -\frac{\sqrt{6}e^2}{R^3} \sum_p C^{20}_{1p1\bar{p}} \left({}_a\langle n_1 j_1 m_{j1} | a_p | njm_j \rangle_a \right) \left({}_b\langle n_2 j_2 m_{j2} | b_{\bar{p}} | njm_j \rangle_b \right) \\
&\equiv \frac{C_3}{R^3},
\end{aligned} \tag{A.2}$$

where C_3 is the electric-dipole coupling coefficient between the two molecular Rydberg states. Using the reduced and Radial matrix element definitions from reference [52], and assuming the stretched state $m_1 = j_1 = l_1 + \frac{1}{2}$, $l_1 = l+1$, $m_2 = j_2 = l_2 + \frac{1}{2}$, and $l_2 = l-1$, we can write Equation A.1 as:

$$C_3 = -\sqrt{\frac{6(l+1)(2l+1)}{l(2l+3)}}\mathcal{R}_{nl}^{n_1(l+1)}\mathcal{R}_{nl}^{n_2(l-1)} \tag{A.3}$$

Under the special condition where $j = l + \frac{1}{2}$ this simplifies to:

$$V_{dd}(R) = -\sqrt{2}\frac{e^2}{R^3}\langle n_1\ell_1||r||n\ell\rangle\langle n_2\ell_2||r||n\ell\rangle \tag{A.4}$$

Therefore the Förster coupling between the two molecular states is $V = C_3/R^3$ and the Hamiltonian is:

$$H_{dd} = \begin{pmatrix} 0 & V_1 & V_2 & \cdots \\ V_1 & \delta_1 & 0 & \\ V_2 & 0 & \delta_2 & \\ \vdots & & & \ddots \end{pmatrix}, \tag{A.5}$$

where δ_i is the Förster defect (molecular state energy difference) of the i^{th} molecular state.

In the limit of a single molecular state with a small Förster defect the dipole-dipole shift of the doubly excited state becomes:

$$U_{dd}(R) = \frac{\delta}{2}\left(1 - \sqrt{1 + \left(\frac{2C_3}{\delta R^3}\right)^2}\right). \tag{A.6}$$

In the limit $\delta R^{-3} \gg C_3$ there is weak coupling and we obtain the expected van der Waals behavior $U_{dd}(R) \approx C_3^2/\delta R^6 \equiv C_6/R^6$. However, for $\delta R^{-3} \ll C_3$ the interaction is now $U_{dd}(R) \approx \frac{\delta}{2} - \frac{C_3}{R^3}$. The effect of a Förster resonance, $\delta \sim 0$, is to increase the critical distance $R_c = C_3^{1/3}$ by a factor of $\delta^{-1/3}$ where the characteristic of the potential changes from R^{-3} to R^{-6}. Careful selection of Rydberg levels with Förster resonances in mind

can decrease the principle quantum number n required to realize a sufficient blockade strength.

A.1 $97D_{5/2}, m_j = 5/2$

The nearly degenerate molecular states which contribute the most to the blockade shift for the first term in Equation A.1 are:

$$97D_{5/2} + 97D_{5/2} \leftrightarrow 99P_{3/2} + 95F_{7/2} \tag{A.7}$$

and

$$97D_{5/2} + 97D_{5/2} \leftrightarrow 98P_{3/2} + 96F_{7/2}. \tag{A.8}$$

Using experimentally determined Rydberg energy defects[86], the Förster defects are $\delta_{(1,2)} = (150, 238)$ MHz respectively.

Since we are only exciting the stretched $|nD_{5/2}, m_j = 5/2\rangle$ state the only electric-dipole allowed fine-structure coupling is to the $|n_1P_{3/2}, m_j = 3/2\rangle + |n_1F_{7/2}, m_j = 7/2\rangle$ molecular state, which are both also stretched states. Therefore the dipole-dipole coupling term, C_3, term for each molecular state is:

$$\begin{aligned} C_3^{(1)} &= -\sqrt{2} \times 21.8 \text{ GHz} \cdot \mu\text{m}^3, \\ C_3^{(2)} &= -\sqrt{2} \times 61.2 \text{ GHz} \cdot \mu\text{m}^3. \end{aligned} \tag{A.9}$$

The $\sqrt{2}$ factor in front of the numerical C_3 terms accounts for the symmetry of the initial molecular state, which was not considered before. If a non-symmetric initial state is used, or if the molecular basis states count both the $nP + n'F$ and $n'F + nP$ states, then the $\sqrt{2}$ term should be dropped. A non-symmetric initial state between identical or different atom species can be used to decrease the Förster defect, δ, and generate stronger interactions between atoms[87].

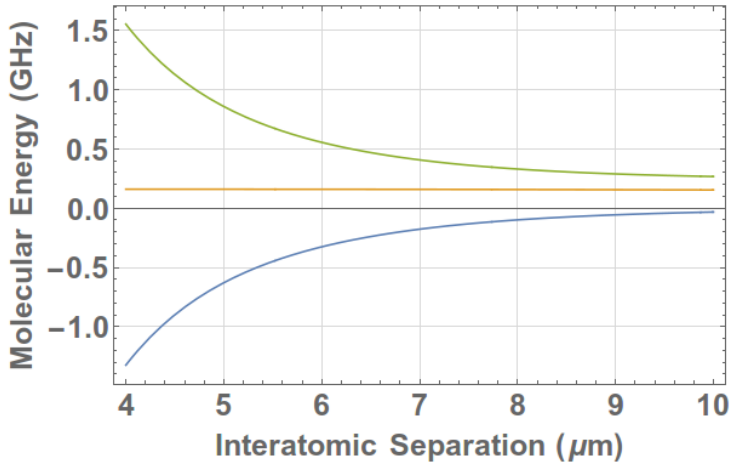

Figure A.1: A simple three molecular state approximation of the Rydberg-Rydberg interaction potentials accounts for most of the long-range interaction. The zero energy point is defined as the $97D + 97D$ disassociation energy limit. The blockading interaction is shown in blue.

We can then build the dipole-dipole interaction Hamiltonian:

$$H_{dd} = \begin{pmatrix} 0 & -\sqrt{2} \times 21.8 & -\sqrt{2} \times 61.2 \\ -\sqrt{2} \times 21.8 & 0.150 & 0 \\ -\sqrt{2} \times 61.2 & 0 & 0.238 \end{pmatrix}, \tag{A.10}$$

and solve for the eigenvalues and eigenvectors of the system. The result is shown in Figure A.1.

In order to observe molecular resonances, it is necessary to add in states that couple to the $nP + n'F$ states such as $n''D + n'''D$ among others.

Appendix B

Expected Background Blow-Away Leakage Rate

This appendix outlines the logic and assumptions behind the Ensemble-Ensemble Blockade background calculation, when cutting on a single atom signal in the control site.

We need data from at least 3 experiments to generate the background rate estimation, a data set with a control site pulse:

$$\hat{\mathcal{B}}(\theta) \equiv \hat{\pi}_1^{C1}\hat{\pi}_1^{T1}\hat{\theta}^{T0}_{\bar{N}_T}\hat{\pi}^{C0}_{\bar{N}_C}, \tag{B.1}$$

and a data set with everything the same except the A_1^C pulse removed:

$$\hat{\mathcal{B}}_{off}(\theta) \equiv \hat{\pi}_1^{C1}\hat{\pi}_1^{T1}\hat{\theta}^{T0}_{\bar{N}_T}, \tag{B.2}$$

and either a multi-atom readout or a single atom loading curve on the control site to obtain the control mean atom number $\bar{N}_C$. The target site atom number, $\bar{N}_T$, can be obtained in a similar way using the pulse sequence in B.2. The blow-away leakage probabilities $\rho_{BA}^{(C,T)}$ can be obtained from the first points in the unblockaded collective Rabi oscillation curves.

Due to the blowaway leakage (on the order of 2-0.1%/atom) a certain false positive rate, ϵ, will occur when cutting on the control site $|F = 1\rangle$ population. To obtain ϵ we need the blow-away leakage rate per atom $\rho_{BA}^{(C)}$ in the control site and the atom number in the control site.

$$\epsilon = \frac{\bar{N}_C \rho_{BA}^{(C)}}{(n_C/n)} = \frac{\text{probability of BA leakage event}}{\text{probability to detect an atom in the control}} \tag{B.3}$$

where n is the total number of shots taken and n_C is the number of shots that pass the control cut. Since the control success rate change with θ_T, ϵ will also depends on θ_T.

When a control event is detected, it is assumed to be either due to a successful Rydberg transfer from $|F = 2\rangle$ to $|F = 1\rangle$, or an erroneous cut. In the first case, under the assumption of perfect blockade, the target can show an atom due to the blowaway leakage in the target site, which occurs at a rate:

$$\bar{N}_T \rho_{BA}^{(T)}. \tag{B.4}$$

In the second case the result is the normal unblockaded evolution of the target site $P_T(\theta_T)$. Combining the two cases with their likelihoods we obtain the background rate equation under the assumption of perfect blockade:

$$P_{bkg}(1_T|1_C) = \epsilon(\theta_T) P_T(\theta_T) + [1 - \epsilon(\theta_T)]\, \bar{N}_T \rho_{BA}^{(T)} \tag{B.5}$$

Appendix C

Closed-Loop Picomotor Alignment System

The actuators are linear piezo inertial actuators where a screw is driven by piezo actuators attached to opposite sides of a split nut that the screw passes through, see Figure C.1. The piezo actuators move in opposite directions slow enough to not slip and turn the screw, the piezo then resets position fast enough to slip and not reverse the screw motion.

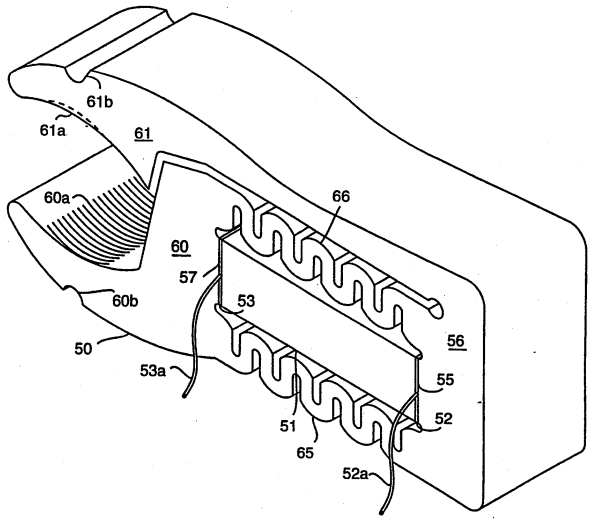

Figure C.1: Diagram of the piezo actuated split nut mechanics that turn the screw.[88]

Commercial closed-loop Picomotor systems are available, however not in the form fac-

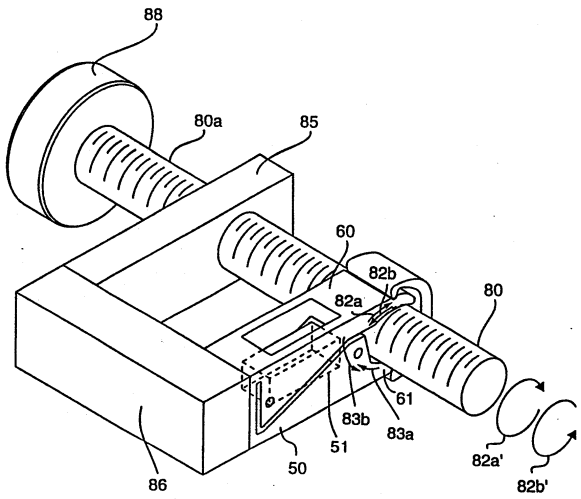

Figure C.2: Diagram of the split nut turning the screw.[88]

tor required to interface with the commercially available 30 mm cage mount XY translator used to translate the alignment lens. Because of the mechanical restriction, and the increased cost, the choice was made to instead develop a closed loop system in house based on a high sensitivity Avago HEDR-55L2-BH07 optical quadrature encoders. The finished assembly and some helpful images can be found in Figure C.3. Most commercial cage mounted XY translators are either not easy to deconstruct or have mechanics that are not kinematically sound when combined with the round screw tip on the Picomotor actuator. The Qoptiq G065070000 XY translator is designed with a round tipped screw actuator and with a custom M10x0.5 mm to 1/4"-40 thread adapter the tiny Picomotor shaft can screw directly into the translator after removing the stock actuator and bushing. The stock springs (0.667 N/mm) in the actuator need to be replaced with weaker (0.47 N/mm) springs, which we purchase from Lee Spring, PN: LC 014AA 08S316. Disassembling of the translator will remove the dry lubricant on the translator. I have had good luck with spraying a bottle of PTFE dry lubricant into a beaker then applying the lubricant to the contact points with a cotton swab before reassembly. Because of excessive seizing on one of the devices, I did successfully use an oil based lubricant to improve performance.

The thumb knob on the actuator needs to be removed from the shaft so a custom

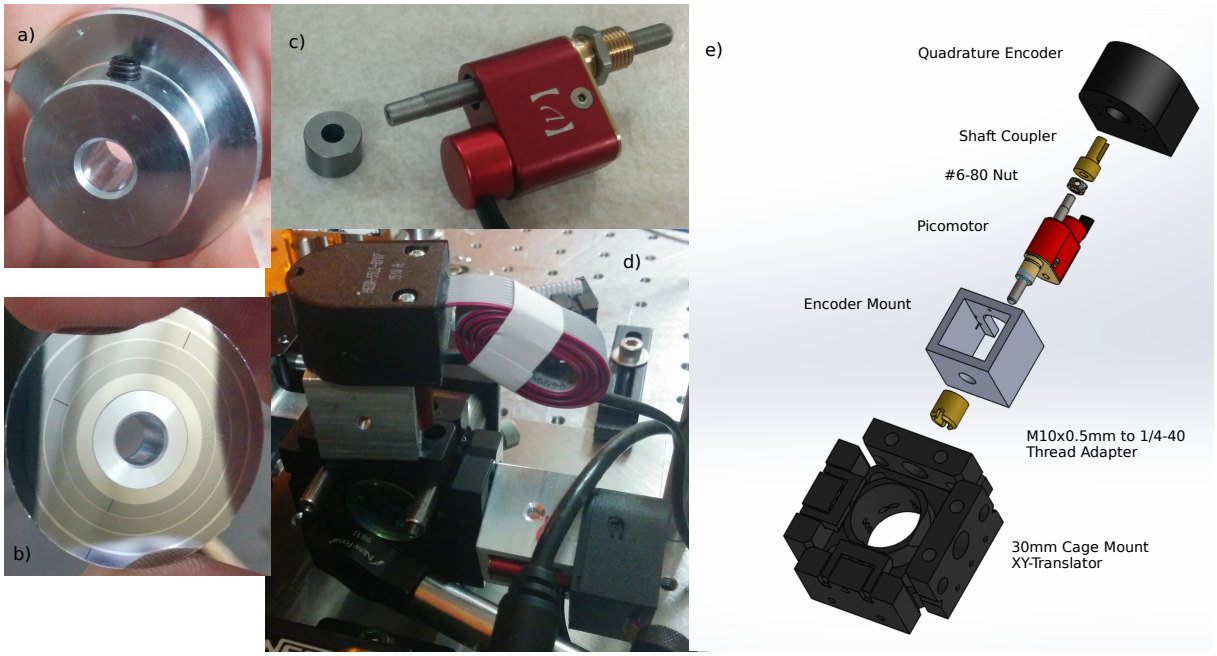

Figure C.3: The custom closed-loop Picomotor mechanics. Do NOT disassemble the encoder other than removing the lid. The markings on the wheel are very easy to damage so leave it in the encoder housing. a) Front and b) back side of the encoder wheel. c) Newport tiny Picomotor 8354 with thumb knob removed. d) An assembled XY translation stage installed in the 780 addressing laser system. e) An exploded view of the components required. The XY translator can be replaced with any appropriate kinematic mount by replacing or removing the thread adapter.

shaft coupler and nut can be mounted on the end of the screw. To remove the knob, use a #6-80 nut on the screw to tighten it against the shank to prevent rotational motion, then put the knob in a vise and twist it to break the Loctite seal. Excessive pressure from the #6-80 nut or torque on the screw when breaking the seal can damage the device, so use caution.[1] The nut and shaft coupler are then attached to the back end of the screw and tightened to prevent loosening. The actuator is then screwed onto the translator with the thread adapter, using a custom encoder mount machined from square stock as a "washer". Excessive tightening of the Picomotor actuator can cause the Picomotor to seize or otherwise malfunction, sometimes permanently damaging it, so resist the temptation to over-tighten. Do not remove the screw from the drive mechanism, because the fine

[1]Based on conversations with the vendor it may be safer to use a solvent, but I have not had the opportunity to try yet.

pitch threads are very fragile. Remove the lid of the encoder, being careful to not mar the the encoder wheel which is also easily damaged.[2] Screw the lid onto the encoder mount.

At this time you should verify that you have the full range of motion expected, because after attaching the encoder you will lose the ability to manually move the actuator screw.

When ready to proceed, insert a hex key into the side of the encoder through a hole used to tighten the M3 set-screw, located on the encoder wheel, on the shaft coupler. Remove the set-screw from the hole and apply Loctite 222MS to the threads of the set-screw to prevent loosening. Reinsert the set-screw into the encoder wheel, leaving the hex key protruding from the side. Align the axis of the shaft coupler to match the set-screw position. Snap the back onto the encoder body, then tighten the set-screw onto the shaft coupler until the shaft can just barely slide axially on the encoder wheel while the set-screw is in the slot. Since the screw will slide in and out in the course of motion it is necessary to having a sliding mate, and necessary to use Loctite to prevent the set-screw from backing its way out of the hole with no pressure on the threads.

The encoder ribbon cable is then attached to a device which can read the encoder state transitions and record the current position. Since the quadrature encoder can only report direction of motion i.e. ± 1 step it is necessary to use a device that can constantly monitor the quadrature encoder signals and can read the values at a rate faster than the states can change for the application. The initial iteration used a Raspberry Pi Single Board Computer (SBC) to monitor the encoder state, however it was not able to read the encoder state fast enough and occasionally missed events on the 780 addressing horizontal channel. Switching to a dedicated decoder IC (Avago HCTL-2032-SC) and a custom Ethernet-capable Arduino Mega 2560 clone (MCU) improved the performance. Code for the control server can be found at reference [89]. Arduino firmware for the decoder chip can be found at reference [90]. The final control loop design can be seen in Figure C.4. It should be noted that in the current configuration positive motion is

[2] Basically just don't touch anything. Ever.

unscrewing the alignment screw so it always steps in the negative direction.

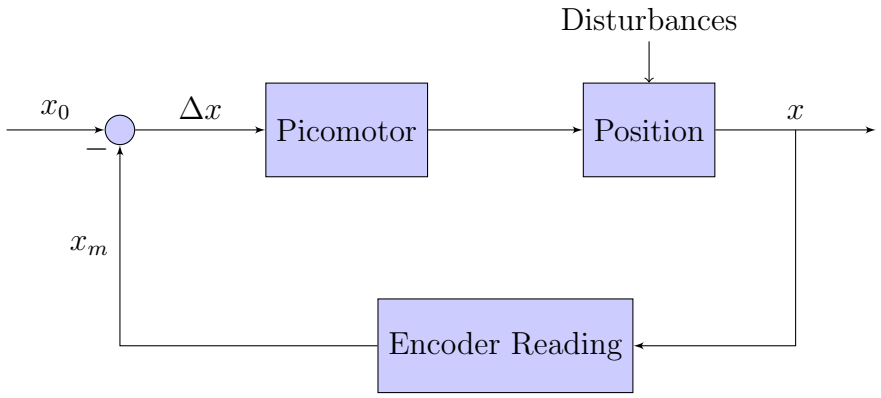

Figure C.4: Control loop diagram for an axis of the closed loop Picomotor system. The ideal screw angle set-point is x_0. On a change of the set-point x_0 a loop is run where the Picomotor movement is set to be 70-80% of the ideal movement to correct the error so the system behaves as an over-damped system and only approaches the set-point from one side, where the screw is pushing to prevent backlash errors. Since the screw position is long-term stable there is no need to run the control loop if there is no change to the set-point.

A diagram showing the specific implementation of the Picomotor control system is shown in Figure C.6. A ZeroMQ TCP server listens for SCPI style commands to move the motor positions. The server handles the low-level telnet interface to the Newport 8742 Picomotor controller as well as reading the screw angle from the MCU monitoring the encoder. The server queues commands so that all commands to the controller are blocking commands, instead of the default where queries can be made while an instruction is in process. The server implements a one-sided "Zeno's Arrow" approach to the set-point, where the movement is 70-90% of the ideal movement and iterated, minimizing overshoot and backlash errors. If the set-point requires counter-clockwise motion to the approach, the set-point is overshot and approached from the clockwise direction. Since the screw position is long-term stable, there is no need to run the control loop if there is no change to the set-point.

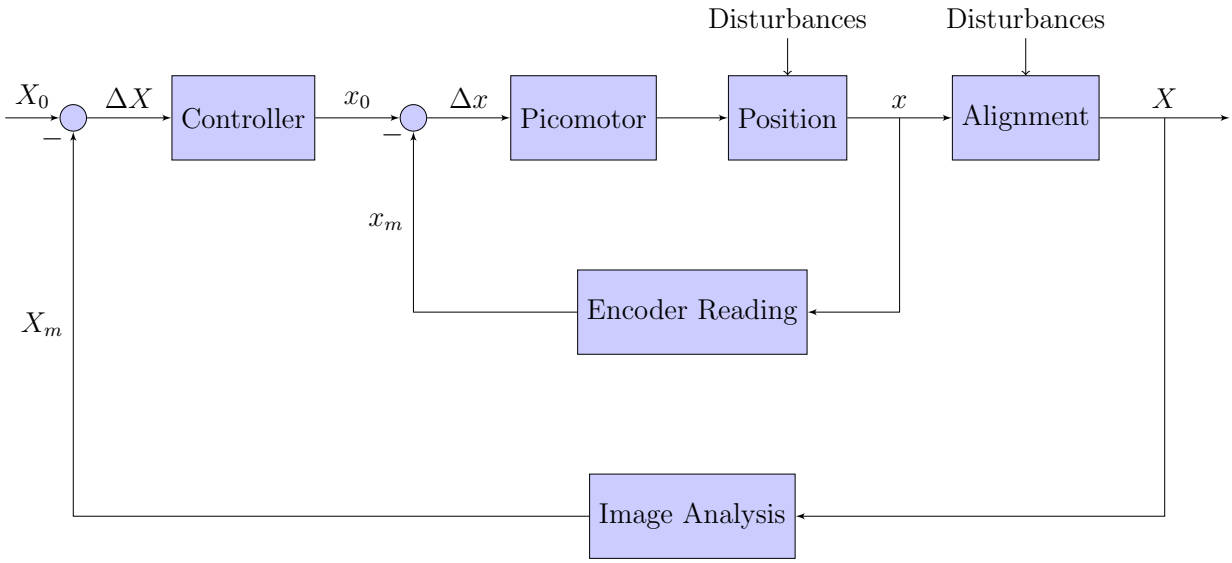

Figure C.5: Control loop diagram for the Automatic Alignment System. An additional feedback loop is added where the lasers are re-imaged onto a CCD camera and the relative positions of the lasers, X_m, are recorded via an analysis script. The set-point for the outer loop, X_0, sets the screw position of the Picomotor loop. X_0 is set to maintain the relative beam separation of the lasers in question after a successful alignment scan to the atoms.

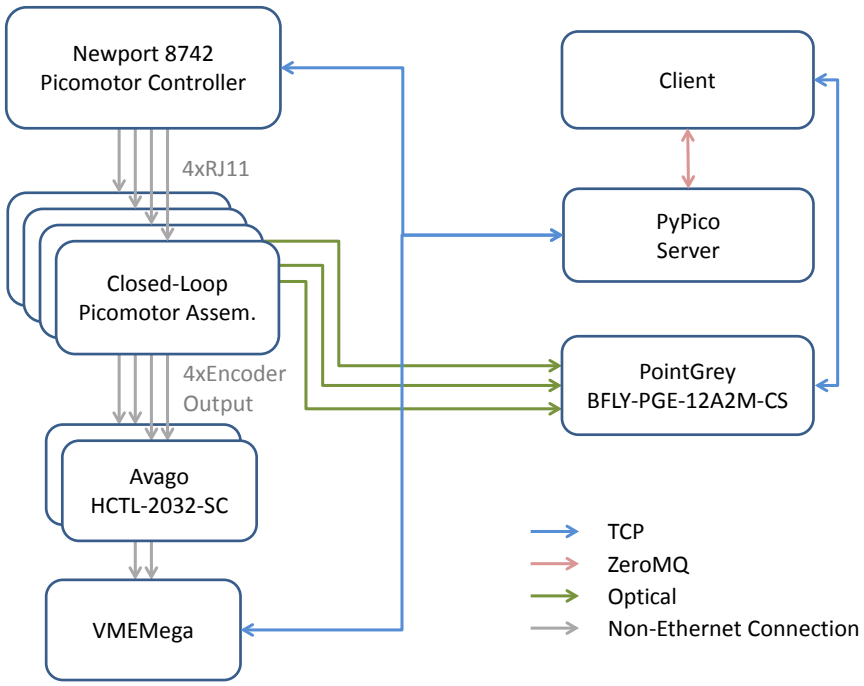

Figure C.6: Specific implementation of the custom closed-loop Picomotor positioner and the Automatic Alignment System. Blue connections are made via TCP/IP, red connections are ZeroMQ REQ/REP sockets, gray connections are non-Ethernet based electrical connections, and green connections represent the lasers which are imaged on the Point Grey CCD camera. Each Avago HCTL-2031-SC decoder IC manages 2 encoder channels. The VMEMega is a custom Arduino Mega 2560 MCU with built-in Ethernet interface which fits into a 3U Eurocard Subrack chassis with a VME J1 backplane. The VME backplane is used as a simple mechanical and electrical distribution network and does not implement the VME protocols. The Avago decoder ICs are installed in a custom 3U Eurocard daughterboard with a form factor that matches the standard Arduino Mega daughtercard pinout. The LAN topology is ignored.

Appendix D

Coil Driver

The coil driver project was a joint undergraduate project by Erik Meyers that I supervised. Sydney Lybert also deserves credit for building and debugging an impressive number of these circuits. At the time of this writing 56 coil driver units have been produced for the labs. The fundamental design was adapted from Alan Stummer's "Triple Coil Driver"[91]. Most of the improvements to the base design are protection circuitry, a modular design, and a pseudo-differential input to prevent ground loops.

The coil driver assembly consists of three units: a coil driver, a front panel, and a custom high-current backplane. The coil driver board provides the basic functionality[92]. The front panel includes over-temperature protection logic, current monitor outputs, and status LEDs[93]. The high-current backplane is a lab-standard developed for high-current or cards that drive inductive loads[94]. The back plane is also used for DC shutter driver boards[95].

The goals of the design were to create generic interchangeable voltage-to-current drivers capable of driving an inductive load at ± 3 A and up to 5 A with small modification. Linear regulators have an intrinsic power dissipation issue. For a load R with a steady state current of I the power dissipated in the transistor regulating the current is $P_t = (V_s - IR)I$. For large over head voltages $V_{oh} = V_s - IR$, the power the transistor

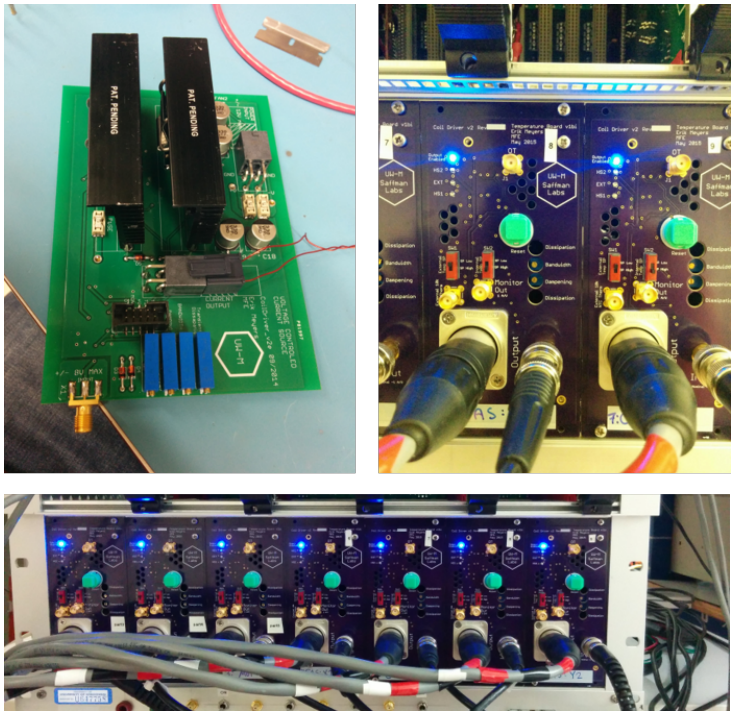

Figure D.1: The coil driver units. Clockwise from top-left: the coil driver board, the coil driver in its box with the purple front panel visible, and a full rack of 7 coil driver units.

must dissipate can be considerable. For example a typical load may be $R = 1\ \Omega$ driven at 3 A, if a supply voltage $V_s = 10$ V is used $P_t = 21$ W. The basic implementation uses forced air cooling and does not have the cooling power to handle this load. Temperature sensors on the transistor heat sinks will automatically short the op-amp to turn off the current if the temperature exceeds ~ 60 C. Unfortunately, switching times are improved with higher supply voltages, so it is common to run higher current coil drivers from a different, lower voltage power supply than lower current drivers that need to operate at higher bandwidths. The coil driver backplane has been designed to allow for units to operate at different supply voltages.

The accuracy of the current (Figure D.2) and current monitor (Figure D.3) calibrations are typically within 1% of nominal, which means in-situ re-calibration is not required for most applications.

The stability has been measured to be good to ± 20 ppm at 1 A after an initial warm-up

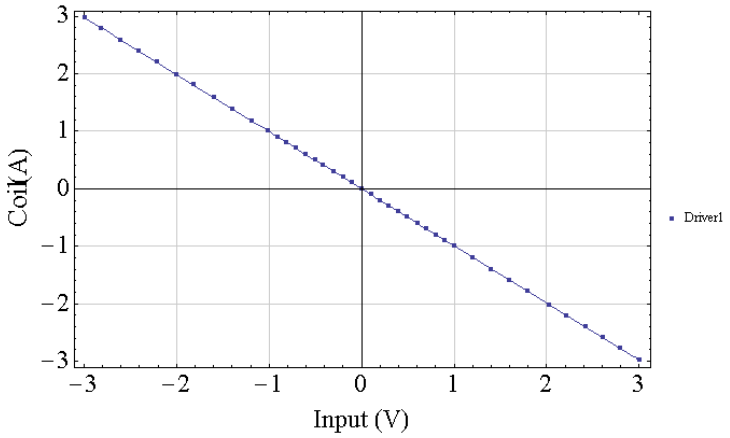

Figure D.2: An example calibration of a coil driver input. The linear fit for this data is $C(V_{in}) = 0.00129657 - 0.994236V_{in}$, where $C(V_{in} = -V_{in})$ is nominal.

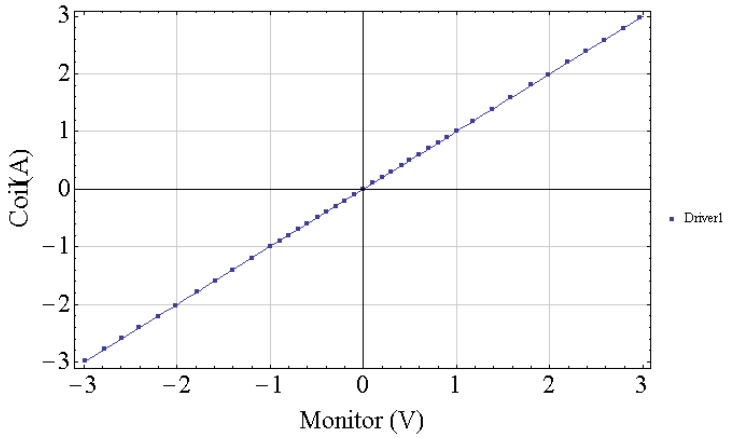

Figure D.3: An example calibration of a coil driver monitor output. The linear fit for this data is $C(V_{mon}) = 0.000271118 + 1.00031V_{mon}$, where $C(V_{mon} = V_{mon})$ is nominal.

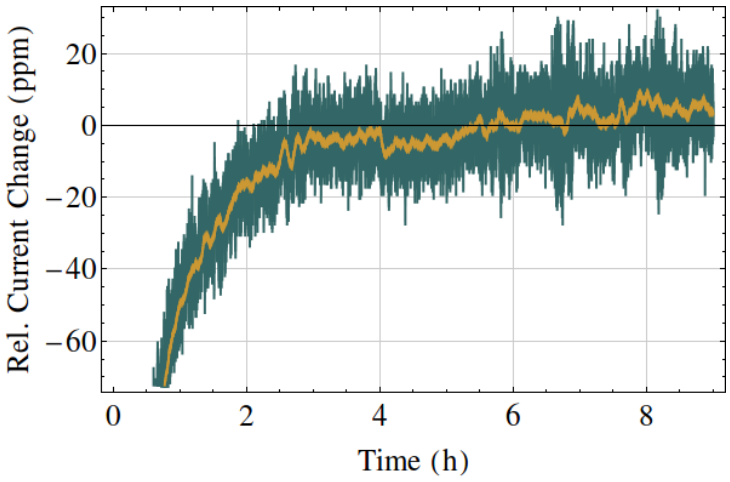

Figure D.4: Current output set at nominally 1 A, where the unit was cold started and drive off a stable, low-noise 5 V with a 400R and 1.6k voltage divider (metal film resistors) to give $\sim$ 1 V input control voltage.

of 3 hours, Figure D.4.

Switching times between DC current levels is an important design consideration. A typical method for improving switching time of an inductive load is to choose an appropriate dissipation resistor so that the LRC circuit is critically damped. This is not a general solution, instead the coil driver uses three feedback paths to compensate for the inductive load: a DC path, a "dampening" path, and a "bandwidth" path. The DC path feeds back to the instantaneous current level read from the low-side shunt resistor. The dampening and bandwidth feedback loops are high-passed measurements of the voltage before and after the load. If the coil undergoes a rapid change in frequency, the bandwidth and dampening paths will have a phase offset and the variable gains for each path allow the user to optimize the switching behavior. For a 1 mH 1 Ω load a $1/e$ switching time of 46 mus is typical.

Without adding additional control complexity, for example a toggle between high and low bandwidth modes, bandwidth and noise must be balanced for the application. The default 3 dB bandwidth is around 3.5 kHz. The current noise is dominated by $1/f$ noise out to 20 kHz. In this bandwidth the current noise is around 550 μA_{rms} for a 1 A current.

Appendix E

VME-derived Subrack System

Subrack systems that share a backplane have advantages over traditional boxed units typically used in lab settings. With some reasonable contraints on system parameters, the un-fun apsects of building electronics such as boxing, connectorizing, and powering units can be standardized. Since the mechanical design of a backplane system is not trivial we have decided to repurpose the 3U VME obsolete backplane with our own lab standard for connections. This allows us to minimize cabling by powering many devices with a single connection, sharing trigger bus lines, and a synchronized clock. We are following the original standard loosly for pinout definitions, such as reusing the +5 V power lines and replacing the ±12 V power with our ±15 V lab standard. The details of the "lab standard" pinout has not been finalized, so I will not be going into specifics. Instead I am laying out in broad strokes the framework for the project. Devices that build on this system are presented in following appendicies and the primary host card, the VMEMega, will be discussed here.

Each rack will have a control card that can sit anywhere in the unit, which will distribute triggers on the backplane to listening devices, as well as a 10 MHz GPS reference clock, and power status indicators. Devices can listen for triggers on the backplane but any device communication necessary will happen through Ethernet, since this technology

is robust, relatively easy to implement, and commercial solutions exist for routing.

We have found it cost effective an easy to build front panels from PCB boards to increase circuit density compared to a metal front panel. Chassis shielding with a PCB front panel can be accomplished by making ground planes on the PCB and plated mounting holes. Since we have ample experience with PCB manufactoring this is a good option.

The VMEMega is a custom Arduino Mega microcontroller design to match the VME's 3U Eurocard formfactor and provide a basis for expansion of simple circuits. Design files can be found at reference [96]. The VMEMega has 3 communication interfaces: USB/Serial, 10 Mbps Ethernet, and timing/triggering over the backplane. Any shield that works with the Arduino Mega will work with the VMEMega provided that the SPI bus connected Ethernet controller pins are not used. The hardware $\bar{CS}$ pin 53 and the Ethernet $R\bar{S}T$ pin 49, must not be used for other purposes. I have developed a command line development environment for compiling and uploading AVR and Arduino based firmware, which can be found at reference [97]. Eventually a set of libraries compatable with the Arduino IDE will be created from these libraries.[1]

[1] Eventually...

Appendix F

Transimpedance Amplifier

One of the challenges of operating a complicated experiment that requires a high degree of stability is the number of parameters that must be monitored and potentially incorporated into a feedback loop. For example, monitoring the lasers powers of the 2D- and 3D-MOT beams in-situ requires 10 detectors. At near 20 detectors per experiment and considering the four other experiments that have or will have similar a requirement, a custom solution is warranted given that a typical integrated transimpedance amplifier can cost upwards of $300 per unit. An advantage of a custom design is that the mechanics can be built to our needs. Furthermore, the circuit boards can be configured to work in "standalone"-mode where the photodiode is mounted some distance away due to space constraints or legacy hardware. Images of the integrate photodiode system can be seen in Figure F.1 and Figure F.2. A circuit schematic is shown in Figure F.3

Development of an optimal transimpedance amplifier is highly dependent on the expected photocurrent and desired output voltage.[1] These specifications set the feedback resistor, R_f, for the amplifier stage, while the photodiode capacitance (plus parasitic capacitance) and transimpedance resistor sets the bandwidth. To determine the maximum bandwidth of the device, we can model the transimpedance amplifier as an inductor

[1]You can read more about this project at my blog: http://www.mebert.org/thread/3, which like most blogs hasn't been updated in years. Also the blog has a custom content manager and totally cool, and not a waste of time.

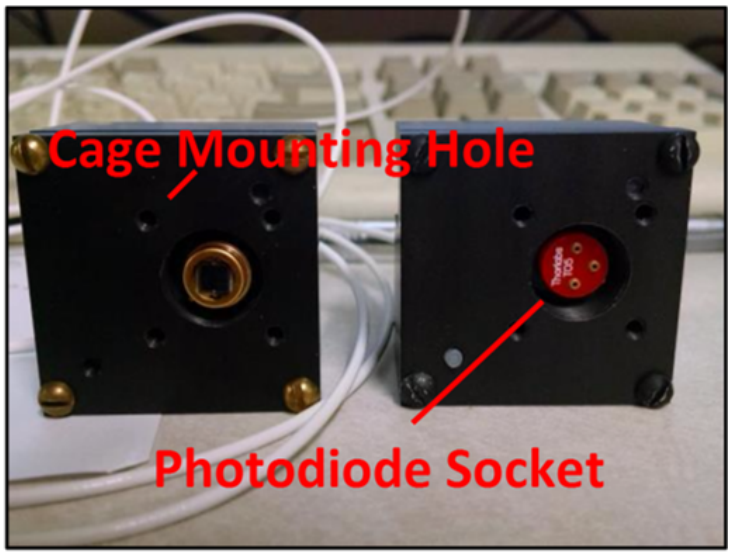

Figure F.1: An I2V_dii integrated transimpedance amplifier circuit enclosed in it's custom machined case.

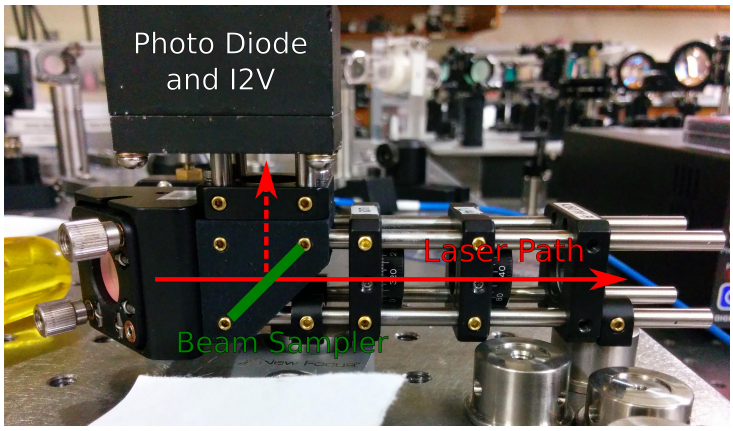

Figure F.2: An example in-situ mechanical set up where the I2V_dii is mounted to a 3D printed 16 mm cage mount that holds a 1/2" beam sampler at 45 degrees in the path of a laser.

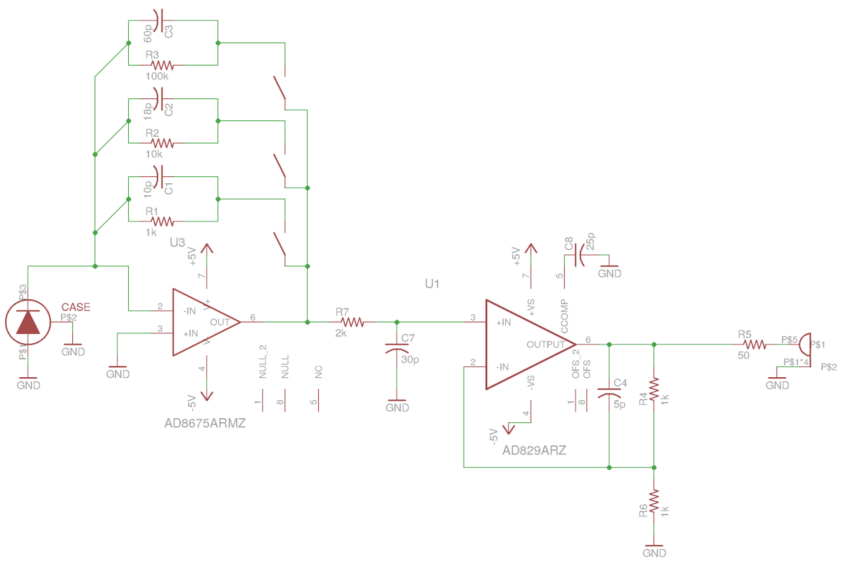

Figure F.3: The I2V_dii circuit schematic.

with inductance $L = R_f/2\pi GBW$, where GBW is the op-amp's gain bandwidth product. Any capacitance in the circuit will create an LC oscillator with resonant frequency $\omega_{LC} = (LC)^{-1/2}$, see Figure F.4. In order to avoid this resonant mode a feedback capacitor C_f is needed to decrease the closed-loop gain so that by ω_{LC} the closed-loop gain is less than unity. A larger bandwidth can be had by decreasing R_f at the cost of signal, or the photodiode capacitance which usually reduces the size of the photodiode.

To choose C_f optimally we use the formula:

$$C_f = \frac{\sqrt{8\pi \times GBW \times C_d R_f + 1} + 1}{4\pi \times GBW \times R_f}, \tag{F.1}$$

which makes sure that the asymptotic voltage loop gain (solid blue line) is equal to the op-amp's open loop gain (dashed red line) at the pole frequency f_p (green line), see Figure F.5. This condition guarantees stable behavior, but the actual design will require a slightly larger C_f to account for parasitics.

We have chosen to design the system for transimpedances of $\{10^3, 10^4, 10^5\}$ V/A, optimized at 10^4 V/A, with C_f's chosen for the FDS100 photodiode. To choose an op-amp we note that for precision op-amps input current i_n and voltage v_n noises are inversely

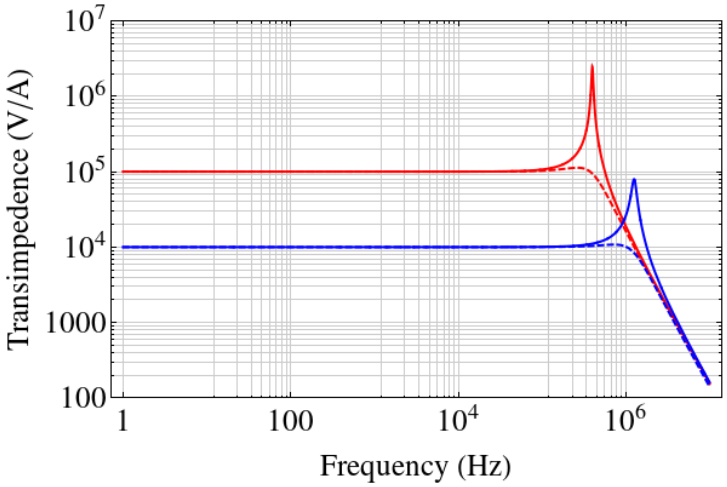

Figure F.4: A simple simulation of the current transfer function for a transimpedance amplifier with finite gain bandwidth product (GBW). The red(blue) curve is for an R_f = 100(10) kΩ. The solid lines demonstrate the resonance if no feedback capacitor C_f is included. The dashed lines include an appropriate C_f.

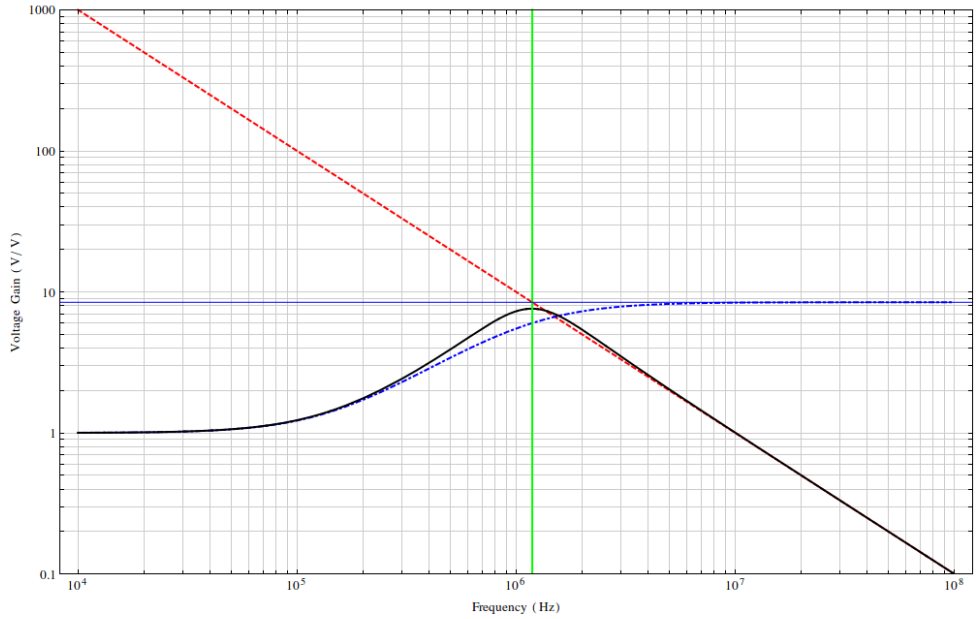

Figure F.5: A diagram demonstrating the characteristic of an optimally chosen feedback capacitor C_f according to Equation F.1. The solid black line is the voltage transfer function (V_{out}/V_{in}). The dashed blue line is the voltage loop gain (assumes infinite GBW), the solid blue line mark the asymptotic voltage-loop gain. The open loop gain of the op-amp is shown as a dashed red line. The choice of capacitor sets the pole frequency, f_p, shown in green. The pole frequency is optimal when it is aligned with the intersection of the asymptotic voltage loop gain and the op-amp open-loop gain.

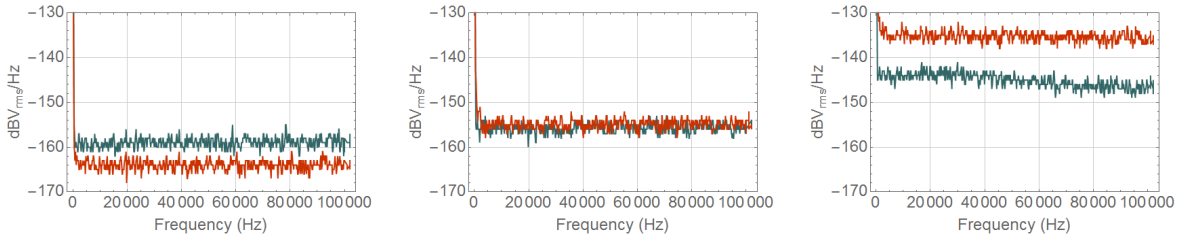

Figure F.6: Technical noise comparisons of the I2V_dii custom circuit (green) and a ThorLabs PDA36A (red) for transimpedance settings of (a) 1 kΩ, (b) 10 kΩ, and (c) 100 kΩ. The PDA36A outperforms our custom circuit, because they use an AD829 which has 4 dB lower voltage noise than the AD8675[99].

proportional. The optimal op-amp would have $v_n/i_n = R_f$ to minimize noise. We chose to use the AD8675 which has a $GBW = 10$ MHz, $i_n = 0.3$ pA/$\sqrt{\text{Hz}}$, and $v_n = 2.8$ nV/$\sqrt{\text{Hz}}$, which you may be surprised to note satisfies the condition $v_n/i_n \sim 10$ kΩ[98]. Another nice feature of the AD8675 is that the 1/f voltage noise is below the white noise floor by 20 Hz.

Comparing the current to voltage converter noise performance to the ThorLabs PDA36A which also uses a FDS100 photodiode, gives the results shown in Figure F.6.

The PDA36A has superior noise performance for lower R_f due to the choice of the AD829 op-amp as the transimpedance amplifier. Our circuit performs better for transimpedances of $R_f > 10$ kΩ since the current noise lower. The 1/f voltage noise of the AD8675 compared to the AD829 can be seen clearly by zooming in on the lower frequencies for $R_f = 10$ kΩ, as shown in Figure F.7

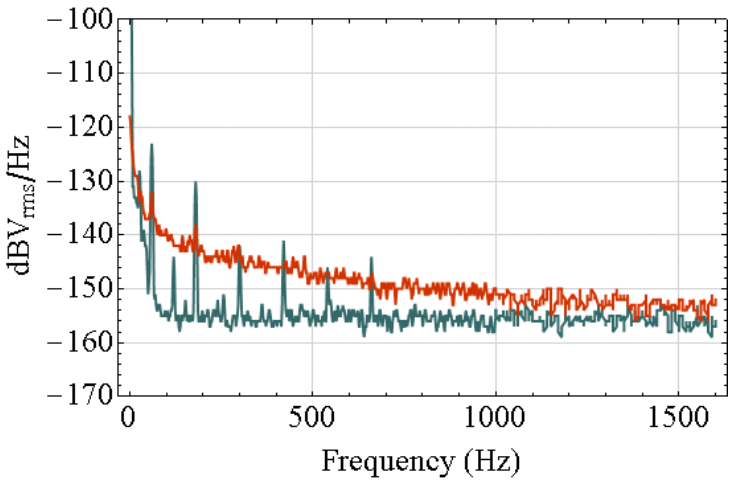

Figure F.7: Technical noise comparisons of the I2V_dii custom circuit (green) and a ThorLabs PDA36A (red) for a transimpedance setting of 10 kΩ at lower frequencies. The improved 1/f noise of the AD8675 is apparent in the data.

Appendix G

Power Distribution

Convenient distribution of power has been an issue in the lab. The previous standard was to have 4 mm "banana-plugs", plugged into a bus bar. This was a problem for a few reasons, namely: noise pick-up, form-factor, reliability and safety. Banana plugs have a standardized spacing of 0.75 in, which a for dual-sided circuit (+V, COM, -V) takes up in excess of 1.5 and requires 3 holes to be drilled. While properly grounding the shielding on the cable is possible with banana plugs, it has not often been done in our lab. Even if the cable was properly shielded, the separation of the banana jacks at the connection nodes would force a break in the shielding. Additionally, the old distribution system was designed to have low impedance between nodes at all frequencies This means noisy devices could add noise to all other devices on the line. Our ability to make cables in the lab depended on reliable construction by undergraduate labor. Any undergraduate (or graduate student) capable of reliably building cables should probably be doing other more important and interesting tasks. Finally, no fuses existed in the system, so a bad device could break itself, something else, or start a fire.

To correct for these factors, we have switched to a new power distribution systems. We have chosen XLR and mini-XLR connectors to route power between nodes, since they are common and designed to function in the audio frequency band where our electronics

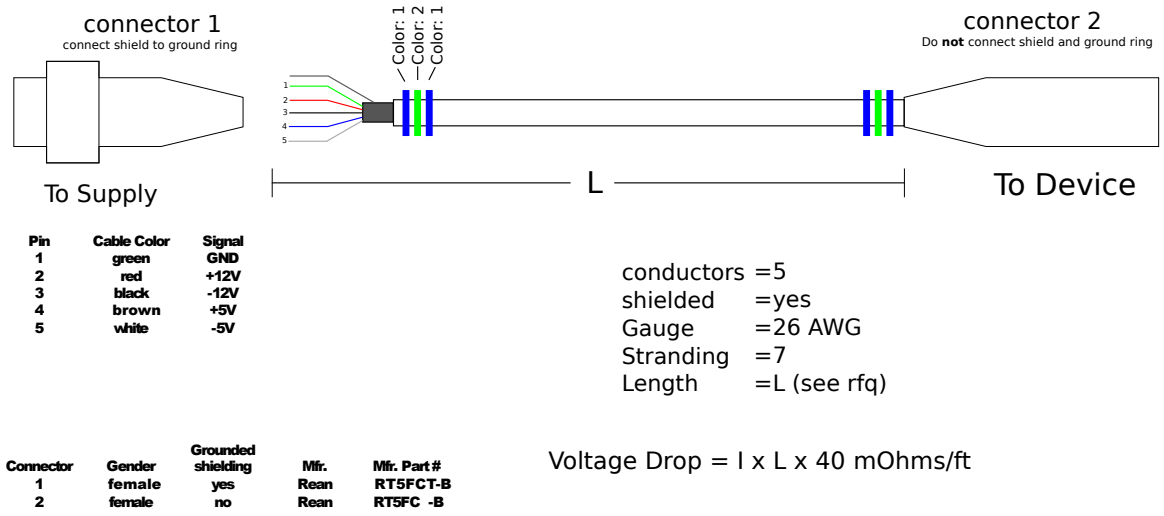

Figure G.1: Technical drawing for sourcing mini-XLR cable for power distribution.

typically operate. This appendix will discuss the distribution of power for the VME-based Power Distribution Units (PDU), but the practices discussed can and should be implemented when designing distribution systems for non-standard voltages. Most of our electronics use ±15(12) V, ±5 V, and COM. We use 5-pin mini-XLR cables that we have manufactured externally in 3, 6, and 10 ft lengths, see Figure G.1. The cables are color coded in a pseudo-unique pattern to help identification of each cable end. The cable shield is connected to common at one end of the cable. This end of cable plugs into the distribution unit. The end is marked, and has a screw-on connector for identification. The device end is plug-in (snap) connector.

The PDU unit is a 3U eurocard format with a VME backplane connector, and pulls ±15(12) V, +5 V, and COM from the VME backplane, see Figure G.2. The PDU has a linear regulator for generating −5 V from the −12 V bus. The +5 V bus typically powers

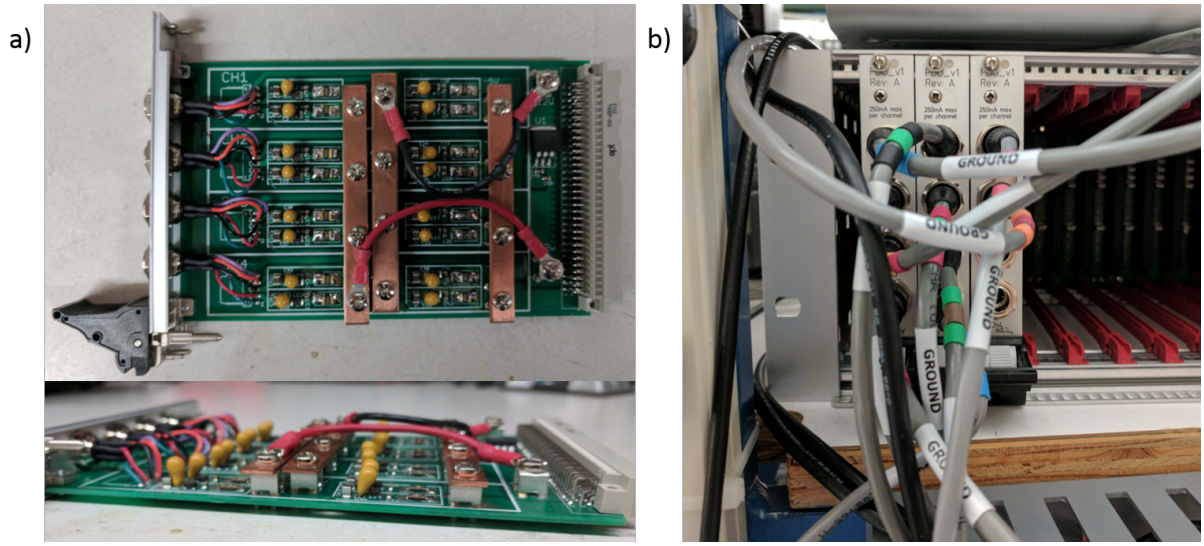

Figure G.2: (a) Image of a PDU card by itself, (b) and in a 3U subrack.

digital electronics. So if an analog +5 V source is desired on a device, it is recommended that device use a linear regulator and generate +5 V from the +15 V line. The schematic for the PDU is shown in Figure G.3. Each output line is individually fused with a PPTC resettable fuse and filtered to prevent noise transfer between devices. A link to the PDU design files can be found at reference [100].

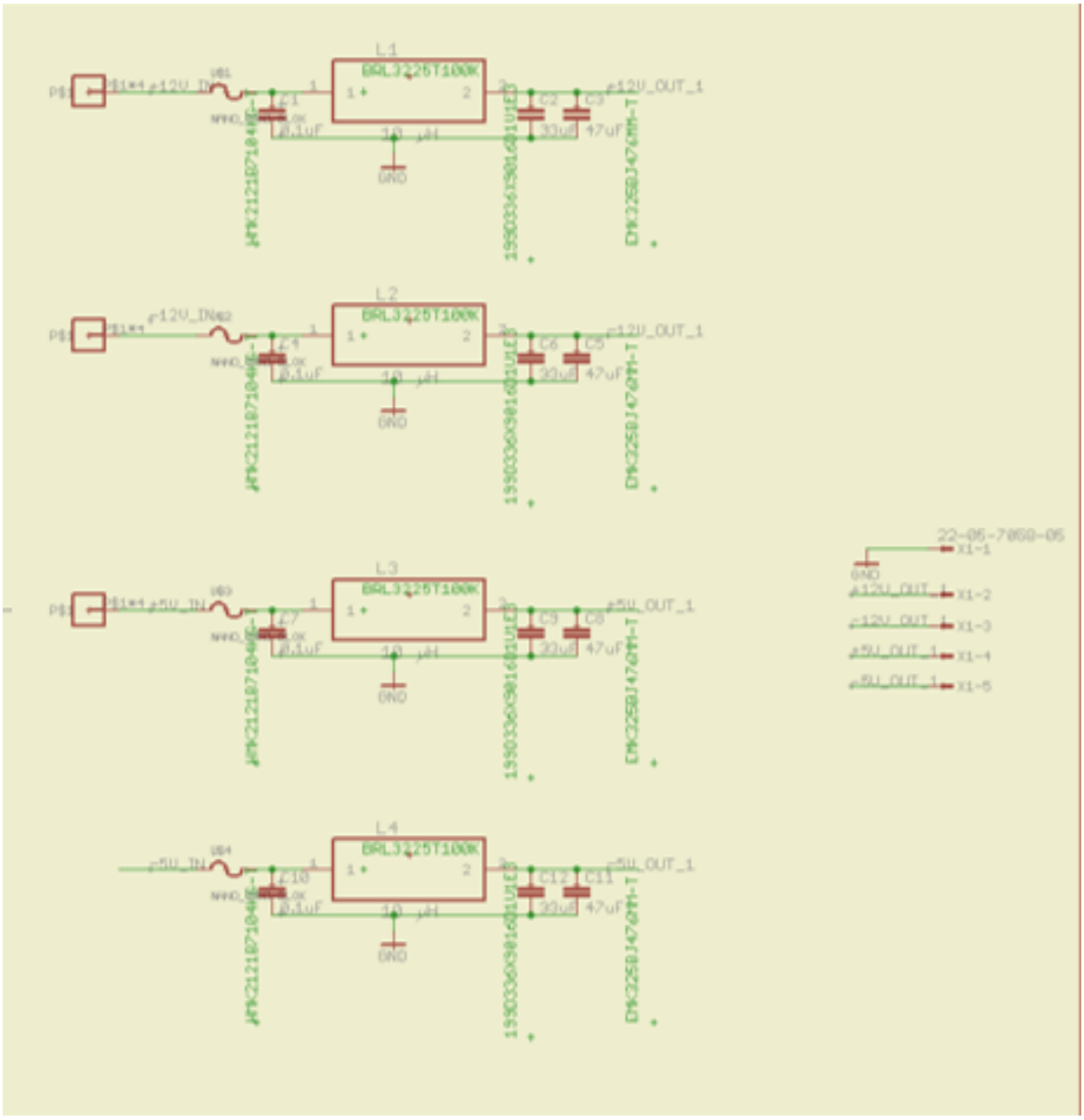

Figure G.3: Electrical schematic for one channel of the PDU card.

Appendix H

MegaDAQ

Monitoring and stabilizing experimental and environmental parameters is important in a sensitive experiment that must run continuously with minimal downtime. Examples of parameters of interest are laser powers, loser lock states, background magnetic fields, lab temperature, and humidity. Understanding and controlling drifts for all of these parameters and more are important to maintaining the performance of the apparatus. Commercial systems are typically either easy to setup but use a proprietary interface or if they are general purpose require a significant amount of effort to integrate and have a high per channel cost. Instead we have developed an Arduino Mega shield based around a Texas Instruments AMC7182 12-bit 16 channel ADC and 12 channel DAC. The design files for the device can be found at reference [101], and a C++ AVR/Arduino driver for the ADC/DAC can be found at reference [102]. The MegaDAQ is designed to work with both a standard Arduino Mega and the lab's custom VMEMega which is a custom Ethernet connected Arduino Mega that matches the VME 3U Eurocard form-factor. Images of the MegaDAQ can be seen in Figure H.1.

The newest version of the MegaDAQ was recently completed where the form factor was changed. The VMEMega host board pictured is from the previous form factor. Normally the front of the two boards will be flush, and a front panel board will provide

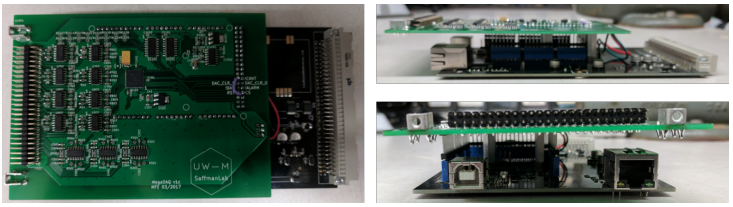

Figure H.1: The current generation MegaDAQ shield connected to the previous generation VMEMega host board.

a connectorized interface.

The ADCs are buffered by pseudo-differential op-amps which serves to isolate input devices and prevent ground loops. Each ADC channel can be electronically switched between ±2.5 V and 0-5 V operation range. The DACs are buffered as well, but only operate in single ended mode with 0-12 V range.

With the VMEMega Analog data can be streamed to the Origin data collection server, described in the next appendix. This is how the laser lock data was acquired in Figure 8.12. Some examples of data streaming can be found at reference [101] in the examples folder.

Appendix I

Origin Data Server

Storing, processing, and displaying large amounts of experimental and environmental data is a common problem in a lab setting. Typically many implementation specific solutions are developed over the course of a graduate student's lifetime. While most graduate students are fully capable of the above tasks, each person solution is typically different an incompatible with solutions developed by other researchers. The Origin data server is an attempt at standardizing the storage of data in a flexible and fast way, that allows for quick and standardized access to all data types stored.

Origin is a simple monitoring server, based on ZeroMQ with options to send data using a compact binary format or a simple JSON object. The data is stored by the server in HDF5 files, MySQL databases, CSV files, or any other format that can match the backend API, making it extremely portable and easy to use. The server was designed to provide a common and uniform interface framework to facilitate the aggregation, storing, and serving of data.

The distinguishing feature of Origin compared to other monitoring systems, such as those designed to monitor large groups of servers, is that the data streams are dynamic instead of monolithic. The server is passive and requires no specialized person to add a data stream. A node registers itself with the server, through a predefined format, the

type of data it will be sending. The server configures the backend to accept the new data stream, then proceeds to store data when it is sent. The data can then be read by polling, or subscribed to and the server will push new data to the subscribed device.

Besides just storing and retrieving data, alerts can be generated by the server for when a data stream meets some condition. For example if a laser becomes unlocked, the atom loading rate changes, or the temperature of the room is rising the user can be notified. Distributed slow feedback systems can be also be implemented through the server, where one device is recording the laser power, while a second device is subscribed to the data stream and adjusts the RF power to an AOM to maintain the power level. Programs can be developed to process heavy data loads live with some latency and then save the results back to the same server. For example, one could implement an analysis that updates atom signal threshold cuts for digitization by comparing the last N camera shots, and then saves the results to the sever, which the experiment controller could be subscribed to.

The system is simple to use and to expand in arbitrary ways as the complexity of the experiment expands, and doesn't require any upfront investment besides setting up a server. The GitHub repository contains more information and should be referenced for specifics [103].

Bibliography

[1]C. J. Ballance, T. P. Harty, N. M. Linke, M. A. Sepiol, and D. M. Lucas, "High-fidelity quantum logic gates using trapped-ion hyperfine qubits", Phys. Rev. Lett. **117**, 060504 (2016).

[2]R. Barends, J. Kelly, A. Megrant, A. Veitia, D. Sank, E. Jeffrey, T. C. White, J. Mutus, A. G. Fowler, B. Campbell, Y. Chen, Z. Chen, B. Chiaro, A. Dunsworth, C. Neill, P. Oalley, P. Roushan, A. Vainsencher, J. Wenner, A. N. Korotkov, A. N. Cleland, and J. M. Martinis, "Superconducting quantum circuits at the surface code threshold for fault tolerance", Nature **508**, Letter, 500–503 (2014).

[3]K. M. Maller, M. T. Lichtman, T. Xia, Y. Sun, M. J. Piotrowicz, A. W. Carr, L. Isenhower, and M. Saffman, "Rydberg-blockade controlled-not gate and entanglement in a two-dimensional array of neutral-atom qubits", Phys. Rev. A **92**, 022336 (2015).

[4]T. Xia, M. Lichtman, K. Maller, A. W. Carr, M. J. Piotrowicz, L. Isenhower, and M. Saffman, "Randomized benchmarking of single-qubit gates in a 2d array of neutral-atom qubits", Phys. Rev. Lett. **114**, 100503 (2015).

[5]A. Bermudez, X. Xu, R. Nigmatullin, J. O'Gorman, V. Negnevitsky, P. Schindler, T. Monz, U. G. Poschinger, C. Hempel, J. Home, F. Schmidt-Kaler, M. Biercuk, R. Blatt, S. Benjamin, and M. Müller, *Assessing the progress of trapped-ion processors towards fault-tolerant quantum computation*, `arXiv:1705.02771 [quant-ph]`, 2017.

[6]S. Boixo, S. V. Isakov, V. N. Smelyanskiy, R. Babbush, N. Ding, Z. Jiang, M. J. Bremner, J. M. Martinis, and H. Neven, *Characterizing quantum supremacy in near-term devices*, arXiv:1608.00263 [quant-ph], 2016.

[7]T. D. Ladd, F. Jelezko, R. Laflamme, Y. Nakamura, C. Monroe, and J. L. O'Brien, "Quantum computers", Nature **464**, 45–53 (2010).

[8]M. Reiher, N. Wiebe, K. M. Svore, D. Wecker, and M. Troyer, *Elucidating reaction mechanisms on quantum computers*, arXiv:1608.00263 [quant-ph], 2016.

[9]C. Chamberland, T. Jochym-O'Connor, and R. Laflamme, "Overhead analysis of universal concatenated quantum codes", Phys. Rev. A **95**, 022313 (2017).

[10]M. D. Lukin, M. Fleischhauer, R. Cote, L. M. Duan, D. Jaksch, J. I. Cirac, and P. Zoller, "Dipole blockade and quantum information processing in mesoscopic atomic ensembles", Phys. Rev. Lett. **87**, 037901 (2001).

[11]E. Brion, K. Mølmer, and M. Saffman, "Quantum computing with collective ensembles of multilevel systems", Phys. Rev. Lett. **99**, 260501 (2007).

[12]A. V. Carpentier, Y. H. Fung, P. Sompet, A. J. Hilliard, T. G. Walker, and M. F. Andersen, "Preparation of a single atom in an optical microtrap", Laser Phys. Lett. **10**, 125501 (2013).

[13]W. S. Bakr, A. Peng, M. E. Tai, R. Ma, J. Simon, J. I. Gillen, S. Fölling, L. Pollet, and M. Greiner, "Probing the superfluid to mott insulator transition at the single-atom level", Science **329**, 547–550 (2010).

[14]M. Endres, H. Bernien, A. Keesling, H. Levine, E. R. Anschuetz, A. Krajenbrink, C. Senko, V. Vuletić, M. Greiner, and M. D. Lukin, "Atom-by-atom assembly of defect-free one-dimensional cold atom arrays", Science **354**, 1024–1027 (2016).

[15]D. Barredo, S. de Léséleuc, V. Lienhard, T. Lahaye, and A. Browaeys, "An atom-by-atom assembler of defect-free arbitrary two-dimensional atomic arrays", Science **354**, 1021–1023 (2016).

[16]F. Serwane, G. Zürn, T. Lompe, T. B. Ottenstein, A. N. Wenz, and S. Jochim, "Deterministic preparation of a tunable few-fermion system", Science **332**, 336–338 (2011).

[17]L. H. Pedersen, and K. Mølmer, "Few qubit atom-light interfaces with collective encoding", Phys. Rev. A **79**, 012320 (2009).

[18]A. Gaetan, Y. Miroshnychenko, T. Wilk, A. Chotia, M. Viteau, D. Comparat, P. Pillet, A. Browaeys, and P. Grangier, "Observation of collective excitation of two individual atoms in the rydberg blockade regime", Nat. Phys. **5**, 115–118 (2009).

[19]Y. O. Dudin, L. Li, F. Bariani, and A. Kuzmich, "Observation of coherent many-body rabi oscillations", Nat. Phys. **8**, 790–794 (2012).

[20]M. Ebert, A. Gill, M. Gibbons, X. Zhang, M. Saffman, and T. G. Walker, "Atomic fock state preparation using rydberg blockade", Phys. Rev. Lett. **112**, 043602 (2014).

[21]J. Zeiher, P. Schauß, S. Hild, T. Macrì, I. Bloch, and C. Gross, "Microscopic characterization of scalable coherent rydberg superatoms", Phys. Rev. X **5**, 031015 (2015).

[22]M. H. Levitt, "Composite pulses", in *Emagres* (John Wiley & Sons, Ltd, 2007).

[23]I. I. Beterov, M. Saffman, V. P. Zhukov, D. B. Tretyakov, V. M. Entin, E. A. Yakshina, I. I. Ryabtsev, C. W. Mansell, C. MacCormick, S. Bergamini, and et al., "Coherent control of mesoscopic atomic ensembles for quantum information", Laser Physics **24**, 074013 (2014).

[24]I. I. Beterov, M. Saffman, E. A. Yakshina, D. B. Tretyakov, V. M. Entin, G. N. Hamzina, and I. I. Ryabtsev, "Simulated quantum process tomography of quantum gates with rydberg superatoms", Journal of Physics B: Atomic, Molecular and Optical Physics **49**, 114007 (2016).

[25]A. T. Gill, "Progress towards deterministic generation of entangled w-states of neutral atoms using rydberg blockade", PhD thesis (University of Wisconsin - Madison, 2014).

[26]M. Saffman, T. G. Walker, and K. Mølmer, "Quantum information with rydberg atoms", Rev. Mod. Phys. **82**, 2313–2363 (2010).

[27]W. Dür, G. Vidal, and J. I. Cirac, "Three qubits can be entangled in two inequivalent ways", Phys. Rev. A **62**, 062314 (2000).

[28]L. Isenhower, E. Urban, X. Zhang, A. Gill, T. Henage, T. A. Johnson, T. Walker, and M. Saffman, "Demonstration of a neutral atom controlled-not quantum gate", Phys Rev Lett **104**, 010503 (2010).

[29]L. Duan, B. B. Blinov, D. L. Moehring, and C. R. Monroe, "Scalable trapped ion quantum computation with a probabilistic ion-photon mapping", Quantum Inf. Comput. **4**, 165–173 (2004).

[30]L. Jiang, J. M. Taylor, A. S. Sørensen, and M. D. Lukin, "Distributed quantum computation based on small quantum registers", Phys. Rev. A **76**, 062323 (2007).

[31]P. Kómár, E. M. Kessler, M. Bishof, L. Jiang, A. S. Sørensen, J. Ye, and M. D. Lukin, "A quantum network of clocks", Nat. Phys. **10**, 582–587 (2014).

[32]P. Kómár, T. Topcu, E. M. Kessler, A. Derevianko, V. Vuletić, J. Ye, and M. D. Lukin, "Quantum network of atom clocks: a possible implementation with neutral atoms", Phys. Rev. Lett. **117**, 060506 (2016).

[33]A. K. Ekert, "Quantum cryptography based on bell's theorem", Phys. Rev. Lett. **67**, 661–663 (1991).

[34]J.-M. Fromenteau, and V. G. Diaz, *Smart optical fibre infrastructure*, tech. rep. WP4041 (Corning, Inc., Corning, NY, Jan. 2012).

[35]L. M. Duan, M. D. Lukin, J. I. Cirac, and P. Zoller, "Long-distance quantum communication and with atomic ensembles and linear optics", Nature, 413–418 (2001).

[36]B. Zhao, M. Müller, K. Hammerer, and P. Zoller, "Efficient quantum repeater based on deterministic rydberg gates", Phys. Rev. A **81**, 052329 (2010).

[37]Y. Han, B. He, K. Heshami, C.-Z. Li, and C. Simon, "Quantum repeaters based on rydberg-blockade-coupled atomic ensembles", Phys. Rev. A **81**, 052311 (2010).

[38]A. G. Fowler, D. S. Wang, C. D. Hill, T. D. Ladd, R. Van Meter, and L. C. L. Hollenberg, "Surface code quantum communication", Phys. Rev. Lett. **104**, 180503 (2010).

[39]M. Saffman, and T. Walker, "Creating single-atom and single-photon sources from entangled atomic ensembles", Phys. Rev. A **66**, 065403 (2002).

[40]L. Li, Y. Dudin, and A. Kuzmich, "Entanglement between light and an optical atomic excitation", Nature **498**, 466–469 (2013).

[41]M. Ebert, M. Kwon, T. Walker, and M. Saffman, "Coherence and rydberg blockade of atomic ensemble qubits", Phys Rev Lett **115**, 093601 (2015).

[42]N. Solmeyer, X. Li, and Q. Quraishi, "High teleportation rates using cold-atom-ensemble-based quantum repeaters with rydberg blockade", Phys. Rev. A **93**, 042301 (2016).

[43]T. A. Johnson, "Rabi oscillations and excitation blockade between ground and rydberg states of single optically trapped rubidium atoms", PhD thesis (University of Wisconsin - Madison, 2008).

[44]E. Urban, "Coherent manipulation of single atom qubits using rydberg states", PhD thesis (University of Wisconsin - Madison, 2009).

[45]L. Isenhower, "Demonstration of rydberg blockade, a neutral atom cnot gate, and entanglement generation", PhD thesis (University of Wisconsin - Madison, 2010).

[46]D. Jaksch, J. Cirac, P. Zoller, S. Rolston, R. Côté, and M. Lukin, "Fast quantum gates for neutral atoms", Phys. Rev. Lett. **85**, 2208 (2000).

[47]A. C. J. Wade, M. Mattioli, and K. Mølmer, "Single-atom single-photon coupling facilitated by atomic-ensemble dark-state mechanisms", Phys. Rev. A **94**, 053830 (2016).

[48]H. Weimer, M. Müller, I. Lesanovsky, P. Zoller, and H. P. Büchler, "A rydberg quantum simulator", Nat. Phys. **6**, 382–388 (2010).

[49]M. T. DePue, C. McCormick, S. L. Winoto, S. Oliver, and D. S. Weiss, "Unity occupation of sites in a 3d optical lattice", Phys Rev Lett **82**, 2262 (1999).

[50]A. Hilliard, Y. Fung, P. Sompet, A. Carpentier, and M. Andersen, "In-trap fluorescence detection of atoms in a microscopic dipole trap", Phys. Rev. A **91**, 053414 (2015).

[51]T. Niederprüm, O. Thomas, T. Manthey, T. M. Weber, and H. Ott, "Giant cross section for molecular ion formation in ultracold rydberg gases", Phys Rev Lett **115**, 013003 (2015).

[52]T. G. Walker, and M. Saffman, "Consequences of zeeman degeneracy for the van der waals blockade between rydberg atoms", Phys. Rev. A **77**, 032723 (2008).

[53]Y. Wang, X. Zhang, T. A. Corcovilos, A. Kumar, and D. S. Weiss, "Coherent addressing of individual neutral atoms in a 3d optical lattice", Phys. Rev. Lett. **115**, 043003 (2015).

[54]S. Kuhr, W. Alt, D. Schrader, I. Dotsenko, Y. Miroshnychenko, A. Rauschenbeutel, and D. Meschede, "Analysis of dephasing mechanisms in a standing-wave dipole trap", Phys. Rev. A **72**, 023406 (2005).

[55]D. Yavuz, P. Kulatunga, E. Urban, T. A. Johnson, N. Proite, T. Henage, T. Walker, and M. Saffman, "Fast ground state manipulation of neutral atoms in microscopic optical traps", Phys Rev Lett **96**, 063001 (2006).

[56]F. Haas, J. Volz, R. Gehr, J. Reichel, and J. Estève, "Entangled states of more than 40 atoms in an optical fiber cavity", Science **344**, 180–183 (2014).

[57]A. Derevianko, P. Kómár, T. Topcu, R. M. Kroeze, and M. D. Lukin, "Effects of molecular resonances on rydberg blockade", Phys. Rev. A **92**, 063419 (2015).

[58]T. Keating, K. Goyal, Y.-Y. Jau, G. W. Biedermann, A. J. Landahl, and I. H. Deutsch, "Adiabatic quantum computation with rydberg-dressed atoms", Phys. Rev. A **87**, 052314 (2013).

[59]A. Schwettmann, J. Crawford, K. R. Overstreet, and J. P. Shaffer, "Cold cs rydberg-gas interactions", Phys. Rev. A **74**, 020701 (2006).

[60]T. Amthor, C. Giese, C. S. Hofmann, and M. Weidemüller, "Evidence of antiblockade in an ultracold rydberg gas", Phys. Rev. Lett. **104**, 013001 (2010).

[61]C. A. Sackett, D. Kielpinski, B. E. King, C. Langer, V. Meyer, C. J. Myatt, M. Rowe, Q. A. Turchette, W. M. Itano, D. J. Wineland, and C. Monroe, "Experimental entanglement of four particles", Nature **404**, 256–259 (2000).

[62]C. Tresp, P. Bienias, S. Weber, H. Gorniaczyk, I. Mirgorodskiy, H. P. Büchler, and S. Hofferberth, "Dipolar dephasing of rydberg *d*-state polaritons", Phys. Rev. Lett. **115**, 083602 (2015).

[63]R. Boddeda, I. Usmani, E. Bimbard, A. Grankin, A. Ourjoumtsev, E. Brion, and P. Grangier, "Rydberg-induced optical nonlinearities from a cold atomic ensemble trapped inside a cavity", J. Phys. B: At. Mol. Opt Phys. **49**, 084005 (2016).

[64]L. Béguin, A. Vernier, R. Chicireanu, T. Lahaye, and A. Browaeys, "Direct measurement of the van der waals interaction between two rydberg atoms", Phys Rev Lett **110**, 263201 (2013).

[65]M. Schlagmüller, T. C. Liebisch, F. Engel, K. S. Kleinbach, F. Böttcher, U. Hermann, K. M. Westphal, A. Gaj, R. Löw, S. Hofferberth, T. Pfau, J. Pérez-Ríos, and C. H. Greene, "Ultracold chemical reactions of a single rydberg atom in a dense gas", Phys. Rev. X **6**, 031020 (2016).

[66]D. Booth, S. Rittenhouse, J. Yang, H. Sadeghpour, and J. Shaffer, "Production of trilobite rydberg molecule dimers with kilo-debye permanent electric dipole moments", Science **348**, 99–102 (2015).

[67]E. Fermi, "Displacement by pressure of the high lines of the spectral series", Nuovo Cimento **11**, 157–166 (1934).

[68]F. T. Arecchi, E. Courtens, R. Gilmore, and H. Thomas, "Atomic coherent states in quantum optics", Phys. Rev. A **6**, 2211–2237 (1972).

[69]J. Dalibard, Y. Castin, and K. Mølmer, "Wave-function approach to dissipative processes in quantum optics", Phys Rev Lett **68**, 580 (1992).

[70]M. Ebert, https://github.com/mfe5003/Rydberg-Blockade-Simulator, 2013.

[71]T. Arpornthip, C. Sackett, and K. Hughes, "Vacuum-pressure measurement using a magneto-optical trap", Phys. Rev. A **85**, 033420 (2012).

[72]C. D. Wallace, T. P. Dinneen, K.-Y. N. Tan, T. T. Grove, and P. L. Gould, "Isotopic difference in trap loss collisions of laser cooled rubidium atoms", Phys Rev Lett **69**, 897 (1992).

[73]S. Gensemer, P. Gould, P. Leo, E. Tiesinga, and C. Williams, "Ultracold 87 rb ground-state hyperfine-changing collisions in the presence and absence of laser light", Phys. Rev. A **62**, 030702 (2000).

[74]T. G. Walker, and P. Feng, "Measurements of collisions between laser-cooled atoms", Adv. At. Mol. Opt. Phy. **34**, 125 (1994).

[75]T. A. Savard, K. M. O'Hara, and J. E. Thomas, "Laser noise induced heating in far off resonance optical traps", in Quantum electronics and laser science conference (1997), QPD6.

[76]M. Ebert, https://github.com/mfe5003/LAC-Discrete-Model, 2013.

[77]M. Saffman, and T. G. Walker, "Entangling single- and n-atom qubits for fast quantum state detection and transmission", Phys. Rev. A **72**, 042302 (2005).

[78]M. M. Dorantes, "Fast non-destructive internal state detection of neutral atoms in optical potentials", PhD thesis (Universitäts- und Landesbibliothek Bonn, 2016).

[79]M. Kwon, M. Ebert, C. Young, T. Walker, and M. Saffman, "Nondestructive fluorescence detection of hyperfine states of rb using an emccd camera", in Bull. am. phys. soc. (2017).

[80]M. J. Gibbons, C. D. Hamley, C.-Y. Shih, and M. S. Chapman, "Nondestructive fluorescent state detection of single neutral atom qubits", Phys Rev Lett **106**, 133002 (2011).

[81]V. Bagnato, L. Marcassa, S. Miranda, S. Muniz, and A. de Oliveira, "Measuring the capture velocity of atoms in a magneto-optical trap as a function of laser intensity", Phys. Rev. A **62**, 013404 (2000).

[82]J. H. Moore, M. A. Coplan, and C. C. Davis, *Building scientific apparatus: a practical guide to design and construction* (Addison-Wesley, London, 1983).

[83]J. Schoser, A. Batär, R. Löw, V. Schweikhard, A. Grabowski, Y. B. Ovchinnikov, and T. Pfau, "Intense source of cold rb atoms from a pure two-dimensional magneto-optical trap", Phys. Rev. A **66**, 023410 (2002).

[84]G. H. Zhang, B. Braverman, A. Kawasaki, and V. Vuletić, "Note: fast compact laser shutter using a direct current motor and three-dimensional printing", Rev. Sci. Instrum. **86**, 126105 (2015).

[85]A. Franzen, *Componentlibrary*, `http://www.gwoptics.org/ComponentLibrary/`.

[86]M. Mack, F. Karlewski, H. Hattermann, S. Höckh, F. Jessen, D. Cano, and J. Fortágh, "Measurement of absolute transition frequencies of 87Rb to nS and nD rydberg states by means of electromagnetically induced transparency", Phys. Rev. A **83**, 052515 (2011).

[87]I. I. Beterov, and M. Saffman, "Rydberg blockade, förster resonances, and quantum state measurements with different atomic species", Phys. Rev. A **92**, 042710 (2015).

[88]F. Luecke, and A. Tuganov, "Piezoelectric actuator for optical alignment screws" (Apr. 1995), U.S. Patent 5,410,206.

[89]M. Ebert, https://github.com/QuantumQuadrate/pypico, 2016.

[90]A. Micklich, https://github.com/QuantumQuadrate/ArduinoDecoder, 2016.

[91]A. Stummer, *Triple coil driver*, https://www.physics.utoronto.ca/~astummer/pub/mirror/Projects/Archives, 2014.

[92]E. Meyers, and M. Ebert, https://github.com/QuantumQuadrate/Coil-Driver, 2013.

[93]E. Meyers, and M. Ebert, https://github.com/QuantumQuadrate/Coil-Driver-Front-Panel, 2013.

[94]M. Ebert, https://github.com/QuantumQuadrate/High-Current-Backplane, 2013.

[95]L. Fleming, https://github.com/QuantumQuadrate/DC-Shutters, 2016.

[96]M. Ebert, https://github.com/QuantumQuadrate/VMEMega, 2017.

[97]M. Ebert, https://github.com/Orthogonal-Systems/ocsbase, 2017.

[98]*36 v precision, 2.8 nv/rthz rail-to-rail output op amp*, AD8675, Rev. E, Analog Devices, Inc. (2017).

[99]*High speed, low noise video op amp*, AD829, Rev. I, Analog Devices, Inc. (2017).

[100]M. Ebert, and L. Fleming, https://github.com/QuantumQuadrate/PDU, 2015.

[101]M. Ebert, https://github.com/Orthogonal-Systems/MegaDAQ, 2017.

[102]M. Ebert, https://github.com/Orthogonal-Systems/amc7812, 2016.

[103]M. Ebert, and I. Wisher, https://github.com/Orthogonal-Systems/Origin, 2017.